frontiers | Research Topics

Editor's challenge in medical physics and imaging: Quantitative medical imaging

Edited by
Thomas Beyer and Ewald V. Moser

Published in
Frontiers in Physics

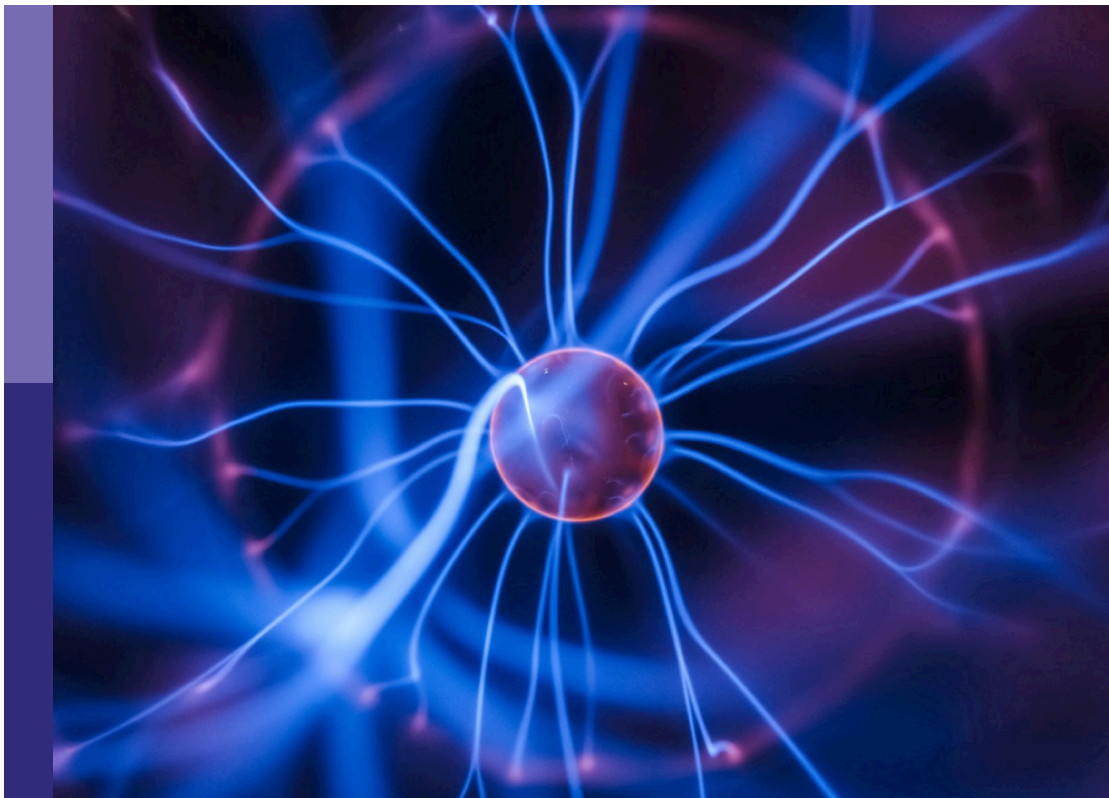

ISSN 1664-8714
ISBN 978-2-8325-5007-6
DOI 10.3389/978-2-8325-5007-6

About Frontiers

Frontiers is more than just an open access publisher of scholarly articles: it is a pioneering approach to the world of academia, radically improving the way scholarly research is managed. The grand vision of Frontiers is a world where all people have an equal opportunity to seek, share and generate knowledge. Frontiers provides immediate and permanent online open access to all its publications, but this alone is not enough to realize our grand goals.

Frontiers journal series

The Frontiers journal series is a multi-tier and interdisciplinary set of open-access, online journals, promising a paradigm shift from the current review, selection and dissemination processes in academic publishing. All Frontiers journals are driven by researchers for researchers; therefore, they constitute a service to the scholarly community. At the same time, the *Frontiers journal series* operates on a revolutionary invention, the tiered publishing system, initially addressing specific communities of scholars, and gradually climbing up to broader public understanding, thus serving the interests of the lay society, too.

Dedication to quality

Each Frontiers article is a landmark of the highest quality, thanks to genuinely collaborative interactions between authors and review editors, who include some of the world's best academicians. Research must be certified by peers before entering a stream of knowledge that may eventually reach the public - and shape society; therefore, Frontiers only applies the most rigorous and unbiased reviews. Frontiers revolutionizes research publishing by freely delivering the most outstanding research, evaluated with no bias from both the academic and social point of view. By applying the most advanced information technologies, Frontiers is catapulting scholarly publishing into a new generation.

What are Frontiers Research Topics?

Frontiers Research Topics are very popular trademarks of the *Frontiers journals series*: they are collections of at least ten articles, all centered on a particular subject. With their unique mix of varied contributions from Original Research to Review Articles, Frontiers Research Topics unify the most influential researchers, the latest key findings and historical advances in a hot research area.

Find out more on how to host your own Frontiers Research Topic or contribute to one as an author by contacting the Frontiers editorial office: frontiersin.org/about/contact

Editor's challenge in medical physics and imaging: Quantitative medical imaging

Topic editors

Thomas Beyer – Medical University of Vienna, Austria

Ewald V. Moser – Medical University of Vienna, Austria

Citation

Beyer, T., Moser, E. V., eds. (2024). *Editor's challenge in medical physics and imaging: Quantitative medical imaging*. Lausanne: Frontiers Media SA.

doi: 10.3389/978-2-8325-5007-6

Table of contents

frontiers | Frontiers in Physics

TYPE Editorial
PUBLISHED 30 May 2024
DOI 10.3389/fphy.2024.1434129

OPEN ACCESS

EDITED AND REVIEWED BY
Federico Giove,
Centro Fermi–Museo storico della fisica e Centro studi e ricerche Enrico Fermi, Italy

*CORRESPONDENCE
T. Beyer,
thomas.beyer@meduniwien.ac.at

RECEIVED 17 May 2024
ACCEPTED 20 May 2024
PUBLISHED 30 May 2024

CITATION
Beyer T and Moser EV (2024), Editorial: Editor's challenge in medical physics and imaging: quantitative medical imaging.
Front. Phys. 12:1434129.
doi: 10.3389/fphy.2024.1434129

Editorial: Editor's challenge in medical physics and imaging: quantitative medical imaging

T. Beyer[1]* and E. V. Moser[2]

[1]QIMP Team, Center for Medical Physics and Biomedical Engineering, Medical University of Vienna, Vienna, Austria, [2]Center for Medical Physics and Biomedical Engineering, Medical University of Vienna, Vienna, Austria

KEYWORDS

imaging, quantification, editor, challenge, AI

Editorial on the Research Topic
Editor's challenge in medical physics and imaging: quantitative medical imaging

In the realm of modern healthcare, the importance of timely and accurate diagnosis cannot be overstated. The advent of various diagnostic modalities has revolutionized patient management, particularly through the use of non-invasive, medical imaging. While effective for straightforward diagnostic tasks, such as identifying fractures or lesions, these methods faced also limitations with the increasing complexity of imaging modalities and the breadth of diagnostic information they provide. The integration of quantitative parameters has significantly enhanced the precision and reliability of medical imaging [1]. Quantitative imaging encompasses measurements of size, density, metabolic and functional parameters, among others, which contribute to more robust and standardized diagnostic assessments.

With the launch of this Editor's Challenge in late summer of 2022, we sought to provide a forum for imaging researchers to present fundamental concepts of quantification within their chosen imaging modalities. We did encourage explorations of the inherent limitations of quantification, such as spatial resolution, contrast, sensitivity, and robustness, in both clinical and research applications. In addition, we sought discussions on strategies to enhance counting statistics, improve signal-to-noise ratios, and develop methodological and algorithmic advancements that yield more reliable quantitative data. The topics of interest included: 1) Fundamentals of quantitative imaging, 2) Algorithmic updates and corrections for deriving quantitative data, 3) Quantitative capabilities across various imaging modalities, 4) Emerging trends to advance the limits of quantification, 5) Utilization of quantitative data in diagnostic and therapeutic contexts, and 6) Incorporation of validated artificial intelligence into quantitative diagnostics.

As always, when soliciting contributions to special issues in journals, initial interest is high while actual contributions come in lower quantities (sic). As it was the case with this challenge. Over the course of 18 months, we received 20 indications of full submissions, of which 16 panned out. All submissions went to peer-review and ultimately, 10 manuscripts have been accepted for inclusion in this Research Topic on Quantitative Medical Imaging. Despite the relatively small number of submissions, it is encouraging to see that the breadth of the papers did cover the range of topics laid out as part of this initiative, and we like to thank all authors for their valuable contributions.

Kumar et al. evaluate the feasibility of using a benchtop X-ray fluorescence (XRF) imaging system for high-resolution, quantitative imaging of tumour models. The study employs a 3D breast cancer model and investigates the use of metallic contrast agents. Results demonstrate the system's capability for detailed spatiotemporal localization of nanoparticles, offering potential for pre-clinical studies and enhanced understanding of cancer pathophysiology.

Hagberg et al. present a study on the use of iron-filled hydrogel clusters as phantoms for quantitative susceptibility mapping (QSM) in MRI. They validate the magnetic properties of these clusters, demonstrating their suitability as model systems for QSM. The phantoms mimic tissue properties and provide a reproducible means for calibrating MRI scanners, potentially improving the accuracy of susceptibility measurements in clinical settings.

Berg and Börner describe the design and development of a resolution phantom using Deep X-ray Lithography (DXRL) for high-resolution MRI and microscopy. Their proposed phantom features grids with varying spatial periods and orientation to assess and improve spatial resolution in the micrometer range. The phantom design aims to enhance quality control and performance in ultra-high-field MRI scanners, contributing to advancements in microimaging techniques. Furthermore, such phantoms might be used also in micro-CT and Optical Coherence Tomography.

Bibiano et al. introduces a novel model-based fitting approach for T_1 mapping in MRI, eliminating the need for waiting times between inversion pulses. The method combines inversion-prepared and unprepared measurements, enabling faster and more accurate T_1 mapping. Validation with phantom and volunteer data demonstrate that the new approach yields T_1 values closely matching reference methods, making it a promising technique for efficient and robust tissue characterization in clinical MRI.

Guidi et al. discuss the advancements in MRI-derived cerebrovascular reactivity (CVR) mapping for assessing vascular dysfunction in brain diseases. The study advocates for high-resolution imaging to better characterize microvascular alterations. By using novel MRI sequences and mild hypercapnic challenges, they were able to improve the spatial specificity of hemodynamic and metabolic measurements, providing deeper insights into neurovascular impairments associated with conditions, such as hypertension and Alzheimer's disease.

Moving on to Computed Tomography (CT), Chung et al. review the principles and clinical applications of CT perfusion (CTP) imaging, focusing on kinetic modelling and diagnostic interpretation. Their paper details the technical considerations for accurate quantitative imaging and discusses the use of CTP in stroke, cancer, and cardiovascular disease. The authors emphasize future research directions, including dose reduction strategies and advancements in CT hardware, to enhance the diagnostic utility of CTP.

Exploring dynamic and parametric imaging in the context of molecular imaging, Khamwan et al. assess 18F-FDG-PET imaging to localize seizure onset zones in drug-resistant epilepsy (DRE) patients. Their findings suggest that parametric approaches may offer superior sensitivity compared to traditional methods, aiding in the accurate localization of seizure origins for effective surgical intervention.

Wanek et al. investigate the distribution of the radiotracer [18F] THK-5317 in preclinical mouse models with tau pathology. Their study highlights sex, age, and strain-related differences in radiotracer uptake across various organs. The authors underscore the significance of incorporating the 3Rs principles (Replacement, Reduction, and Refinement) in preclinical imaging, and suggest that organ-to-blood concentration ratios can serve as effective quantitative parameters for radiotracer studies.

Staying in the field of PET, but moving from pre-clinical to clinical studies, Ferrara et al. examine the potential of low-dose (LD) [18F] FDG-PET/CT imaging protocols in reducing radiation exposure while maintaining diagnostic image quality. Their research involved 19 healthy controls and seven lung cancer patients, comparing LD and standard-dose (STD) imaging. Results indicated that mean standardized uptake values (SUVBW) were similar between LD and STD conditions, except in the heart. Although LD imaging showed increased noise, especially in cancer lesions, the study supports the feasibility of LD-PET/CT for studying multi-organ metabolic patterns in non-oncological contexts.

A major obstacle to PET-based quantification is involuntary patient motion. Tumpa et al. explore the application of deep learning for head motion correction in PET imaging. The proposed neural network effectively registers image volumes, reducing motion artifacts and improving quantification accuracy. The study highlights the potential of deep learning to enhance PET image quality and facilitate more accurate diagnostic assessments in clinical practice.

In conclusion, quantitative imaging represents a transformative advancement in the field of medical diagnostics. This is attested by the selected manuscripts in response to our challenge. By providing objective and reproducible measurements, quantification enhances the accuracy and consistency of diagnostic interpretations, supporting more informed clinical decision-making potentially leading to novel biomarkers. As medical imaging technologies continue to evolve, the integration of quantitative parameters will further refine diagnostic capabilities, enabling early detection and precise monitoring of various diseases. The ongoing research and innovations in this domain underscore the critical role of quantification in achieving better patient outcomes and advancing the frontiers of medical science.

Author contributions

TB: Writing–original draft, Writing–review and editing. EM: Writing–original draft, Writing–review and editing.

Funding

The author(s) declare that no financial support was received for the research, authorship, and/or publication of this article.

Conflict of interest

The authors declare that the research was conducted in the absence of any commercial or financial relationships that could be construed as a potential conflict of interest.

Publisher's note

Reference

1. Beyer T, Bailey DL, Birk UJ, Buvat I, Catana C, Cheng Z, et al. Medical Physics and imaging–A timely perspective. *Front Phys* (2021) 9:634693. doi:10.3389/fphy.2021.634693

frontiers | Frontiers in Physics

TYPE Original Research
PUBLISHED 28 March 2023
DOI 10.3389/fphy.2023.1123315

OPEN ACCESS

EDITED BY
Thomas Beyer,
Medical University of Vienna, Austria

REVIEWED BY
Sungon Lee,
Hanyang Universiy, Erica, Republic of Korea
Alexander F. I. Osman,
Al-Neelain University, Sudan

*CORRESPONDENCE
Dustin R. Osborne,
dosborne@utk.edu

SPECIALTY SECTION
This article was submitted to Medical Physics and Imaging, a section of the journal Frontiers in Physics

RECEIVED 13 December 2022
ACCEPTED 14 March 2023
PUBLISHED 28 March 2023

CITATION
Tumpa TR, Gregor J, Acuff SN and Osborne DR (2023), Deep learning based registration for head motion correction in positron emission tomography as a strategy for improved image quantification.
Front. Phys. 11:1123315.
doi: 10.3389/fphy.2023.1123315

Deep learning based registration for head motion correction in positron emission tomography as a strategy for improved image quantification

Tasmia Rahman Tumpa[1,2], Jens Gregor[2], Shelley N. Acuff[1] and Dustin R. Osborne[1]*

[1]Graduate School of Medicine, The University of Tennessee, Knoxville, TN, United States, [2]Electrical Engineering and Computer Science, The University of Tennessee, Knoxville, TN, United States

Objectives: Positron emission tomography (PET) is affected by various kinds of patient movement during a scan. Frame-by-frame image registration is one of the most practiced motion correction techniques. In recent years, deep learning has shown a remarkable ability to quickly and accurately register images once trained. This paper studies the feasibility of using a deep learning framework to correct 3D positron emission tomography image volumes for head motion in routine positron emission tomography imaging to improve quantification in motion impacted data.

Materials and Methods: A neural network was trained with 3D positron emission tomography image volumes in an unsupervised manner to predict transformation parameters required to perform image registration. A multi-step convolutional neural network (CNN) was combined with a spatial transform layer. Pairs of target and source images were used as input to the network. To prepare the training dataset, a previously published TOF-PEPT algorithm was applied to automatically detect static frames where the patient remained in a relatively steady position and transitional frames where they underwent abrupt motion. A single image volume was reconstructed for each static frame. The image reconstructed from the first static frame served as the target image with images from subsequent static frames being used as source images. The trained neural network predicted transformation parameters that could be used to perform frame-by-frame image-based motion correction but also enabled raw listmode positron emission tomography data correction where individual line-of-responses were repositioned. Line profiles and ROIs were drawn across the reconstructed image volumes to compare performance and quantitative results between standard registration tools and the deep learning technique. Corrected volumes were further compared to motion free images quantitatively using Dice indices.

Results: In total, one hundred 3D positron emission tomography image volumes were used to train the network. Cross-validation was carried out using a 4:1 ratio for the training and test data. A conventional algorithm for affine registration from the Advanced Normalization Tools (ANTs) software package served as a baseline. To evaluate the correction performance, the mean Dice index and standardized uptake value (SUV) were used. Application of the algorithm to clinical data showed good performance with respect to registration accuracy as well as processing time. The neural network yielded a mean Dice index of ~0.87 which was similar to

the advanced Normalization Tools algorithm and did so ~3x faster using a multi-core CPU and ~20x faster with a GPU. Standardized uptake value analysis showed that quantitative results were 30%–60% higher in the motion-corrected images, and the neural network performed better than or close to the advanced Normalization Tools.

Conclusion: The aim of this work was to study the quantitative impact of using a data-driven deep learning motion correction technique for positron emission tomography data and assess its performance. The results showed the technique is capable of producing high quality registrations that compensate for patient motion that occurs during a scan and improve quantitative accuracy.

KEYWORDS

positron emission tomography (PET), head motion correction, positron emission particle tracking (PEPT), time-of-flight (TOF), deep learning, image registration, convolutional neural network, spatial transform layer

1 Introduction

Positron emission tomography (PET) is a non-invasive nuclear medicine imaging procedure that uses radioactive tracers to visualize biochemical changes such as metabolism. Quantitative and qualitative assessment of PET data is affected by various kinds of patient movement such as respiratory and cardiac motion which are non-rigid and periodic by nature, head and whole-body motion which are rigid/affine and irregular by nature, etc. Patient movement leads to degraded image quality, e.g., in the form of blurring, which impacts diagnostic image analysis including but not limited to quantification of standardized uptake values (SUV) and measurement of lesion intensity, size, and location.

Use of external devices constitutes one of the most widely practiced approaches for motion correction. However, the use of such devices is limited by several constraints such as device cost and setup, necessary training, regular maintenance, and, most importantly, retroactive data correction. Attention has therefore shifted toward data-driven motion correction which typically either performs frame-by-frame image registration [1] or event-based correction [1–5]. In frame-based image registration, the listmode data is divided into a sequence of motion-free frames. Images are reconstructed for each frame of data, aligned with a reference frame, and then summed together to create the final image volume. In event-based correction, individual lines of response (LOR) in each frame are repositioned, thereby allowing a single image to be reconstructed from all the raw data. In most cases, registration is carried out by optimizing different similarity criteria in the image domain, e.g., mutual information [6–8], cross-correlation [6, 7, 9], the sum of absolute differences [9, 10], or standard deviation of the ratio of two image volumes [9, 10].

Several traditional methods exist that facilitate image registration [11–14]. These methods aim to numerically solve the optimization problem in an iterative manner over pairs of images. The computation can be very intensive, depending on the complexity of the task. More recently, deep learning has received significant attention as it allows a neural network to learn the underlying patterns of the registration task thereby replacing the costly optimization computation with an inexpensive forward pass of the trained network.

To date, many different deep learning approaches have been proposed, e.g., Convolutional Neural Network (CNN) [15–20], Generative Adversarial Network (GAN) [21–23], and reinforcement learning [24–26]. The neural network can be trained in a supervised or unsupervised way. Supervised learning relies on ground truth transformation parameters [20, 24–28]. In such cases, the network is either trained with simulated images with known ground truth information, or the ground truth information is extracted by applying other methods for the training dataset. In routine clinical applications, it is very difficult to acquire accurate ground truth information which makes supervised learning of a neural network a challenging task. Thus, for medical image applications, unsupervised and self-supervised learning is desired [29].

In 2015, Jaderberg *et al.* [30] introduced their Spatial Transform Network (STN), which allowed unsupervised image registration. STN consisted of three modules, namely, a neural network, a grid generator, and a sampler. Firstly, the neural network was used to learn features from input images and estimate a mapping between them, the grid generator was then used to compute the sampling grid based on the derived transformation parameters, and the sampler finally generated a warped/moved image by carrying out the sampling operation using interpolation. The loss between the warped and target image thus could be used to train the neural network in an end-to-end unsupervised manner. Later, other papers explored similar approaches with different neural networks, such as the use of a Fully Convolutional Network (FCN) by Li *et al.* [19], de Vos *et al.* [15] and the use of a U-net-like architecture by Balakrishnan *et al.* [17] Research on the application of the deep learning approach has continued to enhance the registration performance using a number of different approaches including but not limited to multi-step recurrent network [31], cascaded network [16, 32], multi-scale estimation [18, 33, 34], diffeomorphic registration [35, 36], reducing negative Jacobian determinant [37], and encouraging invertibility [31, 32].

Most of the above-mentioned papers focused on CT and/or MRI image registration. Neural network-based PET image registration, on the other hand, has only been addressed in a limited scope [38–40]. This paper studies deep learning based motion correction for PET with the aim of achieving computational efficiency compared to the conventional iterative approach ensuring the consistency of performance. The multi-step recurrent network by Shen *et al.* [31] formed the basis for the work as it has demonstrated superior performance, particularly for affine registration. We

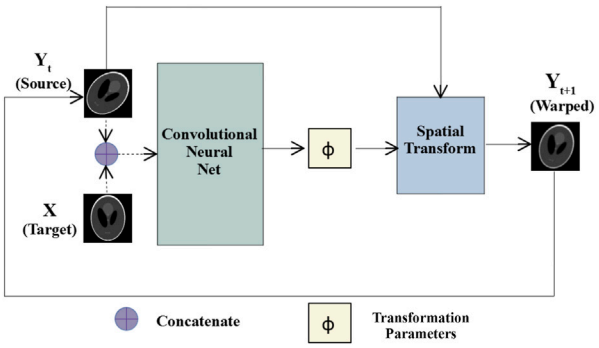

FIGURE 1
Multi-step affine registration network: Initially, source and target images are concatenated and passed as input to a convolutional neural network. The network predicts transformation parameters that are passed along with the source images to a spatial transform layer. The layer generates warped images, which at the next step are passed as the source images to the same network, and the process repeats for k number of steps.

introduced a few modifications as described below. The paper will mainly focus on rigid head motion correction of brain PET data using the more general affine model. The following sections provide a detailed overview of the approach.

2 Materials and methods

2.1 Overview of the image registration approach

The task of image registration can be considered as warping a source image I_{src} to a target image I_{tgt} defined in the spatial domain $\Omega \in R^{h\times w\times d}$. The objective is to find a mapping function $f: I_{src} \rightarrow I_{tgt}$. Letting I_{wrpd} and Φ denote the warped image and the transformation parameters, respectively, the warping operation can be expressed as:

$$I_{wrpd} = f(I_{src}, \Phi) \tag{1}$$

The neural network parameters θ are then optimized in a way that minimizes the dissimilarities between the warped image and fixed images. The network learns by optimizing the image dissimilarity metric denoted by S as follows. That is:

$$\theta^{*} = argmin_{\theta} S\left(I_{wrpd}, I_{tgt}\right) \tag{2}$$

Ultimately, the network is trained to predict the transformation parameters which for a 3D affine registration include transform matrix $A \in R^{3x3}$ and translation vector $t \in R^{3\times 1}$.

2.2 Network architecture

We adopted a multi-step recurrent approach that includes a CNN [31] and a spatial transform layer [30] to train the network in an unsupervised manner. Pairs of source and target images were fed as input to the network and the network made predictions of transformation parameters, which were then passed along with the source image to the spatial transform layer. The grid generator of the spatial transform layer created a sampling grid to warp the moving source image according to the transformation parameters predicted by the network. The sampler then performed linear interpolation to sample and provide the warped image.

With reference to Figure 1, prediction and correction took place in a recurrent manner by repeatedly feeding the warped image back to the same CNN as a new source image which was then registered with the target image. The process is repeated for k number of steps. For the results reported here, we used $k = 3$ and an analysis is presented in Section 3.2 as a support of this choice. The composition of the parameters obtained at each step was used as the final transformation parameters. Letting A_1, A_2, and A_3 denote the affine transform matrices and t_1, t_2, and t_3 the translation vectors, the final solution can be expressed as:

$$\begin{aligned} A' &= A_3 A_2 A_1 \\ t' &= A_3 A_2 t_1 + A_3 t_2 + t_3 \end{aligned} \tag{3}$$

Figure 2 shows the CNN architecture, which was inspired by work by Zhao *et al.* [32] and consisted of a series of convolutional and pooling layers. Except for the final layer, the convolution operations were performed using kernel size 3, stride 1, and a ReLU [41] activation function. At the final layer, two convolution operations were performed to predict the transform matrix and translation vector using kernel size 3 and linear activation functions. In selected layers after convolution, average pooling with kernel size 2 was performed. Section 3.2 speaks to the choice of the network architecture.

2.3 Loss functions

Image dissimilarity loss was modeled by the negative normalized cross-correlation [42] given by:

$$L_{img} = -\frac{\sum_{i\in\Omega}\left(I^{i}_{wrpd} - I_{wrpd}\right)\left(I^{i}_{tgt} - I_{tgt}\right)}{\sqrt{\sum_{i\in\Omega}\left(I^{i}_{wrpd} - I_{wrpd}\right)^{2}\sqrt{\sum_{i\in\Omega}\left(I^{i}_{tgt} - I_{tgt}\right)^{2}}}} \tag{4}$$

where I_{wrpd} and I_{tgt} denote the mean of the warped image and the target image, respectively.

To prevent the transform parameters from overshooting, the following regularizing loss function was used [1]:

$$L_{reg} = ||A - I||_{F}^{2} + ||t||_{2}^{2} \tag{5}$$

where subscript F denotes the Frobenius norm and I is the identity matrix.

These loss functions were combined to form a total loss:

$$L_{total} = \lambda_{img} L_{img} + \lambda_{reg} L_{reg} \tag{6}$$

where λ_{img} and λ_{reg} denote image dissimilarity loss and regularization weighting factors set to 1 and 0.01, respectively,

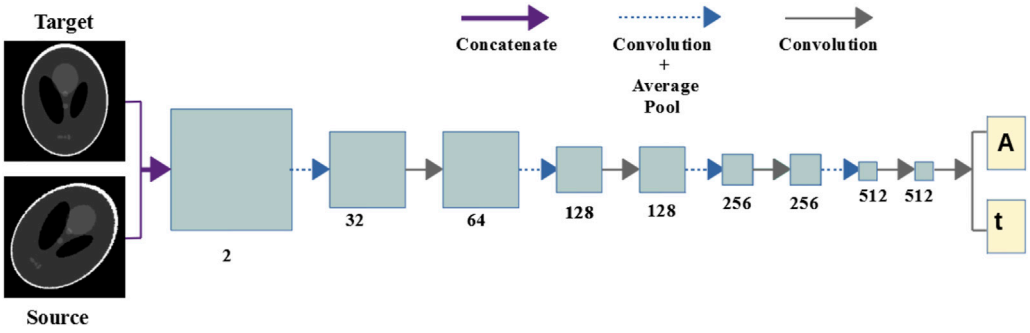

FIGURE 2
Convolutional neural network: The network consists of a series of convolutional and pooling layers after selected convolution operations. Two convolution operations are carried out at the final layer to output the transform matrix and the translational parameters.

with the values determined empirically. Future work will explore this aspect in-depth.

2.4 Data preparation and training details

To prepare the dataset, the PET listmode data was sorted into motion-free static frames using the previously published TOF-PEPT algorithm [43–46]. An image was reconstructed for each frame using the OSEM algorithm available on the 64-slice Biograph mCT Flow PET/CT scanner. We used our institution's standard clinical protocol that calls for 3 iterations, 24 subsets and 5 × 5 Gaussian post-smoothing. The Siemens e7 processing tools (Siemens Healthineers, Knoxville) were used for all data processing and reconstruction. The image volume reconstructed from the first static frame was used as the reference/target image while image volumes reconstructed from subsequent static frames were used as source images.

Five patient studies were conducted in compliance with an Institutional Review Board approved protocol (IRB #3941) using full 64-bit listmode data acquisition. During a 3-min scan, patients rested their heads in random positions and orientations at random time points. Each study thus exhibited a different range of movements and therefore yielded different numbers of static frames.

In order to expand the limited amount of data available to form an adequately large dataset for training the neural network, image volumes were further synthesized from the five patient studies. In total, one hundred 3D PET image volumes were simulated by applying random transformations to the LOR data. Each transformed raw listmode dataset was then histogrammed and sent to the reconstruction algorithm as previously mentioned to create image volumes. To reduce the computational cost associated with the neural network training, images were resized from 400 × 400 × 109 to 128 × 128 × 96 by cropping background with zero-valued voxels and rescaling the result. Cross-validation was used with a 4:1 ratio for the training and test data. Training spanned 100 epochs with 20 steps per epoch and using a batch size of 4. The learning rate was fixed at 1e-4. The network was trained using a computer equipped with a 32-core Intel Xeon E5-2670 CPU and a Tesla V100S GPU.

2.5 Validation and evaluation

Pairs of source and target image volumes were passed to the trained neural network. The network outputted the transformation parameters along with a warped image from the spatial transform layer. An overall motion-corrected image was then produced by registering the source image from each motion-free static frame for the whole scan duration and summing them together. Additionally, the transformation parameters predicted by the trained neural network were applied to the raw listmode data. The LORs within each static frame were all aligned to the reference frame using the predicted transformation parameters. The transformed listmode data was then histogrammed and reconstructed using the Siemens e7 processing tools (Siemens Healthineers, Knoxville).

To evaluate the neural network's image registration capabilities quantitatively, the Dice index was used to measure the similarity between warped and target images:

$$Dice\,(A,B) = \frac{2|A \cap B|}{|A| + |B|} \tag{6}$$

A higher value of the index indicates better performance. The processing time needed for a trained network to perform the registration was used to evaluate the computational efficiency. Lastly, in order to evaluate the motion correction from a clinical perspective, the standardized uptake value (SUV) was studied. The conventional iterative registration algorithm (typeofTransform = "Affine") from the Advanced Normalization Tools (ANTs) software package [11] was used as a baseline against which the performance of the neural network could be compared.

Quantitative analysis of the image data were performed using comparison of line profiles across the brain from each of the image volumes created using a commercial analysis software (Inveon Research Workplace, Siemens Healthineers, Knoxville, TN). Data were loaded into the software, geometric alignment verified, and linear regions of interest were drawn across the brain with line profiles plotted along the direction of the line width. This enabled comparison of SUVs along the profile but to also gave a measure of signal-to-background variance across regions of high and minimal uptake across the region. Peak-to-valley ratios were calculated to provide an estimation of signal-to-noise ratio to more quantitatively illustrate whether the corrected data improved upon the uncorrected images.

TABLE 1 Comparison of performance in image registration.

Study	Mean dice index		Mean computational time (seconds)		
	ANTs	Deep learning	ANTs	Deep learning	
				GPU	CPU
Cross Validation 1	0.82	0.80	2.49	0.15	0.81
Cross Validation 2	0.85	0.84	1.96	0.16	0.96
Cross Validation 3	0.86	0.86	2.08	0.11	0.93
Cross Validation 4	0.91	0.88	2.61	0.10	0.80
Cross Validation 5	0.82	0.81	4.08	0.11	0.80
Mean	0.85	0.84	2.65	0.13	0.86

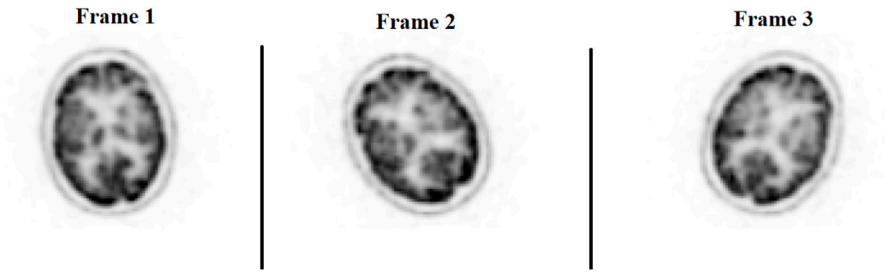

FIGURE 3
Patient Study 1: Illustration of the three motion-free static frames where the patient placed their head in three different positions. A slice of the 3D PET image volume in the axial plane is shown in the figure.

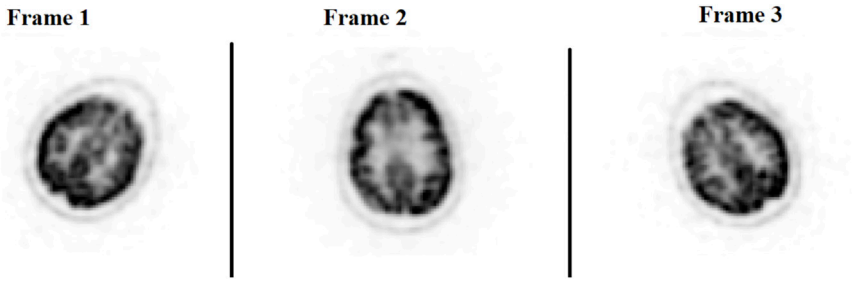

FIGURE 4
Patient Study 2: Illustration of the three motion-free static frames where the patient placed their head in three different positions. A slice of the 3D PET image volume in the axial plane is shown in the figure.

3 Results

3.1 Qualitative and quantitative evaluation of the performance of neural network

Table 1 compares the neural network performance in individual image registration in terms of mean Dice index and computational time against the ANTs algorithm for the synthesized dataset. The neural network performed close to the conventional iterative algorithm but did so ~3x and ~20x faster, respectively, using the multi-core CPU and the GPU.

The ability to generate motion-corrected images was also studied. Figures 3, 4 show motion-free static frames for two patient studies. The trained network was used to register "Frame 2" and "Frame 3" to reference frame "Frame 1." The three frames were then summed to create a motion-corrected image. For comparison, motion-corrected images were created using the ANTs algorithm as well. Figures 5, 6 show axial, coronal, and

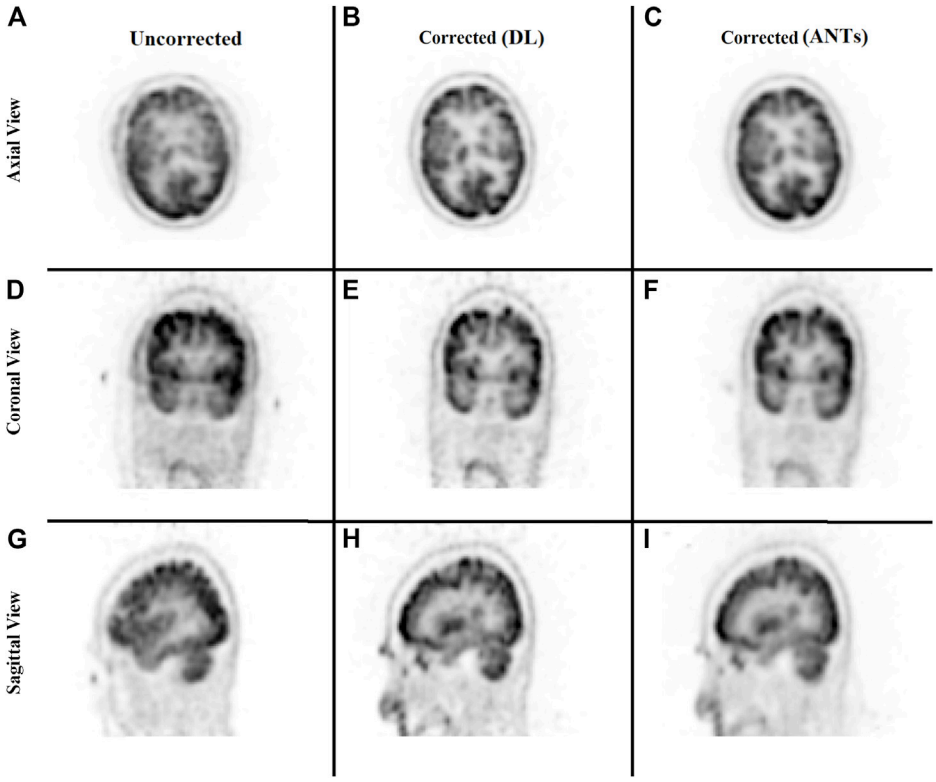

FIGURE 5
Qualitative comparison of the neural network performance in motion correction by means of frame-by-frame image registration. Rows from top to bottom show the sum of the three frames without any correction **(A, D, G)**, correction using the deep learning approach **(B, E, H)**, and the ANTs iterative algorithm **(C, F, I)**, respectively, in the axial, coronal, and sagittal view.

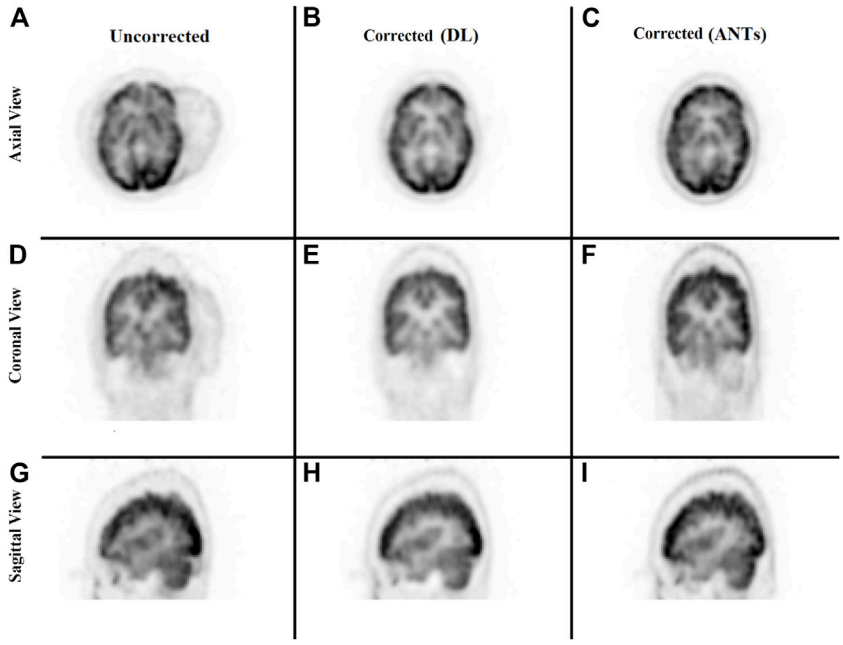

FIGURE 6
Qualitative comparison of the neural network performance in motion correction by means of frame-by-frame image registration. Rows from top to bottom show the sum of the three frames without any correction **(A, D, G)**, correction using the deep learning approach **(B, E, H)**, and the ANTs iterative algorithm **(C, F, I)**, respectively, in the axial, coronal, and sagittal view.

TABLE 2 Comparison of performance in producing motion corrected images.

Study	Mean dice index		Mean computational time (seconds)	
	ANTs	Deep learning	ANTs	Deep learning (GPU)
Cross Validation 1	0.85	0.83	5.74	0.30
Cross Validation 2	0.79	0.82	3.62	0.32
Cross Validation 3	0.93	0.92	3.74	0.22
Cross Validation 4	0.93	0.94	6.62	0.20
Cross Validation 5	0.90	0.91	7.23	0.33
Mean	0.88	0.88	5.39	0.27

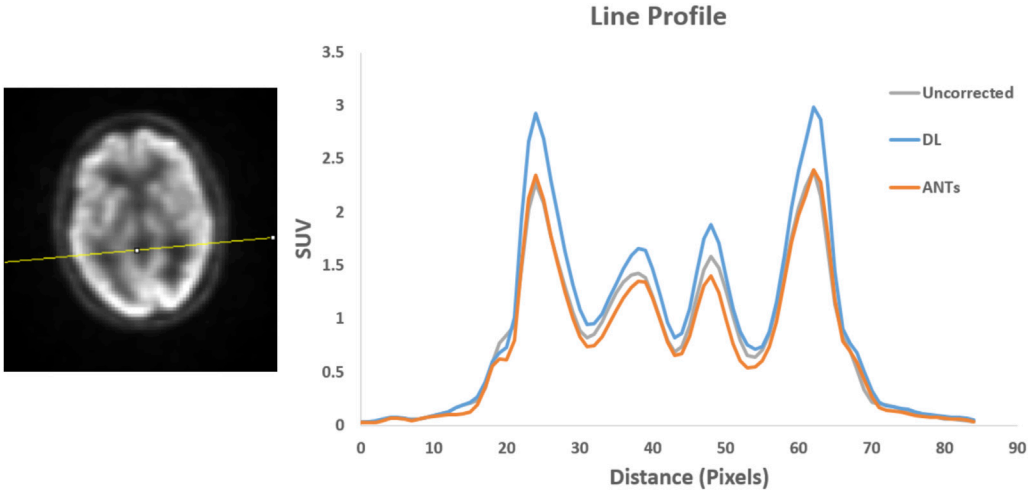

FIGURE 7
Patient Study 1: A region in the brain area (left) where a line profile (right) was manually drawn. The peak-to-valley ratio for the motion-corrected data with the deep learning (DL) approach is shown to be higher than the ANTs method.

sagittal slices of the original uncorrected image and motion-corrected images using the neural network and ANTs software. The qualitative improvement in the motion-corrected images is readily apparent with the neural network and ANTs showing comparable performance. Table 2 compares the neural network performance in producing overall motion-corrected image volumes by means of mean Dice index and computational time. Both qualitative and quantitative reviews show that the deep learning and conventional iterative approaches performed similarly; however, the former provided final results ~20 times faster with the use of a GPU.

Quantitative assessments showed good SUV agreement across the methods. As illustrated by Figures 7, 8, the peak-to-valley ratios of SUVs were 30%–60% higher in the motion-corrected images, with the neural network performing better or similar to ANTs. Good peak-to-valley improvement helps confirm that the correction method is appropriately aligning the data so that regions of uptake are not motion-blurred into areas of lower uptake.

Lastly, a study was conducted to evaluate the correction of the original raw listmode data by repositioning the LORs with the transformation parameters estimated by the trained neural network. Figure 9 provides a qualitative comparison of the uncorrected and motion-corrected image volumes reconstructed from the repositioned listmode data. Motion-corrected image volume achieved sharper details compared to the uncorrected data.

3.2 Analysis of the choice of network architecture

The choice of the network and the step size of the multi-step architecture (defined in Section 2.2) were analyzed by means of two studies. Figure 10 shows the training loss versus epoch with varying step sizes: 1, 2, 3, and 4. We observed that the network learned faster with increasing step size but saturated at step size 4. Thus, a step size of 3 was chosen for network training.

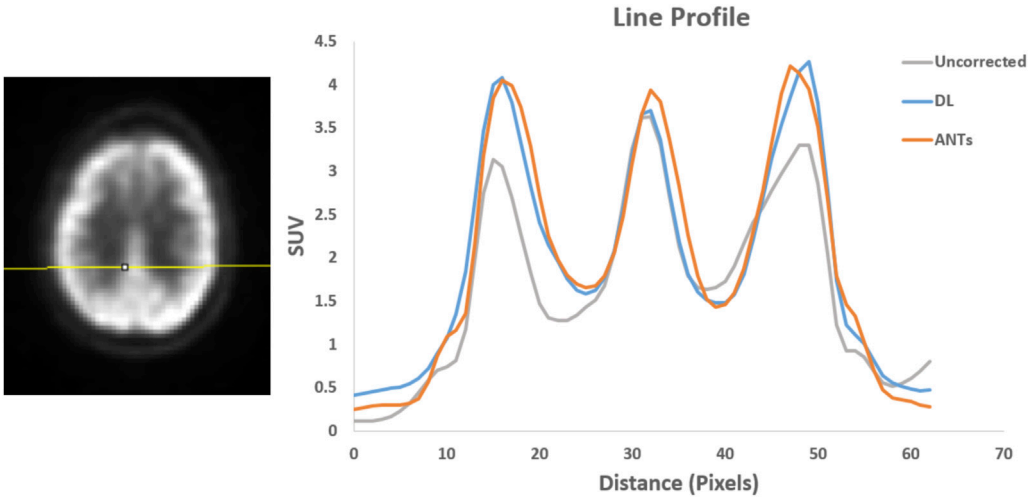

FIGURE 8
Patient Study 2: A region in the brain area (left) where a line profile (right) was manually drawn. The peak-to-valley ratio for the motion-corrected data with the deep learning (DL) approach is close to the ANTs method.

The network performance in image registration was studied by means of Dice scores for four different architectures: 5 convolution stages with 32, 64, 128, 256, and 512 features; 5 convolution stages with 16, 32, 64, 128, and 256 features; 4 convolution stages with 32, 64, 128, and 256 features; and 4 convolution stages with 16, 32, 64, and 128 features. Figure 11 shows the results. The configuration with 5 convolution stages led to better learning, possibly due to having deeper layers with more abstraction. The network, on the other hand, performed better when more features were used.

4 Discussion

This paper focused on studying and presenting the application of deep learning for data-driven PET motion correction.

The deep learning approach for image registration has demonstrated promising performance over the years. Here, a modified version of a multi-step recurrent deep learning approach was adopted to train a neural network for affine registration. The network was trained on a synthesized dataset to predict required transformation parameters in an unsupervised manner using a spatial transform layer that provided warped images to supervise the training.

To prepare the training data, multiple motion-free static frames were identified from the whole scan duration using the previously published motion detection algorithm TOF-PEPT. Images reconstructed from these static frames were used as input to train the network along with a target image reconstructed from a reference frame. The final goal was to perform motion correction by means of frame-by-frame registration with the trained network. The registered image frames were summed together to create the final motion-corrected image. To evaluate against a baseline, the frame-by-frame registration was implemented with the ANTs algorithm as

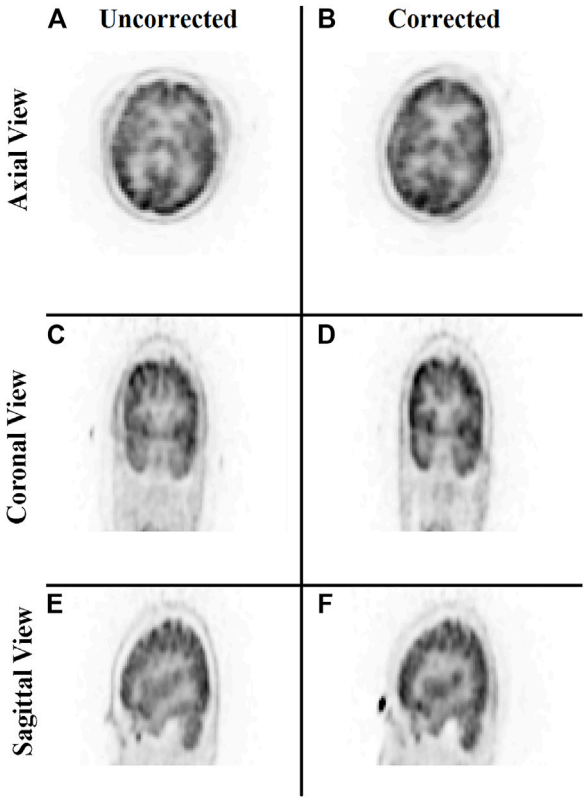

FIGURE 9
Qualitative comparison of the neural network performance in motion correction by remapping raw listmode data. Rows from top to bottom show the sum of the three frames without any correction **(A,C,E)** and correction using the deep learning approach **(B,D,F)**, respectively, in the axial, coronal, and sagittal view.

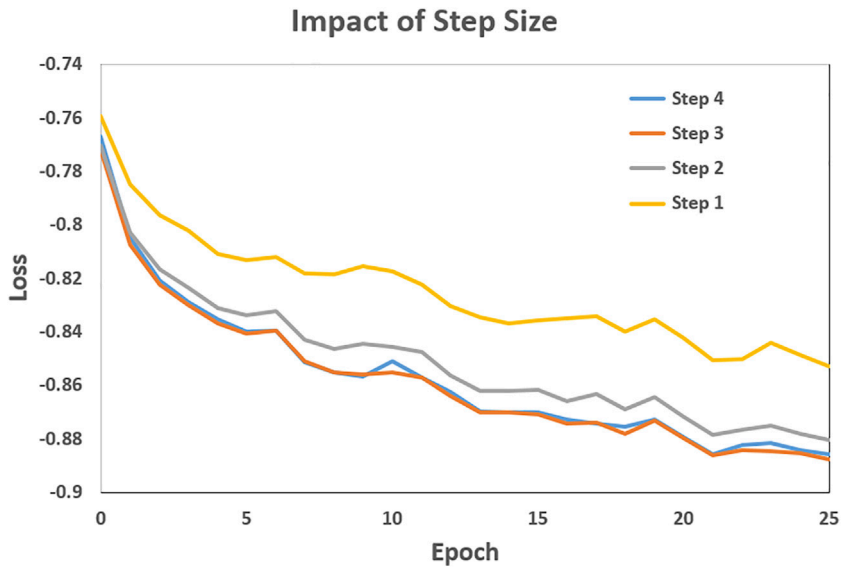

FIGURE 10
The plot of training loss versus epoch demonstrates the neural network performance with changing step sizes from 1 to 4. The network learned faster with increasing step size but saturated at step size 4 for the dataset used.

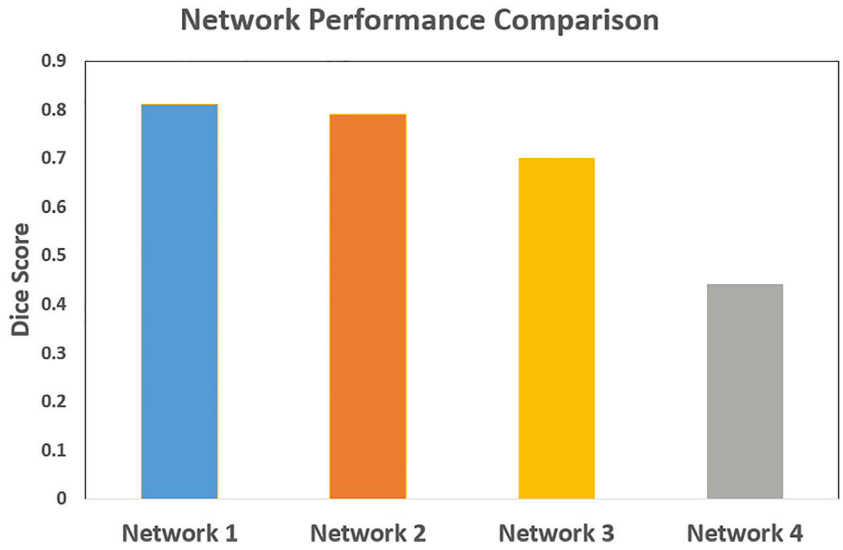

FIGURE 11
The comparison of the neural network performance for four different network architectures by means of Dice score. Network 1: 5 levels of convolution with 32, 64, 128, 256, and 512 features; Network 2: 5 levels of convolution with 16, 32, 64, 128, and 256 features; Network 3: 4 levels of convolution with 32, 64, 128, and 256 features; and Network 4: 4 levels of convolution with 16, 32, 64, and 128 features. The network performed better with 5 levels of convolution, and a higher number of features.

well. Mean Dice indices and manually drawn line profiles across brain regions were used to compare the motion-corrected images from the two methodologies against the uncorrected data. With respect to the iterative algorithm, the neural network yielded comparable and reliable performance both from qualitative and quantitative perspectives with significant improvements in speed. The neural network performed ~3x faster when using a multi-core CPU and ~20x faster with a GPU.

Additionally, the correction of the raw listmode data itself was studied by repositioning the LORs within each static frame according to the transformation parameter predictions by the neural network. A final motion-corrected image volume was

created by sending the remapped listmode data to the image reconstruction tools. With this approach, a reasonable correction could be achieved as presented in this paper. Further improvement in mapping from the image domain to actual scanner geometry and more precise transformation prediction will make it possible to produce more clinically suitable motion-corrected data.

Our group works heavily with radiation oncology supporting various advanced therapy workflows using PET/CT, where multimodal registration can certainly result in mismatches [47]. Although this work focused on our single modality head registration results that typically might only need rigid models, the full intent was to have a generalizable process that can support multimodal PET/CT registration. Ireland, et. Al. presented a study that specifically focused on multimodal head and neck registration showing improvements when using a non-rigid model [48]. Since geometric mismatches between the modalities can occur due to voxel variations, etc. We decided to test the robustness of the deep learning technique using an affine model. This also enabled some level of testing for this specific set of cases as we expected mostly rigid transformation within the same modality and our registration scaling factors were in fact unity indicating confirmation of a rigid transformation.

Lastly, the paper presented two studies that supported and evaluated the choice of network architecture. The first study analyzed the choice of step size, whereas the second study was evaluated four different network architectures with respect to their performance in image registration. The network choice with deeper layers and a higher number of features was found to perform better.

This work aimed to study the feasibility of applying deep learning to correction of affine/rigid motion during routine clinical brain PET imaging. Notwithstanding using a limited amount of real data augmented by synthesized data, results showed promising performance with a reduced computational cost once the neural network has been trained. Limitations of neural network methods such as the one studied here include the general need for large amounts of data and computational resources for training. Future work will aim to further enhance the network performance, study use of a larger amount of real data, and extend application to non-rigid cases, such as respiratory motion correction.

5 Conclusion

This paper explored an unsupervised deep learning approach for PET motion correction by means of 3D image registration. The feasibility of the proposed deep learning approach in the application of motion correction was studied by means of both frame-by-frame image registration and remapping of raw listmode data. Both approaches yielded reasonable corrections. The network performance was compared both qualitatively and quantitatively against a conventional iterative algorithm from the Advanced Normalization Tools (ANTs) software package. The deep learning approach performed on par with the iterative approach, but ~3x faster when using a multi-core CPU and ~20x with a GPU. This work is expected to aid to address the application of a deep learning approach for routine PET motion correction.

Data availability statement

The raw data supporting the conclusions of this article will be made available by the authors, without undue reservation.

Ethics statement

The studies involving human participants were reviewed and approved by University of Tennessee Graduate School of Medicine Institutional Review Board. The patients/participants provided their written informed consent to participate in this study.

Author contributions

TT: Graduate student, manuscript writing, data processing, analysis, code development JG: Student advisor, manuscript writing and revision, mentoring and code development SA: Patient recruitment, data management, clinical acquisition of data DO: Principle investigator, mentor, manuscript writing and revision, code/model development, clinical data acquisition, and recruiting.

Funding

This work is supported by the University of Tennessee Graduate School of Medicine, Knoxville.

Conflict of interest

The authors declare that the research was conducted in the absence of any commercial or financial relationships that could be construed as a potential conflict of interest.

Publisher's note

All claims expressed in this article are solely those of the authors and do not necessarily represent those of their affiliated organizations, or those of the publisher, the editors and the reviewers. Any product that may be evaluated in this article, or claim that may be made by its manufacturer, is not guaranteed or endorsed by the publisher.

References

1. Montgomery AJ, Thielemans K, Mehta MA, Turkheimer F, Mustafovic S, Grasby PM. Correction of head movement on PET studies: Comparison of methods. *J Nucl Med* (2006) 47:1936–44.

2. Jin X, Mulnix T, Gallezot JD, Carson RE. Evaluation of motion correction methods in human brain PET imaging-A simulation study based on human motion data. *Med Phys* (2013) 40:102503. doi:10.1118/1.4819820

3. Bloomfield PM, Spinks TJ, Reed J, Schnorr L, Westrip AM, Livieratos L, et al. The design and implementation of a motion correction scheme for neurological PET. *Phys Med Biol* (2003) 48:959–78. doi:10.1088/0031-9155/48/8/301

4. Menke M, Atkins MS, Buckley KR. Compensation methods for head motion detected during PET imaging. *IEEE Trans Nucl Sci* (1996) 43:310–7. doi:10.1109/23.485971

5. Picard Y, Thompson CJ. Motion correction of PET images using multiple acquisition frames. *IEEE Trans Med Imaging* (1997) 16:137–44. doi:10.1109/42.563659

6. Perruchot F, Reilhac A, Grova C Motion correction of multi-frame PET data. *IEEE symposium conference record nuclear science* 2004., IEEE, pp. 3186–90.

7. Costes N, Dagher A, Larcher K, Evans AC, Collins DL, Reilhac A. Motion correction of multi-frame PET data in neuroreceptor mapping: Simulation based validation. *Neuroimage* (2009) 47:1496–505. doi:10.1016/j.neuroimage.2009.05.052

8. Wardak M, Wong K-P, Shao W, Dahlbom M, Kepe V, Satyamurthy N, et al. Movement correction method for human brain PET images: Application to quantitative analysis of dynamic 18F-fddnp scans. *J Nucl Med* (2010) 51:210–8. doi:10.2967/jnumed.109.063701

9. Lin K-P, Huang S-C, Yu D-C, Melega W, Barrio JR, Phelps ME. Automated image registration for FDOPA PET studies. *Phys Med Biol* (1996) 41:2775–88. doi:10.1088/0031-9155/41/12/014

10. Andersson JL. How to obtain high-accuracy image registration: Application to movement correction of dynamic positron emission tomography data. *Eur J Nucl Med Mol Imaging* (1998) 25:575–86. doi:10.1007/s002590050258

11. Avants BB, Tustison N, Song G. Advanced normalization tools (ANTS). *Insight j* (2009) 2:1–35.

12. Klein S, Staring M, Murphy K, Viergever M, Pluim J. Elastix: A toolbox for intensity-based medical image registration. *IEEE Trans Med Imaging* (2010) 29:196–205. doi:10.1109/tmi.2009.2035616

13. Thirion J-P. Image matching as a diffusion process: An analogy with maxwell's demons. *Med Image Anal* (1998) 2:243–60. doi:10.1016/s1361-8415(98)80022-4

14. Vercauteren T, Pennec X, Perchant A, Ayache N. Diffeomorphic demons: Efficient non-parametric image registration. *NeuroImage* (2009) 45:S61–S72. doi:10.1016/j.neuroimage.2008.10.040

15. Vos BDD, Berendsen FF, Viergever MA, Staring I, Ivana I, et al. End-to-end unsupervised deformable image registration with a convolutional neural network. *Deep learning in medical image analysis and multimodal learning for clinical decision support*. Springer (2017). p. 204–12. doi:10.1007/978-3-319-67558-9_24

16. de Vos BD, Berendsen FF, Viergever MA, Sokooti H, Staring M, Išgum I. A deep learning framework for unsupervised affine and deformable image registration. *Med Image Anal* (2019) 52:128–43. doi:10.1016/j.media.2018.11.010

17. Balakrishnan G, Zhao A, Sabuncu MR, Guttag J, Dalca AV, et al. An unsupervised learning model for deformable medical image registration. *Proc IEEE Conf Comput Vis pattern recognition* (2018) 9252–60. doi:10.1109/cvpr.2018.00964

18. Fan J, Cao X, Yap P-T, Shen D. BIRNet: Brain image registration using dual-supervised fully convolutional networks. *Med Image Anal* (2019) 54:193–206. doi:10.1016/j.media.2019.03.006

19. Li H, Fan Y. Non-rigid image registration using self-supervised fully convolutional networks without training data. 2018 *IEEE 15th international symposium on biomedical imaging (ISBI 2018)*, IEEE, pp. 1075–8.doi:10.1109/isbi.2018.8363757

20. Sokooti H, de Vos BD, Berendsen F, Lelieveldt BPF, Išgum I, Staring M. Nonrigid image registration using multi-scale 3D convolutional neural networks. *International conference on medical image computing and computer-assisted intervention*. Springer (2017). p. 232–9. doi:10.1007/978-3-319-66182-7_27

21. Mahapatra D, Antony B, Sedai S, Garnavi R, et al. Deformable medical image registration using generative adversarial networks. 2018 *IEEE 15th international symposium on biomedical imaging (ISBI 2018)*, IEEE, pp. 1449–53.doi:10.1109/isbi.2018.8363845

22. Fan J, Cao X, Wang Q, Yap PT, Shen D. Adversarial learning for mono- or multi-modal registration. *Med Image Anal* (2019) 58:101545. doi:10.1016/j.media.2019.101545

23. Yan P, Xu S, Rastinehad AR, Wood BJ. w*orkshop on machine learning in medical imaging*. Springer (2018). p. 197–204. doi:10.1007/978-3-030-00919-9_23

24. Krebs J, Mansi T, Delingette H, Zhang L, Ghesu FC, Miao S, et al. Robust non-rigid registration through agent-based action learning. *International conference on medical image computing and computer-assisted intervention*. Springer (2017). p. 344–52. doi:10.1007/978-3-319-66182-7_40

25. Ma K, Wang J, Singh V, Tamersoy B, Chang Y-J, Wimmer A, et al. *International conference on medical image computing and computer-assisted intervention*. Springer (2017). p. 240–8. doi:10.1007/978-3-319-66182-7_28Multimodal image registration with deep context reinforcement learning

26. Liao R, Miao S, de Tournemire P, Grbic S, Kamen A, Mansi T, et al. An artificial agent for robust image registration. *Proceedings of the AAAI conference on artificial intelligence* (2017). doi:10.1609/aaai.v31i1.11230

27. Yang X, Kwitt R, Styner M, Niethammer M. Quicksilver: Fast predictive image registration - a deep learning approach. *NeuroImage* (2017) 158:378–96. doi:10.1016/j.neuroimage.2017.07.008

28. Rohé M-M, Datar M, Heimann T, Sermesant M, Pennec X, et al. SVF-net: Learning deformable image registration using shape matching. *International conference on medical image computing and computer-assisted intervention*. Springer (2017). p. 266–74.

29. Fu Y, Lei Y, Wang T, Curran WJ, Liu T, Yang X. Deep learning in medical image registration: A review. *Phys Med Biol* (2020) 65:20TR01. doi:10.1088/1361-6560/ab843e

30. Jaderberg M, Simonyan K, Zisserman A. Spatial transformer networks. *Adv Neural Inf Process Syst* (2015) 28.

31. Shen Z, Han X, Xu Z, Xu H, Marc N, et al. Networks for joint affine and non-parametric image registration. *Proc IEEE/CVF Conf Comput Vis Pattern Recognition* (2019) 4224–33. doi:10.1109/cvpr.2019.00435

32. Zhao S, Lau T, Luo J, Chang EIC, Xu Y. Unsupervised 3D end-to-end medical image registration with volume tweening network. *IEEE J Biomed Health Inform* (2020) 24:1394–404. doi:10.1109/jbhi.2019.2951024

33. Krebs J, Delingette H, Mailhe B, Ayache N, Mansi T. Learning a probabilistic model for diffeomorphic registration. *IEEE Trans Med Imaging* (2019) 38:2165–76. doi:10.1109/tmi.2019.2897112

34. Guo Y, Bi L, Ahn E, Feng D, Wang Q, Kim J, et al. A spatiotemporal volumetric interpolation network for 4D dynamic medical image. *Proc IEEE/CVF Conf Comput Vis Pattern Recognition* (2020) 4726–35. doi:10.1109/cvpr42600.2020.00478

35. Dalca AV, Balakrishnan G, Guttag J, Sabuncu MR. Unsupervised learning for fast probabilistic diffeomorphic registration. *International conference on medical image computing and computer-assisted intervention*. Springer (2018). p. 729–38. doi:10.1007/978-3-030-00928-1_82

36. Krebs J, Mansi T, Mailhé B, Ayache N, Delingette H. Unsupervised probabilistic deformation modeling for robust diffeomorphic registration. *Deep learning in medical image analysis and multimodal learning for clinical decision support*. Springer (2018). p. 101–9. doi:10.1007/978-3-030-00889-5_12

37. Kuang D, Schmah T. Faim - a ConvNet method for unsupervised 3D medical image registration. *International workshop on machine learning in medical imaging*. Springer (2019). p. 646–54. doi:10.1007/978-3-030-32692-0_74

38. Xia K-j, Yin H-s, Wang J-q. A novel improved deep convolutional neural network model for medical image fusion. *Cluster Comput* (2019) 22:1515–27. doi:10.1007/s10586-018-2026-1

39. Yu H, Zhou X, Jiang H, Kong H, Wang Z, Hara T, et al. Learning 3D non-rigid deformation based on an unsupervised deep learning for PET/CT image registration. *Medical imaging 2019: Biomedical applications in molecular, structural, and functional imaging*. SPIE (2019). p. 439–44. 10.1117/12.2512698.

40. Yu H, Jiang H, Zhou X, Hara T, Yao YD, Fujita H. Unsupervised 3D PET-CT image registration method using a metabolic constraint function and a multi-domain similarity measure. *IEEE Access* (2020) 8:63077–89. doi:10.1109/access.2020.2984804

41. Nair V, Hinton GE. *Rectified linear units improve restricted Boltzmann machines*. ICML (2010).

42. Penney GP, Weese J, Little JA, Desmedt P, Hill D, hawkes D. A comparison of similarity measures for use in 2-D-3-D medical image registration. *IEEE Trans Med Imaging* (1998) 17:586–95. doi:10.1109/42.730403

43. Tumpa TR. *Qualitative and quantitative improvements for positron emission tomography using different motion correction methodologies* (2021).

44. Osborne D, Acuff S, Tumpa T, Hu D, et al. Respiratory motion correction using novel particle tracking techniques. *J Nucl Med* (2017) 58:1362.

45. Tumpa TR, Acuff SN, Gregor J, Lee S, Hu D, Osborne DR, et al. Respiratory motion correction using A novel positron emission particle tracking technique: A framework towards individual lesion-based motion correction. 2018 *40th annual international conference of the IEEE engineering in medicine and biology society* (EMBC), IEEE, pp. 5249–52.doi:10.1109/embc.2018.8513486

46. Tumpa TR, Acuff SN, Gregor J, Lee S, Hu D, Osborne DR. A data-driven respiratory motion estimation approach for PET based on time-of-flight weighted positron emission particle tracking. *Med Phys* (2021) 48:1131–43. doi:10.1002/mp.14613

47. Beyer D, Boellaard T, De Ruysscher R, Grgic D, Lee A, Pietrzyk JA, et al. Integration of FDG- PET/CT into external beam radiation therapy planning. *Nuklearmedizin* (2012) 51(4):140–53. Epub 2012 Apr 3. PMID: 22473130. doi:10.3413/Nukmed-0455-11-12

48. Ireland RH, Dyker KE, Barber DC, Wood SM, Hanney MB, Tindale WB, et al. Nonrigid image registration for head and neck cancer radiotherapy treatment planning with PET/CT. *Int J Radiat Oncology*Biology*Physics* (2007) 68(3):952–7. Epub 2007 Apr 18. PMID: 17445999; PMCID: PMC2713594. doi:10.1016/j.ijrobp.2007.02.017

frontiers | Frontiers in Physics

TYPE Original Research
PUBLISHED 20 April 2023
DOI 10.3389/fphy.2023.1125143

OPEN ACCESS

EDITED BY
Guillem Pratx,
Stanford University, United States

REVIEWED BY
Stefan Bartzsch,
Technical University of Munich, Germany
Antonello Enrico Spinelli,
San Raffaele Scientific Institute, Italy

*CORRESPONDENCE
Melanie Fachet,
melanie.fachet@ovgu.de

†These authors have contributed equally to this work

SPECIALTY SECTION
This article was submitted to Medical Physics and Imaging, a section of the journal Frontiers in Physics

RECEIVED 15 December 2022
ACCEPTED 20 March 2023
PUBLISHED 20 April 2023

CITATION
Kumar K, Fachet M, Al-Maatoq M, Chakraborty A, Khismatrao RS, Oka SV, Staufer T, Grüner F, Michel T, Walles H and Hoeschen C (2023), Characterization of a polychromatic microfocus X-ray fluorescence imaging setup with metallic contrast agents in a microphysiological tumor model.
Front. Phys. 11:1125143.
doi: 10.3389/fphy.2023.1125143

Characterization of a polychromatic microfocus X-ray fluorescence imaging setup with metallic contrast agents in a microphysiological tumor model

Kunal Kumar[1†], Melanie Fachet[1*†], Marwah Al-Maatoq[1], Amit Chakraborty[1], Rahul S. Khismatrao[1], Shreyas V. Oka[1], Theresa Staufer[2], Florian Grüner[2], Thilo Michel[3], Heike Walles[4] and Christoph Hoeschen[1]

[1]Faculty of Electrical Engineering and Information Technology, Institute of Medical Technology, Chair of Medical Systems Technology, Otto von Guericke University, Magdeburg, Germany, [2]Universität Hamburg and Center for Free-Electron Laser Science, Hamburg, Germany, [3]Physics Insitute, Chair of Experimental Physics (Particle and Astro Particle Physics), Friedrich–Alexander University Erlangen–Nürnberg, Erlangen, Germany, [4]Faculty of Process and Systems Engineering, Institute of Chemistry, Core Facility Tissue Engineering, Otto von Guericke University, Magdeburg, Germany

Introduction: Accurate diagnosis and personalized treatments involving site-targeted cancer localization, drug delivery, therapeutic strategy, and disease pathways identification, rely on a precise understanding of biomarker kinetics, drug pharmacokinetics, and mechanistic behaviour of functionalized tracers through *in vitro* and *in vivo* studies. X-ray fluorescence (XRF) computed tomography (XFCT) offers a potential alternative to current 3D imaging techniques for spatiotemporal localization of nanoparticle-tracers with high spatial resolution and sensitivity. In this work, the applicability of a benchtop cone-beam system with a polychromatic X-ray source was examined with regard to physical constraints of engineered tissue models.

Methods: A tissue engineering approach based on a decellularized scaffold was used to establish a 3D breast cancer model with MDA-MB-231 cells in co-culture with primary human fibroblasts. The 3D breast cancer system, in combination with small-animal-sized phantoms, was used to demonstrate the novel integrated pre-clinical imaging approach to perform *in vitro* surrogate investigations and non-destructive analysis on biophantoms. These models are adopted to evaluate the functionality and optimize the setup for high-spatial-resolution, fast, and fully-3D quantitative imaging. Polychromatic X-rays from a microfocus source are used for

Abbreviations: BSA, Bovine Serum Albumin; CBCT, Cone-beam computed tomography; CdTe, Cadmium Telluride; DMSO, Dimethyl sulfoxide; EM, Expectation maximization; FOV, Field of view; FWHM, Full Width at Half Maximum; HE, Hematoxylin-Eosin; HPCD, Hybrid photon counting detector; MAP, Maximum *A Posteriori*; MC, Monte Carlo; MLEM, Maximum likelihood expectation maximization; Mo, Molybdenum; MoNP, Molybdenum nanoparticle; MTT, 3-(4,5-dimethylthiazol-2-yl)-2,5-diphenyltetrazolium bromide; PBS, Phosphate-Buffered Saline; PCD, Photon counting detector; SISmuc, Small intestine submucosa + mucosa; TEM, Transmission electron microscopy; ToA, Time-of-arrival; ToT, Time-over-Threshold; TV, Total variation; XFI, X-ray fluorescence imaging; XRF, X-ray fluorescence; XFCT, X-ray fluorescence computed tomography.

XRF stimulation from conventional Gadolinium (Gd) and nanoparticle-based Molybdenum (MoNPs) contrast agents.

Results and Discussion: The intestinal scaffold allowed the invasion of the breast cancer cells over this barrier and therefore provides a valuable tool to study metastasis formation of tumor cells from epithelial origin. The breast cancer model was well suited for the development and validation of the proposed XRF imaging, with spatial resolution under <2 mm and contrast dose in the order of a few 100 μg/mL (~0.3 mg/mL for Gd and ~0.5 mg/mL for MoNPs), radiation dose in the order of a few 100 cGy (280 cGy for Gd and 94 cGy for MoNPs, with a possible reduction of an order of magnitude for Gd and 67% for MoNPs), and imaging time in the order of 10 min for Gd (33 min total) and 100 min (2.8 h total) for MoNPs, approaching *in vivo* conform conditions for pre-clinical studies. High-resolution XFCT for tissue-engineered cancer models would be of significant interest in biomedical research and diagnostic imaging, e.g., for an increased mechanistic understanding of molecular processes in tumor formation or early cancer detection.

KEYWORDS

tissue engineering, X-ray fluorescence computed tomography, *in vivo* pharmacokinetics, *in vitro* cancer models, nanoparticle contrast agents, molecular imaging

1 Introduction

Engineered tissue models are valuable test systems to study cell homeostasis as well as the development and progression of diseases. The development of microphysiological tissue models opens new possibilities for testing and development of diagnostic and therapeutic approaches at a pre-clinical or translational stage [1]. Composed of various cell types with different tissue origins, three-dimensional (3D) models closely recapitulate tissue architecture and are able to unravel mechanistic insights into tumor formation and metastasis [2]. In the field of cancer research, especially for drug efficacy screening and toxicity testing, many experiments are still performed in traditional two-dimensional (2D) cell cultures, xenografts or small animal models [3]. Although 2D models have the advantage of simple handling, they are unable to mimic the complexity of cell-cell or cell-matrix interactions and this can result in loss of crucial cellular signaling pathways and changes in cell responses to stimuli [4]. Moreover, 2D cultures do not provide satisfactory conservation of cellular properties such as cellular shape, polarization and heterogeneity [5]. In contrast, the collection of pre-clinical data from animal models is usually expensive, time consuming and associated with high regulatory hurdles impairing the fast translation of innovative treatments from bench to bedside [6]. Here, a critical impetus to meaningful pre-clinical theranostic (therapeutic and diagnostic) investigations is the validity of small-animal models to simulate human physiological behaviour, which otherwise manifests significant physiological and metabolic differences. Particularly, in cancer diseases, dissimilarities in animal-human tumor vascularization and drug pharmacology may undermine such investigations [7]. Tissue-engineered 3D models can overcome these limitations and bridge the gap between human relevance, reproducibility and physiological relevance [8]. Similar to *in vivo* conditions, tissue models can reproduce mechanical and biochemical properties that are crucial for cancer development and progression, such as morphology, cellular migration, tissue stiffness and integration of multiple cell types simultaneously [9]. While current standardized approaches in personalized cancer therapy allow cancer classification and prognosis prediction *via* human-relevant pharmacokinetic and pharmacodynamic models, they rely on data from large cohort studies with low specificity on comorbidities [7, 10]. Herein, prediction of individual response is difficult as the data requirement is large and generalized rather than targeted while ignoring individual comorbidities. Therefore, surrogate investigations on replicable patient-derived organoids or tissue cultures may allow systematic evaluations with reproducible results. Recent results indicate a close relationship between the response of 3D *in vitro* cancer models and the patient response to therapy [2]. As such, *in vitro* human-based cell models have the potential to predict patient response to therapy, thereby a valuable tool to study personalised drug response [11]. Moreover, with the development of functional *in vitro* models, complex cell systems such as bioartificial organs with vascular structures and *in vivo*-like organ functionality can be constructed for such investigations.

While non-invasive bio-imaging modalities using near-infrared (NIR) optical photons, like optical fluorescence imaging with, e.g., quantum dots (QDs) and conjugated NP-fluorophores, have been successful in non-ionizing molecular imaging with high spatiotemporal resolution in the sub-millimeter/sub-second (μm-mm/ms-hr) range, they are limited to only superficial depths, therefore, limiting imaging of deep organs and complex bioartificial systems [12, 13]. While in photoacoustic and ultrasound imaging, the spatial resolution is depth dependent due to frequency-dependent acoustic attenuation and decreases significantly at deeper penetration depths, the mechanical coupling of ultrasound receivers in the case of engineered tissue systems and bioreactor systems may be challenging [14–16]. Alternatively, as a non-invasive (neglecting ionizing radiation damage) technique, X-ray fluorescence computed tomography (XFCT) can allow molecular imaging and quantitative analysis of 3D elemental composition inside deep samples and organs. XFCT combines principles of absorption-based CT imaging with emission tomography in the form of X-ray

fluorescence (XRF) detection from elements within the sample [17]. XRF emissions from high atomic number target elements, i.e., contrast agents posed as markers, are typically instigated by the excitation of inner shell electrons from monochromatic X-rays, such as in X-ray fluorescence imaging (XFI) with polarised synchrotron-based sources [18–22]. The resulting XRF photons along with scattered photons are detected and analyzed in order to spectrally identify, spatially localize, and quantify the elemental composition with respect to their photon energies. Owing to the spectroscopic nature of XFCT, the computed tomography extension of XFI, has unique capabilities compared to attenuation or contrast-based imaging modalities (e.g., X-ray CT and its variants), such as inherent specificity due to the characteristic element-specific energy lines of XRF photons, leading to high detection sensitivity of very small marker concentrations [23–26]. Besides, the spatial resolution offered by XFI is adjoining that of morphological imaging modalities (CT, MRI, *etc.*) and substantially higher than that of present functional imaging modalities like PET and SPECT [18, 19, 21].

With the XFCT technique, besides 3D elemental mass localization inside imaging objects, X-ray attenuation maps can also be simultaneously obtained within the same imaging setup. As characteristic XRF photons stimulated from atoms have much higher energies and a higher penetration depth than visible light photons, XRF imaging has fundamentally distinct advantages of high sensitivity in deeper tissues or organs [27]. Here, the XRF penetrability depends on the atomic number (symbol Z) of the target element, with higher Z (or high-Z) leading to higher energy with a squared proportionality on Z [28] and, therefore, a greater transmission probability through large objects from energetic K-shell/L-shell photons [17].

In XFI and pencil beam XFCT, the spatial resolution is primarily determined by the pencil beam diameter, specifically for XFI in the axial and transverse directions, and majorly by the focal depth-dependent detection solid angle in the longitudinal direction [19, 20, 26]. However, in cone-beam XFCT, a full-body fast scanning is possible, allowing full-3D reconstruction of tracer distribution while preserving dynamic tracking, i.e., a higher full-body scanning temporal resolution is offered at the cost of high spatial resolution as delivered by XFI or pencil beam XFCT. The spatial resolution of cone-beam XFCT is primarily limited by scattering noise and instrumentation challenges. Specifically, loss of spatial resolution may occur from the optical components or collimation optics due to geometrical unsharpness in pinhole/parallel-hole collimators from the detection solid angle, septal penetration in the collimator, and collimator scattering. With the use of pixelated hybrid photon counting detectors (HPCD), these losses can also be attributed to correlation effects such as the charge-sharing effect, intrinsic detector scattering, sensor-intrinsic fluorescence, and fluorescence escape. In contrast, PET imaging, which is considered the gold standard for molecular assessment of tissues in cancer clinics, is constrained by fundamental spatial resolution limits arising from positron range and photon non-collinearity. From either imaging technique, a perpetual tradeoff between the scannable field-of-view (FOV) and achievable spatial resolution exists. Moreover, present 3D techniques in PET and SPECT still suffer from inevitable tradeoffs between managing cell viability and feasibility of longitudinal scanning (i.e., repeated imageability over multiple time-points allowing progression studies). This is due to the intrinsic half-life of radionuclides and radioactivity accumulation, specifically for slow biological processes, where the radiation dose is also delivered when imaging is not being performed [19]. Furthermore, it is challenging to confine the radiation dose of the radiotracer to specific target locations in PET and SPECT, as the radiotracer can spread to different regions of the target tissue and organs. In contrast, this is avoided in XFCT due to no intrinsic loss of XRF signals through the use of externally controlled excitations and known scanning regions [19]. These advantages render XFCT a highly promising candidate for a future modality in clinical molecular imaging of high-Z probes such as metallic nanoparticles (NPs) with active or passive tumor targeting [25, 29].

Paralleling synchrotron-based approaches, in benchtop XFCT settings, state-of-the-art lies in spectrally-matched quasi monoenergetic focused pencil-beam (Montel-type X-ray focusing mirror) excitation from liquid metal x-ray tubes that offer high flux, narrowband excitation, and high spatial resolution, but are limited to low atomic number nanoparticles [25, 26]. The high brilliance of, e.g., Indium-based liquid metal source requires NP tracers with K-edges close to the Indium K-alpha emission line at 24–24.2 keV, leaving only a small range of excitable elements with sufficiently high atomic numbers to allow NP multiplexing and minimize losses from XRF signal absorption [18, 25, 26]. Though, as shown in previous studies, the spatial resolution in cone-beam XFCT is currently limited to the millimeter range (>2 mm), higher spatial resolution is achievable through sensitivity enhancement, e.g., from multi-pinhole collimators [23, 24, 27, 30]. However, the design of multi-pinhole collimators entails additional instrumentation challenges. An alternative approach that could yield higher spatial resolution may be a sequential imaging approach, i.e., initial scans with cone-beam XFCT for sparsely localizing XRF signal sources acquired at low radiation doses, followed by high spatial resolution scans using a focused monochromatized beam, e.g., with X-ray focusing mirrors [25, 26]. Here, we chose to demonstrate the feasibility of XRF imaging with a microfocus X-ray source as, in principle, the achievable spatial resolution limit and increase in the flux intensity at the object focus, when coupled with monochromatizing beam-focussing optics, will be influenced by the x-ray focal spot sizes [31, 32].

Considering *in vivo* constraints for pre-clinical investigations, achieving high spatial resolution with currently available benchtop x-ray technology poses a challenging task. The *in vivo* constraints, e.g., for cell tracking and drug delivery studies in live animals (e.g., mice) are expected to have total NP mass in the order of micrograms and sub-millimeter spatial resolution, imaging scan-times within the effective anaesthetized periods, i.e., typically under 60 min, and radiation dose under 30 cGy (lethal dose $LD_{50/30}$ in the range 500–760cGy) corresponding to that of micro-CT imaging [18, 19, 33–35]. In dose-enhanced radiation therapy, the NP contrast doses in the mg/g levels, e.g., with gold nanoparticles (AuNPs), have been found to have a year of survival in mice [25, 36]. For conventional Gadolinium (brand name Dotarem, Gd-DOTA) contrast agents, the intravenous lethal dose for 50% (i.v.-LD_{50}) of mice is typically seen to be 10–15 mmol/kg, while the clinically recommended dose is 0.1 mmol/kg [37, 38]. With MoNPs, dose limits of up to 21 mmol/kg/day for 14 days have been considered

in certain studies, concluding $LD_{50} \geq 83.4$ mmol/kg with no sign of toxicity or mortality [39, 40]. In our study, for imaging the breast cancer models using XFCT, these values are taken as the upper and lower-bound reference values, and the feasibility of high-spatial-resolution imaging is examined.

The recent advances and unique properties of NPs have resulted in a rapid increase in their applications in biomedical and pharmaceutical applications [39]. In XFCT imaging NPs serve as functional or molecular contrast agents, which can be combined with functionalizations for targeted drug delivery and therapy. Compared to conventional contrast agents, NPs offer several advantages such as loadability, tunability and multifunctionality in different medical imaging modalities [41]. A systemic administration of NPs *via* intravenous injection and the subsequent drug delivery to the site of action is achieved through passive and active targeting [42]. In passive drug targeting strategies, the pathophysiological vascular permeability of tumor blood vessels and the enhanced retention in tumor tissue was successfully exploited for NP delivery, while active targeting uses conjugated ligands on the NP surface to improve the drug selectivity for tumor cell-specific biomarkers or receptors [25].

Here, we present a novel integrated pre-clinical approach to perform *in vitro* surrogate investigations and non-destructive analysis on bio fabrications, like engineered 3D tissues, for interventional cancer radiology, assisted through *in situ*, easily accessible benchtop XFCT imaging. In the current work, a tissue-engineered 3D microphysiological breast cancer model is examined in the context of feasibility evaluation and development of a quantitative 3D cone-beam XFCT setup. Compared to conventional 2D cell cultures, the proposed microphysiological cancer model overcomes the lack of histological complexity and functionality to reflect the complex biological behavior in a more accurate way. The quantitative tomographic XRF imaging of NPs in the microphysiological breast cancer model is demonstrated with spatial resolution at scan-times, contrast dose, and radiation dose approaching conform conditions for *in vivo* and *in vitro* experiments. The method is performed *via* passive targeting with metallic contrast agents, namely, a conventional Gd-containing (Z = 64) solution based on Gadoteric acid and MoNPs (Z = 42).

2 Material and methods

2.1 Cell culture

The static 3D tissue culture was performed according to established and standardized protocols on the Small intestine submucosa + mucosa (SISmuc) scaffold derived from a porcine jejunum [43, 44]. The SISmuc scaffold was fixed in a cell crown between two supporting rings. Subsequently, $1 \cdot 10^5$ MDA-MB-231 cells and $7.5 \cdot 10^4$ primary fibroblast cells were seeded on the luminal side of the scaffold. The cell crowns were placed in 12-well plates and covered with approx. 2.5 mL cell culture medium containing 10% FCS (RPMI-1640 for MDA-MB-231 cells and DMEM for primary fibroblasts). The cells were maintained in 5% CO_2 under high humidity at 37 °C and a medium exchange was performed every 2–3 days. After 14 days of culture, the monolayer tissue was assembled to a multilayer structure with the following order: Fibroblast layer, MDA-MB-231 layer followed by a layer of SISmuc scaffold without cells.

Afterwards, the multilayer breast cancer model was treated with Gd-containing contrast agent (Gadoteric acid, brand name Dotarem®, 0.5 mmol/mL) and MoNPs. MoNPs with a particle size less than 100 nm (measured by TEM) and 99.8% purity (trace metal analysis) were purchased from Sigma-Aldrich (St. Louis, United States) in the form of black powder and suspended in deionized distilled water to prepare the required concentrations.

2.2 Immunohistochemistry staining

Scaffolds were fixed in embedding medium Tissue-Tek and stored at −80°C. Prior to staining, the multilayer tissue was cut in cross-sections of 10μm thickness using a microtome (CM3050 S, Leica Microsystems). Immunohistochemistry staining was performed with primary antibodies against Ki67 (Rabbit, 1015, Merck Millipore), Vimentin (Rabbit, EPR3776, Merck Millipore) and Pro-Collagen (Mouse, 3468667, Merck Millipore) with a 2-step HRP polymer detection system (Super Vision 2 HRP Polymer-Kit, DCS Innovative Diagnostik-Systeme, Germany). The primary antibodies for Ki67 and Vimentin were diluted 1:100 and for Pro-Collagen 1:1000 in 0.5% BSA in PBS and incubated at room temperature for 1 h. Nuclei were counterstained by Haematoxylin. Images were acquired using a digital microscope (Evos XL Core, Thermo Fisher Scientific).

2.3 Analysis of cell vitality by Ki67 immunohistochemistry staining

Immunohistochemistry stainings for Ki67 were performed as described above. Three images per sample with a magnification of ×10 were counted for the ratio of Ki67-positive signal (brown color) compared to a Haematoxylin-positive signal (blue color) within the respective tissue layers: I) primary fibroblast layer and II) MDA-MB-231 breast cancer cell layer.

2.4 Cone-beam computed tomography

Three-dimensional linear attenuation maps were obtained using the transmission cone-beam CT (CBCT) technique to account for and correct internal attenuation of incident excitation photons and emitted XRF photons within the sample. Figures 3A,B shows the benchtop XFCT imaging system with the incorporated CBCT arrangement. A series of 6 flat panel array X-ray detectors (RadEye™1, Teledyne Rad-Icon Imaging), each featuring a fully integrated CMOS silicon photodiode array with a scintillator having 24.6 mm × 49.2 mm active area, 48 μm pixel size, and 512 × 1024 matrix, were butted together to integrate a large-area detection into the XFCT setup. A tungsten-target microfocus X-ray tube (Oxford Nova 600) with 90 kV nominal tube voltage, 2.0 mA maximum beam current, 80 W nominal radiographic anode input power, 254 μm Beryllium window (Be, Z = 4), and 14–20 μm diameter focal spot size (at maximum voltage and minimum power) was used as an excitation source for both the CBCT and XFCT imaging

modes. The micro-sized focal spots are critical for spatial resolution enhancement and radiation flux concentration, e.g., *via* coupling with X-ray poly-capillary optics or Bragg-reflection-based bent focusing crystals [31, 32]. Bragg-reflection-based bent mosaic crystals, offering better reflection efficiencies, form a crucial aspect of our future work for focusing and monochromatizing. In the present investigation, we implemented a multi-leaf collimator system on the microfocus x-ray tube to generate cone-beam X-rays without supplementary focusing optics. The custom-made multi-leaf lead (Pb, Z = 82) beam collimation system was mounted and aligned at the tube exit window to allow excitation-beam shaping and minimize inherent leakage radiation. The X-ray tube with the collimation system was mounted on a high-accuracy multi-axis robot arm (KR 60 HA, KUKA) to allow positioning and alignment under different imaging modes. For the tomographic scanning geometry, a rotation stage (URS50CPP, Newport ™) was mounted on a vertical-axis alignment (M-443, Newport ™) platform, needed for the axial positioning within the cone-beam profile and rotational sampling (X-ray projections) of the tissue model phantoms and small-animal-sized calibration phantoms.

Scan parameters for the Gd imaging configuration were set to 90 kV peak tube voltage, operated at 0.9 mA tube current with 0.3 mm Copper (Cu, Z = 29) filtration, with 40.5 cm source-to-isocenter and 55.7 cm source-to-detector distance, allowing a full-field scan. A total of 30 projections were acquired at 12° angular sampling interval and approx. 6 s exposure time per projection.

For MoNP contrast agents, the image acquisition parameters were set to 45 kV peak tube voltage, operated at 1.8 mA tube current with 6 mm Aluminium (Al, Z = 13) filtration, with 16.8 cm source-to-isocenter and 31.5 cm source-to-detector distance. The set tube voltage was higher than the XFCT configuration to allow better contrast in transmission images and lower the overall CBCT scan-time. Here, a total of 60 projections (6° interval) were acquired at approx. 10 s exposure time per projection.

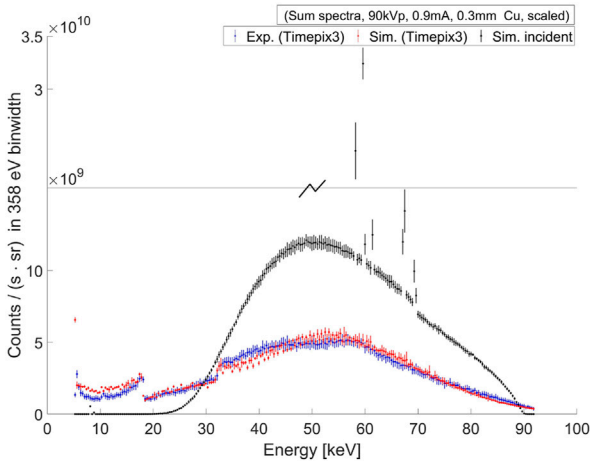

FIGURE 1
A comparison between the experimental and simulated sum-spectra of the excitation beam for the Gd case (with 90 kV tube voltage, 0.9 mA tube current, 0.3 mm copper filter) is shown here. The experimental measurements (blue) were taken using the Timepix3 detector, and simulations (red) were performed using MC (Geant4) particle transport with the Timepix3 sensor charge-transport and digitization model of the read-out electronics. The simulated incident sum-spectrum is obtained at the entrance surface of the detector (black) through surface flux scoring of the incident gamma tracks. Both the measured and simulated spectra are scaled by radiometric correction factors, as neither a physical measurement of direct high-flux is possible by Timepix3 detectors, nor a simulation of a large number of particles with Geant4 is computationally tractable.

2.5 Cone-beam X-ray fluorescence computed tomography

The XFCT imaging geometry consisted of a cone-beam sampling scheme using the same mechanical stage/platform arrangement for tomography with the collimated microfocus X-ray tube, as mentioned in Section 2.4. For XRF detection, energy-resolving X-ray detectors were used for discriminating primary XRF/scattered counts in the XRF signal bins from accompanying secondary (Rayleigh and Compton) events in the neighboring bins since there exists a proportionality between the absorbed energy in the sensor and electron-hole pairs produced upon intrinsic interactions within the atoms of the semiconductor material leading to differentiability between detected signals depending on the sensor energy resolution. In the current XFCT setup, Timepix3 HPCD (55 μm × 55 μm pixels size, ~14 mm × 14 mm active detection area, 1 mm CdTe sensor thickness, ~4–6 keV FWHM energy resolution around Gd XRF energies, Minipix TPX3, Advacam) was irradiated behind circular aperture single-pinhole arrangements. The XRF detector was operated in various modes: Time-of-Arrival (ToA) and Time-over-Threshold (ToT) continuous pixel-event readout mode, giving photon interaction position (pixel coordinates), arrival time, and deposited energy.

For Gd contrast agents, the pinhole collimator was made out of Lead (Pb), having an opening diameter of 0.4 ± 0.05 mm and a thickness of 1.5 ± 0.05 mm. The X-ray tube was operated under the same excitation-beam settings as in CBCT, i.e., at 90 kV tube voltage, 0.9 mA beam current, and 0.3 mm Cu filtering. However, to allow full-field scanning in geometrically/mechanically constrained large CT detector arrangement in the setup, the source-to-isocenter distances were set differently, i.e., for 30 mm internal region-of-interest (ROI) FOV and 20 mm longitudinal FOV, 14 cm source-to-isocenter, 5.5 cm isocenter-to-pinhole, and 1.5 cm pinhole-to-detector distance was used. To minimize the object and geometry-dependent elastic and Compton scattered background, and to improve the signal-to-background ratio, the geometry of the fluorescence detectors and acquisition/post-processing parameters were optimized. Specifically, detector angle optimization for total-scatter minimization (primarily Compton-scattered photons) was carried out for the chosen polychromatic excitation-beam properties (see Figure 1) using Monte Carlo (MC) simulations on the GEANT4 toolkit, and task-specific optimal bin widths were determined under Poisson point process assumptions for sum spectrum binning of the X-ray projection data [21, 45, 46]. The detector was positioned at 42 ± 3° polar angle with respect to the primary photon ray (central projection axis in the imaging mid-plane) in order to minimize the background interference in signal bins. A compressed sensing-based sparse-view image acquisition

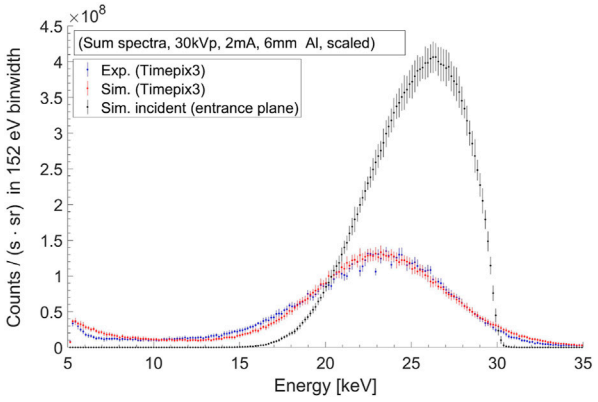

FIGURE 2
Excitation beam sum-spectra in the MoNP case (with 30 kV tube voltage, 2 mA tube current, 6 mm aluminium filter) from experimental measurements using Timepix3 detector (blue), detector simulations (red), and the simulated incident sum-spectrum (black).

strategy was adopted to minimize radiation dose with 10 angular projections (in 360° scan) at an exposure time of 150 s per projection [47].

For MoNP imaging, the pinhole collimator consisted of an opening diameter of 0.4 ± 0.03 mm in 1.2 ± 0.05 mm thick Iron (Fe, Z = 26). Here, Fe was chosen in order to minimize interference from Pb L-shell XRF on the lower end of the Mo K-shell XRF bins. The X-ray tube was operated at 30 kV to minimize intrinsic CdTe XRF interference in Mo K-Shell XRF bins, with 2 mA beam current and 6 mm Al filtration. An approximately 30 mm internal ROI-FOV was realized with 9 cm source-to-isocenter, 4.5 cm isocenter-to-pinhole, and 1 cm pinhole-to-detector distance. For the chosen beam properties (see Figure 2), the detector was positioned at an optimum polar angle of 114 ± 3°. A total of 30 angular projections (in 360° scan) were obtained at an exposure time of 300 s per projection.

2.6 XFCT calibration phantoms and simulated *in vivo* phantoms

Calibration standards in varying concentrations with Gd, based on Gadoteric acid ($C_{16}H_{25}GdN_4O_8$), and MoNPs were used as contrast agents on a custom-made water-equivalent phantom for system characterization and multi-layer *in vitro* 3D tissue models for simulated *in vivo* investigations.

For XFCT calibration experiments, approx. 0.75 mL volume of 0–3.1 mg/mL Gd dilutions (see Figure 3C) made from 0.5 mmol/mL (~78.5 mg/mL) stock solution were filled in polypropylene microcentrifuge tubes (1.5 mL maximum volume, 10 mm diameter, 9° taper angle) and embedded in water-filled 50 mm maximal diameter, ~60 mm high hexagonal borosilicate glass containers behaving as small animal surrogates (see Figure 3C, right). Calibration experiments with MoNPs involved approx. 1.8 mL volume of 0–10 mg/mL MoNP dilutions (see Figure 3D) filled in cryogenic vials (2 mL maximum volume, 12.5 mm diameter) embedded in water-filled phantoms (see Figure 3D, right). The assembled samples of the multilayer breast cancer model (as described in Section 2.1) were each immersed in approx. 12 mL cell culture medium held inside separate borosilicate containers (see Figure 3E) after treatment with 0.16, 0.78, 1.57, and 3.15 mg/mL Gd and 0.01, 0.05, 0.1, and 0.2 mg/mL MoNP. Blank cell crown phantoms (see Figure 3F) were used for task-based optimization of the XFCT system [48].

2.7 XFCT data processing

The ToA and ToT event-information from XFCT projections were used to carry out energy calibration and event clustering (Pixet Pro, Advacam) to reconstruct events degraded by the charge-sharing effect, intrinsic CdTe XRF, and intrinsic Compton scattered events. Contrary to the detection based on large-area single-pixel or multi-pixel detectors, individual small pixels (55 μm) of the Timepix3 sensor led to insufficient detected counts for the *in vivo* scan-time and dose constraints. Therefore, single-pixel spectra were binned together to form sum spectra, and a spatial-filtering-based optimization problem (similar to [21, 49]) was modelled and solved for cone-beam polychromatic X-rays to obtain the subset of pixels that maximizes the signal-to-background ratio (limit set at SNR > 3.29) in each projection (Figure 4 shows the typical XRF spectrum in each projection and the corresponding optimization). The pixels that contribute most to the background counts were eliminated through an iterative process followed by XRF signal maximization until the stopping condition (in percentage of remaining pixels) is reached. The minimum percentage of pixels that can be removed was determined based on the FOV, i.e., 30 mm internal ROI-FOV and 20 mm longitudinal FOV, which is approximately 20% (projected area) of the total detector area. Therefore, assuming a maximum removability of 80%, this limit was set at 4% of the total detector area. Better choices can be made for the lower limit of removable pixel percentage, e.g., based on an expected signal area proportional to target ROI or target organ projection onto the collimated detector. Here, this is defined empirically to avoid divergence of the SNR due to low statistics from a small number of remaining pixels, which may increase the chances of false detection (a non-physical presence of XRF signal [49]). Better estimates can be obtained on a task-specific basis, e.g., for a specific target region of interest with given NP dose and radiation dose limits, through MC simulation studies with structural data of tissue models.

Through the iterative process, signal and background batch fittings were performed for a large number of pixels. The signal region was defined as bins with K-shell XRF energies, i.e., at 42–43 keV and 17–17.5 keV peaks for Gd and MoNPs, respectively, with a spread of $3\sigma_{det}$, (here, σ_{det} is the sigma or the width parameter of the Gaussian fit function representing the detector energy resolution post charge-sharing reconstruction; $\sigma_{det}^{Gd} \approx 3$ keV, $\sigma_{det}^{Mo} \approx 2$ keV). The background region was defined as $\pm 3\sigma_{det}$ around the XRF peaks. For the Gd contrast agent, a Gaussian function with 3rd order polynomial for signal fitting and 3rd order polynomial for background fitting is utilized. Lower-order polynomials were chosen for Gd to optimize the computation time and were found sufficiently appropriate due to the low energy resolution of the detector. For MoNPs, 6th order polynomials were used with an

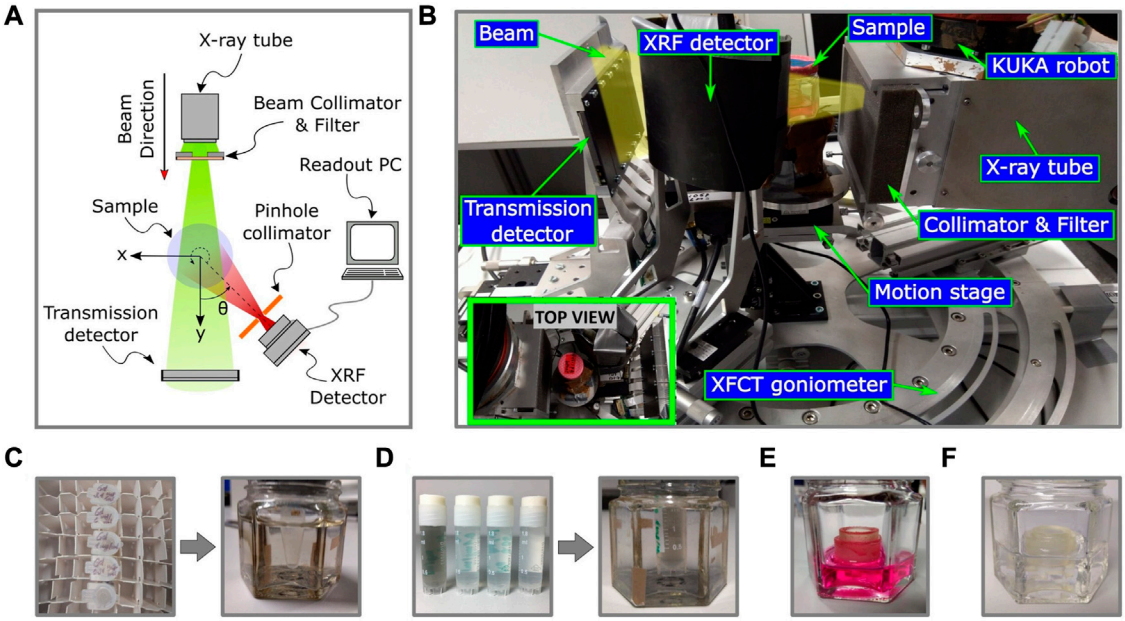

FIGURE 3
The schematic diagram **(A)** and the experimental setup **(B)** of the benchtop XFCT system is shown here, including the imaging phantoms **(C)**, **(D)** **(E)**, and **(F)**. Image **(B)** showcases the imaging geometry and the various components involved, including a microfocus X-ray tube with a collimator and beam filtering system, a motion and mounting platform, a transmission detector, and a shielded XRF detector with single pinhole collimation. The inset image in **(B)** shows the top view of the setup. The Gd **(C)** and MoNP **(D)** calibration samples are embedded in water and held inside borosilicate glass containers. The Gd calibration samples **(C)** have concentrations ranging from 0–3.1 mg/mL, and the MoNP calibration samples are shown in **(D)** (only 0, 0.1, 0.25, and 0.5 mg/mL are shown here). The 3D breast cancer tissue model is immersed in cell growth medium **(E)** and blank cell crown samples are held in water for XRF background analysis **(F)**.

extended background region up to maximum excitation energy (30 keV) to make the fitting process robust towards low-count statistics. The XRF counts in individual remaining pixels were obtained by solving a non-negative least-squares (NNLS) problem with L1 regularization based on their contribution to the net extracted XRF counts.

It is important to note that while the spatial filtering technique delivers a solution to the intrinsic background problem in XFI for large-sized (human-sized) objects by exploiting the spatial anisotropy of single Compton scattering, its applicability to small-animal cases is less warranted [21, 49]. Primarily because, with narrowband and high excitation energies in XFI, which lie far away (taking into account the reduction of fluorescence cross-section) from the XRF signal energy range, the intrinsic background problem becomes quasi-background-free. In this case, the background noise from Compton scattering is less pronounced, as there are not enough multiple energetic scatterings in the small-animal-sized geometry to lose sufficient energy and reach the XRF energy bins. For medium-Z (medium atomic number) contrast agents with adequately high excitation energy and narrow energy bandwidth, the signal background may, at most, consist of higher Compton orders, which leads to a nearly isotropic background spatial distribution. Therefore, spatial noise filtering is unsuitable if higher-order Compton scattering is likely, or if the signal region is already quasi-background-free. Optimization, in this case, may even deteriorate the signal sensitivity. However, this can be exploited in our case, as the excitation energies are close enough to the XRF signal region (see Figures 1, 2), and first-order Compton still poses an anisotropic distribution on the detector surface.

In Figures 5A, B, the spatial distribution of total Compton (i.e., all Compton orders) scattered photons within the Gd K-shell XRF energy range are compared between a cylindrical (having a height of 60 mm and 50 mm diameter) and a spherical (50 mm diameter) water phantom. Here, the calculations over the polar (θ) and azimuthal (ϕ) angles are performed relative to the primary beam direction. In this case, a 4π uncollimated detector was used and the difference in the total Compton scattered photon between the maximum value over the polar angle θ and the detector's optical axis (depicted by a brown dashed line) is slightly less than a factor of two. For the first-order Compton photons (denoted as C1) in Figures 5C, D, this difference is of a factor of two. However, in our simulations with the 4π uncollimated detector, we observed that this difference is more sensitive to the spectral bandwidth of the excitation beam than to the requirement of spatial coherence, i.e., having a pencil-beam-like configuration (see Supplementary Figure S1). With a microfocus source, where narrow bandwidth energies are used *via* spectral beam-shaping filters, a pencil beam configuration may already surpass the scan-time constraints of 30–60 min. Although the utility of pencil beams, also in the polychromatic case, has been well demonstrated for the human-size scale (as noted in [21]), our study acknowledges the limited margin of improvements in small-animal sizes for the optimization problem at hand. Nonetheless, the improvement factor scales with larger-sized objects, e.g., bioreactor systems and bio fabrications, which we intend to use in our future studies.

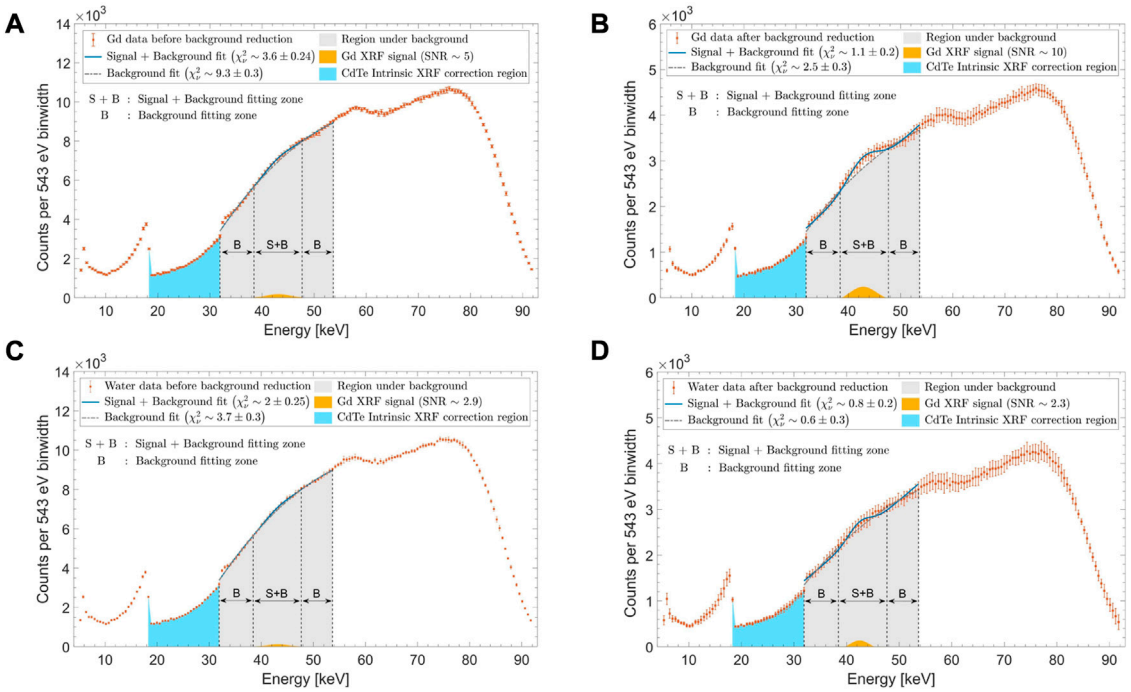

FIGURE 4
Typical XRF sum spectra **(A,C)** prior to and **(B,D)** post signal optimizations are shown here for **(A,B)** 1 mg/mL Gd concentration and **(C,D)** water background (0 mg/mL Gd concentration). An overall fitting region (gray shaded area) is in the energy range of 32–53.5 keV. The background fitting zone "B" is defined in the energy range of 32–38.5 keV and 47.5–53.5 keV, while the signal plus background fitting zone "S + B" is within 38.5–47.5 keV. The extracted Gd XRF signal (shown in yellow) is seen to have **(A)** SNR~5 before optimization and **(B)** SNR~10 post-optimization through background reduction and signal maximization. For water, **(C)** pre-optimization and **(D)** post-optimization SNRs were ~2.9 and ~2.3, respectively.

For the pinhole collimation case, spatial anisotropy of photons within the Gd XRF energy window can be seen by comparing the detected (MC) Compton spatial distributions from Figure 6A, which shows the C1 photons, and Figure 6B, which shows the second-order Compton (denoted as C2) photons. The higher-order Compton scattered photons (only C2 shown in Figure 6B), which reduce spatial anisotropy, are minimized through an intrinsic reduction in small volumes and *via* pinhole collimation. From Figures 6D, E, almost an order of magnitude reduction of C2 photons can be seen compared to C1 photons. In Figures 6D, E, the nonuniformity in the geometric response of the detector is corrected using a pixel-wise analytical model to account for the solid angle effects on the Compton background (see Supplementary Appendix A). The peak normalized solid angle of detection, $\tilde{\Omega}_i$, is used to correct the C1 and C2 profiles along both the horizontal (X-Cut) and vertical (Y-Cut) directions of the detector. In Figure 6C, the pixel-wise analytical model is compared with MC simulations, showing a good agreement. The spatial anisotropy along the horizontal (X-Cut) direction for the C1 profiles in 6D is more evident and arises over the polar angles, where the C1 yield is higher over one-half of the detector. Conversely, the anisotropy of the C2 profiles in 6E significantly decreases about the optical axis. It must be noted that with micron-sized solid target sources exhibiting low electron-beam power density, optimization possibilities for X-ray energy-hardening to minimize interference of Rayleigh and Compton scattered photons in XRF bins are very limited.

2.8 XFCT image reconstruction

Due to the highly undersampled scanning methodology and inherently count-limited nature of XRF imaging, iterative statistical image reconstruction methods were chosen for XFCT. A variation of the maximum likelihood expectation maximization technique (MLEM) with prior, i.e., the MAP (Maximum *A Posteriori*) technique, in the form of Green's one-step late total variation (TV-EM) algorithm is given by Eq 1 [50, 51],

$$\psi_j^{(k+1)} = \frac{\psi_j^{(k)}}{\sum_i a_{ij} + \beta \frac{\partial TV\left(\psi^{(k)}\right)}{\partial \psi_j^{(k)}}} \sum_i a_{ij} \frac{p_i}{\sum_{j'} a_{ij'} \psi_{j'}^{(k)}} \tag{1}$$

where, ψ_j is the relative concentration of the contrast agent, a_{ij} is the contribution from voxel j to projection at i, p_i is the XRF projection at i, β is the regularization parameter controlling the effect of total variation (TV) prior, and $TV\left(\psi^{(k)}\right)$ is the TV norm of the current image estimate $\psi^{(k)}$. For the sparse-view XRF imaging of thin 3D tissue samples, anisotropic TV prior is chosen to slightly weaken the solutions that promote oblique structures (edges). For internal attenuation correction of the excitation and XRF photons, measured attenuation maps from

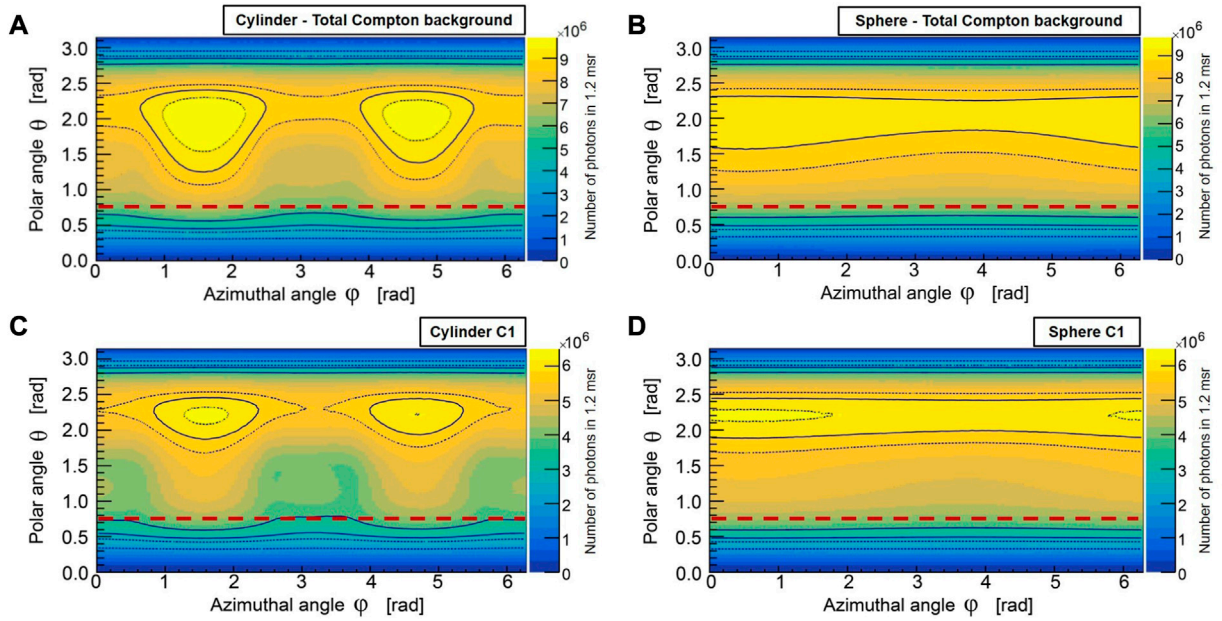

FIGURE 5
The spatial distribution of total Compton **(A**, **B)**, and single-Compton **(C**, **D)** scattered photons in the Gd K-shell energy range for cylindrical and spherical water phantoms are shown here for a 4π uncollimated spherical detector (MC). The brown dashed line represents the polar angle of the detector's optical axis (z-axis of the sensor) with respect to the primary beam direction. The total Compton scattering at the detector's optical axis differs slightly less than a factor of two from the maximum value over the polar angle θ, while the single-Compton scattering differs by a factor of two. The asymmetry observed in ϕ, in the cylindrical water phantom **(A**, **C)**, arises from the excess path length that photons must traverse through the volume along the height of the cylinder compared to its radial direction, resulting in an increased likelihood of higher-order Compton scattering and photoelectric absorption. This effect is also partly due to the collimated incident beam cross-section (30 mm × 20 mm FOV). The spherical water phantom **(B, D)** exhibits weaker asymmetry in ϕ due to its radially symmetric volume geometry.

CBCT scans at effective CT energies and calibrated XRF energies (obtained from simple bilinear scaling methods [52, 53]) were used to find the attenuation coefficients required in the element-by-element product (Hadamard product in matrix form) of the depth-dependent point response (modelled analytically) with the task-specific (object dependent) attenuation factors (calculated using radiological path lengths from Siddon's algorithm [54]), thus, forming the forward projection/system matrices with elements a_{ij}. Here, an additional self-correction applies in the reconstruction step *via* the back-projection process that reduces the chances of false signal detection, whereby if particular background bins are selected posing as XRF signals, which would differ in each projection, the back-projection of the sparse solutions from NNLS will weaken the false signal intensity.

2.9 CBCT image reconstruction

The CBCT projections in MoNP scan settings were reconstructed using FDK cone-beam filtered back-projection algorithm [55]. For CBCT scans with Gd contrasts, an isotropic TV-EM algorithm was used. As reconstruction algorithms are different, comparative quantitative imaging would be more challenging, requiring their effects to be studied more carefully. Here, we are only looking at the general feasibility of the approach.

3 Results

3.1 Development of a microphysiological breast cancer model for molecular imaging with metallic probes

The microphysiological breast cancer model used in this study is based on a biological matrix derived from decellularized porcine jejunum that contains an intact basal membrane and therefore permits rapid engraftment of epithelial cancer cells [44]. Two widely established cell types, the breast cancer cell line MDA-MB 231 and primary fibroblast were seeded onto the matrix. Upon static 3D culture, the breast cancer model could be routinely established and displayed a consistent phenotype with characteristic architecture shown in Figure 7. The upper layer of the breast cancer model consisting of primary human fibroblasts formed a dense cell layer, whereas the breast cancer cell line MDA-MB231 invaded from the second layer into the third layer of SISmuc scaffold indicating the invasive potential of this cell line (see Figure 7). Neither the treatment with different concentrations of MoNPs nor the treatment with Gd-containing contrast agents had an effect on the tissue morphology investigated by HE staining (see Figure 7A).

An immunohistochemistry staining was performed to further investigate the functional and molecular properties of the cancer tissue model. Staining with Ki-67 showed that the highest

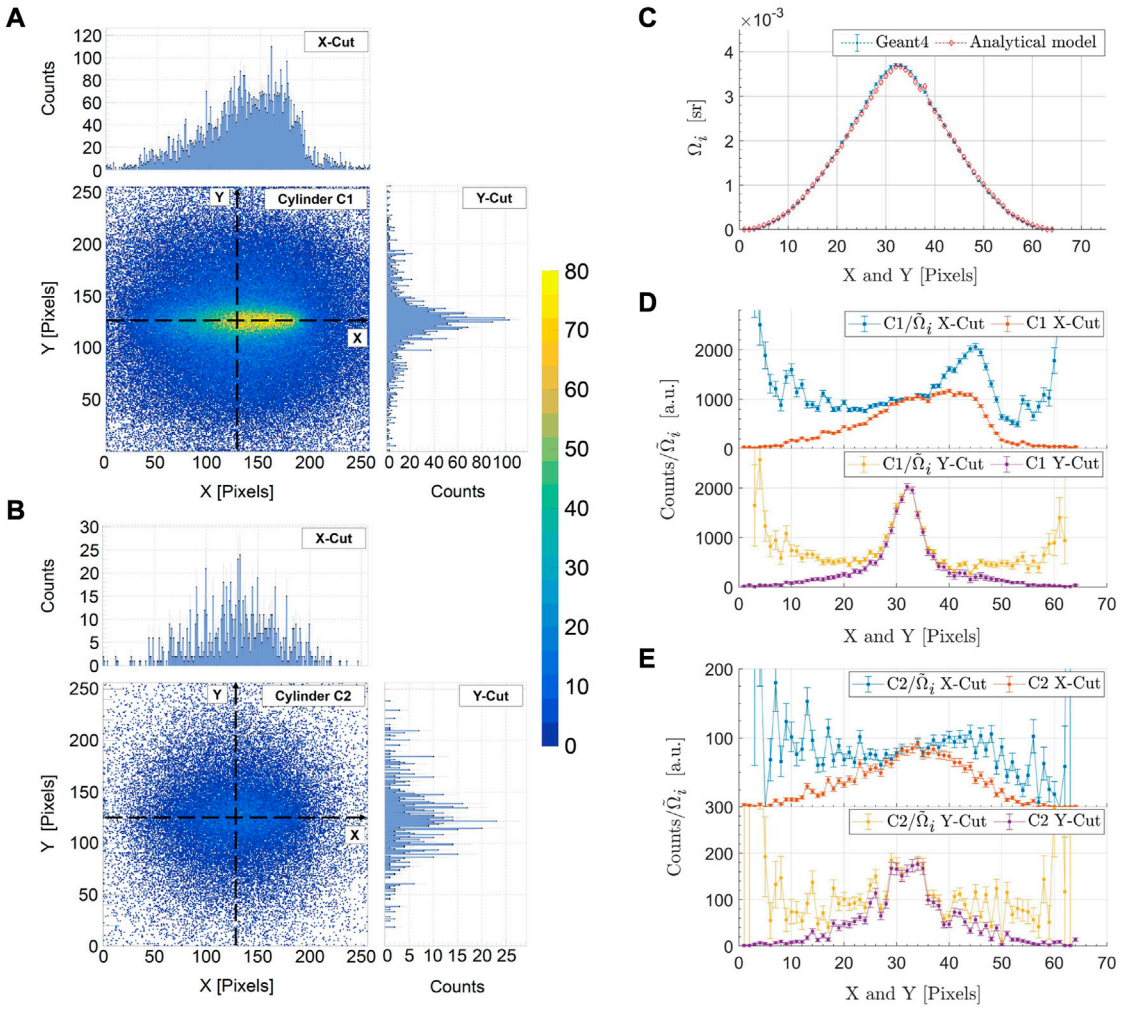

FIGURE 6
The detected (MC) spatial distribution of singly (C1) **(A)** and doubly (C2) **(B)** scattered Compton photons in the Gd K-shell energy range for the single-pinhole collimated detector is shown here. The spatial anisotropy of C1 photons **(A)** about the detector's optical axis can be seen in comparison to the C2 photons **(B)**. The detection solid angle, Ω_i, is compared between MC simulations and an analytical model in **(C)**. The C1 **(D)** and C2 **(E)** photon profiles are shown along the horizontal (X-Cut) and vertical (Y-Cut) directions of the detector. The numerical calculations of the analytical model are performed over a 64 × 64-pixel grid in order to minimize computational efforts, resulting in a rebinning of the data in **(C, D, E)** by combining 4 × 4 pixels.

proportion of proliferative cells (brown color) were found in the second tissue layer that was seeded with MDA-MB 231 cells (see Figure 7B). The MDA-MB 231 cells that invaded the third layer with SISmuc scaffold appeared mainly in a blue nuclei color from the Haematoxylin counter staining pointing towards a higher proportion of non-vital cells. The upper tissue layer covered by a dense layer of primary fibroblasts showed an almost equal proportion between vital and non-vital cells. Due to the non-invasive nature of these cells and the dense cell population, there might be a limited gas and nutrient exchange leading to a higher fraction of non-vital cells compared to the breast cancer tissue layer. The staining with Vimentin served as a marker for intermediate filaments comprising the cytoskeleton. As shown in Figure 7C, for control and low MoNP concentrations, Vimentin is present in both, primary human fibroblasts and MDA-MB 231 cells. Pro-Collagen is a precursor for collagen synthesis, a structural protein in the extracellular matrix found in various connective tissues. In this study, it serves as a marker for potential cytoskeleton remodeling induced by the treatment with contrast agents. Compared to the control condition (see Figure 7D, control), the treatment with MoNPs led to a significant increase in the Pro-Collagen signal (see Figure 7D, at MoNP and Gd treatments), indicating that the treatment with MoNPs and Gd-containing contrast agents already in low concentrations induced cellular processes related to the remodeling of the cytoskeleton.

3.2 Influence of contrast agents on cellular vitality

The influence of the investigated contrast agents in various concentrations on the cell vitality was investigated with immunohistochemistry staining and subsequent counting of Ki-67 positive nuclei (brown signal corresponding to vital cells)

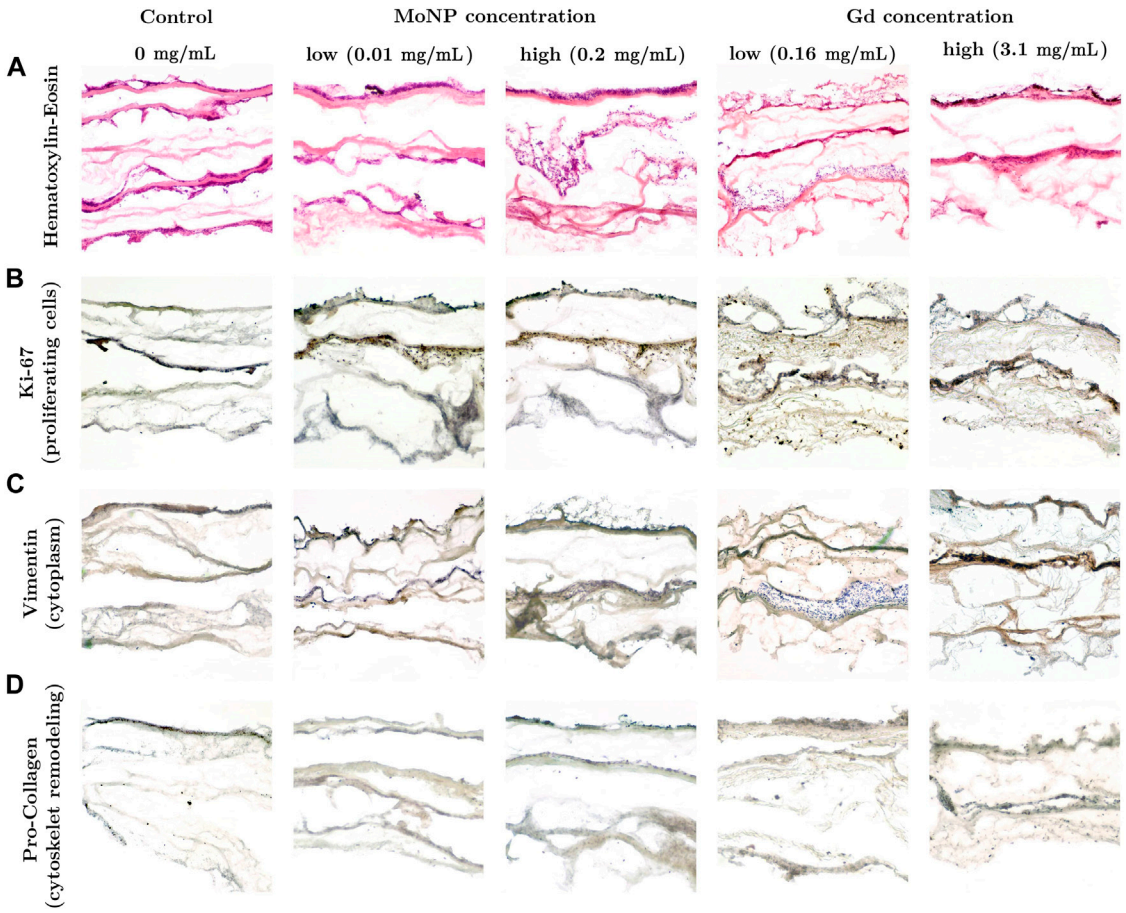

FIGURE 7
(A) HE staining and **(B)** immunohistochemical staining against Ki-67, **(C)** Vimentin and **(D)** Pro-Collagen in the 3D breast cancer model composed of three layers: primary human fibroblasts, MDA-MB-231 and scaffold after 48 h incubation.

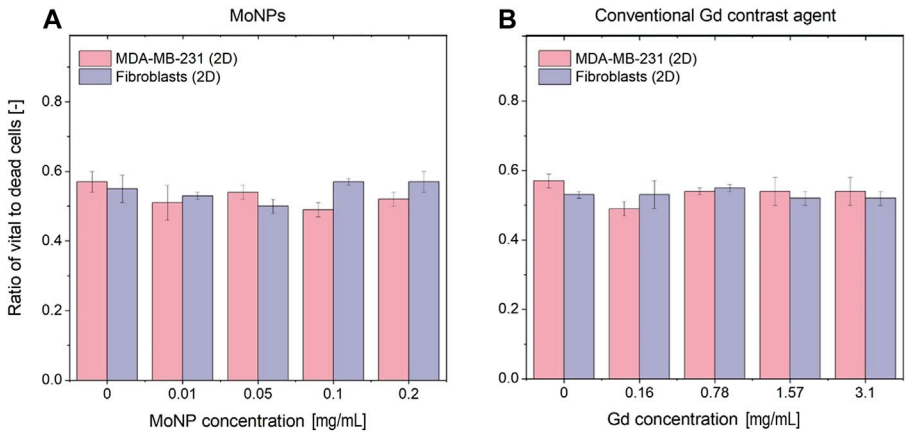

FIGURE 8
Cytotoxicity of the investigated conventional and nanoparticle-based contrast agents measured by Ki-67 immunohistochemistry staining and cell counting **(A)** for MoNP treatment and **(B)** Gd treatments in the 3D tissue-engineered breast cancer model after 48 h incubation. The data points are represented as the mean ± standard deviation of triplicate measurements.

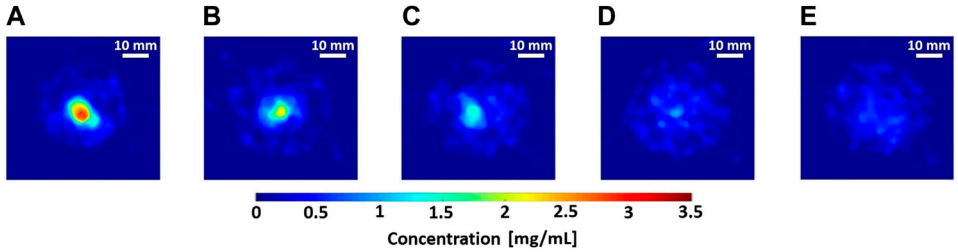

FIGURE 9
(A–E) Reconstructed axial slices of 3.1–0 mg/mL Gd calibration samples (8 mm diameter polypropylene microcentrifuge tubes) embedded in water phantom (50 mm maximal diameter), performed with 10-view projections using anisotropic total variation (TV) based sparsifying transform in Green's one-step-late TV-EM algorithm [50, 51]. Scale bar: 10 mm.

compared to Haematoxylin-positive nuclei (blue color corresponding to dead cells) (see Figures 8A, B). We could not detect any concentration-dependent changes in the vital cell ratio in the two tissue layers for all tested Gd- and MoNP doses. In addition, we found a comparable vitality ratio in the apical fibroblast tissue layer compared to the basal breast cancer cell layer which indicates that there is no impact on the inner tissue layer due to a potential sub-optimal gas or nutrient supply. Furthermore, we performed a 3-(4,5-dimethylthiazol-2-yl)-2,5-diphenyl tetrazolium bromide (MTT) assay under 2D and 3D conditions to assess the cell vitality after treatment with the investigated contrast agents (see Supplementary Appendix C). Under all investigated conditions, the breast cancer cell line MDA-MB-231 had significantly higher absorption signals compared to the primary human fibroblasts in the MTT assay. The treatment of both cell types under 2D and 3D conditions with Gd-containing contrast agents had no effect on the cell vitality for the investigated conditions ranging from 0.16–3.15 mg/mL (see Supplementary Appendix C). For the treatment with MoNPs ranging from 0.01–0.2 mg/mL, we observed an increasing absorption signal for the MTT conversion reaction in both, 2D and 3D conditions. Therefore, we assume that the presence of MoNPs led to an unwanted side reaction for the conversion of the MTT dye in a concentration-dependent manner.

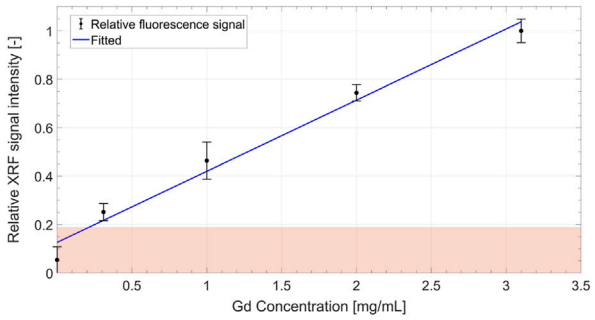

FIGURE 10
Calibration curve showing a linear increase in the relative (normalized by the maximum net XRF signal intensity) net XRF signal intensity with increasing Gd concentration. The boundary of the shaded zone represents the 3σ (i.e., ~ 99.7 %) background level above the intercept of the calibration curve. The XRF signals in this zone are not differentiable from the background noise, therefore, the detection sensitivity is defined as the least detectable sample, i.e., 0.31 mg/mL.

3.3 Development of a cone-beam laboratory XFCT setup for *in vitro* tissue testing

3.3.1 XFCT and CBCT imaging of small-animal-sized phantoms

Here, we present the results of our pilot study on small-animal-sized phantom measurements considering *in vivo*-relevant imaging parameters. MC simulations were carried out for the *in vitro* imaging-task characterization and quantitative performance analysis of the multislice cone-beam XFCT setup. The spatial resolution was estimated using two point-sized emitters, each with a 0.4 mm diameter, embedded in a cylindrical water phantom with a diameter of 50 mm and located at the center of the field of view. For Gd as contrast agents, the sources emitted X-ray photons in the characteristic energy range of the Gd K-shell (42–43 keV). The emitters can be interpreted as point sources with reference to the expected spatial resolution. Assuming at least 3σ (where σ (sigma) represents the standard deviation of the background noise) XRF signal differentiability over the background noise, an achievable spatial resolution of about 1.6 ± 0.1 mm was determined at the $\sim 3.29\,\sigma_{\mathbf{K}_0=\mathbf{K}_1}$ SNR limit, where $\mathbf{K}_0$ and $\mathbf{K}_1$ are noise covariance matrices for each of the two point-sized sources, respectively [48, 56].

Figure 9 shows the reconstructed axial slices of the Gd-containing calibration samples (0–3.1 mg/mL) embedded inside a water phantom. The calibration curve in Figure 10, obtained from the reconstructed data, shows the measured relative net XRF signal intensities for the known Gd calibration concentrations. The relative intensities are obtained through normalization by the maximum net XRF signal intensity. A linear relationship was detected between the relative net XRF signal intensity and Gd concentration, with a slight deviation from zero in the intercept of the regression line. This discrepancy in the intercept of the regression line may be attributed to background noise, but with a larger sample size of low-concentration calibration samples, this trend could potentially be corrected. The minimum detectable Gd concentration of 0.031 wt% (0.31 mg/mL), also the least detectable calibration sample

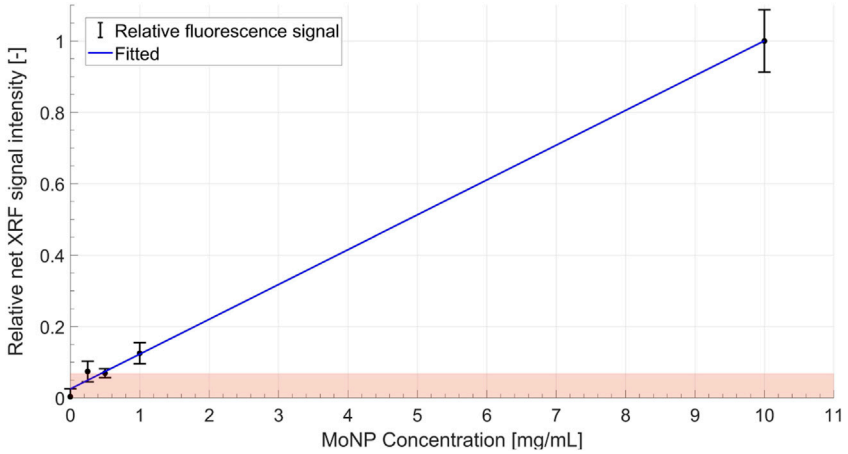

FIGURE 11
Calibration curve showing a linear increase in the relative (normalized by the maximum net XRF signal intensity) net XRF signal intensity with increasing MoNP concentration. Here a relaxed noise limit is considered due to the low-count statistics in MoNP imaging, i.e., the boundary of the shaded zone represents the 1.96σ (i.e., ~ 95 % confidence interval) background level above the intercept of the calibration curve. The detection sensitivity is defined as the least detectable sample, i.e., 0.5 mg/mL.

TABLE 1 System characteristics and imaging metrics for CBCT and XFCT scans performed with MoNPs and conventional Gd-containing contrast agents.

	MoNPs		Gd (Gadoteric acid)	
	CBCT	XFCT	CBCT	XFCT
Excitation beam spectrum	45 kV, 6 mm Al	30 kV, 6 mm Al	90 kV, 0.3 mm Cu	90 kV, 0.3 mm Cu
Incident flux (MC) [photons s^{-1} sr^{-1}]	-	~ $1.9 \cdot 10^{10}$	-	~ $1.34 \cdot 10^{12}$
Detected flux (Timepix3) exp.[a]/sim.[b] [photons s^{-1} sr^{-1}]	-	~ $9.3 \cdot 10^{9}$ / ~ $9.2 \cdot 10^{9}$	-	~ $6.89 \cdot 10^{11}$ / ~ $7.02 \cdot 10^{11}$
X-ray tube power [W]	80	60	80	80
Exposure time per projection [s]	10	300	6	150
Number of projections	60	30	30	10
Dose per projection [cGy]	0.033 @ 1.8 mA	3 @ 2 mA	0.11 @ 0.9 mA	23 @ 0.9 mA
Detection sensitivity [wt%]	-	0.05	-	0.031
Total imaging dose [cGy]	~94		~280	
Total imaging time [h]	~2.8		~0.55	

[a]Experimental data (scaled by radiometric correction factors).
[b]Simulation data (scaled by radiometric correction factors).

concentration, was defined as the XFCT detection sensitivity in the Gd imaging scheme. This sensitivity limit was determined (methodology similar to [23]) as the net measured XRF signal, detectable above the 3σ (3 times the background standard deviation, or the upper limit of the ~ 99.7 % background confidence interval) background noise level over the intercept of the calibration curve.

The XFCT imaging time for the Gd tissue and the phantom scans with 10-view sparse tomography (30 mm interior region-of-interest FOV, 20 mm longitudinal-FOV) was just under ~30 min, including the sample rotation and data acquisition, leading to an estimated (MC) XFCT imaging dose of about 276cGy (~23cGy per projection estimated dose, i.e., the absorbed energy in a scoring volume held inside the 50 mm cylindrical water phantom at the isocenter of the scan cone-beam profile) at the isocenter. The estimated absorbed dose for the CBCT scans, using Gd as a contrast agent for either phantom, was approximately 3.3 cGy (~1.1 mGy per projection) at the isocenter for an exposure time of 6s s per projection.

An achievable spatial resolution of 1.8 mm (1.8 ± 0.2 mm) is estimated for MoNPs using MC simulations, which were conducted as described for the Gd case but with molybdenum K-shell characteristic energies and MoNP scan geometry. The MoNP detection limit (see Figure 11) was estimated with a relaxed noise condition in comparison to the Gd case, i.e., with a 95% confidence interval about the background level. Therefore, the sensitivity in the *in vitro* setting was about 0.05 wt% with an estimated (MC) dose at

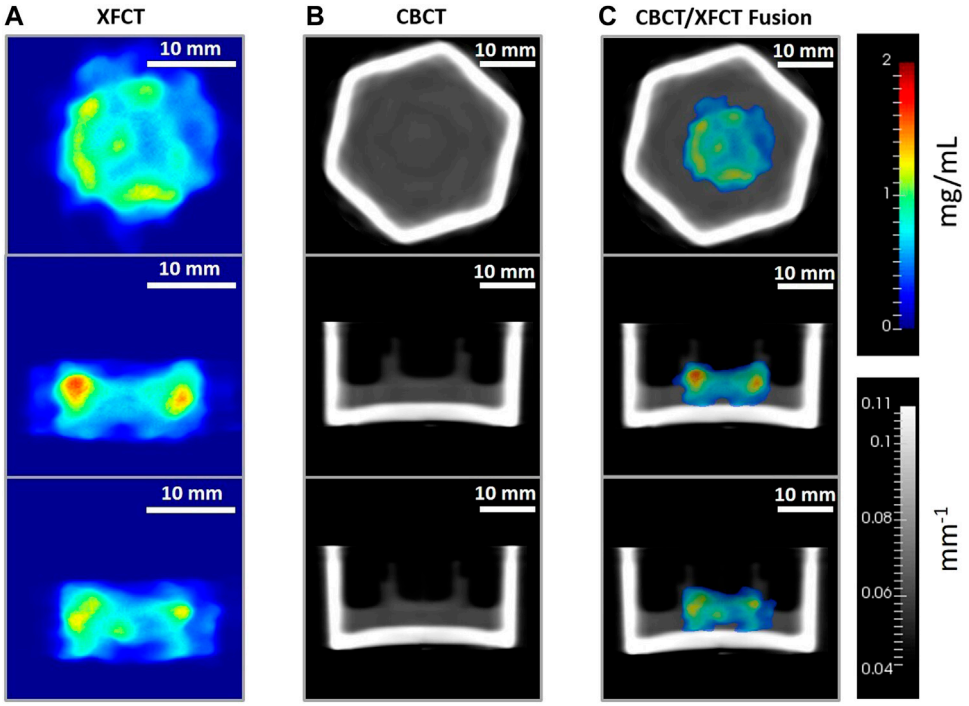

FIGURE 12
Axial (top row), sagittal (middle row), and coronal (bottom row) image planes from the tomographic reconstruction (TV-EM) of the 3D breast cancer tissue model administered with 3.15 mg/mL Gd and incubated over 48 h period. Gd concentration (mg/mL) maps from **(A)** XFCT reconstruction (magnification factor approx. ×1.5), **(B)** linear attenuation coefficient (mm^{-1}) maps of the cell crown/holder held inside borosilicate glass container with cell-culture growth medium, obtained from the CBCT scans, and **(C)** XFCT image data fused with CBCT images. For **(C)**, thresholding < 0.31 mg/mL is applied to the voxels, i.e., cut off below the detection limit. While CBCT remains invariant, the low contrast detectability of the XFCT technique with small added Gd concentrations can be clearly seen. The rainbow color bar shows the Gd concentration (mg/mL). The grayscale color bar shows the attenuation coefficients (mm^{-1}). Scale bar: 10 mm.

the isocenter of ~3 cGy and ~0.33mGy per projection for XFCT and CBCT scans, respectively. This resulted in a total imaging dose of about 94 cGy for MoNPs. The imaging time was about ~ 2.6 h and 12 min for XFCT and CBCT, respectively.

In either imaging configuration, the spatial resolution and low-concentration sensitivity were limited primarily by the small detection area of the Timepix3, constraining the focal distances for the FOV choice and instrumentation challenges of designing multi-pinhole collimation, besides the predominant signal loss effect from intrinsic background interference. Table 1 summarises the primary XFCT and CBCT imaging performance for the two contrast-agent scanning schemes and their respective dose estimates.

3.3.2 XFCT and CBCT imaging of microphysiological breast cancer model as a phantom

In the following section, imaging results of the 3D breast cancer model are reported for the two contrast agents. Figures 12, 13 show the axial, sagittal, and coronal XFCT/CBCT reconstructed slices in the tissue regions for the maximum administered dosages of Gd and MoNPs, respectively, i.e., 3.15 mg/mL Gd and 0.2 mg/mL MoNPs, each incubated over 48 h period. The MoNP detection sensitivity was initially overestimated as 0.01 wt% (subsequently corrected to 0.05 wt%), leading to a maximum administered MoNP dose of 0.2 mg/mL for *in vitro* imaging experiments. Therefore, the MoNP reconstructed images display significant noise from scattered background noise along with XRF signals (proportional to the MoNP concentration) in and around the tissue containing cell-crown regions. The CBCT reconstructed images for the two contrast agents varied primarily due to differences in the reconstruction techniques outlined in section 2.9, angular sampling frequency (i.e., 30 and 60 views for Gd and MoNPs, respectively), and CT energies. The CBCT images for the MoNP case are characterized by the presence of noise and streaky artifacts from the FDK reconstruction algorithm, as seen in Figure 13B. On the other hand, for the Gd case, the positive smoothing parameter (ε = 0.0001) and TV regularization (β = 0.05) were set to reduce streaky artifacts and noise in CBCT images [50].

Figure 14B displays the sampled accumulations of Gd in the central and peripheral uptake regions of tissue-containing reconstructed slices, which were obtained through local-contrast segmentation using Gd concentration thresholds. The average sampled Gd concentration is seen to increase with the increasing administered dose while having lower accumulations in the central tissue regions. The maximum administered dose of 3.15 mg/mL Gd led to an average sampled Gd concentration of 0.85 ± 0.01 mg/mL in the central and 1 ± 0.05 mg/mL in the peripheral regions, respectively. Below the sensitivity limit, i.e., for 0.16 mg/mL dosage, the average accumulations of Gd concentration are overestimated due to sampling errors (identification of tissue regions in local low contrast areas, resulting from background noise).

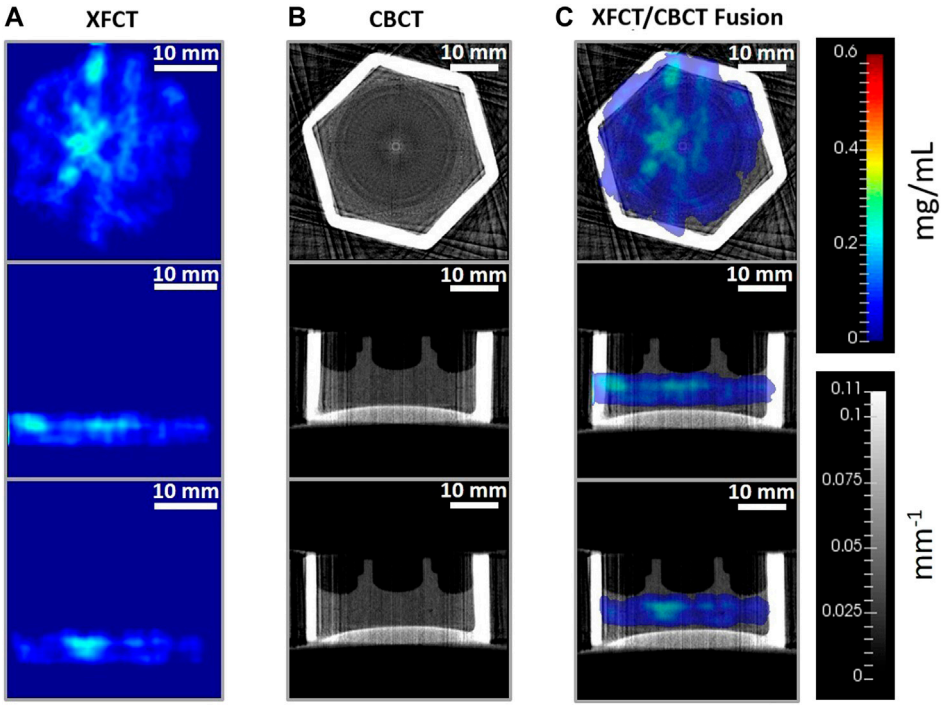

FIGURE 13
Reconstructed axial (top row), sagittal (middle row), and coronal (bottom row) tissue slices from **(A)** XFCT using anisotropic TV-EM algorithm, **(B)** CBCT reconstruction from FDK algorithm, and **(C)** XFCT-CBCT registered images of the multilayer cell-culture sandwich administered with 0.2 mg/mL MoNP solution, imaged at 48h incubation period. The rainbow color bar shows the MoNP concentration (mg/mL). The grayscale color bar shows the attenuation coefficients (mm^{-1}). Scale bar: 10 mm.

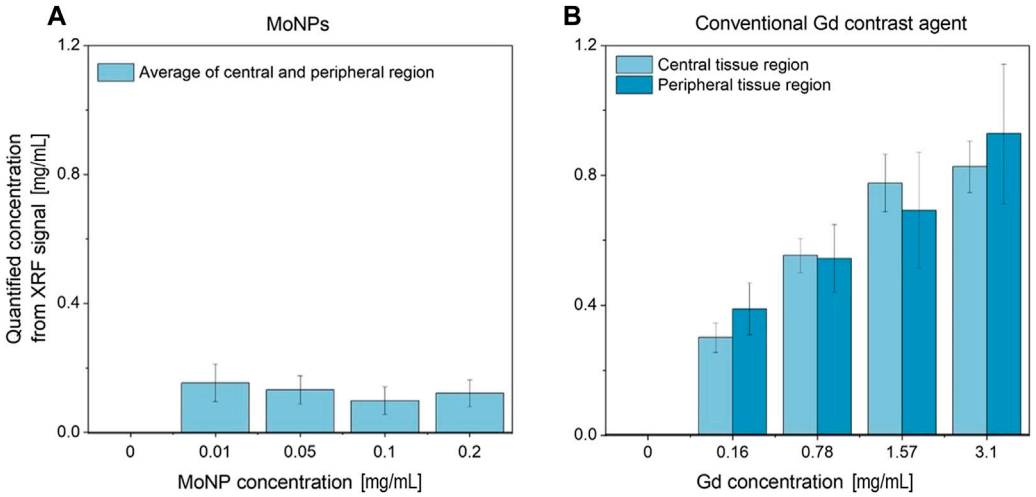

FIGURE 14
(A) Average MoNP and **(B)** Gd uptake concentration sampled (local-contrast-based threshold segmentation) from the reconstructed slices in the central and peripheral (adjacent to cell crown) ROI in the tissue region.

For MoNPs (see Figure 14A) with 0.2 mg/mL and 0.1 mg/mL dosages, as to be expected, the average sampled concentrations were lower than the respective maximum administered doses. However, 0.05 mg/mL and 0.01 mg/mL resulted in significant overestimation from segmentation sampling errors and misclassification of signal and background regions, both during segmentation and signal extraction from curve fittings under relaxed SNR limits (SNR > 2). The extracted signal, otherwise, would be classified as

no signal under standard operating conditions (SNR > 3.29). As pointed out before, the initial overestimation of MoNP detection sensitivity resulted in a maximum administered dose of 0.2 mg/mL, thus, MoNP uptake (see Figure 14A) did not demonstrate an increase with increasing administered dose.

4 Discussion

The results demonstrate the 3D localization capability of the benchtop cone-beam XFCT system for Gd-containing contrast agents and MoNPs for the tissue-engineered microphysiological 3D breast cancer model with *in vivo* mimicking properties. The proposed XFCT imaging technique allows for multislice spatiotemporal reconstruction of elemental composition maps through a dynamic event-based (ToA and ToT) acquisition of X-ray projections while providing X-ray attenuation maps needed for correcting the excitation and fluorescence X-ray intensities. For varying administered Gd doses, the local deposited concentrations in different regions of the target tissue slices were successfully quantified, exhibiting *in vitro* low-contrast imaging performance of the XFCT system. For MoNPs, the maximum administered dose was lower than the detection limit due to an overestimation of the sensitivity limits made prior to the *in vitro* tissue experiments, however, the imaging capability is still demonstrable (see Figure 11) at higher administered NP dosages.

Since a large object volume in the context of small-animal imaging (about 50 mm diameter) is scanned at shorter scan-times, leading to multislice imaging (for example, with 1.6 mm spatial resolution and 20 mm longitudinal FOV, at least 12 axial slices can be reliably reconstructed) with the contrast positions not known *a priori* in the cone-beam volume, there is a larger intrinsic background effect due to an increased proportion of scattered photon generation, particularly in the case of polychromatic excitation sources [21, 57]. Therefore, slightly higher radiation doses per projection are necessitated specifically in comparison to the scanning techniques with high energy resolution single-pixel multichannel detectors in benchtop cone-beam and pencil-beam settings [23–26]. For instance, the multislice 3D imaging scheme for the Gd contrast agents (0.031 wt% detection limit) with low power microfocus X-ray source, presented here, currently requires a radiation dose of ~23 cGy per projection with ~33 min total scan-time in comparison to ~1.87 cGy per projection for a Gold nanoparticle (0.03 wt% detection limit in 30 mm diameter water phantom) single-slice scheme with single-pixel detectors having ~1 h total scan-time, or ~1 cGy per projection for Gd nanoparticles ($NaGdF_4$, 0.18 wt% detection limit in 50 mm diameter water phantom) single-slice fan-beam scheme (linear-array PCDs, 0.5 × 2 mm rectangular pinhole) with ~7.5 min total scan-time [24, 27]. It is also seen for the imaging geometry, *via* MC simulations, that requirement of spectral bandwidth of the incident cone-beam is more critical to background yield reduction (see Supplementary Appendix B).

Besides ineffective dose utilization in the image formation process, limited by the detection solid-angle from the single-pinhole collimation and small area (~14 mm × 14 mm active detection area) pixelated detector, intrinsic detector effects also contribute significant noise to the signal background. Here, the primary detector effects contributing to the sensitivity deterioration, consequently increasing the radiation dose, were the charge-sharing and partial charge deposition from CdTe XRF photons (CdTe presents a fluorescence yield of about 80% and a mean free path of 58 μm and 110 μm for Te and Cd, respectively) in the small-pixel (55 μm) CdTe configuration. Both these effects cause significant distortions in measurements and degradation of the detector energy resolution adding to the XRF signal detectability loss from the scattered photon interference in the signal bins. Though simple charge-sharing reconstruction and CdTe XRF corrections are implemented, an improved approach is necessary, along with instrumentation improvements. Therefore, additionally, our future considerations may involve, e.g., developing dedicated XRF detectors, better suited for high-energy detection. Nonetheless, with ten such single-pinhole (corresponding to the Gd 10-view sparse imaging presented here) detectors arranged in a circular geometry (forming 2π solid angle in the scan mid-plane), an order of magnitude reduction in X-ray dose can be obtained, specifically for the Gd imaging scheme with about 2.3 cGy per projection, therefore reaching small-animal *in vivo* acceptable dose limits, for, e. g., below 30 cGy in mice [33, 58]. Consequently, the total imaging time with parallel acquisition would then be reduced to below ~6 min, far below *in vivo* scan-time constraints, for, e.g., determined by effective anaesthetized period as short as 30–60 min [59, 60]. Furthermore, multi-pinhole collimation in such a configuration may allow additional reduction of the XFCT imaging dose through SNR improvements per projection by a factor equal to the number of pinholes [60]. For the same dose limit, densely sampling systems which capture projections with smaller angular increments would suffer from lower signal statistics per projection, leading to overall sensitivity loss and an increase in total scanning time. A geometric/mechanical arrangement of ten such detectors is completely feasible in the current XFCT setup.

As substantial dose enhancements can be achieved through optimization of the applied X-ray beam energies, under the current imaging configurations, imaging dose (dose per projection of 23 cGy and 7.1 cGy for Gd and MoNPs, respectively) and detection sensitivity (0.031 wt% and 0.05 wt% for Gd and MoNPs, respectively) could be lowered further for a fixed scan-time limit and maximum excitation voltage through improved beam filtration possibilities and (or) quasi-monochromatic beams from high-power X-ray sources, therefore, minimizing low energy radiation dose below K-absorption edges of the contrast agents. Here, the present setup was limited by 90 kV maximum voltage and 80 W maximum tube power, limiting the optimization possibilities of the incident X-ray spectrum for the scan-time limit under 30 min. Also, further enhancement of both detection sensitivity and delivered dose can be achieved, for, e.g., from detailed simulation studies for specific imaging tasks and tissue models. With the application of variance reduction techniques, utilization of well-validated MC-based forward projectors may allow reconstruction without the need for calibration measurements, thus allowing accurate quantification results. For larger objects in cone-beam scanning, the marker accumulation can be far away from the local calibration points and, therefore, quantification may suffer from errors due to shift-variant sensitivities, requiring multiple calibration points for accurate

quantification. Additionally, our future approaches may involve, e.g., using low-dose cone-beam scans for coarse localization and concave reflecting-type optics for cone-beam focusing, allowing higher and variable spatial resolution imaging with higher signal statistics from radiation concentration effects.

5 Conclusion

In this pilot study, we have characterized a benchtop setup for fast, and fully-3D quantitative XRF imaging with a cone-beam X-ray source and a tissue-engineered breast cancer model. We have focused on identifying requirements and demonstrating feasibility with a polychromatic microfocus source using a region-of-interest sparse sampling geometry (10-view for Gd) and reconstruction approach, along with the optimization of components including pixelated CdTe detectors (Timepix3 HPCD, Advacam) and micro-pinhole collimators, excitation beam optimization using beam-shaping filters, and background noise reduction. Considering critical physical constraints inherent to *in vivo* imaging, particularly scanning time, contrast dose, and radiation dose, our optimizations allow for high-spatial-resolution longitudinal imaging that is feasible for both *in vitro* and *in vivo* experiments.

A tissue-engineered microphysiological breast cancer model was used to evaluate the system performance after treatment with conventional Gd-based and nanoparticle (Mo)- based contrast agents. The proposed XRF imaging setup showed the applicability and feasibility of cone-beam methodology for quantitative *in vitro* and *in vivo* NP imaging at an acceptable dosage with a spatial resolution below < 2 mm and contrast dose (~ 0.3 mg/mL for Gd, and ~ 0.5 mg/mL for MoNPs) and imaging time (33 min for Gd and 2.8 h for MoNPs) with a future reduction potential with an order of magnitude. Furthermore, utilizing a ring arrangement of ten micro-pinhole detectors can easily allow for a significant reduction in X-ray dose for small-animal imaging, potentially reaching an order of magnitude decrease, with doses as low as 23 cGy for Gd and 30 cGy for MoNPs. Addressing the Compton scattering problem, which poses the primary limiting factor in this imaging technique, is crucial to achieving high detection sensitivity with polychromatic microfocus sources while minimizing radiation exposure.

Besides assessing the feasibility of high-resolution imaging, challenges and limitations of current cone-beam techniques are outlined, particularly for achieving higher resolution. Current high-flux benchtop X-ray sources, e.g., based on liquid metal targets, which allow high spatial resolution, have limitations in accommodating multiplexed pharmacokinetics across a wide range of nanoparticle-coupled drug candidates due to their restrictions to low-Z nanoparticles. As pointed out, monochromatization is essential to reduce background contribution from Compton scattering. To achieve this, our future investigations will employ bent mosaic crystals that rely on Bragg reflection. These crystals potentially offer high reflection efficiencies suitable for medium-Z nanoparticles and enable beam focusing for higher resolution scans with higher expected SNR. Preceding high-resolution scans, coarse scans can be performed *via* cone-beam XFCT to identify the region of interest. This becomes particularly important when the size scale of the imaging object increases.

Overall, our proposed approach of combining a high-resolution molecular imaging modality and complex tissue-engineered organ models offer new possibilities in translational biomedical engineering for nanodrug screenings and innovative cancer radiology.

Data availability statement

The raw data supporting the conclusion of this article will be made available by the authors, without undue reservation.

Author contributions

MF, KK, HW, and CH conceived the project and designed experiments. MF, HW, KK, and CH developed methodology. MF, KK, MA-M, RK, SO, and AC acquired data. MF and KK analyzed and interpreted data. MF, KK, MA-M, HW, and CH wrote, reviewed, or revised the manuscript. TS, FG, and TM provided technical and material support. HW, FG, TM, and CH supervised the study. All authors read and approved the final manuscript.

Funding

This work was funded by the research grant "Biokinetic and Physical Simulation Studies for the Design of *in Vivo* Imaging Pharmacokinetics" of the Ministry of Science, Energy, Climate Protection and Environment of the Federal State of Saxony-Anhalt (Germany).

Conflict of interest

The authors declare that the research was conducted in the absence of any commercial or financial relationships that could be construed as a potential conflict of interest.

Publisher's note

Supplementary material

The Supplementary Material for this article can be found online at: https://www.frontiersin.org/articles/10.3389/fphy.2023.1125143/full#supplementary-material

References

1. Caddeo S, Boffito M, Sartori S. Tissue engineering approaches in the design of healthy and pathological *in vitro* tissue models. *Front Bioeng Biotechnol* (2017) 5:40. doi:10.3389/fbioe.2017.00040

2. Driehuis E, Kretzschmar K, Clevers H. Establishment of patient-derived cancer organoids for drug-screening applications. *Nat Protoc* (2020) 15:3380–409. doi:10.1038/s41596-020-0379-4

3. Jackson S, Thomas G. Human tissue models in cancer research: Looking beyond the mouse. *Dis Models Mech* (2017) 10:939–42. doi:10.1242/dmm.031260

4. Rodrigues J, Heinrich M, Teixeira L, Prakash J. 3d *in vitro* model (r)evolution: Unveiling tumor-stroma interactions. *Trends Cancer* (2020) 7:249–64. doi:10.1016/j.trecan.2020.10.009

5. Martinez Pacheco S, Driscoll L. Pre-clinical *in vitro* models used in cancer research: Results of a worldwide survey. *Cancers* (2021) 13:6033. doi:10.3390/cancers13236033

6. Singh V, Seed T. How necessary are animal models for modern drug discovery?: Animal models for drug discovery. *Expert Opin Drug Discov* (2021) 16:1391–7. doi:10.1080/17460441.2021.1972255

7. Amin MB, Greene FL, Edge SB, Compton CC, Gershenwald JE, Brookland RK, et al. The eighth edition ajcc cancer staging manual: Continuing to build a bridge from a population-based to a more "personalized" approach to cancer staging. *CA: a Cancer J clinicians* (2017) 67:93–9. doi:10.3322/caac.21388

8. Poornima K, Francis AP, Hoda M, Eladl MA, Subramanian S, Veeraraghavan VP, et al. Implications of three-dimensional cell culture in cancer therapeutic research. *Front Oncol* (2022) 12:891673. doi:10.3389/fonc.2022.891673

9. Sacchi M, Bansal R, Rouwkema J. Bioengineered 3d models to recapitulate tissue fibrosis. *Trends Biotechnol* (2020) 38:623–36. doi:10.1016/j.tibtech.2019.12.010

10. Hormuth DA, Jarrett AM, Lorenzo G, Lima EA, Wu C, Chung C, et al. Math, magnets, and medicine: Enabling personalized oncology. *Expert Rev Precision Med Drug Dev* (2021) 6:79–81. doi:10.1080/23808993.2021.1878023

11. Kim J, Koo B-K, Knoblich J. Human organoids: Model systems for human biology and medicine. *Nat Rev Mol Cel Biol* (2020) 21:571–84. doi:10.1038/s41580-020-0259-3

12. Pelaz B, Alexiou C, Alvarez-Puebla RA, Alves F, Andrews AM, Ashraf S, et al. Diverse applications of nanomedicine. *ACS nano* (2017) 11:2313–81. doi:10.1021/acsnano.6b06040

13. Vu TQ, Lam WY, Hatch EW, Lidke DS. Quantum dots for quantitative imaging: From single molecules to tissue. *Cel Tissue Res* (2015) 360:71–86. doi:10.1007/s00441-014-2087-2

14. Abou-Elkacem L, Bachawal SV, Willmann JK. Ultrasound molecular imaging: Moving toward clinical translation. *Eur J Radiol* (2015) 84:1685–93. doi:10.1016/j.ejrad.2015.03.016

15. Appel A, Anastasio MA, Brey EM. Potential for imaging engineered tissues with x-ray phase contrast. *Tissue Eng B: Rev* (2011) 17:321–30. doi:10.1089/ten.teb.2011.0230

16. Beard P. Biomedical photoacoustic imaging. *Interf focus* (2011) 1:602–31. doi:10.1098/rsfs.2011.0028

17. Chen H, Rogalski M, Anker J. Advances in functional x-ray imaging techniques and contrast agents. *Phys Chem Chem Phys : PCCP* (2012) 14:13469–86. doi:10.1039/c2cp41858d

18. Körnig C, Staufer T, Schmutzler O, Bedke T, Machicote A, Liu B, et al. *In-situ* x-ray fluorescence imaging of the endogenous iodine distribution in murine thyroids. *Scientific Rep* (2022) 12:2903–9. doi:10.1038/s41598-022-06786-4

19. Kahl H, Staufer T, Körnig C, Schmutzler O, Rothkamm K, Grüner F. Feasibility of monitoring tumor response by tracking nanoparticle-labelled t cells using x-ray fluorescence imaging—A numerical study. *Int J Mol Sci* (2021) 22:8736. doi:10.3390/ijms22168736

20. Schmutzler O, Graf S, Behm N, Mansour WY, Blumendorf F, Staufer T, et al. X-ray fluorescence uptake measurement of functionalized gold nanoparticles in tumor cell microsamples. *Int J Mol Sci* (2021) 22:3691. doi:10.3390/ijms22073691

21. Grüner F, Blumendorf F, Schmutzler O, Staufer T, Bradbury M, Wiesner U, et al. Localising functionalised gold-nanoparticles in murine spinal cords by x-ray fluorescence imaging and background-reduction through spatial filtering for human-sized objects. *Scientific Rep* (2018) 8:16561. doi:10.1038/s41598-018-34925-3

22. Pereira G, Lopes R. *X-ray fluorescence microtomography in biological applications* (2011). IntechOpen. doi:10.5772/24535

23. Manohar N, Reynoso F, Diagaradjane P, Krishnan S, Cho S. Quantitative imaging of gold nanoparticle distribution in a tumor-bearing mouse using benchtop x-ray fluorescence computed tomography. *Scientific Rep* (2016) 6:22079. doi:10.1038/srep22079

24. Manohar N, Reynoso FJ, Cho SH. Technical note: A benchtop cone-beam x-ray fluorescence computed tomography (XFCT) system with a high-power x-ray source and transmission CT imaging capability. *Med Phys* (2018) 45:4652–9. doi:10.1002/mp.13138

25. Larsson J, Vogt C, Twengström W, Toprak M, Dzieran J, Henriksson M, et al. High-spatial-resolution x-ray fluorescence tomography with spectrally matched nanoparticles. *Phys Med Biol* (2018) 63:164001. doi:10.1088/1361-6560/aad51e

26. Shaker K, Vogt C, Katsu-Jiménez Y, Kuiper RV, Andersson K, Li Y, et al. Longitudinal *in-vivo* x-ray fluorescence computed tomography with molybdenum nanoparticles. *IEEE Trans Med Imaging* (2020) 39:3910–9. doi:10.1109/tmi.2020.3007165

27. Zhang S, Li L, Chen J, Chen Z, Zhang W, Lu H. Quantitative imaging of gd nanoparticles in mice using benchtop cone-beam x-ray fluorescence computed tomography system. *Int J Mol Sci* (2019) 20:2315. doi:10.3390/ijms20092315

28. Moseley HG. Lxxx. the high-frequency spectra of the elements. part ii. *Lond Edinb Dublin Phil Mag J Sci* (1914) 27:703–13. doi:10.1080/14786440408635141

29. Vernekohl D, Ahmad M, Chinn G, Xing L. Feasibility study of compton cameras for x-ray fluorescence computed tomography with humans. *Phys Med Biol* (2016) 61:8521–40. doi:10.1088/0031-9155/61/24/8521

30. Islamian J, Azazrm A, Mahmoudian B, Gharapapagh E. Advances in pinhole and multi-pinhole collimators for single photon emission computed tomography imaging. *World J Nucl Med* (2015) 14:3–9. doi:10.4103/1450-1147.150505

31. Kumakhov MA. Status of polycapillary optics and perspectives. *Int Conf X-ray neutron Capillary Opt* (2002) 4765:20–5. doi:10.1117/12.489770

32. Kumakhov MA. Capillary optics and their use in x-ray analysis. *X-Ray Spectrom Int J* (2000) 29:343–8. doi:10.1002/1097-4539(200009/10)29:5<343::aid-xrs414>3.0.co;2-s

33. Badea CT, Drangova M, Holdsworth DW, Johnson G. *In vivo* small-animal imaging using micro-ct and digital subtraction angiography. *Phys Med Biol* (2008) 53:R319–50. doi:10.1088/0031-9155/53/19/r01

34. Pittet MJ, Grimm J, Berger CR, Tamura T, Wojtkiewicz G, Nahrendorf M, et al. *In vivo* imaging of t cell delivery to tumors after adoptive transfer therapy. *Proc Natl Acad Sci* (2007) 104:12457–61. doi:10.1073/pnas.0704460104

35. Xia Q, Huang J, Feng Q, Chen X, Liu X, Li X, et al. <p>Size- and cell type-dependent cellular uptake, cytotoxicity and *in vivo* distribution of gold nanoparticles</p>. *Int J nanomedicine* (2019) 14:6957–70. doi:10.2147/ijn.s214008

36. Hainfeld JF, Slatkin DN, Smilowitz HM. The use of gold nanoparticles to enhance radiotherapy in mice. *Phys Med Biol* (2004) 49:N309–15. doi:10.1088/0031-9155/49/18/n03

37. Meyer D, Schaefer M, Doucet D. Advances in macrocyclic gadolinium complexes as magnetic resonance imaging contrast agents. *Invest Radiol* (1990) 25:S53–5. doi:10.1097/00004424-199009001-00025

38. Corot C, Port M, Raynal I, Dencausse A, Schaefer M, Rousseaux O, et al. Physical, chemical, and biological evaluations of p760: A new gadolinium complex characterized by a low rate of interstitial diffusion. *J Magn Reson Imaging* (2000) 11:182–91. doi:10.1002/(sici)1522-2586(200002)11:2<182::aid-jmri16>3.0.co;2-5

39. Mohamed H, Elatawy R, Ghoneim A, El-Ghor A. Induction of fetal abnormalities and genotoxicity by molybdenum nanoparticles in pregnant female mice and fetuses. *Environ Sci Pollut Res* (2020) 27:23950–62. doi:10.1007/s11356-020-08137-0

40. Tice RR, Hayashi M, MacGregor JT, Anderson D, Blakey DH, Holden HE, et al. Report from the working group on the *in vivo* mammalian bone marrow chromosomal aberration test. *Mutat Research/Environmental Mutagenesis Relat Subjects* (1994) 312:305–12. doi:10.1016/0165-1161(94)00016-6

41. Mortezazadeh T, A E M, M K. Glucosamine conjugated gadolinium (iii) oxide nanoparticles as a novel targeted contrast agent for cancer diagnosis in mri. *J Biomed Phys Eng* (2020) 10:25–38. doi:10.31661/jbpe.v0i0.1018

42. Chenthamara D, Subrmaniam S, Ramakrishnan S, Krishnaswamy S, Musthafa ME, Lin F-H, et al. Therapeutic efficacy of nanoparticles and routes of administration. *Biomater Res* (2019) 23:20. doi:10.1186/s40824-019-0166-x

43. Nietzer S, Baur F, Sieber S, Hansmann J, Schwarz T, Stoffer C, et al. Mimicking metastases including tumor stroma: A new technique to generate a three-dimensional colorectal cancer model based on a biological decellularized intestinal scaffold. *Tissue Eng C: Methods* (2016) 22:621–35. doi:10.1089/ten.TEC.2015.0557

44. Wallstabe L, Göttlich C, Nelke L, Kühnemundt J, Schwarz T, Nerreter T, et al. Ror1-car t-cells are effective against lung and breast cancer in advanced microphysiologic 3d tumor models. *JCI Insight* (2019) 4:e126345. doi:10.1172/jci.insight.126345

45. Allison J, Amako K, Apostolakis J, Arce P, Asai M, Aso T, et al. Recent developments in geant4. *Nucl Instr Methods Phys Res Section A: Acc Spectrometers, Detectors Associated Equipment* (2016) 835:186–225. doi:10.1016/j.nima.2016.06.125

46. Shimazaki H, Shinomoto S. A method for selecting the bin size of a time histogram. *Neural Comput* (2007) 19:1503–27. doi:10.1162/neco.2007.19.6.1503

47. Donoho DL. Compressed sensing. *IEEE Trans Inf Theor* (2006) 52:1289–306. doi:10.1109/tit.2006.871582

48. Barrett HH, Myers KJ. *Foundations of image science*. New Jersey, United States: John Wiley and Sons (2013).

49. Blumendorf F. *Background reduction for XFI with human-sized phantoms*. Germany: Staats-und Universitätsbibliothek Hamburg Carl von Ossietzky (2019). Ph.D. thesis.

50. Panin V, Zeng G, Gullberg G. Total variation regulated em algorithm [spect reconstruction]. *IEEE Trans Nucl Sci* (1999) 46:2202–10. doi:10.1109/23.819305

51. Zeng GL, Li Y, Zamyatin A. Iterative total-variation reconstruction versus weighted filtered-backprojection reconstruction with edge-preserving filtering. *Phys Med Biol* (2013) 58:3413–31. doi:10.1088/0031-9155/58/10/3413

52. Burger C, Goerres G, Schoenes S, Buck A, Lonn A, Von Schulthess G. Pet attenuation coefficients from ct images: Experimental evaluation of the transformation of ct into pet 511-kev attenuation coefficients. *Eur J Nucl Med Mol Imaging* (2002) 29:922–7. doi:10.1007/s00259-002-0796-3

53. LaCroix K, Tsui B, Hasegawa B, Brown J. Investigation of the use of x-ray ct images for attenuation compensation in spect. *IEEE Trans Nucl Sci* (1994) 41:2793–9. doi:10.1109/23.340649

54. Siddon RL. Fast calculation of the exact radiological path for a three-dimensional ct array. *Med Phys* (1985) 12:252–5. doi:10.1118/1.595715

55. Feldkamp LA, Davis LC, Kress JW. Practical cone-beam algorithm. *Josa a* (1984) 1:612–9. doi:10.1364/josaa.1.000612

56. Barrett HH, Myers KJ, Hoeschen C, Kupinski MA, Little MP. Task-based measures of image quality and their relation to radiation dose and patient risk. *Phys Med Biol* (2015) 60:R1–R75. doi:10.1088/0031-9155/60/2/R1

57. Ahmad M, Bazalova M, Xiang L, Xing L. Order of magnitude sensitivity increase in x-ray fluorescence computed tomography (xfct) imaging with an optimized spectro-spatial detector configuration: Theory and simulation. *IEEE Trans Med Imaging* (2014) 33:1119–28. doi:10.1109/tmi.2014.2305101

58. Parkins C, Fowler J, Maughan R, Roper M. Repair in mouse lung for up to 20 fractions of x rays or neutrons. *Br J Radiol* (1985) 58:225–41. doi:10.1259/0007-1285-58-687-225

59. Takeda T, Wu J, Huo Q, Yuasa T, Hyodo K, Dilmanian FA, et al. X-ray fluorescent ct imaging of cerebral uptake of stable-iodine perfusion agent iodoamphetamine analog imp in mice. *J synchrotron Radiat* (2009) 16:57–62. doi:10.1107/s0909049508031853

60. Sasaya T, Sunaguchi N, Thet-Lwin T, Hyodo K, Zeniya T, Takeda T, et al. Dual-energy fluorescent x-ray computed tomography system with a pinhole design: Use of k-edge discontinuity for scatter correction. *Scientific Rep* (2017) 7:44143–13. doi:10.1038/srep44143

frontiers | Frontiers in Physics

TYPE Original Research
PUBLISHED 24 April 2023
DOI 10.3389/fphy.2023.1144112

OPEN ACCESS

EDITED BY
Ewald Moser,
Medical University of Vienna, Austria

REVIEWED BY
Paul Summers,
European Institute of Oncology (IEO), Italy
Galina Pavlovskaya,
University of Nottingham, United Kingdom

*CORRESPONDENCE
Andreas Georg Berg,
andreas.berg@meduniwien.ac.at

SPECIALTY SECTION
This article was submitted to Medical Physics and Imaging, a section of the journal Frontiers in Physics

RECEIVED 13 January 2023
ACCEPTED 17 March 2023
PUBLISHED 24 April 2023

CITATION
Berg AG and Börner M (2023), A phantom for the quantitative determination and improvement of the spatial resolution in slice-selective 2D-FT magnetic resonance micro-imaging and -microscopy based on Deep X-ray Lithography (DXRL).
Front. Phys. 11:1144112.
doi: 10.3389/fphy.2023.1144112

A phantom for the quantitative determination and improvement of the spatial resolution in slice-selective 2D-FT magnetic resonance micro-imaging and -microscopy based on Deep X-ray Lithography (DXRL)

Andreas Georg Berg[1,2]* and Martin Börner[3,4]

[1]Center for Medical Physics and Biomedical Engineering, MR-Physics, Medical University of Vienna, Vienna, Austria, [2]High Field MR Centre, Medical University of Vienna, Vienna, Austria, [3]Karlsruhe Nano-Micro Facility (KNMFi), Karlsruhe Institute of Technology (KIT), Karlsruhe, Germany, [4]Institute of Microstructure Technology (IMT), KIT, Karlsruhe, Germany

Introduction: The most important assessed quality-control (QC) criteria for improvements in high-resolution imaging are represented by the contrast-to-noise-ratio and spatial resolution. Ultra-High-Field (UHF) Magnetic-Resonance-scanners (B ≥ 7 T) for medical research allowed for the improvement in spatial resolution up to the microimaging and nominal microscopy range [pixel-size: ps < (100 μm)^2], even *in-vivo* on humans just recently. Preclinical MRI- and dedicated MR-microscopy (MRM) scanners already allow for microimaging and MRM (1-256 μm) but lack a sensible spatial resolution phantom for QC and performance improvements in hardware, pulse-sequencing and MRprotocols. In most scientific MRI articles, the spatial resolution is characterized by the ps, though this measurement parameter only limits the actual resolution.

Methods: Here the Modulation-Transfer-Function (MTF) is used as evaluation concept for the determination of the spatial resolution in MRM using simple intensity profiles. The resolution limit is defined using a critical modulation-level. In approaching visual impressions on spatial resolution an additional criterion derived from the Modulation-depth-to-Noise-Ratio (MNR) is proposed. A practical method for assessment based on a concrete phantom design and its realization is shown.

Results: The phantom design consists of several sets of fine grids, specifically featuring high structural anisotropy for optimum SNR and CNR, with different spatial periods ranging from a_1 = 256 μm down to a_8 = 2 μm, not only for a quick visual qualitative check, but also for quantification of resolution using the MTF for two different spatial encodings in two orthogonal in-plane directions. The challenging demands on the manufacturing technology especially with regard to the aspect-ratio are approached using Deep-X-Ray-Lithography (DXRL) relying on the high brilliance of Synchroton-radiation. Smallest grid plates with width of 4 μm corresponding to 125 line pairs/mm at a plate depth of 100 μm were achieved.

Discussion: MR-microscopic images, originating from a microscopy insert on a human UHF-MR-scanner, were used for demonstration of the evaluation process with two independent resolution-criteria. The developed prototype offers unique possibilities for quantitative resolution QC on UHF human and preclinical MR-scanners. Such a resolution-phantom might be very important for the improvement of MR-pulse-sequences, MR-protocols and even hardware. In principle the phantom can also be used for other microscopic imaging-modalities as for instance μCT and Optical-Coherence-Tomography (OCT).

KEYWORDS

imaging, resolution, quantification, phantom, modulation-transfer-function, MTF, microscopy, XRL

1 Introduction

The spatial resolution represents one of the most important criteria for the quality of an imaging method especially in the case of medical imaging for the early detection of developing pathologies. The quantitation of spatial resolution therefore represents a relevant task for "Quantitative Medical Imaging".

With the growing use of MR micro-imaging, and MRM the issue of spatial resolution is of increasing importance.

We would like to illustrate that relevance of high spatial resolution for medical imaging subsequently in Section 1.1. The reader interested in a short overview on factors influencing spatial resolution (Section 1.2) and a short non-encompassing report on the state of the art on methods for quantification of spatial resolution (Section 1.3) and finally the targeted features of the phantom and evaluation procedure (Section 1.4) is referred to the corresponding subsections.

1.1 Advances in high resolution MRI based medical imaging

In the clinical routine of Magnetic Resonance Imaging (MRI) a Voxel Size (VS) of about 300 × 300 × 2000 μm^3 can be obtained on humans. High spatial resolution in the microimaging range (pixel size (ps): 100–300 μm) has been reported mainly for small Field of Views (FOV) on human extremities, e.g., fingers or toes for the investigation of Vater-Pacini corpuscles, relevant for the loss of vibrational touch sensing, an early change in diabetes [1,2]. Extremities, investigated by high-resolution MRI, might represent radiological models for a variety of pathologies, e.g., bone erosion, inflammation, psoriatic and rheumatic arthritis [3]. The spatial resolution has been identified as a critical obstacle to clinical investigations based on these easily accessible extremities [3]. In principle, the often used 2D-FT MR-method for spatial encoding with slice selective excitation allows for much higher spatial resolution, if specific hardware can be used and the restrictions on the living biological object or humans to be visualized are lifted, in specific: object diameter, tolerable measurement time and tolerance with regard to the magnetic field gradient strength.

A VS of about 30 x 30 x 200 μm^3 [4] may be obtained in preclinicial MR imaging on small animals *in vivo*, performed for instance for pharmaceutical reasons.

Using such dedicated high-resolution MR-scanners the microscopic spatial range (ps < 100 μm x 100 μm) is already available. MRI with pixel size in that spatial range is therefore called MR-microscopy (MRM) [5]. MR-based histology [6] in the microscopic range has been reported on pathologic structural changes in tissue samples *ex-vivo*, for arteriosclerosis [7], arthritic changes in cartilage [8], diabetes related changes in the human skin [9] and ovarian cancer [10].

MRM-based histology (*ex-vivo*) on different tissues has already been demonstrated on high-field (B = 3 and B = 7T) human MR-scanners using additional dedicated hardware [11,12]. A voxel volume of $(100\ \mu m)^3$ has recently been reported on the human brain *ex-vivo* on a 7T UHF MR-scanner [13].

Even *in vivo* on human extremities high spatial resolution based on voxel- and pixel-sizes in the microscopic range has recently been demonstrated using prototype MRI rf-detector hardware [2].

1.2 Relevant factors for spatial resolution in MRI

However, the pixel and voxel size represents only a limit to the spatial resolution. The effective resolution may be significantly less due to spatial distortions, e.g., by magnetic field inhomogeneities or chemical shift artifacts. Also, other sample specific and technical factors might impact the actual achievable spatial resolution, e.g., the linewidth, the signal decay due to T2-relaxation, the magnetic field gradient strength (bandwidth) and gradient switching performance, the signal-to-noise (SN) restriction and even the diffusivity of molecules during MR-detection [5]. In parallel imaging the spatial encoding in MRI is based on the local electromagnetic B1-distribution of distant radio-frequency transmitter and receiver elements. Some of these parameters also depend on the investigated sample.

1.3 Methods for proving spatial resolution in MRI: Actual state

Consequently, the qualitative and quantitative check is recommended on defined test structures (phantoms) in several norms and recommendations on Quality Control (QC) of human MR-scanners. Most available phantoms for QC of spatial resolution are based on one dimensional periodic sets of plates or tubes [14–16]. For practical and manufacturing reasons mostly grid or hole structures are proposed and used for qualitative tests of spatial

resolution with typical structural sizes of plates and diameter of holes of d = 10 mm down to 0.7 mm [16].

In order to test image quality with regard to spatial resolution, and assess modifications for improvements, using hardware, software and MR-protocol modifications in the spatial range of microimaging and microscopy, an objective test structure (phantom), which allows for the quantitative determination of the spatial resolution, is needed [17–19]. A previous design of a phantom for high-resolution MRI featured a smallest spatial structure width of 0.1 mm suitable for the micro-imaging range (≅ 300–100 μm) [19].

In optical imaging quantitative QC on spatial resolution is mainly based on the MTF-concept [20]. Often glass plates using etched orthogonal grid structures of varying periodic distance (a) are used (see as an example for a design: the United States air force target phantom) [21]. Such structures also allow for a quick qualitative check on spatial resolution in the microscopy range by a simple visual inspection for deciding which of the periodic grid lines are still separated. In Computed Tomography (CT) and μ-CT grid sets for the evaluation of the MTF represent a well-established metric tool for the quantitative characterization of the spatial response of the imaging system [22]. μ-CT phantoms, based on silicon grids, do exist with contrast of silicon absorption against air and resin [23]. Using tungsten as absorber material grids do exist with line dimensions down to 0.1 μm [24]. These μ-CT phantoms are not suited for MR-microscopy because the used metal results in a distortion of the electromagnetic B1-field in MRI. In these μ-CT phantoms the thickness of the absorption material is limited to a maximum of about 1 μm due to the very challenging small spatial dimensions. The lithographic processes used, based on silicon technology feature limited aspect ratios (height-to-width ratios) and consequently the high slice thickness used in MR-microimaging and MRM would result in partial volume coverage and signal modulation loss.

The MTF may also be calculated in principle from the Edge Response (ER) or Line Spread Function (LSF) [25]. Due to the sensitivity of the ER to local noise [25] and necessity for processing steps of measured MR-profiles the ER method for QC in MRI is rather seldomly applied.

In MRI on clinical whole body human scanners, phantoms for checking spatial resolution are designed for typical smallest pixel size of 0.5 mm. But no commercially available test structures (phantoms) do exist for the microscopic (<100 μm) range down to 1 μm. Proposals for such phantoms for the microscopic spatial scale do exist [18] and are reported as technical realization on the basis of, e.g., lithographically processed silicon grids [11,26].

For 2D-FT MRI with slice selective excitation the slice thickness is usually chosen to be much bigger than the in-plane resolution (pixel-size) due to the demands on high gradient strength for slice selection, short radio frequency (rf-) pulses and signal to noise ratio (SNR). Ideal phantoms for standard 2D-FT-MRI should exhibit therefore a strong anisotropy with regard to in-plane lateral distance of the grid bars with reference to their structural height in slice (z-) direction. Usual slice thickness in 2D-FT-microscopy ranges between 50 and 200 μm (see, e.g., [9,12,26]). The demands on the manufacturing technology for offering lateral structures down to 1 μm at height of 50–200 μm, corresponding to aspect ratios of about 50–200 are therefore very challenging. Deep X-ray lithography (DXRL) at KNMF using the high brilliance and small divergence of Synchrotron irradiation is in principle capable for the manufacturing of such structures (aspect ratio AR ≅ 50) in polymers down to below 1 μm [27].

With difference to other medical imaging modalities the spatial position in 2D-FT MRI is encoded by spatial phase (spin warp) and frequency encoding in different spatial dimensions. The different encodings may result in different spatial resolutions in the two different directions. A resolution phantom design therefore should allow for the quantitative evaluation of the MTF in 2 orthogonal directions. This might be achieved by orthogonally arranged grid patterns. The MTF can be obtained using lateral profiles in the image crossing the different orthogonally arranged periodic grid lamellae.

1.4 Conceptual approaches, targeted phantom features, and methods

In this manuscript the subsequent aspects of a resolution phantom including resolution analysis for slice selective 2D-FT-MR- microimaging up to the microscopic range are described. The phantom should allow for QC of spatial resolution on High-Field human scanners, already capable of such high-resolution performance, preclinical (animal) MR-scanners and even experimental MR-imaging devices designed for highest spatial resolution. The design and prototype phantoms should not only allow for quick qualitative checks of spatial resolution by simple visual inspection but also should offer the possibility for a quantitative determination of the spatial resolution using the MTF-concept in two orthogonal, for instance phase and frequency encoding, directions. The manuscript is divided into the subsequent three main subject parts: the first two describing the physico-mathematical concept and the realization of the phantom including its QC; the last one presents a demonstration of the qualitative imaging results and evaluation procedure for quantification of the spatial resolution.

1) Concept for quantitative determination of the spatial resolution in two independent directions using a strongly anisotropic 2D-grid structure based on the MTF including 2 independent resolution criteria.
2) Technical realization of prototype 2D-FT resolution phantoms and their QC.
   - Design of a phantom for quantitative determination of the spatial resolution in 2D-FT-MR-microscopy with slice selective excitation up to spatial frequencies of f = 500/mm. This corresponds to a lamella width of 1 μm. The height of the structures should allow for a slice thickness (slth) in MR encoding up to 200 μm ($slth_{max} \leq 200\,\mu m$). The independent evaluation of the MTF in two orthogonal directions with different spatial encodings should be possible.
   - Manufacturing of the phantom using Deep-X-ray-Lithography, artefacts and restrictions in technical realization of the phantom design.
3) Exemplary measurement and evaluation of MR-microscopic images for a Turbo-Spin-Echo (TSE) radiofrequency and gradient pulse sequence with:

- simple qualitative interpretation and
- quantitative evaluation of the spatial resolution

2 Materials and methods

2.1 Concept of the Modulation-Transfer-Function (MTF) for the determination of the spatial resolution, defining criteria

The application of linear communication theory to imaging systems offers the possibility to characterize the main features of an imaging apparatus by the point spread-function (PSF) in the spatial domain and the modulation-transfer-function in the spatial frequency domain assuming linearity and isoplanatism in the imaging procedure [17,20]. The modulation-transfer-function (MTF) is defined as the ratio of the spatial Fourier transform $I_{(fx,fy,fz)}$ of the image intensity distribution in space ($I_{(x,y,z)}$) to that ($O_{(fx,fy,fz)}$) of the object distribution ($O_{(x,y,z)}$). For simplicity we refer subsequently to only one spatial dimension (for instance *x*-direction):

$$MTF_{(f)} = \frac{I_{(fx)}}{O_{(fx)}} \tag{1}$$

The $MTF_{(fx,fy)}$ in the different spatial dimensions, e.g., in the plane (x, y) might be obtained by simple multiplication of the MTFs in orthogonal directions if independence (invariance) is valid. In the ideal case of a single periodic (spatial period a_i) object, the spatial Fourier-component $O_{(1/ai)}$ is equivalent to the amplitude of the object modulation depth O. An ideal test phantom for spatial resolution might be composed of a set of periodically (period a_i) arranged grids with different spatial frequencies $f = 1/a_i$ covering the typical spatial frequencies of the objects to be investigated. The $MTF_{(f)}$ of an imaging system can then easily be measured using an intensity profile delivering the modulation $M_{(f)}$ with standard image analysis software crossing the grids with different spatial periods [14,17]:

$$M_{(f)} = \left[\frac{I_{max} - I_{min}}{I_{max} + I_{min}}\right]_{(f)} \tag{2}$$

I_{max} and I_{min} are referring to the maximum, respectively minimum signal intensity in modulation. The measured intensity modulation $M_{(f)}$ *versus* the available discrete spatial frequencies $1/a_i$ is representing a discrete sampling of the MTF:

$$M_{(f=\frac{1}{ai})} \propto MTF_{(f)} \tag{3}$$

Usually, a rather continuous decrease of the MTF with higher spatial frequencies is observed not only for MRI but also for other imaging modalities. Using grids of plates in MRI only discrete spatial frequencies are available for the measurement of profiles. Interpolation of the Modulation $M_{(f)}$ between these discrete frequencies up to the available highest spatial frequencies determined by the smallest spatial periodic distance might therefore be used for an approximation of the real MTF of the imaging system (see also Figure 12).

In MR imaging devices the relative modulation depth $M_{(f)}$ remains relatively constant at lower spatial frequencies but reduces significantly at higher spatial frequencies. Therefore, a resolution criterion referring to a critical high bandpass cut-off frequency is defined: $f_{cut\text{-}off} \cong 1/a_{cut\text{-}off.}$ Different criteria on the critical amount of reduction in modulation depth with higher spatial frequencies $f = 1/a$ might be used for the quantification of a spatial cut-off frequency $f_{cut\text{-}off,}$ thus defining the spatial resolution, for instance [14]:

$$MTF_{(fcut-off\ 50\%)} = 0.5\, MTF_{(f->0)} \tag{4}$$

or $MTF_{(fcut-off)} = 0.265\, MTF_{(f->0)}$ (Rayleigh criterion), often used in X-ray microscopy [28]. The critical cut-off frequency then might be determined from the intersection of the defined critical modulation level with the MTF by reading the relevant corresponding cut-off frequency $f_{cut\text{-}off,}$ (see. also Figure 12).

We propose an additional criterion related to the relative noise rN, as the qualitative decision on the differentiability of an intensity line *versus* a background signal also depends on noise in the image:

$$Mtf_f \geq kp\, \sqrt{2}\, rN \tag{5}$$

We define the relative noise rN here as the ratio of the standard deviation σ of the background image signal intensity to the maximum modulation depth I_{max}-I_{min} present, e.g., at a low spatial frequency, where the object modulation is approaching the maximum modulation in the image:

$$rN = \frac{\sigma}{I_{max} - I_{min}} \tag{6}$$

The coverage factor kp can be set by the user. It represents a parameter, for which a predefined level of confidence for the difference of the modulation I_{max}-I_{min} from image noise can be achieved [29]. As an example, a high probability $p \cong 0.95$ is achieved for the difference of the signal modulation to noise, setting $kp = 1.95 \approx 2$ (assuming a Gaussian distribution for the signal intensity with standard deviation s and the noise being approximated by the standard deviation $\sigma = s$ of the background signal).

These definitions result in the subsequent criterion for the critical spatial cut-off frequency $f_{cut\text{-}off\_noise}$, for which the modulation reaches a non-significant level ($kp \stackrel{!}{=} 2$):

$$MTF_{(fcut-off\_noise)} = kp\, \sqrt{2}\, rN\,; \left(kp \stackrel{!}{=} 2\right): \tag{7}$$

Other criteria for a higher ($kp > 2$) or lower level of significance ($kp < 2$) with a certain probability might be defined for specific imaging modalities and applications.

2.2 Technical realization of the resolution phantom

2.2.1 Design of resolution test structure (phantom) for MR-microimaging and MRM

2D-periodic structures in the form of two orthogonal grids are proposed to serve as a resolution phantom for MR-microimaging and MRM (Figure 1).

The phantom consists of a whole set of individual grids (Figure 1) of cavities or slits in a solid base material, which might consist of semiconductors, e.g., silicon, ceramics or—at

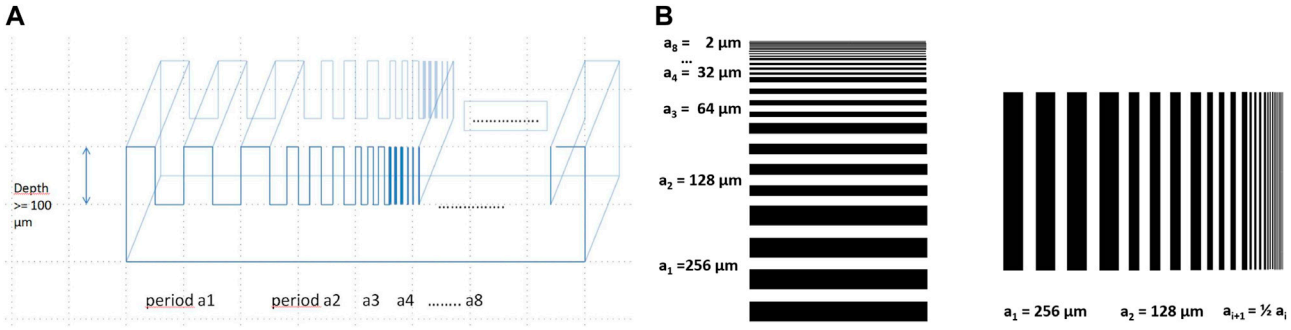

FIGURE 1
(A) (left) Design proposal for the quality control in MR-microscopy. The test structure (phantom) for the qualitative and quantitative determination of the in-plane spatial resolution, shown here only for one dimension, consists of several sets of periodically arranged plate walls (lamellae) characterized by their spatial distance $a_i/2$ at same lateral width ($1\mu m \leq a_i \leq 256$ µm). The envisaged minimum depth of lamellae is designed to be 100 µm, thus featuring strong demands on the aspect-ratio of the manufacturing technology. **(B)** (right) Frontal view of the design for two orthogonal grids, featuring subsequently size-reduced sets of periodically arranged plates with $a_{i+1} = ½\ a_i$. The periodic length a_i is proposed to start at $a_1 = 256$ µm and may range down to $a_8 = 2$ µm. Intermediate steps in DXR-Lithography realization are possible. The two orthogonal arrangements allow for independent analysis of two different spatial directions, e.g., phase (spin warp) and frequency spatial encoding.

best—of polymer type material. The openings are filled with an MR-visible liquid. For the quantitative detection of spatial resolution different sets i of grids with different lateral periodicity a_i are to be manufactured ranging from $a_1 = 256$ µm down to about $a_8 = 2$ µm, e.g., in a small connected phantom of periods $a_i = 2, 4, 8, 16, 32, 64, 128,$ and 256 µm. Using intensity profiles in MR-imaging a qualitative inspection, which of the grid slits still can be differentiated, might be used for a quick estimation of the spatial resolution achieved using the specific hardware and MR-protocol. The modulation-transfer-function (MTF) may be evaluated from these phantoms using single pixel-wide profiles according to the methods described in the previous Section 2.1; Eqs 1–7. The spatial resolution in MR-microimaging and MRM may be quantitatively determined from the cut-off frequency using a criterion for the relative modulation depth (Eq. 4) or the modulation to noise ratio (Eq. 6 and Eq. 7).

Two orthogonal sets of grids allow for the independent evaluation of the spatial resolution in two different orthogonal directions with potentially two different spatial encoding methods in the plane of the slice selection: e.g., frequency and spin warp (phase) encoding as typical for 2D-FT MRI.

The height of the plates with reference to the width (aspect ratio) is very important for MRI slice selective imaging with strong anisotropic voxels, which is usually the case in standard MR 2D-FT high resolution imaging. The selected slice in optimum fits into the z-dimension of the plate (depth d of the plates), in order to profit from the full modulation depth and high SNR. For the 2D-phantoms the depth d of the periodic structures $a_i > 20$ µm is therefore designed to be at least 100 µm. For the others $a_i < =16$ µm the height is designed to be at least 50 µm (for maximum voxel size and SNR reasons). This design poses high demands on the lithographic fabrication process concerning achievable aspect ratios (AR), defined as ratio of depth/lateral width: $= \frac{d}{a/2}$.

2.2.2 Technical realization of the orthogonal grids, fabrication artefacts and restrictions

The strong anisotropy of the design structure adapted to the usually strong anisotropy of voxels in slice selective MR-microimaging poses high demands on the aspect ratios of the µm-sized structures along with aspect ratios of 50–200. Deep X-Ray Lithography (DXRL) using Synchrotron radiation with low divergence <1 mrad is in principle able to offer such µ-structural details in the µm-range using PMMA with sidewall roughness of 20–30 nm [27]. The principle of the manufacturing process is indicated in Figure 2 (see also [30]).

The manufacturing of the resolution phantom, as designed according to Figure 1, was set-up in several steps (see also Figure 2A).

2.2.3 Manufacturing of a high-resolution X-Ray mask

The high-resolution mask consisted of an X-Ray transparent support membrane (titanium foil with a thickness of 2.3 µm) carrying gold structures (2.2 µm thick) to absorb the synchrotron radiation during X-Ray lithography (Figure 2A). This mask allowed for subsequent spatially selective radiation of the PMMA to make it soluble for a wet chemical developer. A CAD-design was first drafted for manufacturing such a mask using electron beam lithography (EBL). The CAD-design was set-up to manufacture several (4×20) orthogonal grid sets ranging from $a/2 = 1$ µm up to $a/2 = 128$ µm. Consequently, after the manufacturing process several grid sets with same design had been available. Each of these grids featured at minimum 3.5 periods of the same plate thickness. In order to mechanically stabilize the thin lamellae below 4 µm thickness (at minimum 100 µm height) against tipping, small supporting struts of about 1 µm size were added perpendicular to the plate structure of the mask design (Figure 2B). They were separated from each other by about 250 µm distance in order to not impact the measurement of the image modulation depth.

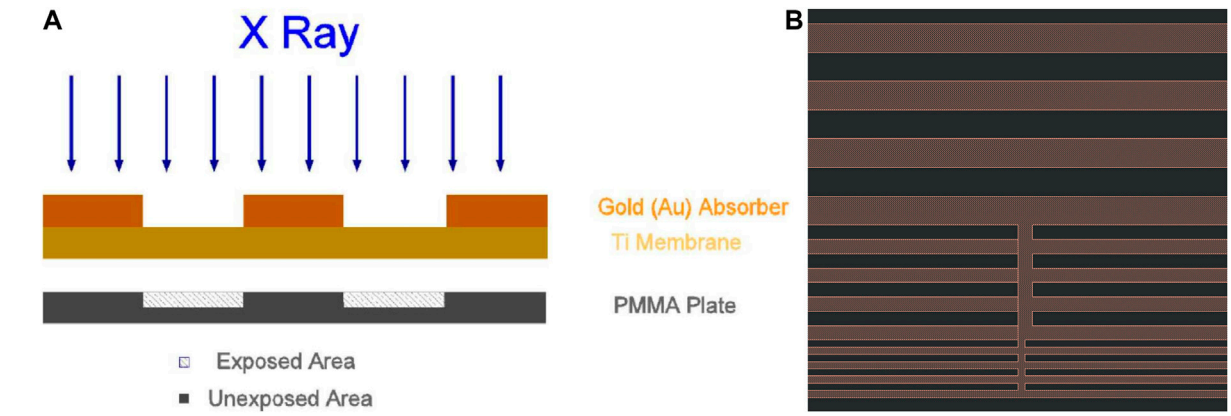

FIGURE 2
(A) Scheme of the lithographic manufacturing process with Synchrotron radiation. The thin titanium (Ti) membrane (brown) serves as a carrier for the thick structured gold mask (dark orange). The gold mask protects the underlying PMMA material from destruction by the high intensity Synchrotron X-ray exposure (blue arrows). **(B)** Enlargement of the CAD-design for the gold mask in the region of the smaller grid sets (a_7 = 4 µm and a_8 = 2 µm). For improving the mechanical stability of the thin but deep lamellae, lateral support struts at 1–2 µm size were added.

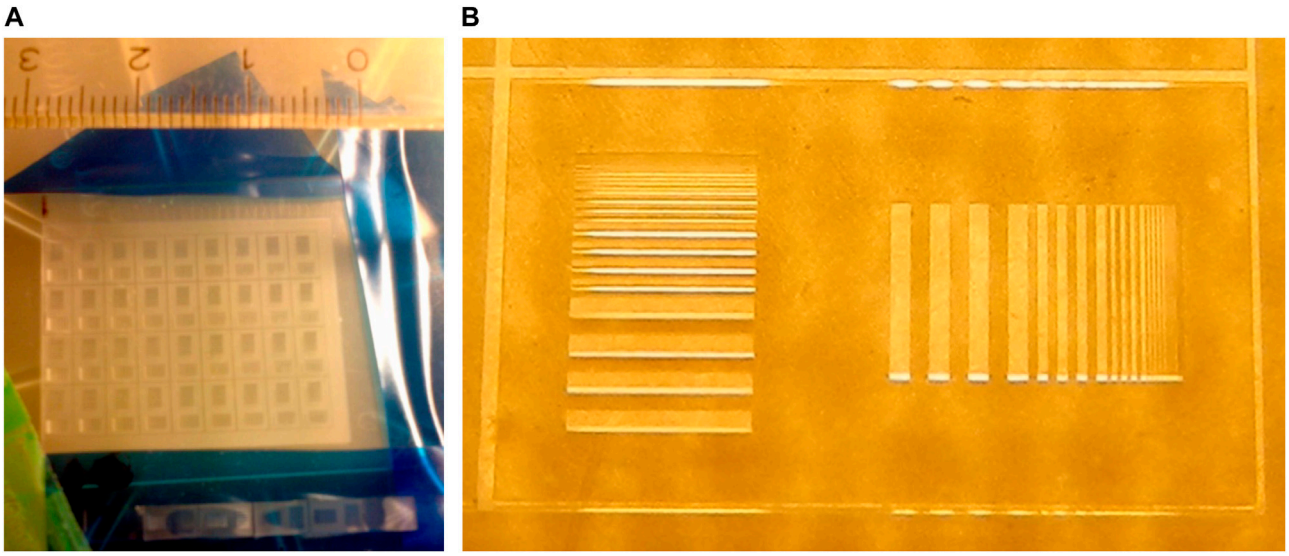

FIGURE 3
(A) Photo of a section of the structured PMMA plate with several resolution phantom grid sets. The realized grid periods a_i vary between 256, 128, 64, 32, 16 and 8 µm. The scale indicates cm. **(B)** Macro photo of one of the phantom prototypes. Two sets of grids are arranged in orthogonal directions for independent analysis of the spatial resolution in phase and frequency encoding direction in 2D-FT MR-imaging. The largest grid with period a_1 = 256 µm can be seen, e.g., at the bottom left.

2.2.4 Synchrotron irradiation

PMMA plates of 900 µm thickness were positioned with X-Ray mask on top to a Synchrotron radiation fan with a width of 100 mm and a Full-Width at Half-Maximum (FWHM) of about 4 mm. Therefore, the whole clamped package of PMMA and mask had to be scanned through the radiation fan to expose the whole design area of 60 × 20 mm^2, which consisted of 80 single rectangularly arranged grid design elements (Figure 3A). The whole exposure process took around 2 h to achieve a bottom dose of around 3 kJ/cm^3 in a depth of 100 µm. We used the beamline *Litho 1* of the Synchrotron radiation source KArlsruhe Research Accelerator (KARA) for that purpose. The Synchrotron radiation is characterized by a small divergence which allows in principle for very steep sidewalls of the remaining PMMA (slope angle $\alpha < 1$ mrad).

2.2.5 Development of phantom grid-structures in PMMA and final preparation of prototypes

The irradiated parts of the PMMA plate were removed by dissolving in a developer consisting mainly of 2-(2-butoxy-

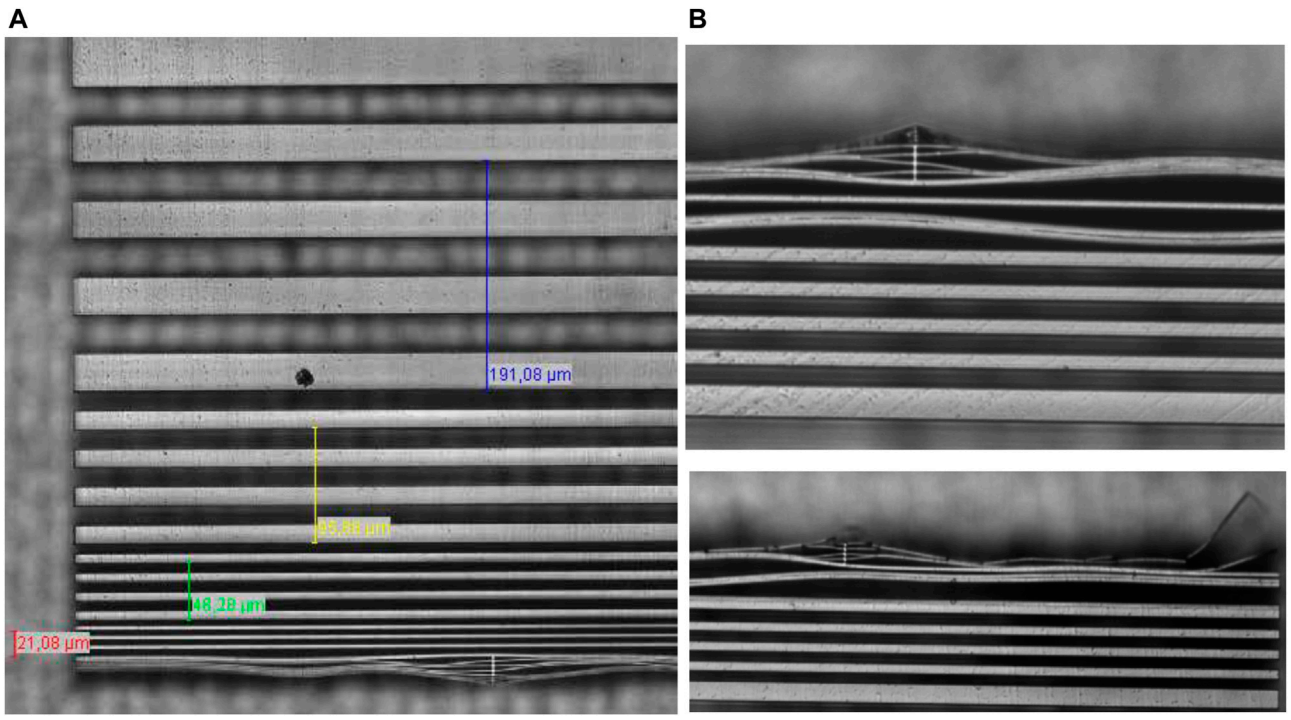

FIGURE 4
(A) Optical microscopic frontal view of the small-scale grids in the XRL phantom. Intact grids with spatial periods of 64 µm (topmost), 32, 16 and 8 µm (lowermost) were observed. The smallest correctly aligned plates featured a spatial width of 4 µm corresponding to a spatial frequency of 125/mm. Plates with even smaller thickness are not aligned parallel anymore and do lack periodicity. The slit to plate thickness ratio is close to one. **(B)** top High resolution optical microscopic frontal view of the smallest scale grids in the XRL phantom. The thin plates of 2 µm thickness were tilted and interfolded with neighbouring plates due to lacking mechanical rigidity. The rectangular, stabilizing bars (top side) were only capable to keep the spatial distance between the plates for lateral distances to about 10–30 µm. **(B)** bottom Lamellae below 2 µm thickness ($a_B/2$ = 1 µm) at top side right border of the grid showed splitting off and destruction.

ethoxy)-ethanol (60 vol%) and tetrahydro-1,4-oxazin (20 vol%) for 3 h (GG, developer for PMMA). An additional dissolving step with a mixture of 2-(2-butoxy-ethoxy)-ethanol (BDG) and water for 20 min followed. At the end the developed Polymethyl-Meth-Acrylate (PMMA) 3D-structure was rinsed for 10 min in deionised water for the removal of left particles and developing liquid. Final prototypes of the resolution phantoms were separated from the complete irradiated hard PMMA plate by sawing.

A macroscopic high-resolution photo of a subsection of the set of orthogonal grid series in the PMMA layer is shown in Figure 3A. A single grid set of one element containing two orthogonal grids is visualized in Figure 3B.

2.2.6 Characterization of quality, challenges and artefacts in manufacturing

A set of phantom prototypes was investigated for the achieved fabrication quality with regard to.

- achievable maximum spatial frequencies,
- plate-slit ratio: achieved lateral width of the plates in comparison to the scheduled open areas in between,
- height of the plates with reference to the width (aspect ratio) and slope,
- manufacturing artefacts and mechanical stability.

For this purpose, the subsequent analysis tools have been used: a) frontal optical microscopic image (distances were digitally gauged); b) Scanning Electron Microscopy (SEM) for more accurate measurements in distances, lateral visual inspections, e.g., for determination of the steepness of the walls, details of artefacts and PMMA-structure; c) MR-microscopy was also helpful in the evaluation of overall distances and height of the microstructures.

2.2.6.1 Evaluation of maximum achievable spatial frequency

The final implementation version featured PMMA plates/lamellae of 100 µm depth in PMMA. Stable and correctly aligned plates were observed at best down to a lateral width of 4 µm (Figure 4). This corresponds to a maximum spatial frequency of f = 1/a = 125/mm.

2.2.6.2 Evaluation of slit opening to solid-plate-thickness ratio

The slit width of the open area in between two plates was compared to the plate thickness using the frontal optical views at the topmost position. The ratio is relevant for the intensity modulation in the MR-image evaluation. For the bigger sized structures, the ratio was close to one; the optically derived distances for smallest aligned lamellae however showed slightly bigger slits than plate thickness, which might have been due to the focus depth of the optical microscope and therefore ranges within errors. Scanning Electron

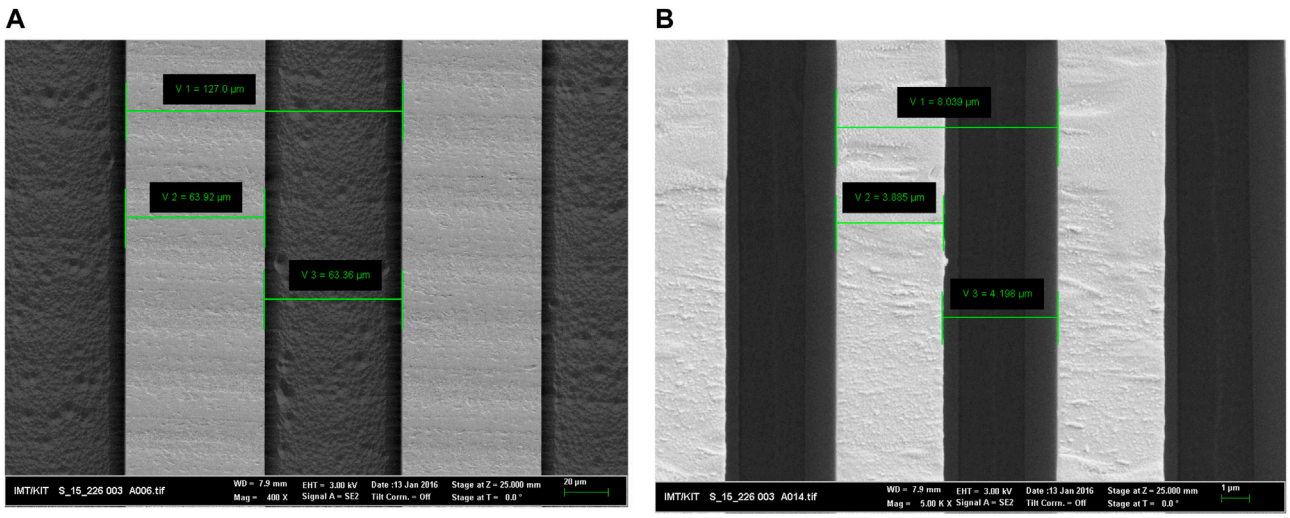

FIGURE 5
(A) SEM frontal view of the grid with nominal spatial period a = 128 µm in the XRL phantom. The slit opening was measured to be 63.4 µm, whilst the width of the bar was indicated to be 63.9 µm. **(B)** SEM frontal view of the small-scale grids in the XRL phantom. The slit width for the smallest correctly aligned plates featured a little higher distance (4.20 µm) than the solid plate thickness (d = 3.89 µm) at the surface.

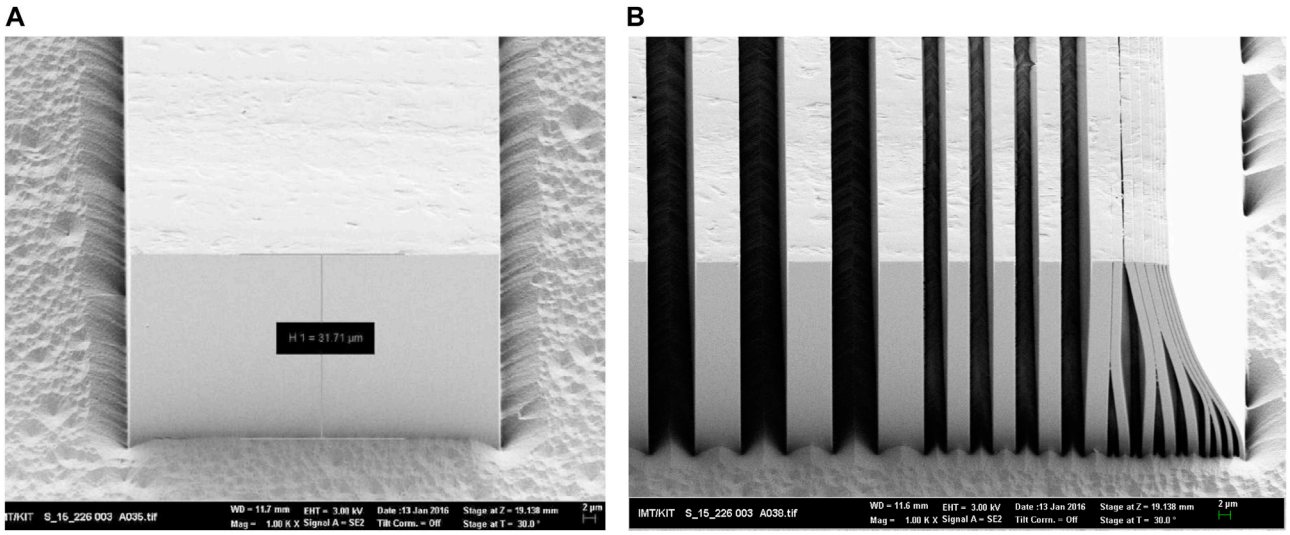

FIGURE 6
(A) SEM lateral view of one plate/lamella (a/2 = 64 µm) for a manufacturing batch with 60 µm nominal structure depth. The actual structure depth was about 63 µm. The orientation of the massive walls against the PMMA-base plate was excellent, close to 90°. Note the small grooves at both sides at the foot of the 64 µm wide plate. Please also note, that the SEM view was obtained with a tilting angle of 30°, which results in a distortion (shortening by factor 2 in indicated scale) in depth direction. **(B)** SEM view of the DXRL phantom (60 µm depth) in the high spatial frequency region. The grid plates with smallest width, still aligned correctly, feature a spatial distance (a/2) of about 4 µm (aspect ratio: ≅ 15). Note the excellent slope of the rigid PMMA walls close to 90° with no measurable difference between the width at top and bottom position.

Microscopy (SEM) evaluations featured improved accuracy and resolution. They also offered the possibility for lateral views and evaluation at different depth (Figures 5, 6).

The slit-to plate-thickness-ratio (duty cycle) for the highest spatial frequency f = 125/mm amounted to 1.08. The other spatial frequencies featured ratios even closer to one. These values are considered to be excellent in comparison to other manufacturing technologies.

2.2.6.3 Aspect ratio and slope

The height of the plates with reference to their width (aspect ratio) could only be checked using lateral views available with SEM

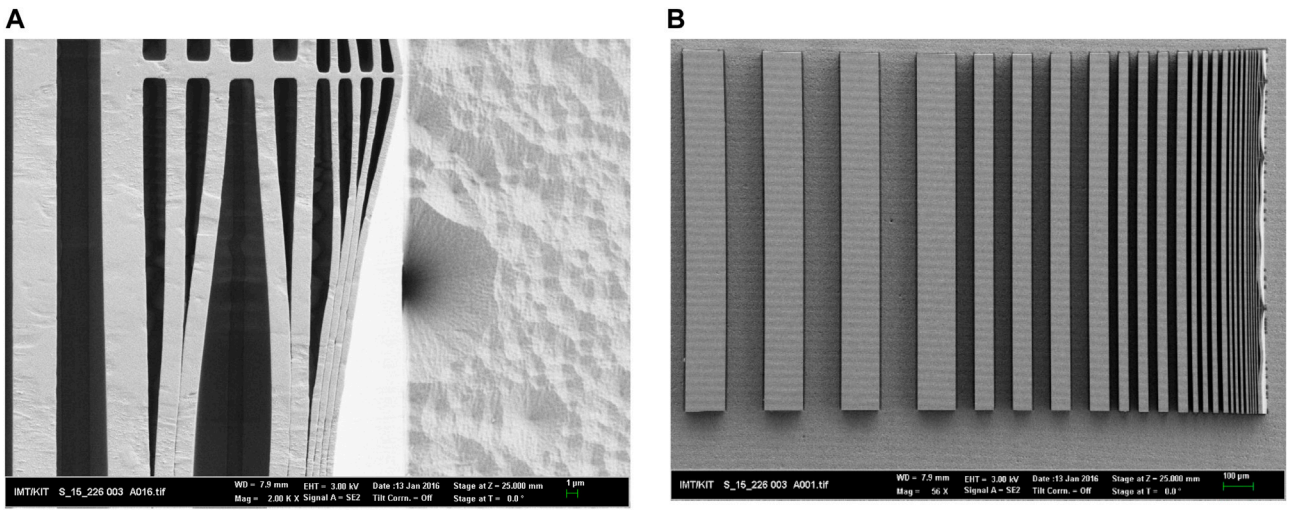

FIGURE 7
(A) SEM frontal view of the section with grid of high spatial frequency. The smallest usable aligned plates featured a width a/2 = 4 μm. The smaller lamellae (2 μm) bowed and tilted against each other destroying periodicity or even miss opening in between. Stabilizing bars rectangular to these lamellae have been implemented in the design (top), but these were only able to keep alignment of the plates on lateral distances of about 10–30 μm. **(B)** Overview frontal SEM image of a well performing phantom. The grids shown range with periodicity a in between $a_i/2$ = 128 μm, 64, 32 16, 8 and 4 μm. All of them could be used for quantitative evaluation of the MTF [here in *x*-direction (left-right)]. The smaller ones exhibit bowing and non-aligned lamellae.

for low lithographic depth of about 30 μm in first batches (Figure 6). The full depth was evaluated in the final batch (depth ≅ 100 μm) using MR-microscopy lateral (sagittal) views.

In etching based lithographic technologies usually the lateral open areas (slit opening) in between the massive bars on top of the structured grids feature a broadening with comparison to the bottom deep areas due to the different time of the lateral etching process. This results in non-rectangularly formed plates and a slope of the side walls deviating from 90°. Using DXRL no differences between top and bottom width of the grid lamellae/plates could be detected within measurement accuracy (slope = 90°). In this work the depth (height) of the massive plates in the different grids was evaluated to be d ≅ 100 μm using MRM. Thus, the highest aspect ratio (AR) was achieved for the intact correctly aligned and mechanically stable plates of 4 μm width: AR = 100 μm/4 μm = 25. The SEM views demonstrated, that smaller lamellae can be obtained in principle by DXRL, but these have not been mechanically stable for the specific phantom design with high lamellae length at 100 μm depth demonstrated by the tilting against each other (Figure 4B and Figure 6B).

2.2.6.4 Artefacts and mechanical stability

The main technological problem in manufacturing of the highly anisotropic grid structures was represented by the mechanical stability of the thin lamellae beyond about 4 μm thickness (Figure 6B). The consequence of the mechanical instability resulted in bowing of the thin plates at 2 μm thickness (Figure 7A). This results in non-aligned parallel plates, such destroying periodicity. The even smaller lamellae tilt against each other and glue together when being flushed with developer liquid. This artefact could already be observed in the optical frontal microscopy views (Figures 4A, B). More details could be observed in the high-resolution SEM images (Figure 7A).

For the very thin lamellae below 2 μm width, additional bars rectangular to the plane of the lamellae are added to mechanically stabilize height and distance. This principle worked but only for lateral distances of about 10–30 μm length.

There had been differences in the quality of the final phantom grids, some of them showing hardly any destruction in the outermost lamellae. The areas close to the stabilizing rectangular bars could in principle be used to check spatial resolutions with f = 250/mm or even 500/mm in the direction rectangular to the stabilized lamellae (e.g., *x*-direction), if the associated lateral (y-) pixel size would be chosen to be smaller than the bowing distance, for example, in the shown example: about 5–10 μm.

A frontal overview of a well manufactured prototype is shown in Figure 7B. Note the excellent parallel alignment of the grid plates down to lamellae of 4 μm width, corresponding to spatial frequencies of f = 125/mm at about 100 μm height. According to our knowledge this frequency is sufficient for checking the spatial resolution of all commercially available MRM systems.

2.3 Aspects of phantom sample preparation for optimum quantification of resolution in MRI-microimaging

Please note that the PMMA structure cannot be visualized directly as the T2-relaxation time is too short for standard MR-spin echo encoding. Therefore, the final phantom was designed such that the solid PMMA-grid is open to at least two different lateral directions. This design allows for the quick entering of the MR-visible liquid, for instance water or silicon oil. The prototype phantom grids were positioned inside of a small glass

tube (inner diameter di = 4 mm), which was filled with silicon oil instead of water in order to avoid the disposition of air bubbles especially in the small slits, often observed for water fillings (Figure 8). Water, in general, exhibits high dielectric permittivity (with reference to silicon oil) related to low wavelength of the used radiofrequency fields in MRI, which might result in dielectric resonances and B1 inhomogeneity artifacts for large body phantoms [31]. However, this feature of water represents no problem for the usage of small sized phantom containers as proposed here. The fixation of the PMMA grid phantom plate was performed by styrene foam, as we observed movements of some of the tiny grids during the measurements.

2.4 MR-microimaging and microscopy

2.4.1 Hardware and MR-protocols

MR-microimaging and MRM for checking the suitability of the manufactured prototype test pattern was performed on a high-field (7 T) human MR-scanner (Siemens *Magnetom 7T*) equipped with a prototype strong gradient system (G = 750 mT/m) and sensitive radio-frequency detectors (rf-coils) [12].

A slice-selective (2D-FT) Turbo-Spin-Echo (TSE) sequence ("tse2d1_10") with different spatial encoding in the two orthogonal directions (frequency (x) and phase encoding (y)) was evaluated using different nominal spatial resolution with PS = 78 × 78 μm^2 down to PS = 31 × 31 μm^2 in-plane and a slice thickness of 120 μm (Figure 9).

3 Magnetic resonance exemplary evaluation

3.1 Quality control on spatial resolution: Procedure for qualitative check

A quick qualitative determination of the spatial resolution might easily be obtained from a visual inspection of the MR-image. An example of such an evaluation is shown in Figure 9.

Firstly the reference slice is carefully aligned with the plane of the two rectangular grids (see Figure 9B). Using a 64 × 128 Mtx a pixel size of 78 × 78 μm^2 for the microscopy regime is obtained (Figure 9A). The grids with periodicity a down to $a_1/2$ = 128 μm can be differentiated. A minimum resolution of 128 μm can be proved for both frequency (left-right) and phase (top-bottom) encoding direction for the Turbo-Spin-Echo sequence (bandwidth bw = 100 Hz). However, the single lamellae at lateral width and distance of 64 μm of the grid with half periods $a_2/2$ = 64 μm cannot be differentiated any more.

Increasing the matrix size to 96 × 192 at similar FOV (4.8 × 9.8 mm^2) results in smaller pixels (50 × 51 μm^2). The nominally higher resolution can be proved by qualitative inspection of the MR-microscopic images (Figure 9C). The slits with $a_2/2$ of 64 μm in phase (y-) and frequency encoding (x-) direction can be differentiated. Please note, that two slits of the grid lamellae in phase encoding direction can hardly be separated due to partial volume coverage of the neighbouring pixels. Such an appearance is typical for a case when the pixel size approaches the grid pattern with regard to size (Moiré-effect). It is hardly observed any more, if the pixel size is further reduced to, e.g., ps: 39 × 39 μm^2 (Figure 9D).

3.2 Quality control on spatial resolution: Procedure for quantitative check

The procedure is explained on the example of an MR-microscopic image (pixel size ps: 31 × 31 μm^2, Mtx: 160 × 320, 3 slices, slth = 120 μm, TA = 96 s, bw = 100 Hz) positioned in the plane of the grid (coronal) using a slice selective Turbo-Spin-Echo sequence (TSE) with phase encoding in y- and frequency encoding in *x*-direction (Figure 10).

The example demonstrates a case where a) the pixel size (31 μm) is close to one of the grid modulations periods ($a_3/2$ = 32 μm) and b) the modulation to noise is rather low (signal to noise ratio ≅ 672/73 ≅ 9 for the signal originating from the largest grid).

The modulations are determined as mean values of differences between the separate maxima and minima in intensity (I_{max}-I_{min})

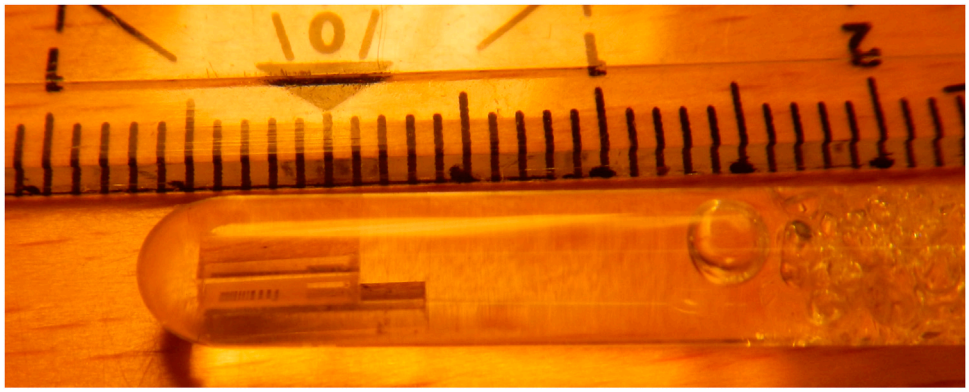

FIGURE 8
Macroscopic photo of the final resolution phantom in a small glass tube (inner diameter di = 4 mm). The PMMA-layer with the two orthogonal grids is embedded in silicon oil, which acts as MR-active filling liquid in the slits. The resolution phantom is fixed in this prototype design using a styrene foam showing air bubbles at right hand side (scale numbers indicating cm).

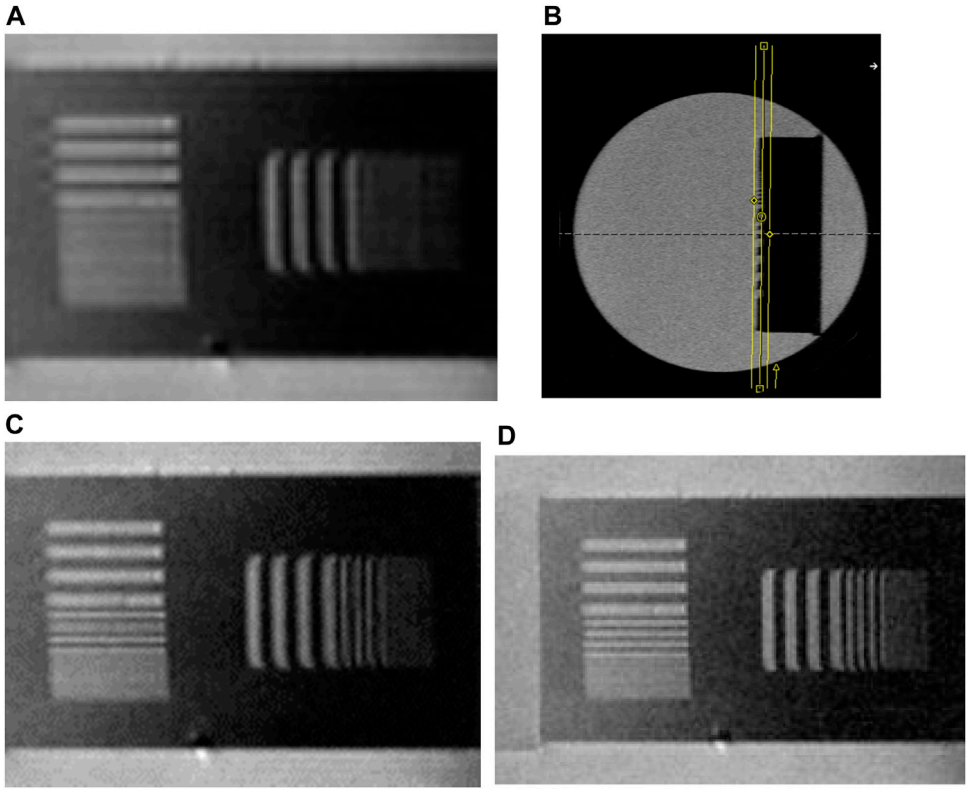

FIGURE 9
(A) In-plane (coronal) slice selective MRM-scan (pixel-size ps: 78 × 78 μm^2; slth = 120 μm; Matrix Mtx: 64 × 128, FOV: 5 × 10 mm^2). Only the grid with periodicity $a_1/2$ = 128 μm can be detected in frequency (x) and phase encoding direction (y). The smaller ones cannot be resolved. From qualitative inspection the resolution of the MR-scan is proved to be at minimum 128 μm. **(B)** MR-axial scan of the phantom used as localizer for accurate placement of the MR-excited slice in the plane of the 2 orthogonal grids. The transverse (axial) scan crosses the vertical grid and thus allows for positioning of the slice. **(C)** In-plane slice selective MRM-scan (Voxel-Size VS.: 50 × 51 × 120 μm^3). Mtx: 96 × 192, middle of 3 slices, phase encoding direction: (y). Only the grids with half periodicity $a_i/2$ = 128 μm, and 64 μm can be differentiated. The smaller ones cannot be resolved. From qualitative inspection the resolution of the MR-scan is proved to be at minimum 64 μm. Note the apparently lower modulation depth for the second slit of the $a_2/2$ = 64 μm grid in phase-encoding (y-) direction which appears at lower intensity than the other maxima due to partial volume coverage of the tiny slit by the neighbouring pixels. **(D)** In-plane (coronal) slice selective MRM-scan (ps: 39 × 39 μm^2, slth = 120 μm). Mtx: 128 × 256, middle of 3 slices, phase encoding direction: (y). Only the grids with periodicity $a_1/2$ = 128 μm, and $a_2/2$ = 64 μm can be differentiated. The partial volume coverage artefact, as observed in **(C)** for one slit in phase encoding direction disappeared. The smaller grid lamellae cannot be resolved. From qualitative inspection the resolution of the MR-scan is proved to be at minimum 64 μm.

for all of the 4 periods with the same spatial slit distance. For the grid-period featuring a slit width (a/2) close to the pixel size only the maximal 2 amplitudes (1 maximum 2 minima) are evaluated [14] due to the problem of possible unfavourable phase shifts between pixel grid and phantom grid (Moiré-pattern effect, see subsection below). Table 1 indicates the measured modulation depth from the profile using I_{max}-I_{min} data from fig. 10 and 11. For the low spatial frequencies also a systematic regression analysis using sine functions may be used. (Figure 11 blue and green colour lines). The data is normalized to the modulation I_{max}-$I_{min\ (K=2\pi/256\ \mu m)}$ of the lowest spatial frequency.

The normalized data on modulation variation with spatial frequency is visualized in Figure 12 as plot of the modulation-transfer function.

The cut-off frequency $f_{cut\text{-}off,\ 50\%} = K_{50\%}/2\pi$ can be determined from the regression analysis (sigmoidal fitting curve in Figure 12) reading the spatial frequency on *x*-axis for the 50% level for the MTF (black horizontal dashed line): $f_{cut\text{-}off,\ 50\%}$ = 14.5 line pairs/mm. This spatial frequency corresponds to a half period a/2 = 34.5 μm.

The cut-off frequency for the modulation to noise criterion (Eq. 7) results in a higher spatial frequency: $f_{cut\text{-}off,\ noise}$ = 19.4 line pairs/mm corresponding to a half period a/2 = 26 μm close to the phantom slit width of 32 μm. For this reason, the grid (slit width 32 μm) still can be qualitatively detected by visual inspection (Figure 10), though in single line profiles the modulation disappears for some slits (unfavorable pixel position to slit-bar position and low SNR).

4 Discussion

Quality control regarding the spatial resolution in MR-microimaging and MRM was mainly performed by qualitative inspection using objects with known structural sizes in the range of the assumed spatial resolution, mostly close to the pixel size, e.g.,

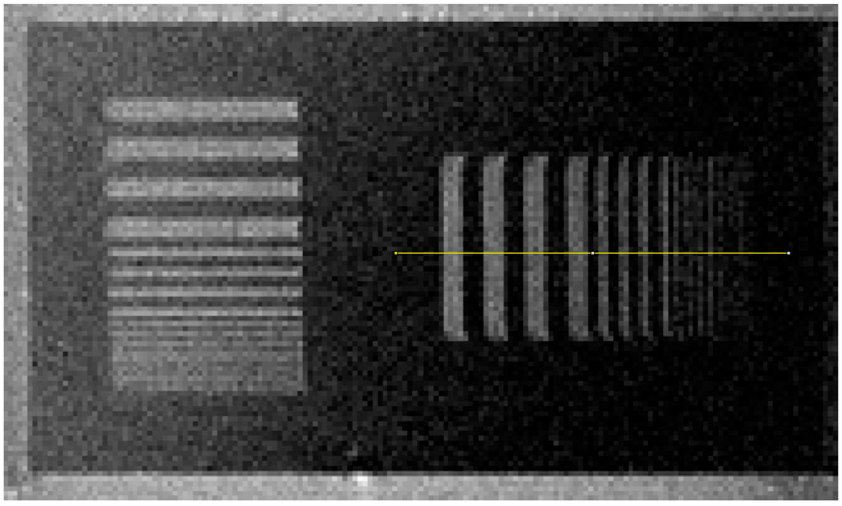

FIGURE 10
2D-FT MR-scan with slice selective excitation in the layer of the 2 orthogonal grid sets (cor, VS.: 31 × 31 × 120 μm; Mtx: 160 × 256). The grid with $a_3/2$ = 32 μm is difficult to be detected. For quantitative evaluation using the MTF the path of a profile of 1 pixel width for the evaluation of the modulation depth (Figure 11B) in frequency encoding direction (x: left-right) is indicated. The noise is calculated as standard deviation σ in a ROI close to the profile outside of the grid (σ = 73.4).

TABLE 1 Calculated data for the modulation depth originating from a single line profile (Figure 10 and Figure 11). The noise criterion level is calculated from Eq. 7 from the noise defined for practicability as the standard deviation ($s = \sigma_{background}$) in a Region of Interest (ROI) outside of the grid but close to the path of the profile ($\sigma_{background}$ = 73.4).

K [2π/μm]	1/256	1/128	1/64	1/32	Noise criterion level
$M = (I_{max}-I_{min})/(I_{max} + I_{min})$	0.88+-0.04	0.79+-0.06	0.40+-0.02	0.27+-0.07	0.31
$M/M_{K=2\pi/256\ \mu m}$	1.00 ± 0.04	0.9 ± 0.07	0.45+-0.03	0.31+-0.08	0.35

tiny polymer beads [32]. The relevance of the concept of the MTF and Point Spread Function (PSF) for describing principal limits in spatial resolution in MRI has long been recognized [17,33]. Systematic investigations based on the MTF however, have been rare and, when performed in the context of MR-microimaging or MRM, have been mainly relying on lithographically etched structures using silicon wafer material as available for microelectronics [11,26].

Pixel sizes down to 1 × 4 μm^2 have been reported [26] using an experimental MR-microscopy system with strong gradients (G = 12 T/m). The authors also indicated the necessity for tools for proving spatial resolution up to this 1 μm regime. They indicated their limitation to letter lines of 3 μm at 75 μm depth. The corresponding MR images were characterized by high slice thickness and anisotropic voxels (ΔV = 1 × 4 × 75 μm^3). Two lines of 5 μm width were resolved. The same authors also reported about the difference between pixel size and spatial resolution and the challenges in the manufacturing of resolution phantoms and objects with strong anisotropy necessary for high slice thickness and SNR. Their approach for manufacturing of phantoms with advanced deep lithographic etching processes was based on anisotropic plasma etching in silicon.

With difference, we demonstrate the use of an alternative deep anisotropic lithographic method based on Synchrotron irradiation (DXRL) for the manufacturing of sets of orthogonal grids.

Technical realizations featuring a full set of grids with varying spatial frequencies were restricted in structural depth mainly due to the limited aspect ratio achievable in standard lithographic etching processes, as an example to about 32 μm slit width at about 160 μm structural depth (AR ≅5) [11]. High aspect ratios (ratio of lateral structural width to structural depth) in small grids allow for the positioning of MR-selected slices within the grid plane and simultaneous QC on spatial resolution in two independent spatial directions. In standard 2D-FT imaging these are connected to different spatial encoding principles, i.e., phase and frequency encoding. The possibility for in plane detection of two orthogonal grids at high structural depth allows for high SNR due to the higher voxel size even, when single, one pixel wide profile lines are used. Moreover it opens potential for the adjustment and increase of the SNR by the selection of broader line profiles.

Apart from lateral etching the use of silicon phantoms may also suffer from the inherent magnetic susceptibility difference between the silicon material and the MR-visible liquid. In MRI QC the liquid chosen is usually a water solution with added paramagnetic salts for reducing the repetition time TR and subsequently the measurement time. The susceptibility difference might result in spatial magnetic field fluctuations resulting in spatial distortions dependent on the

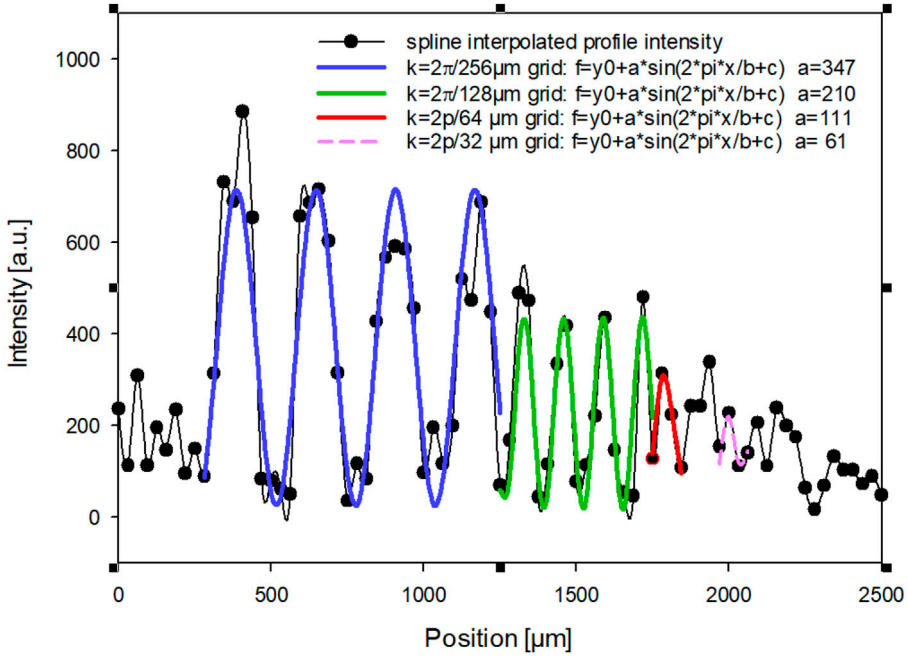

FIGURE 11
Intensity profile along the path indicated in Figure 10 for evaluation of the relative modulation depth and the MTF. Evaluated regions for determination of maxima and minima are indicated by colour encoded lines (fit data for modulations with high SNR are plotted). The profile line is only one pixel wide (31 µm) and features a modulation to noise ratio for the lowest spatial frequency (left) $MNR_{(K=2\pi/256\ \mu m)} \cong 9.2$.

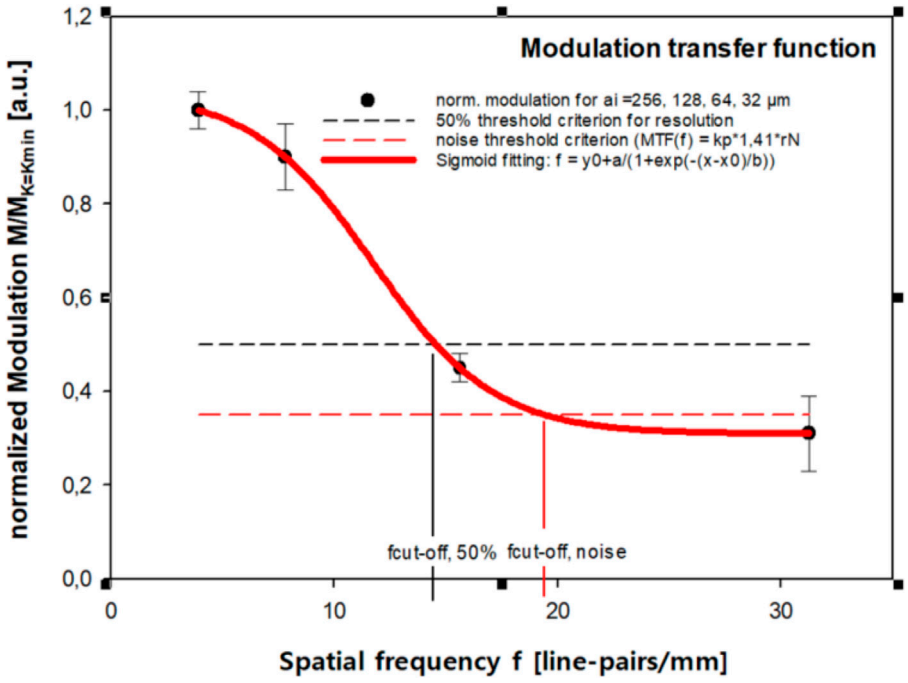

FIGURE 12
Normalized Modulation transfer function (MTF). The modulation of the signal intensity normalized to the signal modulation at lowest spatial frequency $M/M_{K=Kmin}$ (Table 1; Figure 11) is plotted vs. the spatial frequency f. A sigmoidal function (4 parameter fit) describes the data well and may be used for the evaluation of the cut-off frequency corresponding to the two different resolution criteria by interpolation. The resolution criterion level (50%-MTF level: $fcut\text{-}off_{50\%}$ = 14.5 line pairs/mm) is indicated by the dashed horizontal black line. The Modulation-to Noise-criterion (M_{crit} = kp $\sqrt{2}$ $\sigma_{noise}/<I_{max}\text{-}I_{min}>$; kp = 2) is also shown as red dashed line ($f_{cut\text{-}off\_noise}$ = 19.40 line pairs/mm).

phantom and its orientation to the magnetic field. Such phantom-induced spatial distortions due to susceptibility differences increase with magnetic field strength. Silicon based resolution phantoms might, therefore, not be ideally suited for MR-microscopy, which is typically performed on high magnetic field magnets in order to benefit from increased signal to noise ratio.

Both of these restrictions are overcome using PMMA phantoms fabricated by DXRL [34] along with chemically inert silicon oil used as an MR-visible liquid, which also is less sensitive to air bubble appearance than water solutions.

The structural draft was designed for the very challenging minimum structural width of 1 μm at 100 μm depth (AR = 100). Actually, aspect ratios of AR = 4 μm/100 μm = 25 at very steep side walls along with high duty cycles could be achieved using the very low divergence of the Synchrotron radiation for structuring the PMMA polymer down to 4 μm sized plates (lamellae). The main restriction in the manufacturing of the phantoms was represented by the mechanical stability of the thin lamellae plates below 4 μm at height of 100 μm. SEM and OM results showed that the lateral stabilization by bars rectangular to the grid lamellae was successful only to lateral length of about 30 μm at maximum, nevertheless thus confirming the effectiveness of the supporting tiny side bars with regard to the mechanical stability in principle. Future realizations with thin bar width at about 30 μm interval distance could permit the production of grids with 4 μm slit width or even smaller plates.

The phantom application was demonstrated for several examples of protocols with QC for spatial resolution on a microscopy insert to a high-field 7T human scanner. A quick qualitative check of spatial resolution in two different spatial directions for phase and frequency encoding could be performed in the microscopy regime (ps < 100 μm) at the same time using a coronal or sagittal slice positioned within the plane of the grid. The spatial distortions due to susceptibility differences are small even at low bandwidth for this phantom. Also, the procedure for the quantitative evaluation of the interpolated MTF of an MRM TSE protocol was demonstrated on principle within an example of low SNR. The cut-off frequency for a predefined modulation threshold (50%) has been determined by interpolation of the discrete MTF evaluations. In addition, the spatial resolution, limited by the modulation-to-noise (MNR) criterion, could be determined using the MTF graph with inserted noise level indication. From our experience there might be some practical problems, inaccuracies and uncertainties in quantitative evaluations on grid structures with regard to the proposed MTF procedure**,** which are shortly discussed below.

4.1 Pixel position with reference to grid modulation (Moiré-pattern effect)

In unfavourable situations, when pixel size is close to the smallest slits, one pixel might be positioned such that ½ of it is covering a massive bar (no signal) and the other half is situated in the slit with the MR-active liquid (max. signal); the next pixel might experience a similar situation. In such a case (phase difference between the pixel grid and the phantom grid $\Delta\phi = \pi/2$) there is hardly any difference in signal observed (medium grey level for both pixels: the modulation disappears for neighbouring pixels (M = 0). If these pixels would be shifted by half the slit width against the grid such that the phase shift between the pixel and grid pattern vanishes ($\Delta\phi = 0$), the modulation could be maximal (one pixel covering the slit, the next pixel covering the bar): *M*th = 1 (problem of dependence of modulation depth on the phase difference between pixel grid and phantom grid modulation phase: aliasing or Moiré-effect).

This effect might be effectively reduced by slightly tilting the profile path against the investigated encoding direction. The procedure results in a varying phase shift for the 4 different slits and the modulation for the slit and bar with maximum modulation depth may be evaluated as proposed in [14].

4.2 Noise overlay on modulation

For quantitative evaluation of the modulation depth the evaluation of intensity maxima I_{max} and minima I_{min} does include the additional contributions of the noise. A quantitatively potentially more precise procedure would therefore include a regression analysis (fitting) of the periodically modulated intensity by a set of periodic rectangular functions for the amplitudes including a constant intensity offset y_0 and a phase fitting parameter for each spatial frequency of the phantom grid ($K_i = 2\pi/a_i$) thus removing noise fluctuations. However, this approach fails if the pixel size approaches the grid pattern half period due to aliasing (Moiré-effect). In practice the influence of noise on the measurement might be reduced by averaging of the several different maxima-minima differences in order to obtain a mean modulation for all of the 4 slit bar periods.

4.3 Interpolation inaccuracy

The cut-off frequency is determined using a regression analysis for the discrete K_i measured MTF data and interpolation from this fitting procedure. The evaluation is subject to errors in the indiviudal modulation measurement. The measurement of modulation is limited to discrete spatial frequencies and interpolation might not accurately represent actual modulation values. The interpolation related inaccuracy could be improved using smaller steps ΔK_i, e.g., by adding a grid with slit width of 48 μm in between 32 and 64 μm width or adding in design two sets of grids in parallel, one starting at $a_1/2$ = 128 μm (64 32, . . . 4 μm) and the second starting at 96, 48, . . . 2 μm. However, this 2-grid solution demands for two profiles for the improved discretized MTF evaluation.

The investigated prototype phantom offered maximum spatial frequencies corresponding to the 4 μm slit width (f = 1/(8 μm) = 125 mm^{-1}, 125 lp/mm) in manufacturing, which would have been sufficient for presumably more than 99% of the published MR-microscopy reports.

4.4 Position of slice and ROI for MNR evaluation, B1-inhomogeneity

The measurement of noise, estimated by the standard deviation in a ROI outside of the MR visible object, might be varying with the

position of the ROI. An example might be represented by sensitivity encoding with several rf-coils as the noise might depend on the distance to the most relevant rf-sensor. Each MRI-sensor (rf-coil) features a local sensitivity distribution. This might result in a local variation of signal intensity and modulation. We therefore propose, to position the ROI for noise measurement as close as possible to the measured modulation profile (see comment in the legends of Figure 10).

The slice should be positioned as accurately as possible in the level layer of the grid. Otherwise, the measured image and profile could pass regions outside of the grid resulting in additional offset intensity with a) positive sign (if the image slice is located above the grid in the MR-active liquid) or b) negative if the slice is located in the massive plate giving no signal to modulation. The necessity for accurate positioning is especially relevant, if the slice thickness approaches the grid height.

4.5 Sample dependent spatial resolution

We would like to point within this discussion also to a more general aspect of QC on spatial resolution: the impact of sample specific characteristics on the capability of an MR-imaging system to differ spatially between neighboring objects.

There are several physical and chemical properties of the sample itself, which might have impact on the spatial resolution of an MR imaging device (see, e.g., [5,35]). These are for instance: the magnetic susceptibility and its inhomogeneity, the chemical environment of the detected 1H-nuclei (chemical shift difference between neighboring voxels), the diffusivity of the molecules, the molecular mobility, the MR-signal dephasing, characterized by T2* with regard to the linewidth of the spectral signal and the signal decay by T2 in Multi-echo-encoding pulse sequences. Though the discussion of all of these factors is beyond the scope of this article, we would like to demonstrate this impact by an example:

We might consider the extreme case of porous media, where magnetic susceptibility differences between the solid material and the enclosed liquids or gases are estimated to result in internal magnetic field gradients G_{int} up to few 10^{ths} of T/m [36]. Such strong internal gradients result in high linewidth (lw $\cong \gamma\, G_{int}\, \Delta x$) for the individual volume at interest at pixel size Δx and very short T2* decay of the MR-signal. Assuming a pixel size and distance of 10 μm and an internal sample specific field gradient G_{int} = 20 T/m for the extreme case of a porous rock media, a high linewidth of the MR-signal (lw ≅ 8.52 kHz/pixel) is expected. Even maximum available gradient hardware on special microscopy systems as, for instance, featuring a gradient strength G = 12 T/m [26], are not capable to separate these two pixels at 10 μm distance in frequency encoding direction (not considering limitations due to the necessity for quick acquisition of data during the fast signal decay).

The actual achieved spatial resolution in MRI (close to the limits of an apparatus) might be sample specific (as is the case for other imaging modalities) and the spatial resolution *in vivo* on humans might differ between regions close to "porous media" like the lung or close to the ear channel and homogenous (with regard to B-field) regions, e.g., the cerebellum in the human brain. A typical linewidth in human tissue after shimming is in the order of 70 Hz, similar to the linewidth we have measured for the resolution phantom with silicon oil (lw ≅ 65 Hz).

Actually, this sample specific aspect represents the reason, why phantoms with defined MR-relevant properties and low magnetic susceptibility differences are proposed for QC on spatial resolution and recommended in guidelines for QC on spatial resolution [14–16]. Strong susceptibility differences resulting potentially in strong magnetic field local gradients are present around air bubbles in water and should be avoided in phantoms for QC for geometric accuracy or spatial resolution. For avoiding air bubbles and susceptibility differences we used silicone oil, which - in connection to the PMMA material - resulted in a low value of the spectral linewidth of the phantom.

The availability of a standardized resolution phantom, without necessity for dealing with varying biological tissue characteristics with impact on resolution, facilitates the systematic improvements and optimization of MR-scanner hardware, pulse sequences and even MR protocol optimization. With regard to spatial resolution the phantom, in principle, allows to study not only the impact of gradient performance, e.g., strength and switching behavior, but the influence of most of the multifold factors originating from the individual local specific MR-apparatus installation. This includes the impact of main hardware components, magnetic field (B_0-) homogeneity, rf-transmission and reception (rf-coils), postprocessing of data including nominal resolution enhancement by Deep Learning and AI-routines. Even MR-protocol parameters (like shimming protocols, bandwidth, Turbo factors in TSE, EPI-factor, GRAPPA factor, fast, and slow gradient switching) usually adjustable by the operator on the MR-scanner might be evaluated for their impact on the spatial resolution of the image.

Consequently, the described phantom might be a very useful tool for optimizing MR-protocols for improving resolution in the microimaging range, available now also on clinical MR-scanners. In addition, the microscopy range of animal scanners and even hardware performance of the best performing MR-microscopy scanners could profit from such a resolution phantom. We wish to offer these phantoms for systematic QC to interested users for research and resolution improvement on their specific MR-scanner, if we are asked for, as long as already manufactured phantoms are available.

4.6 Perspectives for usage with other imaging modalities

In principle the manufactured phantoms, prospectively, can also be used for other high-resolution imaging methodologies, for example, μCT [22, 23, 24] or Optical Coherence Tomography (OCT) [37]. There are options for varying the contrast in these imaging modalities by adding different add-ons to the MR-visible liquid. Such a resolution phantom for MR-microscopy and perspectives for other imaging modalities did not yet exist.

5 Summary and conclusion

A phantom design for the quality control on spatial resolution in MR-microimaging and microscopy is proposed. In specific the grid test structure is designed for the qualitative inspection based on the minimum distinguishable grid pattern and the quantitative measurement of the MTF for spatial resolution up to 500 lp/mm. Several prototypes, specifically designed for slice selective 2D-FT encoding, were manufactured using the extraordinarily high aspect ratios available with Synchrotron based Deep X-Ray Lithography (DXRL) in the polymer PMMA. They were checked for the achieved maximum spatial frequencies, aspect ratio and duty cycle using optical and electron microscopy. A minimum slit width ($a_{min}/2$ = 4 µm) at about 100 µm lamellae depth was achieved corresponding to 125 lp/mm.

This phantom for QC allows for a quick qualitative check on spatial resolution in two independent spatial encoding directions at high SNR due to the usability at high slice thickness with small pixel sizes as typically used for 2D-FT slice selective MRI. Examples for visual qualitative inspection are shown for several MR-protocols with pixel size in the MR-microscopic regime (ps < 100 µm).

A simple physico-mathematical practical procedure is proposed for MR-evaluation for deriving a quantitative number on spatial resolution based on the MTF. The critical level of modulation for defining a resolution criterion is fixed and the practical method for the evaluation of the cut-off frequency is shown. In approaching visual impressions on spatial resolution in images an additional criterion derived from the modulation depth to noise ratio (MNR) is suggested. Two different spatial encoding methods (e.g., frequency and spin warp encoding) can be evaluated using one single MRI measurement of this prototype phantom. The evaluation is demonstrated on the example of a slice selective fast Turbo-spin-echo (TSE) MRM protocol with low SNR. The spatial distortions due to susceptibility differences are considerably low with comparison to silicon based phantoms with water from our experience, thus offering best performance also for high field MR-scanners. The prototype phantom not only offered the possibility for a quick qualitative visual impression of the spatial resolution *via* grid pattern differentiation but also allows for the determination of quantitative numbers on the spatial resolution. Though the envisaged minimum structural size of 1 µm in the realized specimen could not be achieved, the developed prototype offers already unique possibilities for the quantitative evaluation of 2D spatial resolution within QC in slice selective 2D-FT imaging for commercial preclinical and prototype research MR-microscopy systems.

Due to the improvements in hardware, effective spatial encoding by small rf-coil arrays and high sensitivity achieved especially at Ultra-High-Field human MR-scanners the microscopic range with pixel size below 100 µm becomes more relevant for the early medical diagnosis of pathologies and already has been reached in specific applications. The quantitative proof of the actual spatial resolution and improvements might be achieved using the described phantom or similar designs not only for preclinical high-resolution MRM, but also for such UHF human scanners. DXRL is especially suited for the anisotropic voxel sizes typical for slice selective 2DFT.

The proposed phantoms might also be used for systematic improvement of MRI hardware for spatial encoding, pulse sequence optimization and adjustment of MR-protocol parameters. In principle the manufactured phantoms prospectively can also be used for other high resolution imaging methodologies as, for example, µCT or optical coherence tomography (OCT). Such a resolution phantom for MR-microscopy did not yet exist.

Data availability statement

The raw data supporting the conclusion of this article will be made available by the authors, without undue reservation.

Author contributions

Concept and idea: AB; project author: AB; project manager at KNMF: MB; DXRL realization: MB; SEM-quality control images: MB; MR-microimaging and microscopy: AB; postprocessing and evaluation: AB; manuscript draft: AB; discussion and correction: MB + AB; corresponding author: AB.

Funding

Financial support via KNMFi-project 2015-013-006488 and Basic Funding by the Center for Medical Physics and Biomedical Engineering, Medical University of Vienna is acknowledged.

Acknowledgments

We acknowledge the Karlsruhe Nano Micro Facility (KNMF) (www.kit.edu/knmf) of the Karlsruhe Institute of Technology (KIT) for provision of access to instruments at their laboratories and equipment.

Conflict of interest

AGB is owner of a patent on MR-microscopy phantoms [18].

The remaining authors declare that the research was conducted in the absence of any commercial or financial relationships that could be construed as a potential conflict of interest.

The handling editor EW declared a past collaboration with the author(s) AGB.

Publisher's note

References

1. Széles JC, Csapó B, Klarhöfer M, Balássy C, Hoda R, Berg A, et al. *In vivo* magnetic resonance micro-imaging of the human toe at 3 Tesla. *Magn Reson Imaging* (2001) 19(9):1235–8. doi:10.1016/s0730-725x(01)00461-1

2. Laistler E, Dymerska B, Sieg J, Goluch S, Frass-Kriegl R, Kuehne A, et al. *In vivo* MRI of the human finger at 7 T. *Magn Reson Med* (2018) 79:588–92. EPub March 10, (2017). doi:10.1002/mrm.26645

3. Rogelj L, Dolenec R, Tomšič MV, Laistler E, Simončič U, Milanič M, et al. Anatomically accurate, high-resolution modeling of the human index finger using *in vivo* magnetic resonance imaging. *Tomography* (2022) 8(5):2347–59. doi:10.3390/tomography8050196

4. Bruker *Bruker.com. Products and solutions, preclinical imaging*, Billerica: Bruker Corporation. (2022). Available at: https://www.bruker.com/de/products-and-solutions/preclinical-imaging/mri/ultra-high-field-magnetic-resonance-imaging.html [Accessed January 15, 2023].

5. Callaghan PT. *Principles of Nuclear Magnetic Resonance Microscopy*. Oxford: Clarendom Press (2003).

6. Johnson GA, Cofer GP, Fubara B, Gewalt SL, Hedlund LW, Maronpot RR. Magnetic resonance histology for morphologic phenotyping. *J Magn Reson Imaging* (2002) 16(4):423–9. doi:10.1002/jmri.10175

7. Berg A, Sailer J, Rand T, Moser E. Diffusivity- and T2 imaging at 3 Tesla for the detection of degenerative changes in human-excised tissue with high resolution: Atherosclerotic arteries. *Invest Radiol* (2003) 38(7):452–9. doi:10.1097/01.RLI.0000068620.17569.83

8. Berg A, Singer T, Moser E. High-resolution diffusivity imaging at 3.0 T for the detection of degenerative changes: A trypsin-based arthritis model. *Invest Radiol* (2003) 38(7):460–6. doi:10.1097/01.rli.0000078762.72335.57

9. Hanson P, Philp CJ, Randeva HS, James S, O'Hare JP, Meersman T, et al. Sodium in the dermis colocates to glycosaminoglycan scaffold, with diminishment in type 2 diabetes mellitus. *JCI Insight* (2021) 6(12):e145470. doi:10.1172/jci.insight.145470

10. Tardieu M, Lakhman Y, Khellaf L, Cardoso M, Sgarbura O, Colombo PE, et al. Assessing histology structures by *ex vivo* MR microscopy and exploring the link between MRM-derived radiomic features and histopathology in ovarian cancer. *Front Oncol* (2022) 19(11):771848. doi:10.3389/fonc.2021.771848

11. Berg A, Wanzenboeck H, Hesjedal T, Moser E. MR-Microscopy at 35 µm on a whole body MR-system: Quality control by modulation-transfer-function and applications. In: *Proc. ISMRM/ESMRMB joint annual meeting*. Glasgow (2001). p. 925.

12. Berg A, Potthast A, Starewicz P. MR-MICROSCOPY on a human 7T-SCANNER. In: *Proc. ISMRM/ESMRMB 2010*. Stockholm, Sweden (2010). p. 1048.

13. Edlow BL, Mareyam A, Horn A, Polimeni JR, Witzel T, Tisdall MD, et al. 7 Tesla MRI of the *ex vivo* human brain at 100 micron resolution. *Sci Data* (2019) 6:244. doi:10.1038/s41597-019-0254-8

14. Lerski RA, de Certaines JD. Performance assessment and quality control in MRI by Eurospin test objects and protocols. *Magn Reson Imaging* (1993) 11:817–33. doi:10.1016/0730-725x(93)90199-n

15. European Norm. *Evaluation and routine testing in medical imaging departments; Part 3-7: Acceptance and constancy tests – determination of essential image characteristics of magnetic resonance equipment* (2005). EN 61223-3-7 (IEC 62B/575/CDV) 2005.08.01.

16. American College of Radiolog. *MR accreditation program; phantom test guidance for use of the small MRI phantom*. American College of Radiolog (2022). Available at: https://www.acraccreditation.org/-/media/ACRAccreditation/Documents/MRI/SmallPhantomGuidance.pdf (Accessed December 11, 2022).

17. Rossmann K. Point spread function, line spread-function and modulation-transfer-function. *Radiology* (1969) 93:257–72. doi:10.1148/93.2.257

18. Berg A. *Testphantom zur Kontrolle der Abbildungsqualität in der hochortsauflösenden NMR-Bildgebung. German Patent no. DE19904635*. German Patent office München/Germany (1999).

19. Fellner C, Muller W, Georgia J, Taubenreuther U, Fellner F, Kalender W. A high-resolution phantom for MRI. *Magn Reson Imaging* (2001) 19:899–904. doi:10.1016/s0730-725x(01)00397-6

20. Wright S, Cameron HG, Barrett F. "Biomimetic Vision sensors" (chapter 1.2.2.2). In: L Aklesh RJ Martin-Palma, editors. *Engineered biomimicry*. Elsevier (2013). doi:10.1016/B978-0-12-415995-2.00001-5

21. USAF. *USAF resolution test chart* (1951). Available at: https://de.wikipedia.org/wiki/USAF-Chart (Accessed Dec 12, 2022).

22. Ghani MU, Zhou Z, Ren L, Li Y, Zheng B, Yang K, et al. Investigation of spatial resolution characteristics of an *in vivo* micro computed tomography system. *Nucl Instrum Methods Phys Res A* (2016) 21(807):129–36. doi:10.1016/j.nima.2015.11.007

23. Langner O, Karolczak M, Rattmann G, Kalender WA. Bar and point test patterns generated by dry-etching for measurement of high spatial resolution in micro-CT. World congress on medical Physics and biomedical Engineering, munich, Germany. *IFMBE Proc* (2009) 25(2):428–31.

24. JIMA. *Microchart Japan inspection instruments manufacturers association (JIMA) RT-RC04* (2021). Available at: https://www.jima.jp/content/pdf/catalog_rt_rc04_eng.pdf (Accessed January 12, 2021).

25. Judy PF, Balter S, Bassano D, McCullough EC, Payne JT, Rothenberg L. *AAPM report No. 1;* PHANTOMS FOR PERFORMANCE EVALUATION AND QUALITY ASSURANCE OF CT SCANNERS. American Association of Physicists in Medicine (1977).

26. Lee SC, Kim K, Kim J, Yi JH, Lee S, Cheong C. MR microscopy of micron scale structures. *Magn Reson Imaging* (2009) 27:828–33. doi:10.1016/j.mri.2009.01.002

27. Karlsruhe Nano Micro Facility (KNMFi). *Technologies: Deep X-ray lithography (XRL)* (2022). Available at: https://www.knmf.kit.edu/XRL.php (Accessed Dec 14, 2022).

28. Chen YT, Lo TN, Chu YS, Yi J, Liu CJ, Wang JY, et al. Full-field hard x-ray microscopy below 30 nm: A challenging nanofabrication achievement. *Nanotechnology* (2008) 19:395302. doi:10.1088/0957-4484/19/39/395302

29. Baldock C, Murry P, Kron T. Uncertainty analysis in polymer gel dosimetry. *Phys Med Biol* (1999) 44:N243–6. doi:10.1088/0031-9155/44/11/402

30. Saile V, Wallrabe U, Tabata O, Korvink JG. LIGA and its applications. In: *Advanced micro & nanosystems 7*. Weinheim: Wiley VCH (2009). Available at: https://download.e-bookshelf.de/download/0003/7450/04/L-G-0003745004-0002368046.pdf.

31. Gach HM. Technical note: T1and T2 and complex permittivities of mineral oil, silicone, oil, and glycerol at 0.35, 1.5, and 3 T. *Med Phys* (2019) 46(4):1785–92. doi:10.1002/mp.13429

32. Ciobanu L, Seeber DA, Pennington CH. 3D MR microscopy with resolution 3.7 microm by 3.3 microm by 3.3 microm. *J Magn Reson* (2002) 158:178–82. doi:10.1016/s1090-7807(02)00071-x

33. McFarland EW. Time-independent point-spread function for NMR microscopy. *Magn Reson Imaging* (1992) 10(2):269–78. doi:10.1016/0730-725x(92)90486-j

34. Berg A, Börner M. Quantification of microscopic spatial resolution on MR-scanners using micro-phantoms manufactured with Deep-X-ray Lithography. *Proc Int Soc Mag Reson Med* (2020) 28:4267.

35. Glover P, Mansfield P. Limits to magnetic resonance microscopy. *Rep Prog Phys* (2002) 65:1489–511. doi:10.1088/0034-4885/65/10/203

36. Song YQ, Cho H, Hopper T, Pomerantz AE, Sun PZ. Magnetic resonance in porous media: Recent progress. *J Chem Phys* (2008) 128:052212. doi:10.1063/1.2833581

37. Lichtenegger A, Harper D, Augustin M, Eugui P, Muck M, Gesperger J, et al. Spectroscopic imaging with spectral domain visible light optical coherence microscopy in Alzheimer's disease brain samples. *Biomed Opt Express* (2017) 8:4007–25. doi:10.1364/boe.8.004007

38. Steckner M, Drost D, Prato F. Computing the modulation-transfer-function of a magnetic resonance imager. *Med Phys* (1994) 21(3):483–9. doi:10.1118/1.597310

frontiers | Frontiers in Physics

TYPE Original Research
PUBLISHED 27 July 2023
DOI 10.3389/fphy.2023.1209505

OPEN ACCESS

EDITED BY
Ewald V. Moser,
Medical University of Vienna, Austria

REVIEWED BY
Richard Bowtell,
University of Nottingham,
United Kingdom
Peter Van Gelderen,
National Institute of Neurological Disorders and Stroke (NIH), United States
Andreas Georg Berg,
Medical University of Vienna, Austria

*CORRESPONDENCE
Gisela E. Hagberg,
gisela.hagberg@tuebingen.mpg.de

RECEIVED 20 April 2023
ACCEPTED 17 July 2023
PUBLISHED 27 July 2023

CITATION
Hagberg GE, Engelmann J, Göring E, Cuña EG and Scheffler K (2023), Magnetic properties of iron-filled hydrogel clusters: a model system for quantitative susceptibility mapping with MRI. *Front. Phys.* 11:1209505. doi: 10.3389/fphy.2023.1209505

Magnetic properties of iron-filled hydrogel clusters: a model system for quantitative susceptibility mapping with MRI

Gisela E. Hagberg[1,2]*, Jörn Engelmann[1], Eberhard Göring[3], Enrique G. Cuña[4,5] and Klaus Scheffler[1,2]

[1]High Field Magnetic Resonance Center, Max Planck Institute for Biological Cybernetics, Tübingen, Germany, [2]Department for Biomedical Magnetic Resonance, University Hospital, Tübingen, Germany, [3]Department Solid State Spectroscopy, Max Planck Institute for Solid State Research, Stuttgart, Germany, [4]Medical Physics, Centro Uruguayo de Imagenología Molecular, Montevideo, Uruguay, [5]Centro Uruguayo de Imagenología Molecular, Montevideo, Uruguay

Quantitative approaches in clinical Magnetic Resonance Imaging (MRI) benefit from the availability of adequate phantoms. Ideally, the phantom material should reflect the complexity of signals encountered *in vivo*. In the present study we validate and characterize clusters consisting of sodium-polyacrylate embedded in an alginate matrix that are unloaded or loaded with iron for Quantitative Susceptibility Mapping (QSM), yielding a non-uniform iron distribution and tissue-mimicking MRI properties. Vibrating sample magnetometry (VSM) was used to characterize the phantom material and verify the accuracy of previous MRI-based observations of the QSM-based molar susceptibility (χ_M). MRI at 14.1 T with high resolution acquisitions was used to determine the size of hydrogel clusters and to further investigate the suitability of the phantom material as a model system for QSM at high field. VSM demonstrated that the iron-solution used for manufacturing the phantoms consisted of ferric iron. The χ_M of clusters with a constant iron-to-polyacrylate-ratio (8.3 µg/mg) observed with VSM was 50.7 $\pm$ 8.0 ppb mM^{-1} but showed a tendency towards saturation at total iron concentrations >1 mM. On unwrapped and background corrected phase-images obtained with gradient-echo MRI and an isotropic voxel size of 37 µm at 14.1T, the iron-free clusters had a roundish shape and blurry border with an equivalent sphere diameter of 276 $\pm$ 230 µm and a QSM of 7 $\pm$ 7 ppb. Iron-loading led to strong phase wrapping, necessitating the use of short echo times, or short inter-echo delays below 10 ms at 14.1 T. The equivalent sphere diameter of the iron-loaded clusters was estimated to 400–500 µm as verified using different MRI modalities (spin-echo, inversion recovery, and gradient echo MRI). With a constant iron-to-polyacrylate ratio, the cluster density was 10 mm^{-3} mM^{-1} iron. In agreement with previous observations, χ_M of samples with a constant amount of polyacrylate was 50.6 $\pm$ 11.4 ppb mM^{-1} at 3 T while samples containing clusters with a constant iron-to-polyacrylate-ratio yielded χ_M = 56.1 $\pm$ 6.3 ppb mM^{-1} at 3T and 55.6 $\pm$ 0.7 ppb mM^{-1} at 14.1 T. In conclusion we found that the molar susceptibility of the proposed model system corresponds to that predicted for ferritin *in vivo* loaded with 3000 iron atoms. The reproducibility was within 12% across MR scanners, batches, and phantom types and compared well with results obtained with vibrating sample magnetometry.

KEYWORDS

magnetic susceptibility, iron–oxide, phantom, quantitative MRI, quality control

Introduction

Magnetic susceptibility is a fundamental property in MRI and is useful to characterize the microstructure of tissue in quantitative terms. Indeed, quantitative susceptibility mapping (QSM) has been used to measure calcifications, venous oxygen saturation and iron content [1–9]. QSM has also recently been proposed as a tool to estimate the plaque load in patients with Alzheimer's disease (AD) [10].

An important advantage of QSM is that its quantitative values do not depend on the strength of the static magnetic field at which the measurements are carried out, unlike other MRI properties. Therefore, QSM lends itself to multi-center studies and widens the applicability and comparability of MRI results between sites compared to other quantitative parameters. On the other hand, the quality of the QSM results depends on and can be influenced by the image acquisition itself and the many different processing steps that are required to quantify susceptibility. Therefore, novel procedures that can be used to ascertain a correct quantification, not only in terms of reproducibility but also accuracy, is a requirement. To verify different post-processing algorithms, suitable data sets in form of actual *in vivo* acquisitions [11] or realistic simulations [12] have been made available.

Development of QSM phantoms suitable to assess the many factors influencing quantification are underway, and contain single susceptibility sources [13, 14] or mixtures [15] aimed to capture more of the complexity encountered *in vivo*. Indeed, iron, which is the most abundant susceptibility source in the brain is not homogeneously distributed in the tissue with reported iron concentrations of 0.56 mM in the cytoplasm and 0.96 mM in the nucleolus of neurons and up to 3.05 mM on average in oligodendrocytes [16].

We recently developed a phantom consisting of iron which is clustered in hydrogels [17]. QSM was measured at 3 T (two different vendors), 7T and 9.4 T for a phantom containing vials with different iron concentrations (12.5–100 µg/mL aqueous solution) corresponding to about half of those typically found for non-haeme iron in brain tissue *in vivo* (25–223 µg/mL brain) [18].

In healthy subjects, the reported QSM contrast related to non-heme iron in healthy subjects falls within a range of 0.52–1.34 ppb per µg iron per g tissue [19–22]. These values translate into 1700–4300 iron atoms per ferritin molecule, assuming a susceptibility of 520 ppm for fully loaded (4300 iron atoms) ferritin [23]. In the parietal cortex of *ex vivo* brain, a load of 1500 iron atoms has been observed [24]. QSM contrast can also be defined in terms of molar susceptibility, χ_M (which we have previously termed "QSM-relaxivity", in analogy with the longitudinal and transverse relaxation parameters [17]) to quantify the iron concentration that changes the magnetic susceptibility by 1 ppm, or perhaps rather 1 ppb, which more reflects the subtle field effects observed in human brain tissue. Assuming ferritin with an iron load of 4300, χ_M is 72 ppb mM^{-1} iron, while a load of 1700 corresponds to 28 ppb mM^{-1}, considering a brain tissue density of 1.04 g/mL [25] and taking into account the difference in the fraction of macromolecules between brain regions.

The proposed clustered Iron phantom yielded a molar susceptibility, that is, within the range of that expected for ferritin, being 54 ± 13 ppm mM^{-1} as an average value observed across four different scanners at three sites. However, validation of the observed QSM values through magnetometry measurements were lacking. Therefore, in the present study, we performed vibrating sample magnetometry, MRI-assessments at 3 T with the protocol established previously, complemented by MRI at 14.1 T using high resolution acquisition with voxel sizes between 0.037 and 0.2 mm.

Methods

Sample preparation

As described previously (cfr Figure 1 in Ref. 17), the samples consisted of iron solutions at four different concentrations (0.2, 0.4, 0.8, and 1.6 mM) placed in 4 mL cylindrical scintillation counting vials (high density polyethylene, # HEE8.1 Carl Roth, Germany, height: 53 mm, diameter: 14 mm). The samples were manufactured in two steps. In step 1, 0.04 g alginate (Alginic acid sodium salt, Carl Roth, Germany) per milliliter of water with 30 µmol/L gadoteric acid (Dotarem, Guerbet, France) added to shorten T_1 were mixed overnight (>12 h), until a clear, slightly yellowish, highly viscous liquid/gel was obtained. Next, 0.0125, 0.025, 0.05, or 0.1 mg/mL free iron (single-element atomic absorption spectrometry (AAS) standard-solution, 1,000 mg/L, matrix: 2% HNO_3; Carl Roth, Germany) was absorbed in sodium polyacrylate (NaPA), Spectra/Gel Absorbent, Spectrum, United States) to generate iron clusters, by stirring until the liquid was completely absorbed and homogeneously distributed in the NaPA gel. This could be recognized by the uniform distribution of the red-brown coloration (probably due to hydrolysis and formation of increasingly poorly soluble condensates of $(FeOOH)_x$ aq.) produced during mixing in the solid polyacrylate hydrogel. Either a fixed amount (120 mg in Phantom 4, which was the same as for Phantom 1 used in our previous multi-centre study [17]) or increasing amounts of NaPA were used (15, 30, 60 or 120 mg for Phantom 2 and 3, to keep the mass ratio of iron to sodium polyacrylate fixed at 8.3 µg Fe/mg NaPA). To prepare the final samples, 10 mL of the alginate/Dotarem mixture from step 1 was added and the samples mixed thoroughly. Finally, the samples were allowed to stand until all air bubbles were gone. For the MRI acquisition, the samples were then resuspended with 1 mL syringes, avoiding the formation of air bubbles, and transferred to the scintillation vials until these were completely filled. When closing the vials, any larger inclusion of air below the lid must be avoided. This thus yielded final iron concentrations of 0.2, 0.4,0.8, and 1.6 mM for both phantom types, which were kept at room temperature throughout the study. In the first type (each vial contained the same fixed amount of NaPA), samples with a varying amount of iron per cluster were obtained. In the second type, a fixed amount of iron per cluster were generated. As will be shown in the course of the present work, the second type of phantom allowed to spatially separate single clusters from each other, and in different vials with increasing amounts of iron, an increasing number of clusters could be observed (cfr Figure 12, Figure 13, Figure 14). For the magnetometry measurements, samples without any NaPA clustering agent ('free iron') were also manufactured.

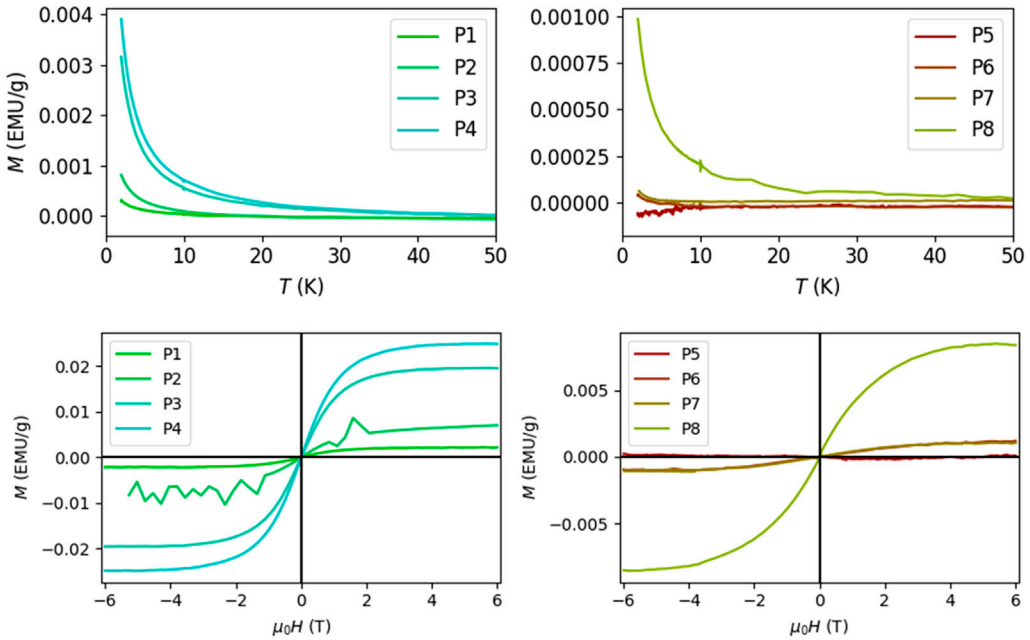

FIGURE 1
Result of Vibrating Sample Magnetometry for free (P1-P4) and clustered (P5-P8) iron samples with concentrations 0.2 mM (samples P1 and P5), 0.4 mM (P2, P6), 0.8 mM (P3, P7) and 1.6 mM (P4, P8). There was an increase in magnetization with decreasing temperature at 0.2T, following the Curie-Weiss law. At a temperature of 2 K, the magnetization of the sample changed with the externally applied magnetic field H. The induced magnetization saturated when H = ±4 T and the relationship could be fitted using a Brillouin function The small reference Gadolinium signal (not shown) has been removed from each curve.

Magnetometry

Magnetometry was performed using a commercially available SQUID magnetometer (MPMS3, Quantum Design GmbH, Darmstadt, Germany). The system was operated in the vibrating sample magnetometry (VSM) mode. Measurements were performed on the samples containing free iron and the iron-clusters with a constant iron-load. The AAS standard iron solution alone was also measured at the two highest concentrations. For each sample, slightly less than 1 g was gently positioned on a thin glass-membrane positioned at mid-height of a cylindrical high purity quartz cuvette, substituting the conventional straw holder. The change in magnetization (2 s averaging) as a function of temperature was measured at 0.2 T (2000 Oerstedt). The temperature was lowered from 300 to 2 K, first at a rate of 50 K/min, and below 250 at 10 K/min. At a temperature of 2 K, the change in magnetization as a function of the applied external field $\mu_0 H$ between ±6 T was assessed (10 s averaging). The hysteresis curve was fitted with a Brillouin function. The results obtained from the samples total magnetization (expressed in electromagnetic units per Gram, emu/g) was converted from this CGS unit to ppm values in SI units based on the density of the samples obtained with mass-calculation and multiplication with 4π.

MRI acquisition

For scanning at 3 T (Prisma fit, Siemens Healthineers, Erlangen Germany, software: Syngo MR E11), all vials were placed inside a water-filled (0.9% NaCl) cylindrical, ca. 3.2 L plastic (consumer-grade) container (height: 160 mm, diameter: 160 mm). The 2-channel body coil was used for transmission and the 64-channel head/neck coil for image acquisition. After "standard mode" start shim and the acquisition of a localizer image, field-map shimming was performed on the field-of-view (FoV) used for multi-echo gradient-echo 3D imaging (MGRE). Magnitude and phase MGE images were acquired with echo times (TE) from 6 to 42 ms in steps of 6 ms; repetition time (TR) of 53 ms; nominal flip angle (FA) 18°; matrix size of 288 × 288 × 144; FoV of 174 × 174 × 86 mm [3]; acceleration factor (GRAPPA) of 2 and acquisition time (TA) of 14 min 41 sec. Phase images were used for QSM pipeline processing, magnitude images were used for morphological reference. Image reconstruction and coil-combination was performed using the manufacturers standard methods ("adaptive combine" and "Matrix optimization off").

At 14.1 T (Biospec 141/30, Bruker Corporation, Billerica MA, United States, software: Paravision 360) images were acquired for each vial separately using the standard birdcage volume transmit/receive coil with a diameter of 35 mm. The scanning protocol consisted of 1) global and localized field-map shimming within a cylinder covering the center of the vial; 2) MGRE with TE from 2.5 to 15 m in steps of 2.5 m, TR = 20 m; FA = 10°. The FoV was 20 × 20 × 38.4 mm^3 and the matrix (100 × 100 × 192) set to obtain voxel-sizes of 200 μm (TA = 6min24 s); 3) MGRE with an isotropic voxel size of 75 μm (FoV = 19.2 × 19.2 × 38.4 mm^3, matrix = 256 × 256 × 512), TE from 3 to 23 in steps of 4 m, TR = 37 m, FA = 10° (TA = 1 h 21 min). For both MGRE sequences, the total read-out bandwidth

was kept constant at BW = 100 kHz; 4) a single gradient echo with a FoV of 50 × 19 × 19 mm [3], matrix of 1340 × 512 × 512, yielding a voxel size of ca. 37 μm, acquired at a TE = 17 ms and with TR = 42.85 ms, FA = 12° (TA = 3h12 min), BW = 44.25 kHz; 5) a set of inversion recovery 3D MPRAGE images with voxel size of 200 μm and inversion times TI = 25, 100, 200, 400, 600, 800, 1,000, 1,400, 1800 ms, TR = 2000 ms, FA = 8° (each with TA = 25 min 44 s); 6) multi-slice multi-spin-echo MRI with voxel size 200 μm, TE between 6 and 120 in steps of 6 ms, TR = 1000 ms, same FoV and matrix as for the MPRAGE measurement (TA = 5h7 min); 7) multi-contrast diffusion weighted imaging with voxel size 200 μm, TE = 19 ms, TR = 500 ms and b-values of 50, 100, 300, 600, 1,000, 1500 mm^2/s, applied in 6 spatial directions (TA = 3 h). The on-line calculation tool in Paravision 360 was used to generate maps for the apparent diffusion coefficient.

Image analysis

Parametric maps of the longitudinal and effective transverse relaxation rates were fitted with a steepest-descent Levenberg-Marquardt algorithm. R_2^* maps were generated by fitting the square of the magnitude signal. R_1 maps were generated voxel-wise from the magnitude data. Fits were performed twice, after determining the TI at which the minimum signal was measured. For the first fit, all data points acquired at TI ≤ TI_{min} were assigned a negative sign, for the second fit only datapoints below TI_{min} were assigned a negative sign. The T1-fit that yielded the smallest coefficient-of-variance was chosen for each voxel. T_2 maps were obtained using the extended phase graph modelling as described previously [26].

Quantitative susceptibility maps at 3 T were generated with MEDI+ (http://pre.weill.cornell.edu/mri/pages/qsm.html), as described previously in a multi-centre study [17]. Multi-echo MEDI results were obtained using non-linear analysis of the complex MRI values with the *Fit_ppm_complex_TE* function [27–29], followed by unwrapping with the region growing algorithm, and background field removal by the projection onto dipole fields (PDF) method [30] prior to application of the morphology enabled dipole inversion algorithm [31], with a lambda value of 1,000. The radius of the kernel used for spherical mean value (SMV) correction was 5.

At 14.1 T the same MEDI pipeline, but without self-referencing and with SMV = 0.5 was used to generate QSM for each separately measured vial (non-linear multi-echo combination). Multi-echo results were also combined according to a linear function, from the B0 field obtained with ROMEO [32] (linear multi-echo combination). Finally, we also evaluated QSM results from single echo images using Laplacian unwrapping followed by RESHARP [33] background removal using Tikhonov regularization with a factor of 10^{-3} prior to dipole inversion with the iLSQR algorithm in STI Suite v3.0 (https://people.eecs.berkeley.edu/~chunlei.liu/software.html).

For the 3 T data, regions-of-interest were defined using the first echo of the 600 micron images and the applet "volumeSegmenter" available in Matlab version R2021b (v 9.11). For each vial, the paintbrush tool was used to define a circle placed within the vial in the bottom slice, and the active contour tool was used to define a region-of-interest covering each vial. Next, the binary file, containing one where a vial voxel is present and zeros otherwise, was smoothed with a gaussian 10 voxel smoothing kernel, and finally a 50% threshold was used. The so-called "CSF_Mask" (cerebrospinal fluid mask) used for self-referencing in MEDI+ was defined by drawing a polygon at the center of the container, just below the vial holder, followed by the active control tool and the erode tool, with a radius of 10 and 4 iterations. Mean values for the MRI parameters were extracted for each vial and used for further analysis.

For the 14.1 T data, segmentation of clusters was performed in Matlab (R2018b, The MathWorks Inc). The iron-free clusters were identified in the unwrapped and background corrected phase image acquired with a 0.037 mm voxel-size, after gaussian smoothing with sigma = 2 (using function: *imgauss3filt*) followed by histogram equalization (*histeq*) and thresholding at 0.97. For the images obtained with 0.2 mm voxels, image-modality dependent signal thresholding was carried out to identify the clusters, as described in Results.

Components of the clusters, connected in 3D, were identified with *bwconncomp,* considering 26 connected neighbouring voxels (voxels with a shared side or corner), followed by *regionprops3* to approximate the size of each cluster by a sphere with the same volume, and obtain the equivalent sphere diameter. Mean values for the MRI parameters were extracted for the clusters and voxels classified as background. The QSM values in the background was used as a reference value for the measurements carried out at 14.1 T.

To evaluate the relationship between the measured parameters (VSM, qMRI parameters, number of clusters found) and the iron concentration in the samples, to determine the molar susceptibility χ_M, linear regression analysis was performed using *fitlm*, and the 95% confidence interval was evaluated with *predict* in Matlab version R2021a (v 9.10).

To identify voxels where static dephasing and dynamic averaging occurred, the magnitude decay data was fitted voxel-wise by a stretched exponential function [34]:

$$S(TE) = S_0 \cdot e^{-\frac{\left(TE \cdot R_2^{*,eff}\right)^b}{b}} \quad (1)$$

where TE is the echo time, S_0 is the magnitude at a TE = 0, $R_2^{*,eff}$ is the effective relaxation rate, and b is the stretching factor yielding b = 1 for a mono-exponential function and b = 2 for a Gaussian function. Voxels with b > 1.9 were segmented and assigned to the "static dephasing" category, and voxels with 0.6 < b < 1.4 to the "dynamic averaging" category.

Results

Vibrating sample magnetometry

The change in magnetization with decreasing temperature followed a Curie-Weiss relationship, and the Brillouin function was used to fit the change in magnetization with the external field (Figure 1). The magnetization of free iron was markedly stronger than that of the clustered iron. The magnetization of the samples was saturated at applied magnetic fields of ±4 T.

The iron-solution, which is available as a reference standard for atomic absorption spectroscopy yielded a magnetic moment of 5 ± 0.2μ_B (expressed per iron atom in units of the Bohr magneton, μ_B =

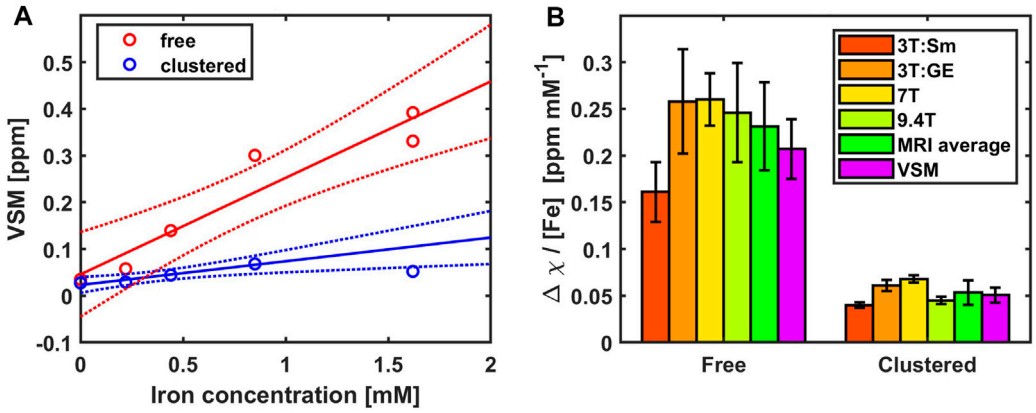

FIGURE 2
Validation of MRI results with vibrating sample magnetometry (VSM) and MRI. **(A)** VSM susceptibility values of the phantom materials increased linearly with iron concentration for the free iron samples (red), yielding a slope of 207 ± 32 ppb mM^{-1} iron (adjusted coefficient of determination = 0.89, p = 0.00298). The samples containing clustered iron (blue) at concentrations < 1 mM yielded a linear increase of 50.7 ± 8.0 ppb mM^{-1} iron (adjusted coefficient of determination = 0.929, p = 0.0238) and an offset of 23 ± 4 ppb. The 95% confidence interval of the linear fits are shown as dotted lines. **(B)** The results obtained with VSM are compared with the molar susceptibility determined in a multi-centre MRI study [17] where free and clustered iron samples were measured at 3T (Sm, Siemens; GE, General Electrics), 7T and 9.4T. The average across the four scanners compares favourably with the results obtained using VSM.

$9.274.10^{-24}$J/T) from the Brillouin function fit, which corresponds well with iron in its Fe^{3+} oxidation form (five electrons in shell 3 days).

The alginate embedding of the phantom material also contained small amounts of Gadolinium (30 μM), with significantly lower influence on the saturation magnetization than iron (60%–1000% lower for free iron and 6%–300% for clustered iron). It was not possible to perfectly disentangle the influence of the two and quantify the magnetic moment of each type of ion. As an estimate, the samples containing free iron had a magnetic moment in the range of about 3–4.5 μ_B, while in the samples containing clustered iron, lower values of ca. 1 μ_B were observed. The data showed a tendency towards a decrease in magnetic moment with increasing iron concentrations.

The total susceptibility in emu/g, measured at the saturation level and converted to the SI-unit ppm for each sample, was used as a global measure of magnetization of the samples containing the phantom materials (Figure 2). The total magnetization increased linearly with iron concentration for the free iron samples, yielding a molar susceptibility of 207 ± 32 ppb mM^{-1} iron (adjusted coefficient of determination = 0.89, p = 0.00298) and an offset, which was not significantly different from zero (46 ± 33 ppb). Exclusion of the highest iron concentration yielded 326 ± 45 ppb mM^{-1} iron (adjusted coefficient of determination = 0.946, p = 0.0182) and an offset of 10 ± 22 ppb. The fit for the clustered iron including all concentrations was non-significant, since the magnetization measured for the clusters with the highest iron concentration was lower than at the lower concentrations. Excluding this observation yielded a χ_M of 50.7 ± 8.0 ppb mM^{-1} iron (adjusted coefficient of determination = 0.929, p = 0.0238) and an offset of 23 ± 4 ppb. One may speculate that at higher concentrations antiferromagnetic coupling occurs within the clusters, which could explain the relatively low magnetization found in the sample with clustered iron. Such a tendency could possibly also be found, since the increase in magnetization measured at the three lowest concentrations was linear, while the magnetization at the highest concentration deviated slightly from predictions based on the lowest three concentrations.

MRI at 3 T

R_2* and QSM maps were obtained from GRE MRI acquisitions at 3 T using isotropic 0.6 mm voxel sizes and compared for different batches of clustered iron with a 1.6 mM iron concentration and the same iron load (8.3 μg Fe/mg NaPA Figure 3). Batch 1 was used previously in the multi-centre study [17], while Batch 2–4 were made for the present study. The multicentre Batch 1 had homogeneous clusters yielding R_2* values that were similar across voxels (sharper histogram distributions). Batch 2–4 were manufactured after a change of personnel and relative to batch 1, the newer batches had a shift towards higher R_2* and a more than threefold wider distributions of R_2* values. The QSM histograms were more similar across batches, although in the present study Batch 2–4 had a ca. 30% wider distribution and a slightly lower average QSM value than Batch 1. A higher QSM value reflect a stronger coherent shift of the magnetic field within the voxel, and the wider distribution a more prominent field inhomogeneity across the vial. This suggests on the one hand that Batches 2–4 had a more heterogenous distribution of iron, both across and within voxels, and on the other hand, that the batches could be manufactured in a reproducible way.

The vials in Batch 4 had an increasing amount of iron and a fixed amount of polyacrylate (120 mg), while in Batch 2 and 3 each cluster had a fixed iron-to-polyacrylate ratio (of 8.3 μg Fe/mg NaPA). The widths of the QSM histograms were similar at the highest iron concentration while the width of Batch 4 (Figure 4A) was one-third of Batches 2 and 3 for the lowest concentration (Figure 4B). This is consistent with a more homogeneous distribution of iron in presence of large amounts of NaPA, while a non-uniform iron

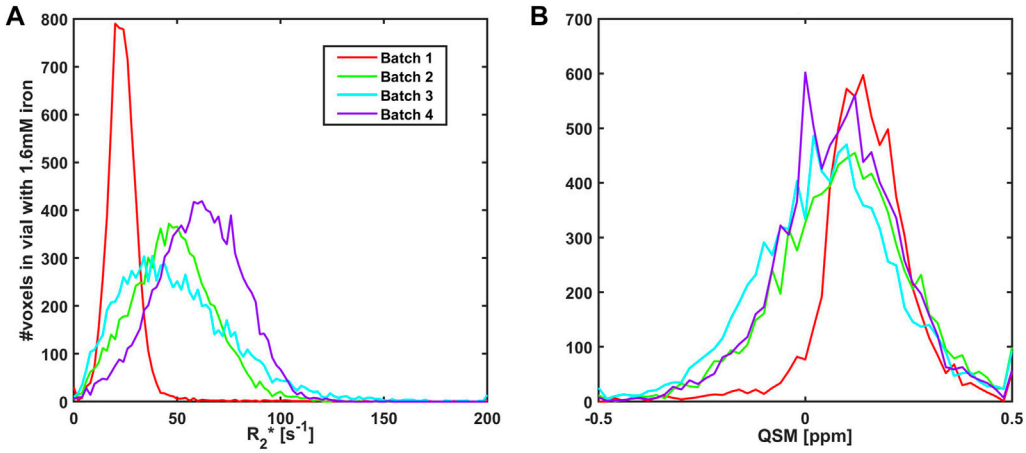

FIGURE 3
Histograms showing the distribution of R_2* **(A)** and QSM **(B)** values at 3T using 0.6 mm voxels in vials containing 1.6 mM iron and 120 mg sodium polyacrylate for different batches yielding an iron-load of 8.3 µg Fe/mg NaPA. Batch 1 (solid red line) was used in a previous multi-centre study [17] while the remaining three batches (green, cyan and violet solid lines, Batch 2–4) were manufactured for the present study. Batch 2–4 had similar R_2* distributions that were more than three times wider than for Batch 1, while the range of QSM values was ca. 30% wider than previously.

distribution is at hand when iron is accumulated in a few clusters in presence of a fixed iron-to-polyacrylate ratio. In both types of samples, a clear shift towards higher QSM values with increasing iron concentrations was observed (Figures 4C, D). The molar susceptibility was 50.6 ± 11.4 ppb mM^{-1} for Batch 4 (adjusted coefficient of determination = 0.863, p = 0.0469). This value is in agreement with results obtained previously in presence of clusters with a varying iron load in the multi-centre study, which was 54 ± 13 ppb mM^{-1} across scanners [17]. With a constant Fe-to-NaPA-ratio and an increasing number of clusters, similar results were obtained for the samples: χ_M = 56.1 ± 6.3 ppb mM^{-1} iron (adjusted coefficient of determination = 0.963, p = 0.0122).

MRI at 14.1 T

The samples containing clusters with a constant iron-to-polyacrylate ratio were further characterized by MRI at 14.1 T using different isotropic voxel sizes between 0.037 and 0.2 mm and different qMRI methods.

At the highest resolution, only single echo images with a TE of 17 ms were available (Figure 5). At this TE, the phase images obtained with iron-filled clusters were wrapped multiple times, which could not be perfectly corrected during QSM processing. The iron free clusters stood out as local, slightly more paramagnetic entities compared to the background exhibiting a broad QSM histogram (0.007 ± 0.007 ppm higher). The equivalent sphere diameter of the iron-free clusters estimated in this image series was 276 ± 230 µm.

With larger voxels of 0.075 mm, the phase images obtained at echo times of 3 ms could be unwrapped, while at 11 ms only the phase images obtained with iron-free samples were completely unwrapped (Figure 6). QSM was obtained with different processing pipelines: single echo analysis, non-linear (MEDI) or linear (ROMEO) multi-echo combination. For the iron-loaded clusters, the unwrapped and background corrected as well as the QSM images looked less blurred at the earlier echo time compared to the later TE where phase unwrapping was incomplete. On the other hand, the weak paramagnetic effect in the iron-free clusters disappeared in the noise at the early TE, and only emerged at the later TE. Non-linear and linear echo combination resulted in QSM results that were comparable to those obtained at the first TE for the iron-loaded clusters, but with reduced noise. For the iron-free clusters, the multi-echo analysis methods yielded results that were similar to the late echo images. The images obtained with MEDI were slightly more eroded, owing to the use of spherical mean value correction.

Similar results were obtained with voxel sizes of 0.2 mm at echo times of 2.5 and 7.5 ms, although the QSM contrast in the iron-free clusters was less prominent even after multi-echo combination (Figure 7).

The QSM maps were zero-referenced to the median QSM value found in voxels with a R_2* value below 30 s^{-1}, that were assumed to be iron-free based on the upper bound of the 95% confidence-interval of the R_2* value found for the sample containing iron-free clusters (Table 1). The QSM histograms were symmetric and narrow for MEDI (Figure 8B). With the pipelines based on the first single echo (Figure 8A) and the linear echo combination (Figure 8C) methods, a second peak appeared at high QSM-values. It was particularly prominent for the vial with the highest concentration and for acquisitions with the smaller voxel sizes yielding a larger within-vial standard deviation than with 0.2 mm voxels (Figures 8D–F), indicating that more of the heterogeneity of the phantom material could be assessed at the higher resolution, which allowed local iron clusters to be resolved. Using these 0.075 mm voxels, a QSM-based molar susceptibility of 43.0 ± 0.2 ppb mM^{-1} (adjusted coefficient of determination = 0.992, p < 0.00257) was obtained with MEDI, and even lower values of 21.8 ± 1.3 and 22.7 ± 1.9 ppb mM^{-1} with the single echo and the ROMEO-based pipelines, respectively. This discrepancy was mirrored by more well-defined QSM values with narrow distributions for MEDI (Figure 8B).

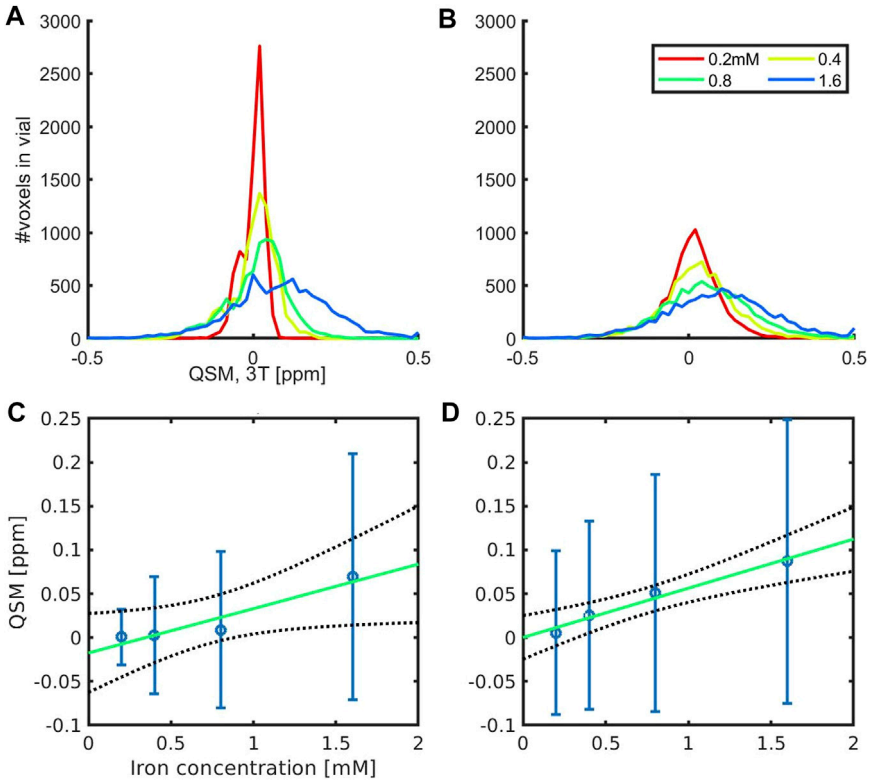

FIGURE 4
QSM histograms **(A,B)** and molar susceptibility, χ_M **(C,D)**, measured at 3 T for two types of phantoms. In Batch 4 **(A,C)**, an increasing amount of iron and a fixed amount of polyacrylate (120 mg) was used, while in Batch 2 **(B,D)** a fixed iron-to-polyacrylate ratio (8.3 µg Fe/mg NaPA) was used **(B,D)**. Results for four different iron concentrations: 0.2 mM (solid red line), 0.4 mM (yellow), 0.8 mM (green) and 1.6 mM (blue) are shown. QSM processing was performed with the MEDI + pipeline using zero-referencing to the surrounding water, and a regularization lambda factor of 1000, in agreement with a previous multi-centre study. The average QSM values and within-vial standard deviations are shown for Batch 4 with varying iron-load per cluster **(C)** and Batch 2 **(D)** with a constant iron-load. Linear regression analysis yielded a χ_M of 50.6 ± 11.4 ppb mM^{-1} iron (adjusted coefficient of determination = 0.863, $p = 0.0469$) and 56.1 ± 6.3 ppb mM^{-1} iron (adjusted coefficient of determination = 0.963, $p = 0.0122$), respectively. The 95% confidence intervals for the linear regression analysis are shown as dotted black lines.

With a voxel-size of 0.2 mm, χ_M was more similar to the results obtained previously at 3–9.4 T: 55.6 ± 0.7 ppb mM^{-1} (adjusted coefficient of determination = 1, $p < 0.0001$) using MEDI, 56.7 ± 1.0 for the single echo approach and 56.0 ± 0.7 ppb mM^{-1} for the linear echo combination.

The R_2* relaxivity was substantially smaller with the 0.075 mm voxels: 42.1 ± 0.7 s^{-1} mM^{-1} (adjusted coefficient of determination = 0.999, $p < 0.0003$) than with 0.2 mm: 100.3 ± 0.6 s^{-1} mM^{-1} (adjusted coefficient of determination = 1, $p < 0.0001$). Taken together, these results suggest that at the higher resolution, the within voxel field is more homogeneous. Depending on the QSM pipeline, sub-regions with different iron-concentrations can be separated. The 0.2 mm voxels are of a size similar to the clusters and may work as a matched filter that allows the combined effect of local iron inclusions within the voxel to be assessed. In this situation, comparable results were obtained across QSM-pipelines. The QSM-based χ_M obtained with the non-linear echo combination available with MEDI was less dependent on the voxel size than the other two pipelines.

The relationship between R_2* and QSM values obtained from the multi-echo gradient images with 0.075 and 0.2 mm voxel sizes (Figure 9) was further evaluated on a voxel-by-voxel basis, for different classes of voxels with specific R_2* values. For this purpose, the range of R_2* values between 1 and 501 s^{-1} were subdivided into 500 bins, and the average QSM value for each bin was extracted. These QSM values reached a plateau for voxels with R_2* values above 200 s^{-1} regardless of voxel size and processing pipeline. In Figure 10, the high variability of R_2* values within the clusters is illustrated.

The QSM values at the plateau were similar across iron concentrations, reaching levels of 175–223 ppb for voxels of 0.2 mm, with similar results at 0.075 mm using MEDI. The single echo and ROMEO pipelines yielded lower average QSM values at the plateau (119–158 ppb).

Below the plateau, a linear relationship between the two qMRI parameters was found. To investigate the increase in R_2* for each ppb change in QSM, voxels with a range of R_2* values between 50 and 150 s^{-1} were selected, yielding an increase of 0.07 ± 0.01 s^{-1} per Tesla for each ppb of change in the measured susceptibility. This value is slightly lower than for spherical particles in the static dephasing regime for which a value of 0.11 s^{-1} T^{-1} ppb^{-1} iron can be predicted [23, 35]. The diffusion weighted MRI signal decreased according to a monoexponential function and the apparent diffusion coefficient was ca. 1.7 μm^2/ms, corresponding to a diffusion length of 5–10 µm for echo-times between 2.5 and 10 ms. In view of the large cluster size, as shown in Figure 5 and analysed in more detail in the next paragraph, one could thus expect that effects caused by

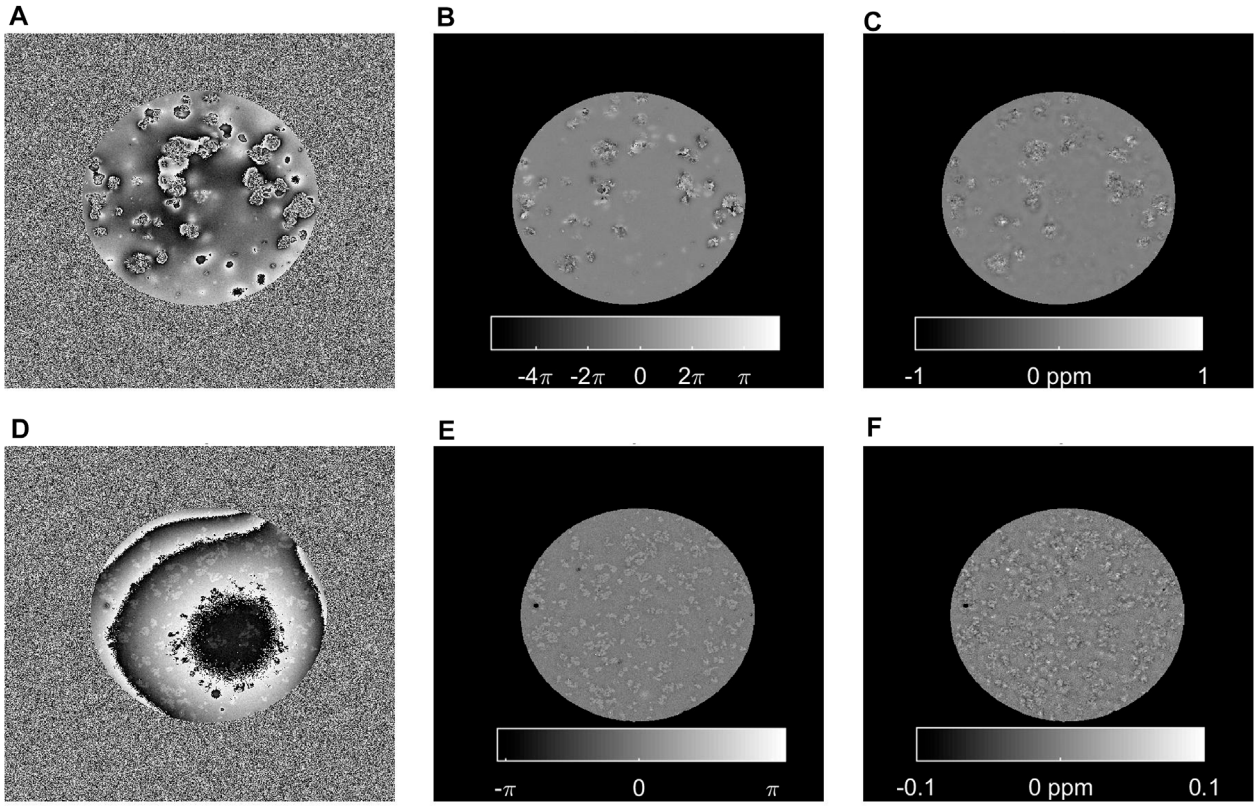

FIGURE 5
Single gradient echo phase and QSM images of samples containing clusters with 0.4 mM iron and 60 mg polyacrylate **(A–C)** or without iron and 120 mg polyacrylate **(D–F)**. High-resolution (voxel size: 0.037 mm), single echo (TE = 17 ms) MRI was performed at 14.T. The raw phase **(A,D)**, measured at this echo time is wrapped multiple times at the locations of the iron-containing clusters, while no large phase jumps are present in proximity of clusters without iron, although a large background field can be noticed. After unwrapping and background field correction, some uncorrected local field deviations can be discerned **(B)** resulting in inhomogeneous QSM images **(C)** for the iron-clusters. On the contrary, in absence of iron, Laplacian unwrapping and RESHARP background field correction reveal small local entities with deviating field **(E)**, corresponding to the iron-free sodium polyacrylate clusters that are more paramagnetic (0.007 ± 0.007 ppm) than the surrounding voxels **(F)**.

static dephasing can be observed. However, the non-uniform spatial distribution of iron within the clusters, and the large voxel-sizes used may impede observation of such effects. Along these lines of thought, we identified voxels that exhibited dynamic averaging and static dephasing effects according to (Eq. 1) (Figure 10). Of these voxels, only 14% or less were located within the clusters, as defined by a 0.2 ppm QSM cut-off value in the MEDI images. Within the clusters, QSM values were similar, while R_2* varied greatly (corresponding with the results in Figure 9). This observation is consistent with an overall shift in the magnetic field, combined with a high (root-mean-squared) variation in the magnetic field within the voxels located inside the clusters. Possibly, these QSM results reflect the saturation effect observed with VSM at the highest iron concentration, caused by locally high levels of iron agglomeration.

Segmentation of clusters and qMRI results with 0.2 mm voxel size

Segmentation of clusters was performed using four different image modalities, acquired with a voxel size of 0.2 mm: quantitative T_2-maps, T_1-weighted MRI, and quantitative R_2*-maps. Since the cluster size can depend on the cut-off used, we chose various cut-offs based on image intensity histograms (Figure 11) observed with the 0.8 mM sample, which had the highest susceptibility in the VSM measurement, and with QSM maps at the plateau values determined in Figure 9. The qMRI values inside the clusters, as well as the cluster size, expressed as the diameter of a sphere with the same volume as the segmented clusters, were determined (Table 1).

Using the T_2-maps, the hydrogel clusters without iron were segmented as voxels with a T_2 value above 180 m, while iron-containing clusters were identified as voxels with T_2 below 50 m. For reasons of the B_1 (in)homogeneity of the coil used, only the most central slices were analysed (15 slices covering 3 mm along the axial field-of-view). Without iron, the contrast difference between the hydrogel and its surrounding was just about discernible while the iron-loaded clusters showed a stronger contrast difference (Figure 12). The size of the segmented clusters was 248 ± 335 μm, while the iron-loaded clusters appeared larger in the quantitative T_2 images reaching sizes around 500 μm (Table 1). At the highest concentration, the clusters could not be separated well and appeared as a mixture of very small and a few very large clusters. Despite the rather crude 0.2 mm spatial sampling, iron-free clusters had a size that corresponded with the size of 276 ± 230 μm determined using 37 μm voxels (shown in Figure 5).

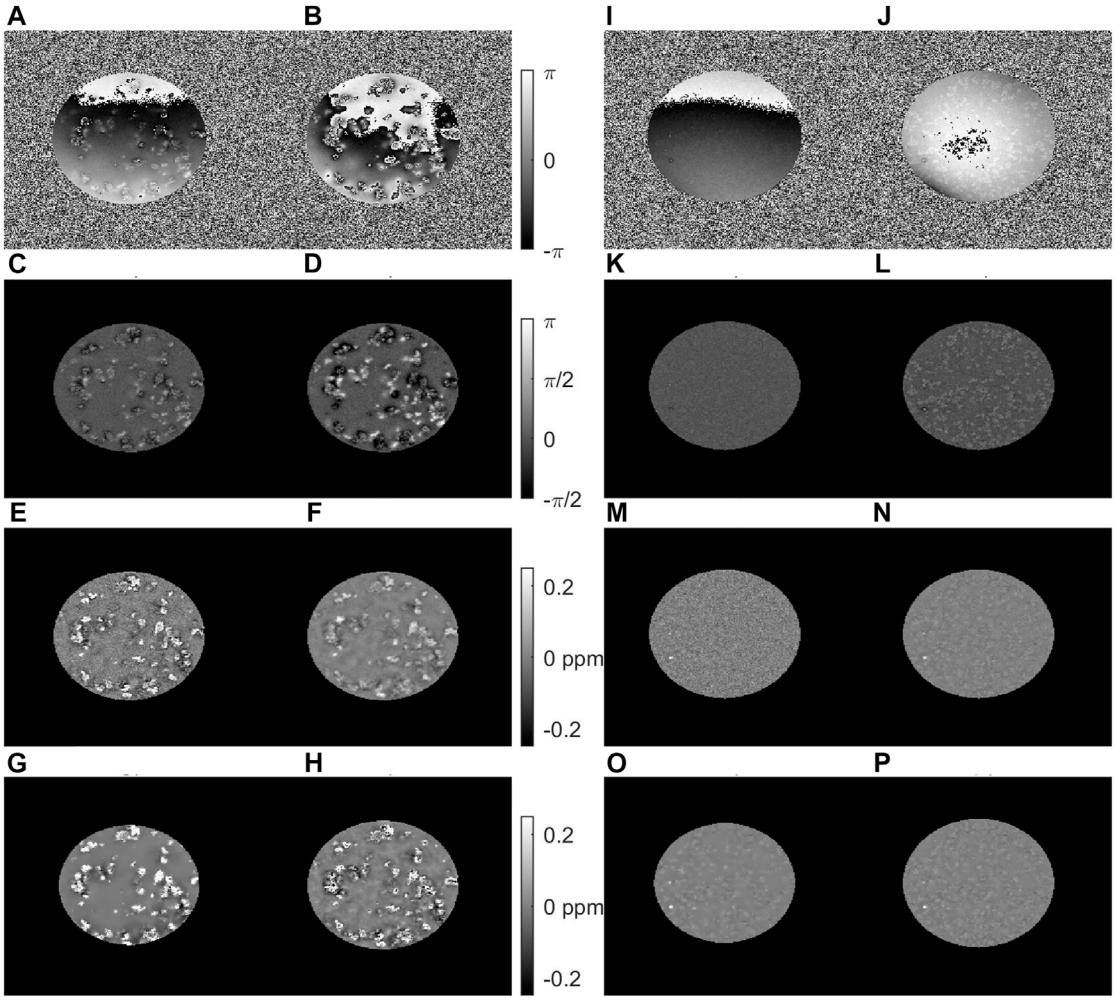

FIGURE 6
Results from multi gradient echo imaging of samples containing clusters with 0.4 mM iron and 60 mg polyacrylate **(A–H)** or without iron and 120 mg polyacrylate **(I–P)** measured at 14.1 T with 0.075 mm voxels. The raw phase **(A,B)** and **(I,J)**, and the phase after Laplacian unwrapping and RESHARP background field correction (c-d, k-l) are shown at TE = 3 ms **(A,C,I,K)** and TE = 11 ms **(B,D,J,L)**. QSM results for single echo analysis at TE = 3 ms **(E,M)**, and TE = 11 ms **(F,N)** and multi-echo analysis using nonlinear echo combination in MEDI **(G,O)** and linear echo-combination in ROMEO **(H,P)** are shown. Some issues linked with insufficient phase unwrapping in proximity of iron-loaded clusters at the later echo time yield a more blurred appearance of the clusters in the QSM images obtained with single echo analysis, compared to the early echo time and the echo combination methods. In iron-free clusters, the small paramagnetic effect that could be detected at a higher resolution (Figure 5) can still be discerned at the late echo time and after echo-combination.

A higher number of clusters could be observed in the T_1-weighted images and the R_2*-maps, since good image quality could be obtained across a larger axial field-of-view of 19.2 mm.

In the T_1-weighted image acquired with an inversion time of 800 m, the contrast between iron-loaded clusters and the surrounding was high (Figure 13). The T_1 weighted image and a cut-off of 20 a.u. yielded cluster sizes around 400 µm that were smaller and had smaller standard deviations than in the T_2-map. The number of clusters detected with the highest cut-off value increased linearly, yielding an iron-dependent cluster density of 9.0 mm^{-3} mM^{-1}+1.2 (DoC:0.967, $p < 0.0112$). Within the segmented clusters there was no change in the longitudinal relaxation rate R_1 with increasing iron concentration.

Cluster segmentation using the R_2*-maps was performed by thresholding at 100, 200 and 450 s^{-1} (Figure 14). The average cluster size did not increase significantly with iron concentration and varied largely reaching sizes of 1–1.2 mm because of insufficient separation between clusters. This led to large standard deviations for the cluster size, especially at the highest iron concentration (Table 1). Using the highest cut-off value there was a tendency towards a linear increase in the number of clusters with iron-concentration, yielding a cluster density of: 10 mm^{-3} mM^{-1}+1.3 (DoC:0.814, $p < 0.064$). At none of the cut-offs, an increase in the R_2* relaxation rate with increasing iron concentrations was found. The same increase in cluster density was obtained from the QSM maps obtained with the linear echo combination and a cut off of 0.4 ppm.

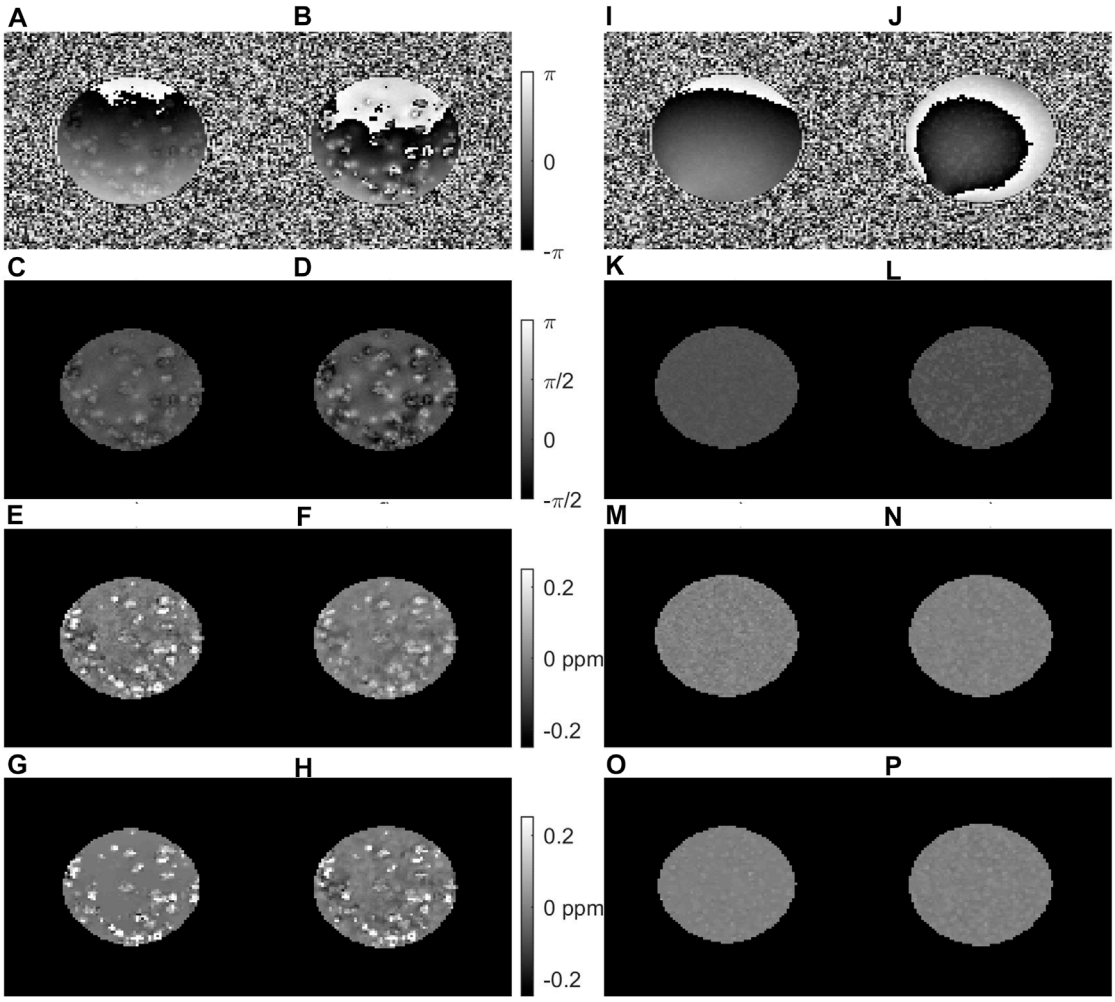

FIGURE 7
Results from multi gradient echo imaging of samples containing clusters with 0.4 mM iron and 60 mg polyacrylate **(A–H)** or without iron and 120 mg polyacrylate **(I–P)** measures at 14.1 T with 0.2 mm voxels. The raw phase **(A,B)** and **(I,J)**, and the phase after Laplacian unwrapping and RESHARP background field correction **(C,D,K,L)** are shown at TE = 2.5 ms **(A,C,I,K)** and TE = 7.5 ms **(B,D,J,L)** with the corresponding QSM results for single echo analysis **(E,F,M,N)**, non-linear MEDI **(G,O)** and linear ROMEO **(H,O)** multi-echo combination. Similar to the results obtained with 0.075 voxels (Figure 6), the QSM contrast is suppressed at the later echo time in iron-loaded clusters, while the multi-echo QSM processing pipelines yield similar contrast.

Discussion

The availability of well-characterized phantoms suitable to assess the many factors influencing quantification are fundamental to facilitate clinical use of quantitative MRI methods, but pose some challenges, especially if the aim is to mimic tissue microstructure [36]. In the case of quantitative susceptibility mapping (QSM) with MRI, such phantoms are of value since many factors, related to the MRI measurement, on one hand, and the processing pipeline on the other hand influence the level of accuracy and precision that can be achieved. The use of tissue-mimicking phantom materials allows to assess the influence of each factor in detail in a setting that should be as realistic as possible, given the complexity of MRI signals arising from the tissue *in vivo*.

QSM is based on the successful acquisition of high quality phase images, obtained using a fully spoiled gradient-echo MRI sequence. The quality of the phase images depends on the available signal-to-noise ratio in the magnitude images, and therefore on factors like the magnetic field strength at which the measurement is carried out as well as the echo-time and voxel size used for image acquisition. Using MRI, the measured signal phase is assumed to evolve linearly with the echo-time, but the phase values will be aliased into the $\pm\pi$ range during image acquisition. Provided that the range of susceptibility values that will be encountered within the tissue is known, the echo time—or in case of multi-echo sequences: the inter-echo delay time—can be used as a scaling factor to achieve an "adequate" amount of phase aliasing. Just how much aliasing that can be tolerated depends on the type of unwrapping used during QSM processing. Unwrapping [32, 37–42] can go astray if the echo-time is too long and/or if the tissue susceptibility differences are too large, which for instance can happen in presence of local tissue bleedings [41]. Others have reported echo-time dependence of QSM results [43], suggesting the presence of non-linear phase evolution that also may need consideration.

TABLE 1 Size and qMRI values of hydrogel clusters. Clusters were identified on different imaging modalities acquired with an isotropic voxel size of 0.2 mm at 14.1 T. The cluster size (in μ m) was expressed as the diameter of an equivalent sphere with the same volume as the cluster. The observed average and standard deviation (SD) relaxation rates: R_2, R_1, and R_2* and QSM values (from the first echo) within the segmented clusters are listed for different iron concentrations. [a]The iron-free clusters could only be reliably segmented in the T_2-maps, therefore the global average within the vial is shown for T_1 and R_2* and QSM. The standard deviations (SD) for the cluster size and the qMRI values are indicated in parentheses.

Cluster size [μ m]					qMRI value inside cluster				
Size in T_2 maps with cutoff: 180/50 ms					**R_2 values [s^{-1}]**				
0 mM	**0.2 mM**	**0.4 mM**	**0.8 mM**	**1.6 mM**	**0 mM**	**0.2 mM**	**0.4 mM**	**0.8 mM**	**1.6 mM**
248 (335)	475 (184)	475 (250)	496 (370)	248 (1,106)	4.9 (0.5)	24.9 (3.8)	28.1 (6.3)	28.3 (6.1)	30.3 (7.5)
Size in T_1 weighted MRI with cutoff: 20 [au]					**R_1 values [s^{-1}]**				
0 mM	**0.2 mM**	**0.4 mM**	**0.8 mM**	**1.6 mM**	**0 mM**	**0.2 mM**	**0.4 mM**	**0.8 mM**	**1.6 mM**
-	394 (188)	394 (191)	394 (229)	358 (266)	0.50[a] (0.07)	1.31 (0.23)	1.46 (0.40)	1.51 (0.42)	1.58 (0.39)
Size in R^*_2 maps with cutoff: 200 s^{-1}					**R^*_2 values [s^{-1}]**				
0 mM	**0.2 mM**	**0.4 mM**	**0.8 mM**	**1.6 mM**	**0 mM**	**0.2 mM**	**0.4 mM**	**0.8 mM**	**1.6 mM**
-	424 (216)	394 (303)	394 (513)	313 (1,638)	7.7[a] (7.7)	288 (89)	342 (136)	343 (135)	359 (146)
Size in QSM with cutoff: 0.2 ppm					**QSM values [ppm]**				
0 mM	**0.2 mM**	**0.4 mM**	**0.8 mM**	**1.6 mM**	**0 mM**	**0.2 mM**	**0.4 mM**	**0.8 mM**	**1.6 mM**
-	394 (168)	394 (214)	424 (375)	248 (846)	0.000 0.011	0.254 (0.042)	0.289 (0.069)	0.295 (0.073)	0.308 (0.087)

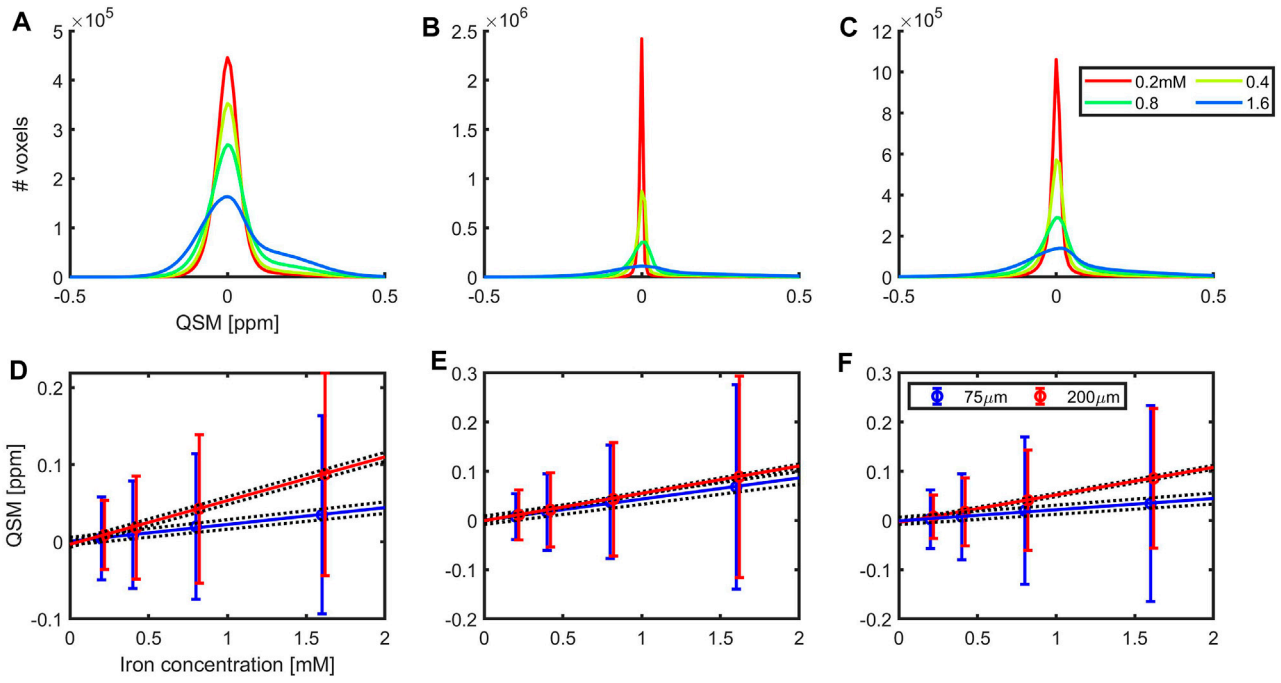

FIGURE 8
QSM histograms of results obtained at 14.1 T with 0.075 mm voxels **(A–C)** and molar susceptibility **(D–F)** for vials containing clusters with a fixed iron-to-polyacrylate ratio (8.3 µg Fe/mg NaPA) with iron concentrations of: 0.2 mM (solid red line), 0.4 mM (yellow), 0.8 mM (green) and 1.6 mM (blue). QSM processing was performed with the first single echo **(A,D)**, non-linear MEDI **(B,E)** or linear ROMEO **(C,F)** echo combination. The average QSM values and within-vial standard deviations are shown for data acquired with a 0.075 and 0.2 mm voxel size. The χ_M was more similar across voxel-sizes with nonlinear MEDI-based echo combination than with the other two processing pipelines.

Besides phase unwrapping, unwanted background field components [9, 33, 44–47]need to be removed prior to the final dipole inversion step [20, 48–50] required to obtained the final QSM results. As an alternative, one-step QSM approaches, which utilize combined unwrapping and background removal can be used [51–53]. Other emerging QSM techniques are based on total field

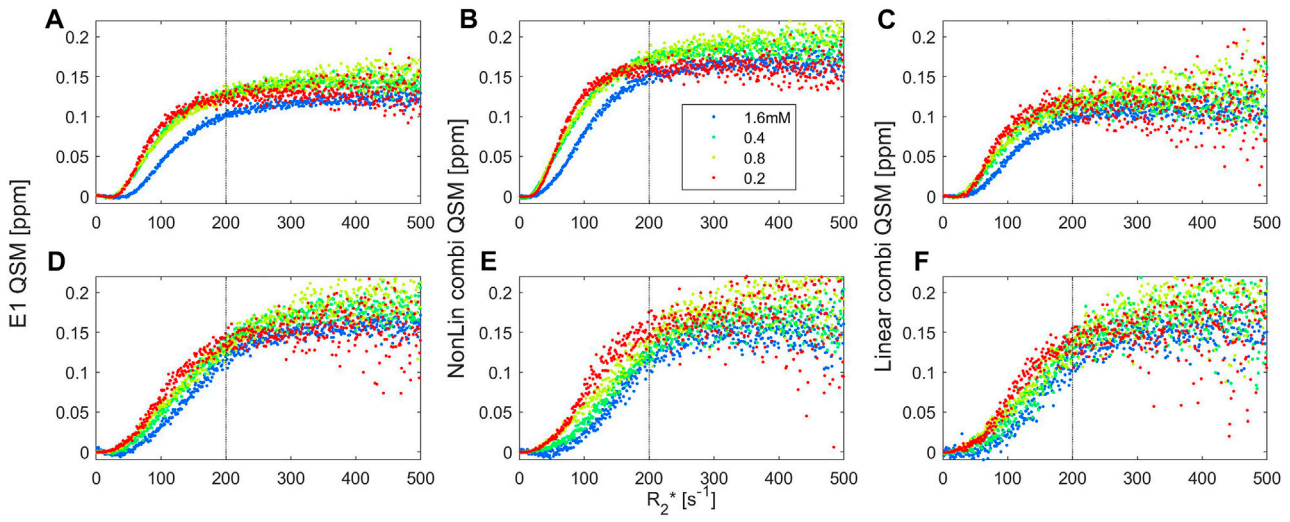

FIGURE 9
Relation between QSM values for voxels with a defined R_2* value between 1 and 501s^{-1}, subdivided into 1 s^{-1} bins. The images were obtained by multi-echo GRE using 0.075 mm **(A–C)** and 0.2 mm **(D–F)** voxel sizes for samples with a fixed iron-to-polyacrylate ratio (8.3 μg Fe/mg NaPA) and a total iron concentration of 0.2 (red dots), 0.4 (green), 0.8 (yellow) or 1.6 mM (blue). QSM values were obtained through single-echo analysis at the first echo time **(A,D)**, and by multi-echo analysis based on nonlinear echo combinations in MEDI **(B,E)** or by linear echo combination from the field map obtained with ROMEO **(C,F)**. A linear relationship between QSM and R_2* values between 50 and 150 s^{-1} and a plateau above 200–250 s^{-1} are found for all iron concentrations, voxel sizes and QSM processing pipelines.

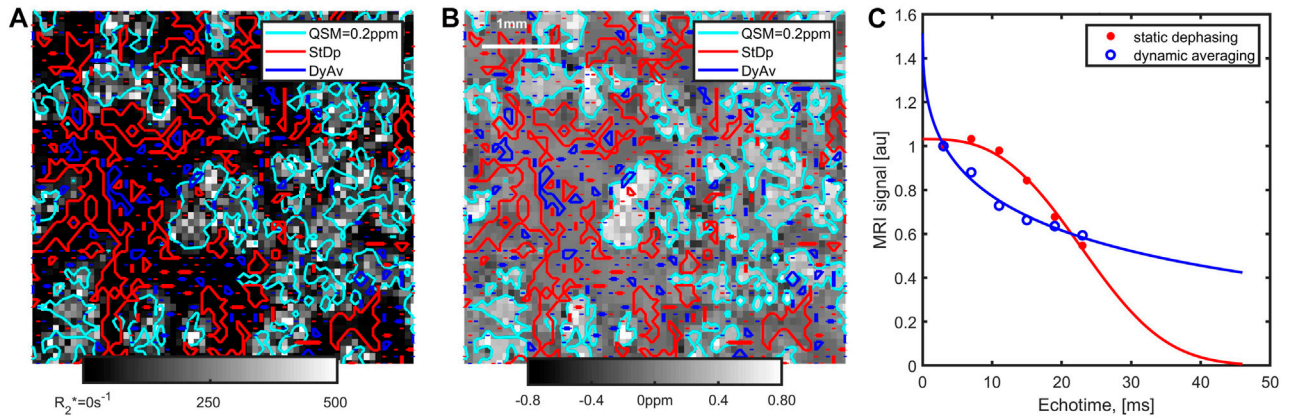

FIGURE 10
Zoomed-in views of the R_2* **(A)** and MEDI-QSM **(B)** observed with 0.075 voxels for the sample with 1.6 mM iron. The cyan iso-contour lines for a QSM value of 0.2 ppm are outlined on both images. On the R_2* maps, the large variability in the local R_2* values within the clusters can be noted (cfr Figure 9). Several voxels, mainly located outside the clusters, exhibit static dephasing behaviour, and others show evidence of dynamic averaging, as further evidenced in the **(C)** time-series showing the average magnitude signal within segmented voxels.

inversion [54] and deep learning approaches [55]. Besides the QSM processing pipeline itself, other factors such as the type of coil-combination algorithm [56, 57] or brain-tissue masking method employed [58] can influence quantification [21].

One possibility to assess the influence of such factors is to perform *in vivo* measurements of healthy subjects and compare the obtained QSM results in different brain regions with expected non-haeme tissue iron concentration. The mathematical expression describing the expected age-dependent increase in tissue iron [18] lends itself well for such comparisons of the measured QSM-contrast in the healthy human brain. A method that quantifies the iron-dependent QSM-contrast k_{Fe}, (unit [ppb/[μg/g]) has been made available for the QSM challenge 2016 data and can be adapted for use at individual sites [21, 59]. However, in case of multi-centre studies, such assessments may require that volunteers travel between sites to assure the protocols are comparable. Other issues can arise if several different types of acquisition protocols are to be assessed, since there is an upper limit to the total scan duration, that is,

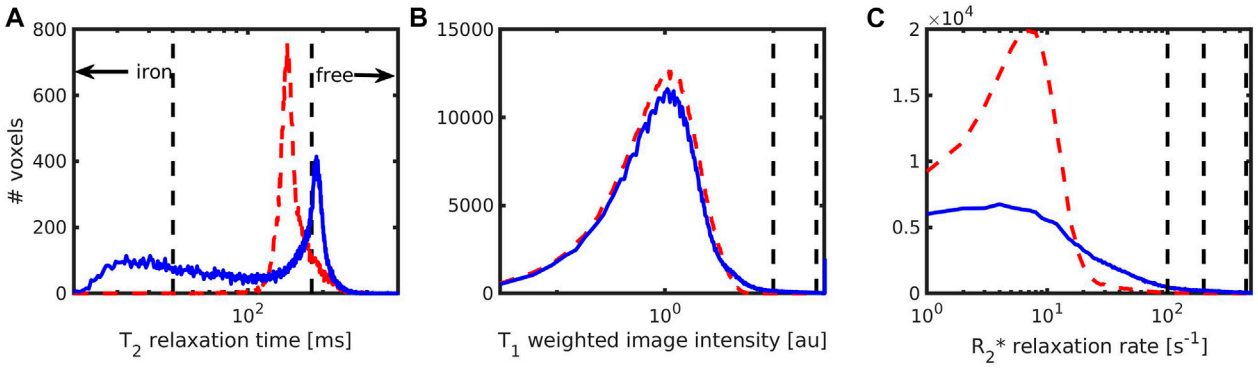

FIGURE 11
Intensity histograms for samples without (0mM, red dashed line) and with (0.8 mM, blue solid line) iron, using three MRI modalities and 0.2 mm voxels measured at 14.1 T. Histograms were obtained from **(A)** T_2-maps **(B)** T_1-weighted MPRAGE images with an inversion time of 800 ms; **(C)** quantitative R_2* maps. The location of the different cut-offs used for segmentation of iron-containing and iron-free clusters are shown as black dashed vertical lines. Note that the iron-free clusters could only be observed in the T_2-maps.

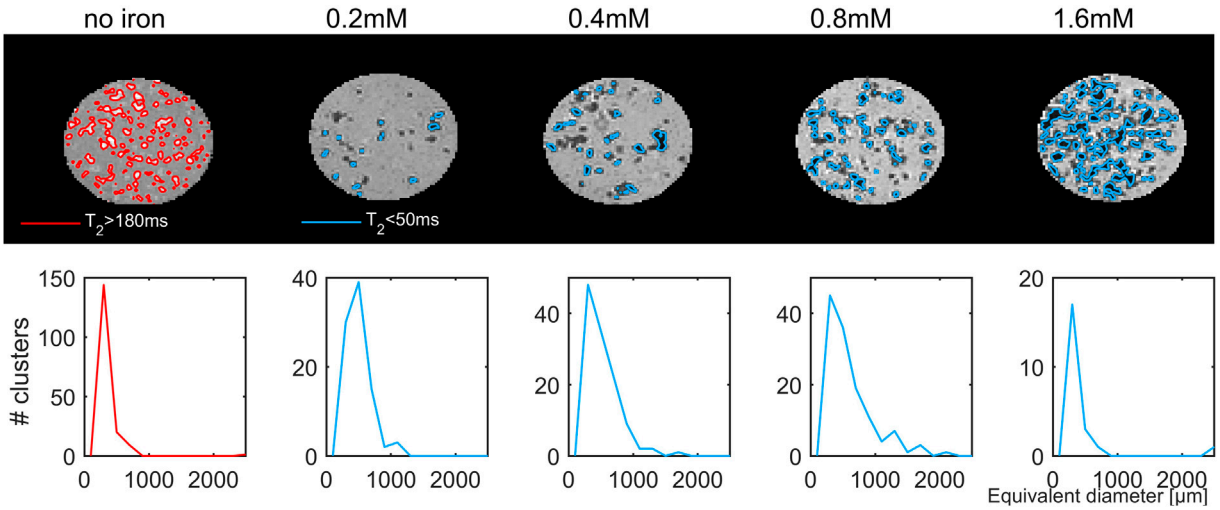

FIGURE 12
Maps (axial view) of the transverse relaxation time, T_2, for samples measured with a voxel size of 200 µm at 14.1 T (upper row). Clusters without iron were identified as voxels with T_2 > 180 ms (red), and clusters with iron T_2 < 50 ms (blue). The corresponding size distributions, expressed as the diameter of a sphere with the same volume as the segmented clusters are shown in the lower row.

acceptable *in vivo*, besides issues related to motion during image acquisition. Therefore, a more practical solution to allow informed decisions based on an iterative optimization process to be made, that includes adjustment of each and single step if needed, is the use of adequate phantoms.

Ideally, the phantom material should reflect the complexity of the tissue and have magnetic properties that are comparable to those found *in vivo*. Today, besides phantoms containing single susceptibility sources [13, 14] more complex mixtures [15], able to mimic more of the complexity present *in vivo*, are available. In a previous multi-center study, we introduced a phantom for QSM that contains iron (available as a standard for atomic absorption spectroscopy), either in form of a homogeneous solution, "free" iron, or as small iron clusters after absorption of the iron in a hydrogel consisting of sodium polyacrylate [17]. The iron concentrations used for the phantom were about half of those typically found for non-haeme iron in brain tissue *in vivo*. The average molar susceptibility that was observed across three magnetic field strengths and four scanners was 0.231 ± 0.047 ppm mM^{-1} and 0.054 ± 0.013 ppm mM^{-1} for the free and clustered iron, respectively. The QSM contrast of the proposed clustered iron thus corresponded to the χ_M for ferritin with an iron-load of 3000 atoms, and falls within the range of 28–72 ppb mM^{-1} iron expected for ferritin in the human brain [19–22].

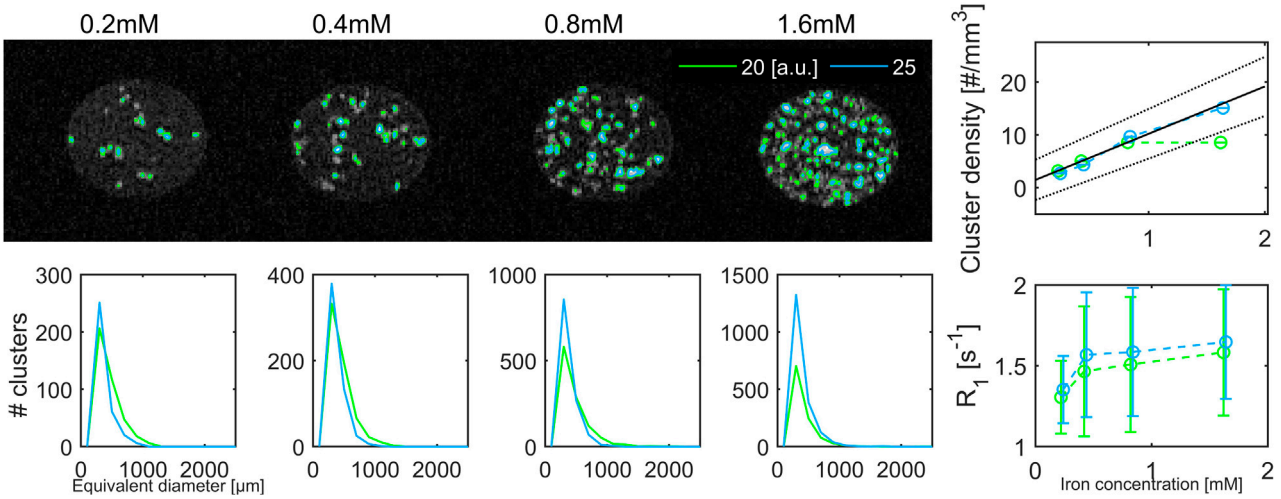

FIGURE 13
T_1-weighted MRI images with an inversion time of 800 ms and a voxel size of 200 μm at 14.1 T. Iron-containing clusters were segmented at two thresholds (20 a.u. green, 25 a.u. blue solid line). The size-distribution for the segmented clusters were similar. The cluster density increased significantly with increasing iron load for clusters segmented with a cut-off of 25 a.u. The corresponding R_1 relaxation rate reached a plateau for iron concentrations of 0.4 mM and above.

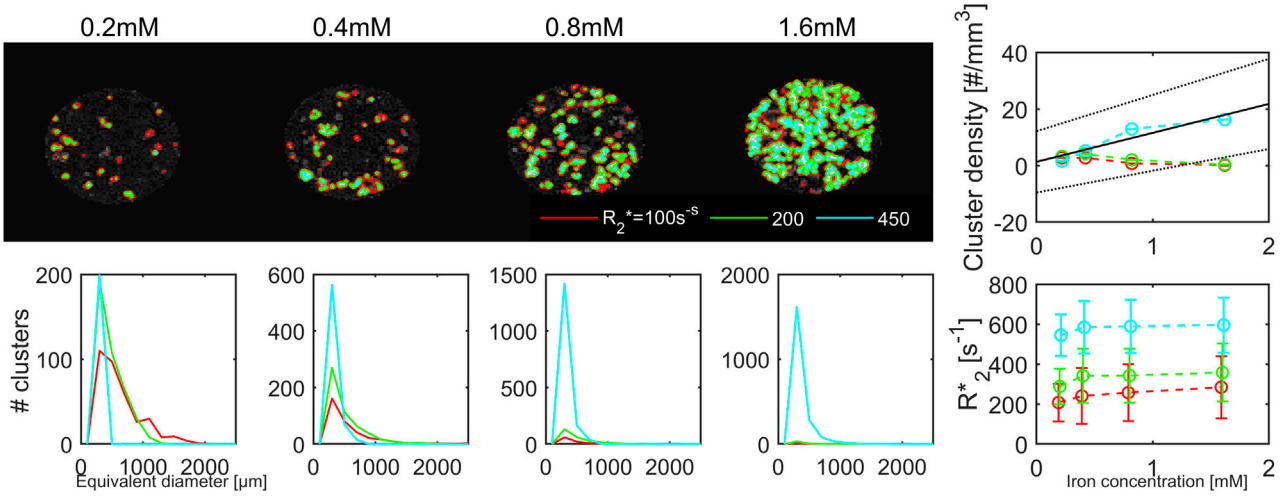

FIGURE 14
Maps of the effective transverse relaxation rate, R_2*, acquired with a voxel size of 200 μm at 14.1 T. Iron-containing clusters were segmented at three thresholds: 100 s^{-1} (red solid line), 200 s^{-1} (green) and 450 s^{-1} (cyan). At the highest threshold there was a tendency for a linear increase in cluster density with increasing iron load. No significant change in R_2* with increasing iron concentrations were observed.

However, in the previous study, validations through magnetometry measurements were lacking. Moreover, details of the clusters, like their size and spatial distribution, had not been obtained, motivating the present work. Another unknown factor was the possibility to manufacture comparable batches of the phantom material. A general feature of the phantom material, that we already had noted in our previous study, is that the spatial distribution of iron clusters can be hard to control during manufacturing but can be assessed "*post hoc*" in R_2* and QSM images. Therefore, we used MRI at 3 T with identical imaging and QSM processing protocols as in the previous study in order to assess reproducibility. The batches manufactured in the present study had higher R_2* values and showed a higher variability in R_2* across the containing vials than previously. The QSM values, on the other hand, were found to be more similar across different batches. These observations underline the importance of the manufacturing process. The size and the spatial distribution of the iron-loaded regions will likely depend on the details of the mixing of iron-loaded poly-acrylate hydrogel and the alginate matrix. At the moment, this is done manually, which can have some drawbacks with respect to reproducibility. When scaling-up the sample preparation, switching to mechanical mixing (for instance by using higher

speed, blade-like stirrers) might help to produce more homogeneous samples.

With regard to stability of the iron clusters, it can be noted that sodium poly-acrylate is a super-absorbent polymer, which can absorb its own mass multiple times (in our case: a volume corresponding to more than 8 times its own weight). This hydrogel has been employed for removal of heavy metal contamination, owing to its anionic carboxylate binding sites [60]. These can coordinate to Fe^{3+} in various configurations at the molecular scale, and thus can stably bind large amounts of iron (15 mM). The reddish-brown colour appearing when mixing the (acidic) iron standard solution with the (basic) poly-acrylate suggests an increase of pH and subsequent formation of hydrolysis and formation of increasingly poorly soluble condensates of $(FeOOH)_x$ aq. up to insoluble $Fe(OH)_3$. The formation of these larger condensates will further prevent the diffusion of iron out into the alginate matrix. Our previous results [17] were obtained during a 3 months' time period, during which the phantom was transported between three laboratories across two continents (in a hand-luggage) and kept at room temperature.

Introducing further variability, we decided to compare two types of phantoms: vials containing a variable amount of iron and fixed amount of NaPA on the one hand and a fixed iron-to-polyacrylate ratio, yielding a fixed amount if iron per cluster and an increasing number of clusters, on the other hand. The first type of phantom corresponds to the one used in our previous study [17], while the second type facilitates observation of single clusters. Regardless of these manipulations, the χ_M results observed were comparable with values between 50 and 56 ppb mM^{-1}, provided that the voxel-size used for MRI acquisition was larger than the size of the clusters.

Although a clear, iron-concentration dependent shift in QSM could be observed, it was accompanied by a large standard deviation across the vial, most likely explained by the large susceptibility difference between the clusters and the alginate surrounding. The standard deviation was particularly large in the phantoms where both the amount of iron and alginate were increased, reflecting that when there is no surplus of polyacrylate, the surrounding alginate remains free from iron, at least to a large extent. The difference in susceptibility between the embedding media and the polyacrylate thence lead to large QSM variability. More fine-scaled variability could be captured when using voxel-sizes that were smaller than the clusters at 14.1T, but also led to a suppression of the observed molar susceptibility. Indeed, with 0.075 voxels, the molar susceptibility derived from the entire vial as a region of interest, was very different from that observed at 3T, especially with the single-echo and ROMEO combination approaches, which had wider QSM histograms than MEDI (Figure 8). Only with a voxel-size of 0.2 mm, which approaches the estimated cluster size, the molar susceptibility at 14.1 T became comparable to the values observed at 3 T with a voxel size of 0.6 mm.

Besides average QSM values, quantifying histogram features could furnish additional, clinically relevant parameters, since generally the distribution of QSM values can be large even within selected anatomical regions-of-interest. Recently Lancione et al [61], showed that the distributions of QSM values observed *in vivo* within iron-containing structures, like the dentate nucleus and the putamen can be quite large (as shown in the Supporting Figure S4 of that publication). These workers report that specific histogram features, like the standard deviation, the 75th and the 90th percentile were useful parameters to distinguish between Parkinsonian and cerebellar multiple system atrophy.

Although we cannot pinpoint the exact cause for the differences between the current and previous batches, one possible contributor may have been differences in the oxygenation state of the iron between batches, besides differences in the actual spatial distribution of the clusters occurring during manufacturing. The exact oxygenation state at hand can change R_2^* yielding greater relaxivity values in presence of ferric than ferrous iron [62, 63]. In addition, ferric iron can fall out and yield a reddish colour. Therefore, it is interesting to note that the clusters generated through the addition of sodium polyacrylate to the iron solution could be visually identified as red dots, which were particularly prominent in the vials containing the highest iron concentration. The change in colour could indicate precipitation of iron inside the hydrogel clusters. However, in order to unambiguously determine the oxygenation state, the use of Mössbauer spectroscopy can be envisaged in future studies [64].

In order to further characterize the phantom material, we used vibrating sample magnetometry, which is a highly accurate and precise technique to assess magnetic properties. Notably, magnetometry has been used previously to assess human tissue [65–69]. Through measurements of the magnetization as a function of temperature, and as a function of the external field, both the type of magnetism and the magnetic moment can be identified. VSM of samples containing the pure iron-solution used for manufacturing the phantom was measured and showed the presence of iron with a magnetic moment of approximately $5\mu_B$, which corresponds to ferric Fe^{3+} iron which has an effective, magnetic moment of $5.92\ \mu_B$[23] when spin-only effects without nuclear couplings are considered.

We furthermore used VSM to ascertain the susceptibility of the phantom material as a whole, since separation of the contributions from the iron and the small amounts of added Gadolinium ions to the alginate embedding was not perfect. The total magnetization of the sample was found to increase linearly with iron concentration, yielding a molar susceptibility of 207 ± 32 ppb mM^{-1} for the free and 50.7 ± 8.0 ppb mM^{-1} for the clustered iron. These values compare favourably with our previous observations in the multi-centre study [17]. Interestingly, the measured magnetic moment in the samples containing clustered iron at the highest concentration was below the value predicted based on concentrations below 1 mM. This indicates that the total signal is not simply the sum of all saturated iron magnetic moments. One may speculate that at higher concentrations antiferromagnetic coupling occurs, which could explain the relatively low magnetization observed in the sample with the highest iron concentration. This effect does not necessarily have to be a solid-state phenomenon. Such phenomenon could arise if the iron is strongly bound in the clusters and subregions with different magnetic moment directions are at hand. As antiferromagnetism, via superexchange, is not a rare phenomenon, we would like to suggest that the reduced saturation is caused by a significant fraction of iron, which are antiferromagnetically coupled on a molecular basis. In line with this, qMRI with 0.075 mm voxels showed that QSM saturates within the clusters, while R_2^* varied strongly, possibly due to locally high levels of iron with different magnetic moments. Antiferromagnetic

coupling has been observed for magnetite composed of highly ordered, alternating ferric and ferrous iron. To better investigate such sub-lattice ordering effects, X-ray diffraction can be performed. Also, ferritin has a highly complex behaviour as observed with magnetometry, allegedly deriving from the presence of superparamagnetism counteracted by anti-ferromagnetic coupling in its core [70]. Antiferromagnetic coupling effects must not necessarily be manifest in our MRI measurements, which were performed at room temperature with long echo-times of a few milliseconds during which diffusion averaging can occur. Therefore, in this respect VSM yielded more precise and detailed information.

Macroscopic MRI properties can be influenced by packing densities. For iron-loaded ferritin aggregated inside liposomes, transverse relaxation occurs at rates in MRI that are 6 times faster than ferritin outside such liposomes [71]. In our previous study using whole-body scanners operating at 3, 7, and 9.4T, we observed an R_2*-related relaxivity which increased linearly with magnetic field strength by 4.00 s^{-1} mM^{-1} T^{-1}, albeit with a (non-significant) intercept of 5.61 s^{-1}. From these numbers, one can predict an R_2* relaxivity of 61.6 s^{-1} mM^{-1} at 14.1 T. The batches manufactured in the present study reached 100 s^{-1} mM^{-1}, consistent with a higher packing density than previously attained.

Segmentation using high thresholds yielded maximal R_2* values of 200–500 s^{-1} within the clusters, which are reminiscent of the range of 155–310 s^{-1} expected for ferritin at 14.1T, based on an increase in R_2' of 0.11 s^{-1} T^{-1} ppb^{-1} iron for spherical particles in the static dephasing regime [23]. On the other hand, in a transition zone surrounding the cluster core, R_2* increased as 0.07 ± 0.01 s^{-1} T^{-1} ppb^{-1} iron, suggesting that averaging effects can occur to a certain extent.

At the highest image resolution used, with an isotropic voxel size of 37 μm, the iron-free clusters had a roundish, snow-flake like appearance with a blurred border. Each cluster occupied a volume that corresponded to a sphere with an equivalent diameter of ca. 250 μm, while after iron-loading the size of the clusters increased to 500–600 μm. To avoid the "blooming-effect" of dephased magnetization in gradient echo images, we complemented observations of the cluster size based on R_2* and QSM images with measurements using spin-echo and short-echo time inversion-recovery MRI. Overall, these techniques yielded similar results regarding the cluster size.

Since the amount of the polyacrylate hydrogel always matched the volume of the iron solution added to the samples, we expected each cluster detected to have the same iron-load, and that the cluster density depends on the iron concentration. The result of the image analysis with voxel sizes of 200 μm was in line with this hypothesis but only when high thresholds were used for cluster segmentation. In that case, the cluster density increased with increasing iron concentration. The qMRI parameters observed within the clusters were the same across all samples.

Taken together, these results point towards iron-loaded clusters with molar susceptibility and R_2* values reminiscent of ferritin *in vivo*. Reproducibility of QSM results across scanners, batches, and phantom types was within 12% and compared well with results using vibrating sample magnetometry. Using 0.2 mm voxel sizes, the clusters could be delineated and separated from the surrounding, while with voxels of 0.075 mm and below, a heterogeneous spatial distribution of iron with saturated QSM values within single clusters emerged. Around the clusters, heterogeneous MRI signal behaviour, with voxels exhibiting static dephasing effects as well as dynamic averaging could be identified. In future studies, it would be of interest to push the spatial resolution further, even more towards the diffusion length to better assess the impact of such local iron inclusions on MRI.

Data availability statement

The raw data supporting the conclusion of this article will be made available by the authors, without undue reservation.

Author contributions

GH: Conceptualization methodology investigation formal analysis software (MRI) writing—original draft, EG: Methodology investigation formal analysis software (VSM) writing—review and editing EC: formal Analysis (MRI 3T) writing—review and editing JE. resources validation writing—review and editing KS: funding acquisition, supervision writing—review and editing. All authors contributed to the article and approved the submitted version.

Funding

We gratefully acknowledge the EU-LACH Grant #16/T01-0118, and ERC Advanced Grant #834940 for supporting this work.

Conflict of interest

The authors declare that the research was conducted in the absence of any commercial or financial relationships that could be construed as a potential conflict of interest.

Publisher's note

References

1. Loureiro JR, Himmelbach M, Ethofer T, Pohmann R, Martin P, Bause J, et al. *In-vivo* quantitative structural imaging of the human midbrain and the superior colliculus at 9.4T. *Neuroimage* (2018) 177:117–28. doi:10.1016/j.neuroimage.2018.04.071

2. Tuzzi E, Balla DZ, Loureiro JRA, Neumann M, Laske C, Pohmann R, et al. Ultra-high field MRI in Alzheimer's disease: Effective transverse relaxation rate and quantitative susceptibility mapping of human brain *in vivo* and *ex vivo*

compared to histology. *J Alzheimer's Dis* (2020) 73(4):1481–99. doi:10.3233/JAD-190424

3. Ghassaban K, Liu S, Jiang C, Haacke EM. Quantifying iron content in magnetic resonance imaging. *Neuroimage* (2019) 187:77–92. doi:10.1016/j.neuroimage.2018.04.047

4. Biondetti E, Rojas-Villabona A, Sokolska M, Pizzini FB, Jäger HR, Thomas DL, et al. Investigating the oxygenation of brain arteriovenous malformations using quantitative susceptibility mapping. *Neuroimage* (2019) 199:440–53. doi:10.1016/j.neuroimage.2019.05.014

5. Hametner S, Endmayr V, Deistung A, Palmrich P, Prihoda M, Haimburger E, et al. The influence of brain iron and myelin on magnetic susceptibility and effective transverse relaxation - a biochemical and histological validation study. *Neuroimage* (2018) 179:117–33. doi:10.1016/j.neuroimage.2018.06.007

6. Stüber C, Morawski M, Schäfer A, Labadie C, Wähnert M, Leuze C, et al. Myelin and iron concentration in the human brain: A quantitative study of MRI contrast. *Neuroimage* (2014) 93(1):95–106. doi:10.1016/j.neuroimage.2014.02.026

7. Wharton S, Bowtell R. Effects of white matter microstructure on phase and susceptibility maps. *Magn Reson Med* (2015) 73(3):1258–69. doi:10.1002/mrm.25189

8. Deistung A, Schweser F, Wiestler B, Abello M, Roethke M, Sahm F, et al. Quantitative susceptibility mapping differentiates between blood depositions and calcifications in patients with glioblastoma. *PLoS One* (2013) 8(3):e57924. doi:10.1371/journal.pone.0057924

9. Schweser F, Atterbury M, Deistung A, Lehr BW, Sommer K, Reichenbach JR. Harmonic phase subtraction methods are prone to B1 background components. *Proc Intl Soc Mag Reson Med* (2011) 37(9):2657.

10. Tuzzi E, Loktyushin A, Zeller A, Pohmann R, Christoph L, Scheffler K, et al. Exploration of cortical ß-Amyloid load in Alzheimer's disease using quantitative susceptibility mapping at 9.4T. Available at: https://www.medrxiv.org/content/10.1101/2022.09.23.22280290v1 (Accessed September 25, 2022).

11. Langkammer C, Schweser F, Shmueli K, Kames C, Li X, Guo L, et al. Quantitative susceptibility mapping: Report from the 2016 reconstruction challenge. *Magn Reson Med* (2018) 79(3):1661–73. doi:10.1002/mrm.26830

12. Marques JP, Meineke J, Milovic C, Bilgic B, Chan K, Hedouin R, et al. QSM reconstruction challenge 2.0: A realistic *in silico* head phantom for MRI data simulation and evaluation of susceptibility mapping procedures. *Magn Reson Med* (2021) 86(1):526–42. doi:10.1002/mrm.28716

13. Olsson E, Wirestam R, Lind E. MRI-based quantification of magnetic susceptibility in gel phantoms: Assessment of measurement and calculation accuracy. *Radiol Res Pract* (2018) 2018:1–13. doi:10.1155/2018/6709525

14. Deh K, Kawaji K, Bulk M, Van Der Weerd L, Lind E, Spincemaille P, et al. Multicenter reproducibility of quantitative susceptibility mapping in a gadolinium phantom using MEDI+0 automatic zero referencing. *Magn Reson Med* (2019) 81(2):1229–36. doi:10.1002/mrm.27410

15. Emmerich J, Bachert P, Ladd ME, Straub S. A novel phantom with dia- and paramagnetic substructure for quantitative susceptibility mapping and relaxometry. *Phys Med* (2021) 88:278–84. doi:10.1016/j.ejmp.2021.07.015

16. Reinert A, Morawski M, Seeger J, Arendt T, Reinert T. Iron concentrations in neurons and glial cells with estimates on ferritin concentrations. *BMC Neurosci* (2019) 20(1):25–14. doi:10.1186/s12868-019-0507-7

17. Gustavo Cuña E, Schulz H, Tuzzi E, Biagi L, Bosco P, García-Fontes M, et al. Simulated and experimental phantom data for multi-center quality assurance of quantitative susceptibility maps at 3 T, 7 T and 9.4 T. *Phys Med* (2023) 110:102590. doi:10.1016/j.ejmp.2023.102590

18. Hallgren B, Sourander P. The effect of age on the non-haemin iron in the human brain. *J Neurochem* (1958) 3(1):41–51. doi:10.1111/j.1471-4159.1958.tb12607.x

19. Chai C, Zhang M, Long M, Chu Z, Wang T, Wang L, et al. Increased brain iron deposition is a risk factor for brain atrophy in patients with haemodialysis: A combined study of quantitative susceptibility mapping and whole brain volume analysis. *Metab Brain Dis* (2015) 30(4):1009–16. doi:10.1007/s11011-015-9664-2

20. Schweser F, Deistung A, Lehr BW, Reichenbach JR. Quantitative imaging of intrinsic magnetic tissue properties using MRI signal phase: An approach to *in vivo* brain iron metabolism? *Neuroimage* (2011) 54(4):2789–807. doi:10.1016/j.neuroimage.2010.10.070

21. Hagberg GE, Eckstein K, Tuzzi E, Zhou J, Robinson S, Scheffler K. Phase-based masking for quantitative susceptibility mapping of the human brain at 9 4T. *Magn Reson Med* (2022) 88(5):2267–76. doi:10.1002/mrm.29368

22. Zheng W, Nichol H, Liu S, Cheng Y-CN, Haacke EM. Measuring iron in the brain using quantitative susceptibility mapping and X-ray fluorescence imaging. *Neuroimage* (2013) 78:68–74. doi:10.1016/j.neuroimage.2013.04.022

23. Duyn JH, Schenck J. Contributions to magnetic susceptibility of brain tissue. *NMR Biomed* (2017) 30(4):e3546. doi:10.1002/nbm.3546

24. Dedman DJ, Treffry A, Candy JM, Taylor GAA, Morris CM, Bloxham CA, et al. Iron and aluminium in relation to brain ferritin in normal individuals and Alzheimer's-disease and chronic renal-dialysis patients. *Biochem J* (1992) 287(2):509–14. doi:10.1042/bj2870509

25. DiResta GR, Lee J, Arbit E. Measurement of brain tissue specific gravity using pycnometry. *J Neurosci Methods* (1991) 39(3):245–51. doi:10.1016/0165-0270(91)90103-7

26. Hagberg GE, Bause J, Ethofer T, Ehses P, Dresler T, Herbert C, et al. Whole brain MP2RAGE-based mapping of the longitudinal relaxation time at 9.4 T. *Neuroimage* (2017) 144:203–16. doi:10.1016/j.neuroimage.2016.09.047

27. Kressler B, de Rochefort L, Liu T, Spincemaille P, Jiang Q, Wang Y. Nonlinear regularization for per voxel estimation of magnetic susceptibility distributions from MRI field maps. *IEEE Trans Med Imaging* (2010) 29(2):273–81. doi:10.1109/TMI.2009.2023787

28. Bernstein MA, Grgic M, Brosnan TJ, Pelc NJ. Reconstructions of phase contrast, phased array multicoil data. *Magn Reson Med* (1994) 32(3):330–4. doi:10.1002/mrm.1910320308

29. de Rochefort L, Brown R, Prince MR, Wang Y. Quantitative MR susceptibility mapping using piece-wise constant regularized inversion of the magnetic field. *Magn Reson Med* (2008) 60(4):1003–9. doi:10.1002/mrm.21710

30. Liu T, Khalidov I, de Rochefort L, Spincemaille P, Liu J, Tsiouris AJ, et al. A novel background field removal method for MRI using projection onto dipole fields (PDF): Improved background field removal method using PDF. *NMR Biomed* (2011) 24(9):1129–36. doi:10.1002/nbm.1670

31. Liu J, Liu T, de Rochefort L, Ledoux J, Khalidov I, Chen W, et al. Morphology enabled dipole inversion for quantitative susceptibility mapping using structural consistency between the magnitude image and the susceptibility map. *Neuroimage* (2012) 59(3):2560–8. doi:10.1016/j.neuroimage.2011.08.082

32. Dymerska B, Eckstein K, Bachrata B, Siow B, Trattnig S, Shmueli K, et al. Phase unwrapping with a rapid opensource minimum spanning tree algorithm (ROMEO). *Magn Reson Med* (2021) 85(4):2294–308. doi:10.1002/mrm.28563

33. Sun H, Wilman AH. Background field removal using spherical mean value filtering and Tikhonov regularization. *Magn Reson Med* (2014) 71(3):1151–7. doi:10.1002/mrm.24765

34. Blümich B, Perlo J, Casanova F. Mobile single-sided NMR. *Prog Nucl Magn Reson Spectrosc* (2008) 52(4):197–269. doi:10.1016/j.pnmrs.2007.10.002

35. Yablonskiy DA, Haacke EM. Theory of NMR signal behavior in magnetically inhomogeneous tissues: The static dephasing regime. *Magn Reson Med* (1994) 32(6):749–63. doi:10.1002/mrm.1910320610

36. Fieremans E, Lee H. Physical and numerical phantoms for the validation of brain microstructural MRI: A cookbook. *Neuroimage* (2018) 182:39–61. doi:10.1016/j.neuroimage.2018.06.046

37. Schofield MA, Zhu Y. Fast phase unwrapping algorithm for interferometric applications. *Opt Lett* (2003) 28(14):1194–6. doi:10.1364/ol.28.001194

38. Cusack R, Papadakis N. New robust 3-D phase unwrapping algorithms: Application to magnetic field mapping and undistorting echoplanar images. *Neuroimage* (2002) 16(3):754–64. doi:10.1006/nimg.2002.1092

39. Karsa A, Shmueli K. Segue: A speedy rEgion-growing algorithm for unwrapping estimated phase. *IEEE Trans Med Imaging* (2019) 38(6):1347–57. doi:10.1109/TMI.2018.2884093

40. Eckstein K, Dymerska B, Bachrata B, Bogner W, Poljanc K, Trattnig S, et al. Computationally efficient combination of multi-channel phase data from multi-echo acquisitions (ASPIRE). *Magn Reson Med* (2018) 79(6):2996–3006. doi:10.1002/mrm.26963

41. Cronin MJ, Wang N, Decker KS, Wei H, Zhu W-Z, Liu C. Exploring the origins of echo-time-dependent quantitative susceptibility mapping (QSM) measurements in healthy tissue and cerebral microbleeds. *Neuroimage* (2017) 149:98–113. doi:10.1016/j.neuroimage.2017.01.053

42. Robinson S, Schödl H, Trattnig S. A method for unwrapping highly wrapped multi-echo phase images at very high field: Umpire. *Magn Reson Med* (2014) 72(1):80–92. doi:10.1002/mrm.24897

43. Sood S, Urriola J, Reutens D, O'Brien K, Bollmann S, Barth M, et al. Echo time-dependent quantitative susceptibility mapping contains information on tissue properties. *Magn Reson Med* (2017) 77(5):1946–58. doi:10.1002/mrm.26281

44. Özbay PS, Deistung A, Feng X, Nanz D, Reichenbach JR, Schweser F. A comprehensive numerical analysis of background phase correction with V-SHARP. *NMR Biomed* (2017) 30(4):e3550. doi:10.1002/nbm.3550

45. Gulani V, Calamante F, Shellock FG, Kanal E, Reeder SB. Gadolinium deposition in the brain: Summary of evidence and recommendations. *Lancet Neurol* (2017) 16(7):564–70. doi:10.1016/S1474-4422(17)30158-8

46. Li W, Wu B, Liu C. Quantitative susceptibility mapping of human brain reflects spatial variation in tissue composition. *Neuroimage* (2011) 55(4):1645–56. doi:10.1016/j.neuroimage.2010.11.088

47. Zhou D, Liu T, Spincemaille P, Wang Y. Background field removal by solving the Laplacian boundary value problem. *NMR Biomed* (2014) 27(3):312–9. doi:10.1002/nbm.3064

48. Zheng W, Nichol H, Liu S, Cheng YN, Haacke EM. Measuring iron in the brain using quantitative susceptibility mapping and X-ray fluorescence imaging. *Neuroimage* (2013) 78:68–74. doi:10.1016/j.neuroimage.2013.04.022

49. Shmueli K, de Zwart JA, van Gelderen P, Li T-Q, Dodd SJ, Duyn JH. Magnetic susceptibility mapping of brain tissue *in vivo* using MRI phase data. *Magn Reson Med* (2009) 62(6):1510–22. doi:10.1002/mrm.22135

50. Liu T, Wisnieff C, Lou M, Chen W, Spincemaille P, Wang Y. Nonlinear formulation of the magnetic field to source relationship for robust quantitative susceptibility mapping. *Magn Reson Med* (2013) 69(2):467–76. doi:10.1002/mrm.24272

51. Sun H, Ma Y, MacDonald ME, Pike GB. Whole head quantitative susceptibility mapping using a least-norm direct dipole inversion method. *Neuroimage* (2018) 179: 166–75. doi:10.1016/j.neuroimage.2018.06.036

52. Liu Z, Kee Y, Zhou D, Wang Y, Spincemaille P. Preconditioned total field inversion (TFI) method for quantitative susceptibility mapping. *Magn Reson Med* (2017) 78(1):303–15. doi:10.1002/mrm.26331

53. Langkammer C, Bredies K, Poser BA, Barth M, Reishofer G, Fan AP, et al. Fast quantitative susceptibility mapping using 3D EPI and total generalized variation. *Neuroimage* (2015) 111:622–30. doi:10.1016/j.neuroimage.2015.02.041

54. Wen Y, Spincemaille P, Nguyen T, Cho J, Kovanlikaya I, Anderson J, et al. Multiecho complex total field inversion method (mcTFI) for improved signal modeling in quantitative susceptibility mapping. *Magn Reson Med* (2021) 86(4):2165–78. doi:10.1002/mrm.28814

55. Jung W, Bollmann S, Lee J. Overview of quantitative susceptibility mapping using deep learning: Current status, challenges and opportunities. *NMR Biomed* (2022) 35(4): e4292. doi:10.1002/nbm.4292

56. Bollmann S, Robinson SD, O'Brien K, Vegh V, Janke A, Marstaller L, et al. The challenge of bias-free coil combination for quantitative susceptibility mapping at ultra-high field. *Magn Reson Med* (2018) 79(1):97–107. doi:10.1002/mrm.26644

57. Hagberg GE, Eckstein K, Cuna E, Robinson S, Scheffler K. Towards robust QSM in cortical and sub-cortical regions of the human brain at 9.4T: Influence of coil combination and masking strategies. *Proc Intl Soc Mag Reson Med* (2020) 28:3786.

58. Schweser F, Robinson SD, de Rochefort L, Li W, Bredies K. An illustrated comparison of processing methods for phase MRI and QSM: Removal of background field contributions from sources outside the region of interest. *NMR Biomed* (2017) 30(4):e3604. doi:10.1002/nbm.3604

59. Hagberg GE. PhasMask4QSM (2022). Available at: https://github.com/ghagberg/PhaseMask4QSM.

60. Baigorri R, García-Mina JM, González-Gaitano G. Supramolecular association induced by Fe(III) in low molecular weight sodium polyacrylate. *Colloids Surf A Physicochem Eng Asp* (2007) 292(2-3):212–6. doi:10.1016/j.colsurfa.2006.06.027

61. Lancione M, Cencini M, Costagli M, Donatelli G, Tosetti M, Giannini G, et al. Diagnostic accuracy of quantitative susceptibility mapping in multiple system atrophy: The impact of echo time and the potential of histogram analysis. *Neuroimage Clin* (2022) 34:102989. doi:10.1016/j.nicl.2022.102989

62. Dietrich O, Levin J, Ahmadi S-A, Plate A, Reiser MF, Bötzel K, et al. MR imaging differentiation of Fe2+ and Fe3+ based on relaxation and magnetic susceptibility properties. *Neuroradiology* (2017) 59(4):403–9. doi:10.1007/s00234-017-1813-3

63. Birkl C, Birkl-Toeglhofer AM, Kames C, Goessler W, Haybaeck J, Fazekas F, et al. The influence of iron oxidation state on quantitative MRI parameters in post mortem human brain. *Neuroimage* (2020) 220:117080. doi:10.1016/j.neuroimage.2020.117080

64. Papaefthymiou GC. The Mössbauer and magnetic properties of ferritin cores. *Biochim Biophys Acta - Gen Subj* (2010) 1800(8):886–97. doi:10.1016/j.bbagen.2010.03.018

65. Birkl C, Langkammer C, Krenn H, Goessler W, Ernst C, Haybaeck J, et al. Iron mapping using the temperature dependency of the magnetic susceptibility. *Magn Reson Med* (2015) 73(3):1282–8. doi:10.1002/mrm.25236

66. Sharma SD, Fischer R, Schoennagel BP, Nielsen P, Kooijman H, Yamamura J, et al. MRI-based quantitative susceptibility mapping (QSM) and R2* mapping of liver iron overload: Comparison with SQUID-based biomagnetic liver susceptometry. *Magn Reson Med* (2017) 78(1):264–70. doi:10.1002/mrm.26358

67. Kumar P, Bulk M, Webb A, van der Weerd L, Oosterkamp TH, Huber M, et al. A novel approach to quantify different iron forms in *ex-vivo* human brain tissue. *Sci Rep* (2016) 6(1):38916. doi:10.1038/srep38916

68. Brem F, Hirt AM, Winklhofer M, Frei K, Yonekawa Y, Wieser HG, et al. Magnetic iron compounds in the human brain: A comparison of tumour and hippocampal tissue. *J R Soc Interf* (2006) 3(11):833–41. doi:10.1098/rsif.2006.0133

69. Svobodova H, Kosnáč D, Tanila H, Wagner A, Trnka M, Vitovič P, et al. Iron–oxide minerals in the human tissues. *BioMetals* (2020) 33(1):1–13. doi:10.1007/s10534-020-00232-6

70. Brooks RA, Vymazal J, Goldfarb RB, Bulte JWM, Aisen P. Relaxometry and magnetometry of ferritin. *Magn Reson Med* (1998) 40(2):227–35. doi:10.1002/mrm.1910400208

71. Wood JC, Fassler JD, Meade T. Mimicking liver iron overload using liposomal ferritin preparations. *Magn Reson Med* (2004) 51(3):607–11. doi:10.1002/mrm.10735

frontiers | Frontiers in Physics

TYPE Perspective
PUBLISHED 27 September 2023
DOI 10.3389/fphy.2023.1248021

OPEN ACCESS

EDITED BY
Ewald V. Moser,
Medical University of Vienna, Austria

REVIEWED BY
Jun Hua,
Johns Hopkins University, United States

*CORRESPONDENCE
Federico Giove,
federico.giove@uniroma1.it

RECEIVED 26 June 2023
ACCEPTED 14 September 2023
PUBLISHED 27 September 2023

CITATION
Guidi M, Giulietti G, Biondetti E, Wise R and Giove F (2023), Towards high-resolution quantitative assessment of vascular dysfunction.
Front. Phys. 11:1248021.
doi: 10.3389/fphy.2023.1248021

Towards high-resolution quantitative assessment of vascular dysfunction

Maria Guidi[1], Giovanni Giulietti[2], Emma Biondetti[3,4], Richard Wise[3,4] and Federico Giove[1,5]*

[1]Museo Storico della Fisica e Centro Studi e Ricerche Enrico Fermi, Rome, Italy, [2]Neuroimaging Laboratory, Fondazione Santa Lucia IRCCS, Rome, Italy, [3]Institute for Advanced Biomedical Technologies, University "G. d'Annunzio" of Chieti-Pescara, Chieti, Italy, [4]Department of Neuroscience, Imaging and Clinical Sciences, University "G. d'Annunzio" of Chieti-Pescara, Chieti, Italy, [5]Laboratory of Neurophysics and Neuroimaging (NaN), Fondazione Santa Lucia IRCCS, Rome, Italy

Neurovascular alterations are increasingly recognized as a key feature of many brain diseases. They can manifest as a reduction in resting cerebral blood flow or cerebrovascular reactivity (CVR) in the whole brain or in specific regions, depending on the underlying condition. Neurovascular impairment is observed in hypertension, Alzheimer's disease, stroke, multiple sclerosis and cerebral small vessel disease. Magnetic resonance imaging (MRI)-derived CVR mapping is a reliable marker of vascular dysfunction and has been performed mainly at standard functional MRI (fMRI) resolutions of 2–3 mm using the blood oxygen level dependent (BOLD) contrast. However, vascular alterations may occur at a finer scale (i.e., in the capillary bed) which would be better characterized with smaller voxel sizes. Capillaries in gray matter deliver oxygen and glucose to neural tissue and are arranged in a mesh structure, with variable density across the cortical depth. Given that the human cortex is, on average, 2.5 mm thick, submillimetric voxel sizes are effective in increasing the spatial specificity of measurements of hemodynamic and metabolic changes. Novel MRI sequences offer the possibility to map physiological parameters at high resolution with relatively simple experimental setups. In particular, pairing the BOLD acquisition with a contrast sensitive to blood volume changes, while administering a mild hypercapnic challenge, allows for simultaneous mapping of CVR, cerebral metabolic rate of oxygen consumption and other relevant parameters at a high resolution and can be performed at the clinical field strength of 3 T. We propose that this approach will help provide crucial insights into vascular impairment.

KEYWORDS

BOLD, fMRI, VASO, calibrated fMRI, $CMRO_2$, CVR, SVD, AD

Abbreviations: AD, Alzheimer's disease; ASL, arterial spin labeling; BBB, blood-brain barrier; BOLD, blood oxygen level dependent; CAA, cerebral amyloid angiopathy; CBF, cerebral blood flow; CBV, cerebral blood volume; $CMRO_2$, cerebral metabolic rate of oxygen consumption; CO_2, carbon dioxide; CSF, cerebrospinal fluid; CVR, cerebrovascular reactivity; $EtCO_2$, end-tidal CO_2; fMRI, functional magnetic resonance imaging; GM, gray matter; GRE, gradient echo; M, calibration parameter; MCI, mild cognitive impairment; MRI, magnetic resonance imaging; NVU, neurovascular uncoupling; $PaCO_2$, arterial partial pressure of CO_2; SE, spin echo; SNR, signal-to-noise ratio; SS-SI-VASO, slice-saturation slab-inversion VASO; SVD, small vessel disease; T1, longitudinal relaxation time; TE, echo time; TR, repetition time; VASO, vascular-space occupancy; WM, white matter.

1 Introduction

Neurodegenerative diseases represent a huge socio-economic burden in aging societies. Magnetic resonance imaging (MRI) offers information about different brain features non-invasively and it is widely employed in the detection of structural damage. Functional alterations, however, may initiate years before anatomical alterations and are important in the picture of disease pathophysiology. Therefore, reliably mapping vascular dysfunction and identifying early biomarkers should aid prevention and catalyze the development of therapies.

MRI contrast based on the blood oxygen level dependent (BOLD) effect is widely exploited in brain research. BOLD-based functional MRI (fMRI) is largely confined to clinical or basic research due to its nonquantitative nature and its dependency on multiple parameters, which are related partly to baseline tissue structure and physiology [1] and partly to underlying dynamic changes in cerebral blood flow (CBF), cerebral blood volume (CBV) and cerebral metabolic rate of oxygen consumption ($CMRO_2$). Other fMRI techniques that have found a comparatively large application in clinical studies are arterial spin labeling (ASL), for quantifying perfusion, and cerebrovascular reactivity (CVR) mapping based on BOLD or ASL. These have been applied to the study of aging, stroke, tumor, dementia, multiple sclerosis, brain injury, arterial stenosis, and more [2].

Other quantitative, less explored, fMRI techniques include vascular-space occupancy (VASO) [3], able to quantify changes in CBV, and calibrated fMRI, which relies on a simple model of the BOLD signal for extracting $CMRO_2$ [4–6]. These techniques have found limited application in disease states, for reasons including the lack of standardized protocols, limited contrast-to-noise and more difficulties in data acquisition and processing compared to BOLD. In this perspective article, we propose that VASO and calibrated fMRI at high resolutions can add valuable information to the picture of vascular impairment because of their straightforward physiological interpretation and their closer link to the microvasculature compared to BOLD [7]. Indeed, many neurodegenerative diseases are accompanied by (or originate from) a microvascular dysfunction, which can be assessed by observing the effects on microvascular parameters (CBF and CBV) or metabolic parameters ($CMRO_2$), as reported, for example, by Klinkmueller et al. in the case of Huntington's disease [8].

For microvascular assessment, imaging at submillimetric resolution is needed, since the average human cortical thickness is about 2.5 mm [9] and, thus, gray matter (GM) voxels having similar or larger sizes are typically affected by severe partial volume contamination by the surrounding cerebrospinal fluid (CSF) and white matter (WM), which has a different vascularization. Moreover, in terms of vascular density and function, the cortex is organized in a layered structure [10] and it has been shown that voxel sizes of about 0.8 mm are capable of distinguishing layer-specific activation in certain areas based on haemodynamic responses [11].

Calibrated fMRI is currently limited in resolution. In order to calibrate the BOLD signal, in addition to the BOLD contrast, a "vascular" contrast needs to be acquired (usually ASL for mapping CBF) while modulating the arterial partial pressure of carbon dioxide ($PaCO_2$). The experiments are typically performed at low image resolutions (e.g., $3.5 \times 3.5 \times 3–8\ mm^3$) [12], which are often dictated by the low signal-to-noise ratio (SNR) of ASL sequences.

VASO-fMRI, on the other hand, has been recently proven to be feasible at submillimetric resolutions (0.8 mm) at the clinical field strength of 3 T [13], therefore it represents a good candidate for microvascular state assessment in disease. Additionally, in the framework of calibrated fMRI, it has been shown that the term related to CBF changes can be replaced by a term related to CBV changes (obtainable with VASO) via Grubb's law, while assuming different coupling exponents for venous and total CBV changes [14, 15]. Therefore, VASO can be used to obtain submillimetric maps of $CMRO_2$ changes [14].

This perspective article is structured as follows: Section 2 focuses on disease states characterized by microvascular impairment; Section 3 describes the parameters that can be derived from MRI in order to assess microvascular dysfunction in such diseases; Section 4 proposes an acquisition protocol and functional paradigm for mapping the parameters listed.

2 The microvascular component in neurodegenerative diseases

While submillimetric VASO and calibrated fMRI have been proven feasible for the characterization of the microvascular component in healthy individuals [13, 14], we suggest that the same methodology may be useful in the study of disease states. A dysfunctional microvasculature is indeed common in many pathological conditions, such as small vessel disease (SVD), vascular dementia, Alzheimer's disease (AD), ischemic stroke, brain tumors, cerebral amyloid angiopathy (CAA), mild cognitive impairment (MCI), Huntington's disease, Parkinson's disease, among others [16]. We focus here on SVD, AD and brain tumors as case studies for investigating microvascular impairment.

2.1 Small vessel disease

Cerebral small vessel disease includes a wide spectrum of cerebrovascular diseases that involve endothelial dysfunction of capillaries, small arteries and small veins in the brain, leading to blood-brain barrier (BBB) dysfunction, impaired vasodilation, vessel stiffening, dysfunctional blood flow and interstitial fluid drainage, WM rarefaction, ischemia, inflammation, myelin damage, and secondary neurodegeneration [17]. The underlying neurobiological mechanisms are, to date, not clear, and SVD is generally assessed by looking at macroscopic or mesoscopic manifestations, such as WM hyperintensities, lacunas, microbleeds, perivascular spaces, or small subcortical infarcts. In terms of hemodynamic measures, a reduction in CVR and CBF has been observed [18]. Given the microvascular nature of the disease, mapping microvascular reactivity and the possible related metabolic impairment can help clarify the underlying mechanisms and pathological effects of the observed alterations [19].

2.2 Alzheimer's disease

AD is characterized by amyloid-β accumulation and impaired CVR [20], but the relationship between these alterations is not clear.

One hypothesis is that amyloid-β accumulation may directly induce vascular dysfunction by impairing vasorelaxation, but therapies aimed at amyloid-β plaque reduction are not effective in reversing cognitive decline [21].

Another hypothesis identifies the microvasculature and related inflammatory processes as fundamental in the pathogenesis of AD [22]. In particular, a CBF reduction is currently the earliest known change associated with the disease, and the mechanism behind it might be a pericyte-driven constriction of capillaries [23]. It is hypothesized that this constriction and the associated hypoperfusion are the precursors of amyloid-β accumulation via upregulation of the BACE1 enzyme. Capillary dysfunction and microvascular CVR reduction were additionally observed to be associated with symptom severity [24, 25], and resting $CMRO_2$ was found to be reduced in a calibrated BOLD study in AD patients [26].

2.3 Brain tumors

Brain tumors are accompanied by strong alterations in the vasculature (e.g., angiogenesis), which often lead to a local disruption in the neurovascular coupling, also termed neurovascular uncoupling (NVU). Even low grade brain tumors show some degree of NVU [27]. In practice, this may cause a reduced or absent BOLD response to functional tasks in the region affected, even if neuronal activation is present [28]. Distinguishing regions of NVU from regions effectively lacking neuronal response is very important in presurgical planning to avoid excess surgical resection [27, 28]. In place of task-based BOLD fMRI, CVR mapping is generally preferred as it relies on a purely vascular stimulus. CVR mapping was found to be superior (i.e., able to identify NVU regions also in low and intermediate brain gliomas) to perfusion mapping with T2* dynamic susceptibility contrast [27]. Increasing spatial resolution in CVR maps and adding a vascular contrast (such as CBV-weighted) is important for precise localization and characterization of the tissue affected.

3 Quantitative parameters for high resolution mapping of vascular dysfunction

In the following, we list quantitative fMRI-derived parameters useful in the study of neurovascular disease and that can be mapped at high resolution at 3 T.

3.1 Cerebral blood volume

Mapping of CBV with MRI without the use of contrast agents can be achieved with vascular-space occupancy [3]. VASO is an inversion recovery technique exploiting the different T_1 of blood and tissue ($T_{1,tissue} < T_{1,blood}$) for creating a contrast sensitive to CBV changes. In the original VASO formulation the images were acquired at the time of blood nulling [3], while more recent implementations showed that different inversion times can be used, as long as a difference in the T_1 weighting of the two compartments is achieved [29, 30]. When the vasculature dilates, either following a metabolic demand of the tissue or a vasodilatory stimulus, the volume of blood in a responding voxel increases. VASO measures quantitative changes in blood volume, which can be expressed as a percentage change or in volume units, but VASO does not quantify baseline CBV.

The slice-saturation slab-inversion VASO (SS-SI-VASO) [31], developed at 7 T, permits the acquisition of gradient-recalled echo (GRE)-BOLD and VASO contrasts interleaved by adding a second excitation pulse at each repetition time (TR). VASO demonstrated a high specificity for the capillaries, arterioles and intracortical arteries [32, 33], making it a valuable tool for high-resolution fMRI [34]. Recently, the VASO implementation acquiring BOLD volumes concomitantly has been adapted for high-resolution applications at 3 T, where it has been shown capable of distinguishing layer-dependent activation [13], thus reflecting a microvascular sensitivity.

Using the VASO sequence requires some effort in setting up a working protocol, dealing with the lower SNR and longer TRs compared to BOLD, as well as a less standardized data processing. Examples of protocols for submillimetric acquisitions can be found at https://github.com/layerfMRI/Sequence_Github/tree/master/3T.

3.2 Cerebrovascular reactivity

Cerebrovascular reactivity (CVR) reflects the capacity of brain vessels to dilate or constrict in response to a vasoactive stimulus. MRI-based CVR is generally expressed as percent BOLD or ASL signal change per mmHg change in end-tidal carbon dioxide ($EtCO_2$) [2]. Despite the relative simplicity of the measure, it is one of the most reliable MRI-derived predictors of cerebrovascular impairment and has been applied in the study of several diseases, including SVD and AD [2, 35, 36].

Since GRE-BOLD signal changes are heavily weighted towards the venous macrovasculature, both due to an inherent weighting towards larger vessels and to dHb-containing compartments [37], CVR maps based on such contrast show similar features. In order to target microvascular CVR, different sequences should be employed, such as ASL, spin-echo (SE)-BOLD, or VASO. In particular, VASO-based CVR could be interesting due to the high resolutions achievable and the observed stability to hypercapnic stimuli [14]. In one study, VASO reactivity was found to be more negative (i.e., larger CBV increase) in patients with carotid artery disease compared to healthy controls [38].

3.2.1 Vasodilatory stimuli

CVR mapping with MRI can be achieved with administration of carbon dioxide (CO_2)-enriched gas [2], breath holding [39] or amplitude of resting-state fluctuations in CO_2 [40]. CVR mapping has been performed at a variety of spatial resolutions, determined by the BOLD or ASL acquisition protocol used. For CVR mapping at high resolution, inhalation of a CO_2-enriched gas mixture (typically 5% CO_2) is preferable over the other approaches because it gives the strongest increase in CBF and thus improves the contrast-to-noise ratio (CNR), while being safe

and well tolerated [41]. A few studies have indeed successfully mapped CVR at voxel sizes below 2 mm using breathing manipulations [2, 42]. In particular, a recent study by Schellekens et al. reports depth-dependent profiles of CVR using GRE-BOLD and SE-BOLD, showing a detectable variation with cortical depth [15].

3.3 Cerebral metabolic rate of oxygen consumption

BOLD signal changes in a voxel during a task of interest can be modeled according to Eq. 1 [4]:

$$\frac{\Delta BOLD}{BOLD_0} = M\left[1 - \left(\frac{CBV_v}{CBV_{v,0}}\right)\left(\frac{CBF}{CBF_0}\right)^{-\beta}\left(\frac{CMRO_2}{CMRO_{2,0}}\right)^{\beta}\right] \quad (1)$$

where CBV_v is the CBV contributing to BOLD signal changes ("venous" CBV), M is the calibration parameter which corresponds to the maximum BOLD signal change (BOLD = M for complete deoxy-hemoglobin washout from the vasculature), β is a magnetic-field dependent exponent, and the subscript 0 indicates quantities at baseline.

It is generally assumed that CBV and CBF are coupled via Eq. 2:

$$\frac{CBV_v}{CBV_{v,0}} = \left(\frac{CBF}{CBF_0}\right)^{\alpha} \quad (2)$$

where α is a coupling constant, often taken to be equal to 0.38 [43].

The goal of calibrated fMRI is isolating the $CMRO_2$ term from the Eq. 1: to this end, a pure CBF or CBV sensitive contrast needs to be acquired in addition to BOLD, and the calibration parameter M needs to be estimated. For extracting M a vasoactive, isometabolic ($CMRO_2/CMRO_{2,0} \sim 1$) stimulus is used, which introduces a BOLD dependency only on CBF or CBV (measurable) if Eq. 2 is assumed [4, 5].

Most calibrated fMRI studies use ASL sequences for mapping CBF and extract CBV via Eq. 2. Since the technique allows for voxelwise mapping, the resolution achievable by ASL at 3 T dictates the resolution of $CMRO_2$ maps. For submillimetric applications, CBV mapping can be used and CBF changes estimated by Eq. 2, while assuming a different coupling exponent for venous and total CBV changes [14, 15].

Other approaches for $CMRO_2$ mapping have been introduced using different gas mixtures or without exogenous gas manipulations. Existing acquisition techniques and modelling approaches have been recently reviewed [44, 45].

4 Functional paradigms for multiparametric mapping at high resolution

Given the sequences currently available, we propose that it is possible to obtain, in less than 30 min at 3 T, submillimetric maps of 1) BOLD-based CVR; 2) VASO-based CVR; 3) the calibration parameter M; 4) relative changes in $CMRO_2$ elicited by a task of interest; 5) BOLD signal changes elicited by the same task; 6) VASO signal changes elicited by the same task.

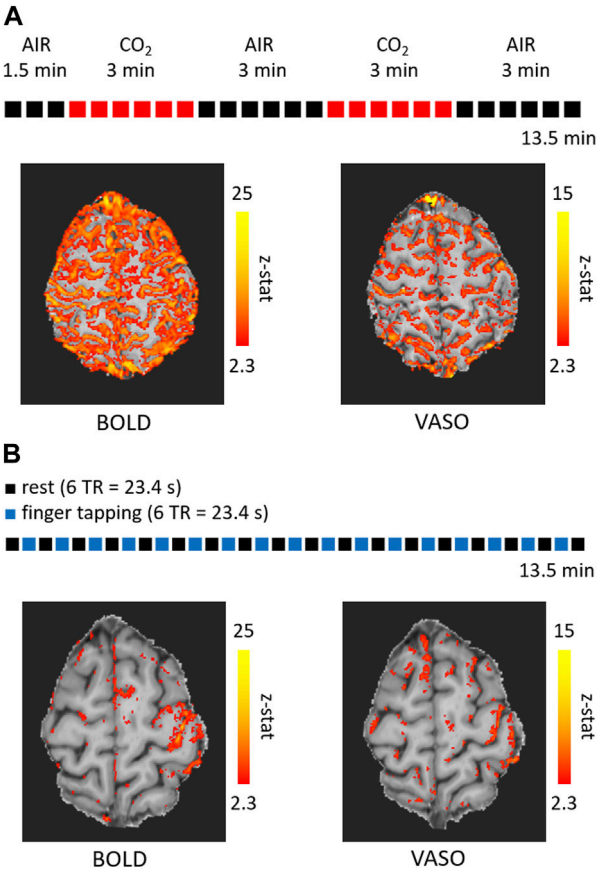

FIGURE 1
Activation maps overlaid on the mean of the VASO timecourse obtained with the acquisition of 210 pairs of volumes (210 BOLD volumes and 210 VASO volumes) at a isotropic resolution of 0.9 mm for a breathing paradigm involving hypercapnia **(A)** and a right-hand finger tapping task **(B)**. The duration was 13.5 min (TR = 3.9 s) for each run.

To this end, the use of the VASO sequence with a 3D readout [13] has shown to be suitable for submillimetric fMRI at 3 T.

Figure 1 shows the activation maps obtained for two tasks using the same acquisition protocol. The sequence used was the 3 T VASO [13] with the following acquisition parameters: isotropic nominal resolution = 0.9 mm, matrix size = 188 × 188 × 28, echo time (TE) = 21.2 ms, TR = 3.9 s (this refers to the time it takes to acquire a BOLD-VASO pair of volumes), 210 measurements (210 BOLD volumes and 210 VASO volumes), partial Fourier = 6/8, GRAPPA = 3, bandwidth = 1,026 Hz/Px, echo spacing = 1.1 ms, inversion delay = 550 ms, flip angle = 30° with a variable flip angle scheme [13], water selective excitation achieved with long binomial 1-1 pulses. The acquisition was performed on a Siemens Prisma 3 T (Siemens Healthineers, Erlangen, Germany) scanner and a 32-channel head coil. Informed consent was obtained according to international standards, the study was approved by the Ethical Committee of Fondazione Santa Lucia, CE/2022_010.

One acquisition was performed during a breathing challenge consisting of an alternation of medical air and 5%-CO_2-enriched air administration (Figure 1A), for a total acquisition time of

13.5 min. The other acquisition was performed during a functional task consisting of an alternation of right-hand finger tapping for 6 TRs and rest for 6 TRs (Figure 1B). For both acquisitions, the timecourses were corrected for motion using the ASL toolbox based on SPM [46, 47]. Statistical activation maps were obtained using FSL FEAT [48] and z-stats are reported in Figure 1. A detectable activation was present for both contrasts and conditions, with BOLD generating larger clusters as expected. The submillimetric voxel size of 0.9 mm allows to have 2 to 4 voxels within the gray matter thickness and to reduce partial voluming with the neighboring CSF and WM. Nevertheless, the large BOLD signal changes following the pial venous vasculature are located outside the GM and reduce the spatial specificity. VASO signal changes have in general a lower amplitude and are more affected by noise, which result in smaller clusters as in Figure 1, while the specificity of the signal changes is less compromised by the pial vasculature (more clearly visible in Figure 1B).

This preliminary dataset confirms that it is possible to have a statistically significant response in both BOLD and VASO timecourses for a functional run of 13.5 min (210 BOLD-VASO pairs of volumes).

With the two datasets referred to in Figure 1, the signal changes in BOLD and VASO upon hypercapnia can be used to estimate the calibration parameter M across gray matter from Eq. 1 (assuming Eq. 2), and the signal changes in BOLD and VASO elicited by the finger tapping task can then be used to estimate changes in $CMRO_2$ from the same equation, once M has been calculated.

4.1 Limitations

The proposed multiparametric acquisition can offer a multi-faceted window into microvascular dysfunction, by mapping vascular and metabolic features concomitantly at 3 T and at voxel volumes below 1 mm^3.

The submillimetric VASO sequence has been introduced only recently at 3 T and has some limitations. First of all, the low SNR of 10–20 [13] limits its flexibility: tasks associated with small effect sizes are hard to detect, unless the acquisition time is largely increased. Moreover, the generation of the VASO contrast has some timing constraints that impact the TR duration: the typical TR is about 4–5 s (for the acquisition of a full BOLD-VASO pair) for slab protocols.

Additionally, the breathing challenge could create excessive discomfort in patient populations, both due to wearing a mask and being in a hypercapnic state. Therefore, it is important to familiarize each subject with the gas challenge prior to scanning. An earlier study showed an increase in participant dropouts for AD patients compared to healthy control for the breathing challenge [26].

While CVR mapping is reliable and has been applied in disease, the same does not hold for calibrated fMRI. Calibrated BOLD models rely on several assumptions, which, even at typical image resolutions, might not be a good approximation of the real underlying mechanisms. Such limitations could be exacerbated at higher resolutions where the spatial heterogeneity of the vasculature is resolved. Most notably, the flow-volume coupling expressed by Grubb's relationship is unlikely to hold true with the same exponent for small voxel sizes and between healthy subjects and patients. Therefore, differences in $CMRO_2$ between a healthy group and a disease group could stem from a disrupted CBF-CBV coupling rather than a true metabolic difference. To avoid such bias, imaging CBF, CBV, and BOLD concomitantly [8] is preferable, but CBF mapping via arterial spin labeling at high resolution is challenging [49], therefore studying the flow-volume coupling relationship experimentally in humans is difficult.

If using VASO in the calibrated BOLD framework, the CBV at baseline needs to be assumed. A fixed fraction of 5.5% [50] might be acceptable considering that the microvascular blood density, which is the major factor responsible for VASO signal changes for short stimulations, is relatively homogeneous across the cortical depth [10, 51]. During hypercapnic stimulations, however, the fraction of VASO signal change coming from venous blood increases [52], challenging the assumption of a fixed baseline blood fraction.

Finally, the assumption of isometabolism during gas administration has been challenged in several studies. Although there is not a definitive answer, some evidence suggests a reduction, rather than an increase, in $CMRO_2$ of up to 13% during a 5%-CO_2 gas challenge [53]. However, this value depends on the concentration of arterial CO_2 and on the length of the respiratory challenge, with shorter epochs having less impact on $CMRO_2$ [2].

5 Discussion and conclusion

We propose that, to obtain more insight into neurovascular diseases, several contrasts and approaches sensitive to microvascular function should be used at 3 T and at submillimetric resolutions. The acquisition scheme that we propose here involves the use of VASO at 3 T (BOLD and CBV-weighted contrast interleaved) with a gas manipulation inducing hypercapnia, and a functional task. Scanning under these conditions for less than 30 min makes it feasible to obtain maps of BOLD and VASO signal changes for each condition, CVR, regional $CMRO_2$ changes and M at a submillimetric resolution.

Data availability statement

The raw data supporting the conclusion of this article will be made available by the authors, without undue reservation.

Ethics statement

The studies involving humans were approved by the Ethical Committee of Fondazione Santa Lucia. The studies were conducted in accordance with the local legislation and institutional requirements. The participants provided their written informed consent to participate in this study. Written informed consent

was obtained from the individual(s) for the publication of any potentially identifiable images or data included in this article.

Author contributions

MG: Conceptualization, data collection and analysis, writing. GG: Conceptualization, data analysis, writing. EB, RW, and FG: Conceptualization, writing.

Funding

MG is funded by Regione Lazio POR-FESR 2014-2020 A0375-2020-36648, "FISASMEM—Fisiologia dell'aging: sviluppo di metodi MRI quantitativi." This work was partially conducted under the framework of the Departments of Excellence 2018-2022 initiative of the Italian Ministry of Education, University and Research for the Department of Neuroscience, Imaging and Clinical Sciences (DNISC) of the University of Chieti-Pescara, Italy. This work was partially funded by European Union—Next Generation EU, by Ministero della Salute—Ricerca Corrente Linea 1 and Regione Lazio; Ministero dell'Istruzione, dell'Università e della Ricerca; European Commission. This project has received funding from the European Union's Horizon Europe research and innovation programme under the Marie Skłodowska-Curie Grant Agreement No. 101066055—acronym HERMES. Views and opinions expressed are however those of the author(s) only and do not necessarily reflect those of the European Union or the European Research Executive Agency (REA). Neither the European Union nor the granting authority can be held responsible for them.

Acknowledgments

We would like to thank Laurentius Huber, Harald E. Möller, and Lasse Knudsen for helpful discussion and support.

Conflict of interest

The authors declare that the research was conducted in the absence of any commercial or financial relationships that could be construed as a potential conflict of interest.

Publisher's note

References

1. Lu H, Zhao C, Ge Y, Lewis-Amezcua K. Baseline blood oxygenation modulates response amplitude: Physiologic basis for intersubject variations in functional MRI signals. *Magn Reson Med Official J Int Soc Magn Reson Med* (2008) 60:364–72. doi:10.1002/mrm.21686

2. Liu P, De Vis JB, Lu H. Cerebrovascular reactivity (CVR) MRI with CO2 challenge: A technical review. *Neuroimage* (2019) 187:104–15. doi:10.1016/j.neuroimage.2018.03.047

3. Lu H, Golay X, Pekar JJ, Van Zijl PC. Functional magnetic resonance imaging based on changes in vascular space occupancy. *Magn Reson Med Official J Int Soc Magn Reson Med* (2003) 50:263–74. doi:10.1002/mrm.10519

4. Davis TL, Kwong KK, Weisskoff RM, Rosen BR. Calibrated functional MRI: Mapping the dynamics of oxidative metabolism. *Proc Natl Acad Sci* (1998) 95:1834–9. doi:10.1073/pnas.95.4.1834

5. Hoge RD, Atkinson J, Gill B, Crelier GR, Marrett S, Pike GB. Investigation of BOLD signal dependence on cerebral blood flow and oxygen consumption: The deoxyhemoglobin dilution model. *Magn Reson Med Official J Int Soc Magn Reson Med* (1999) 42:849–63. doi:10.1002/(sici)1522-2594(199911)42:5<849::aid-mrm4>3.0.co;2-z

6. Bulte DP, Kelly M, Germuska M, Xie J, Chappell MA, Okell TW, et al. Quantitative measurement of cerebral physiology using respiratory-calibrated MRI. *Neuroimage* (2012) 60:582–91. doi:10.1016/j.neuroimage.2011.12.017

7. Iannetti G, Wise RG. BOLD functional MRI in disease and pharmacological studies: Room for improvement? *Magn Reson Imaging* (2007) 25:978–88. doi:10.1016/j.mri.2007.03.018

8. Klinkmueller P, Kronenbuerger M, Miao X, Bang J, Ultz KE, Paez A, et al. Impaired response of cerebral oxygen metabolism to visual stimulation in Huntington's disease. *J Cereb Blood Flow Metab* (2021) 41:1119–30. doi:10.1177/0271678x20949286

9. von Economo CF, Koskinas GN. *Die cytoarchitektonik der hirnrinde des erwachsenen menschen*. New York City: J. Springer (1925).

10. Duvernoy HM, Delon S, Vannson JL. Cortical blood vessels of the human brain. *Brain Res Bull* (1981) 7:519–579. doi:10.1016/0361-9230(81)90007-1

11. Bandettini PA, Huber L, Finn ES. Challenges and opportunities of mesoscopic brain mapping with fMRI. *Curr Opin Behav Sci* (2021) 40:189–200. doi:10.1016/j.cobeha.2021.06.002

12. Sleight E, Stringer MS, Marshall I, Wardlaw JM, Thrippleton MJ. Cerebrovascular reactivity measurement using magnetic resonance imaging: A systematic review. *Front Physiol* (2021) 12:643468. doi:10.3389/fphys.2021.643468

13. Huber L, Kronbichler L, Stirnberg R, Ehses P, Stoecker T, Fernandez-Cabello S, et al. Evaluating the capabilities and challenges of layer-fMRI VASO at 3T. *Aperture Neuro* (2023) 3:1–17. doi:10.52294/001c.85117

14. Guidi M, Huber L, Lampe L, Gauthier CJ, Möller HE. Lamina-dependent calibrated BOLD response in human primary motor cortex. *Neuroimage* (2016) 141:250–61. doi:10.1016/j.neuroimage.2016.06.030

15. Schellekens W, Bhogal AA, Roefs EC, Báez-Yáñez MG, Siero JC, Petridou N. The many layers of BOLD. The effect of hypercapnic and hyperoxic stimuli on macro-and micro-vascular compartments quantified by CVR, M, and CBV across cortical depth. *J Cereb Blood Flow Metab* (2023) 43:419–32. doi:10.1177/0271678x221133972

16. Chen JJ. Functional MRI of brain physiology in aging and neurodegenerative diseases. *Neuroimage* (2019) 187:209–25. doi:10.1016/j.neuroimage.2018.05.050

17. Wardlaw JM, Smith C, Dichgans M. Small vessel disease: Mechanisms and clinical implications. *Lancet Neurol* (2019) 18:684–96. doi:10.1016/s1474-4422(19)30079-1

18. Paschoal AM, Secchinatto KF, da Silva PHR, Zotin MCZ, Dos Santos AC, Viswanathan A, et al. Contrast-agent-free state-of-the-art MRI on cerebral small vessel disease—part 1. ASL, IVIM, and CVR. *NMR Biomed* (2022) 35:e4742. doi:10.1002/nbm.4742

19. Zwanenburg JJ, van Osch MJ. Targeting cerebral small vessel disease with MRI. *Stroke* (2017) 48:3175–82. doi:10.1161/strokeaha.117.016996

20. Cantin S, Villien M, Moreaud O, Tropres I, Keignart S, Chipon E, et al. Impaired cerebral vasoreactivity to CO2 in Alzheimer's disease using BOLD fMRI. *Neuroimage* (2011) 58:579–87. doi:10.1016/j.neuroimage.2011.06.070

21. Andrieu S, Coley N, Lovestone S, Aisen PS, Vellas B. Prevention of sporadic alzheimer's disease: Lessons learned from clinical trials and future directions. *Lancet Neurol* (2015) 14:926–44. doi:10.1016/s1474-4422(15)00153-2

22. Steinman J, Sun H-S, Feng Z-P. Microvascular alterations in Alzheimer's disease. *Front Cell Neurosci* (2021) 14:618986. doi:10.3389/fncel.2020.618986

23. Korte N, Nortley R, Attwell D. Cerebral blood flow decrease as an early pathological mechanism in Alzheimer's disease. *Acta Neuropathologica* (2020) 140:793–810. doi:10.1007/s00401-020-02215-w

24. Nielsen RB, Egefjord L, Angleys H, Mouridsen K, Gejl M, Møller A, et al. Capillary dysfunction is associated with symptom severity and neurodegeneration in Alzheimer's disease. *Alzheimer's Demen* (2017) 13:1143–53. doi:10.1016/j.jalz.2017.02.007

25. Jellinger K, Attems J. Prevalence and impact of cerebrovascular pathology in Alzheimer's disease and parkinsonism. *Acta Neurol Scand* (2006) 114:38–46. doi:10.1111/j.1600-0404.2006.00665.x

26. Lajoie I, Nugent S, Debacker C, Dyson K, Tancredi FB, Badhwar A, et al. Application of calibrated fMRI in Alzheimer's disease. *NeuroImage: Clin* (2017) 15:348–58. doi:10.1016/j.nicl.2017.05.009

27. Pillai JJ, Zacà D. Comparison of BOLD cerebrovascular reactivity mapping and DSC MR perfusion imaging for prediction of neurovascular uncoupling potential in brain tumors. *Tech Cancer Res Treat* (2012) 11:361–74. doi:10.7785/tcrt.2012.500284

28. Agarwal S, Sair HI, Pillai JJ. The problem of neurovascular uncoupling. *Neuroimaging Clin* (2021) 31:53–67. doi:10.1016/j.nic.2020.09.003

29. Ciris PA, Qiu M, Constable RT. Non-invasive quantification of absolute cerebral blood volume during functional activation applicable to the whole human brain. *Magnet Reson Med* (2014) 71:580–90. doi:10.1002/mrm.24694

30. Huber L, Finn ES, Chai Y, Goebel R, Stirnberg R, Stöcker T, et al. Layer-dependent functional connectivity methods. *Prog Neurobiol* (2021) 207:101835. doi:10.1016/j.pneurobio.2020.101835

31. Huber L, Ivanov D, Krieger SN, Streicher MN, Mildner T, Poser BA, et al. Slab-selective, BOLD-corrected VASO at 7 Tesla provides measures of cerebral blood volume reactivity with high signal-to-noise ratio. *Magnet Reson Med* (2014) 72:137–48. doi:10.1002/mrm.24916

32. Akbari A, Bollmann S, Ali TS, Barth M. Modelling the depth-dependent VASO and BOLD responses in human primary visual cortex. *Hum Brain Mapp* (2023) 44:710–26. doi:10.1002/hbm.26094

33. Lu H, van Zijl PC. A review of the development of Vascular-Space-Occupancy (VASO) fMRI. *Neuroimage* (2012) 62:736–42. doi:10.1016/j.neuroimage.2012.01.013

34. Huber L, Handwerker DA, Jangraw DC, Chen G, Hall A, Stüber C, et al. High-resolution CBV-fMRI allows mapping of laminar activity and connectivity of cortical input and output in human M1. *Neuron* (2017) 96:1253–63.e7. e7. doi:10.1016/j.neuron.2017.11.005

35. Chen JJ. Cerebrovascular-reactivity mapping using MRI: Considerations for Alzheimer's disease. *Front Aging Neurosci* (2018) 10:170. doi:10.3389/fnagi.2018.00170

36. Blair GW, Doubal FN, Thrippleton MJ, Marshall I, Wardlaw JM. Magnetic resonance imaging for assessment of cerebrovascular reactivity in cerebral small vessel disease: A systematic review. *J Cereb Blood Flow Metab* (2016) 36:833–41. doi:10.1177/0271678x16631756

37. Uludağ K, Müller-Bierl B, Uğurbil K. An integrative model for neuronal activity-induced signal changes for gradient and spin echo functional imaging. *Neuroimage* (2009) 48:150–65. doi:10.1016/j.neuroimage.2009.05.051

38. Donahue MJ, Jan van Laar P, Van Zijl PC, Stevens RD, Hendrikse J. Vascular space occupancy (VASO) cerebral blood volume-weighted MRI identifies hemodynamic impairment in patients with carotid artery disease. *J Magn Reson Imaging Official J Int Soc Magn Reson Med* (2009) 29:718–24. doi:10.1002/jmri.21667

39. Urback AL, MacIntosh BJ, Goldstein BI. Cerebrovascular reactivity measured by functional magnetic resonance imaging during breath-hold challenge: A systematic review. *Neurosci Biobehavioral Rev* (2017) 79:27–47. doi:10.1016/j.neubiorev.2017.05.003

40. Golestani AM, Wei LL, Chen JJ. Quantitative mapping of cerebrovascular reactivity using resting-state BOLD fMRI: Validation in healthy adults. *Neuroimage* (2016) 138:147–63. doi:10.1016/j.neuroimage.2016.05.025

41. Spano VR, Mandell DM, Poublanc J, Sam K, Battisti-Charbonney A, Pucci O, et al. CO2 blood oxygen level–dependent MR mapping of cerebrovascular reserve in a clinical population: Safety, tolerability, and technical feasibility. *Radiology* (2013) 266:592–8. doi:10.1148/radiol.12112795

42. Bhogal AA, Philippens ME, Siero JC, Fisher JA, Petersen ET, Luijten PR, et al. Examining the regional and cerebral depth-dependent BOLD cerebrovascular reactivity response at 7 T. *Neuroimage* (2015) 114:239–48. doi:10.1016/j.neuroimage.2015.04.014

43. Grubb RL, Jr, Raichle ME, Eichling JO, Ter-Pogossian MM. The effects of changes in PaCO2 cerebral blood volume, blood flow, and vascular mean transit time. *Stroke* (1974) 5:630–9. doi:10.1161/01.str.5.5.630

44. Chen JJ, Uthayakumar B, Hyder F. Mapping oxidative metabolism in the human brain with calibrated fMRI in health and disease. *J Cereb Blood Flow Metab* (2022) 42:1139–62. doi:10.1177/0271678x221077338

45. Germuska M, Wise RG. Calibrated fMRI for mapping absolute CMRO2: Practicalities and prospects. *Neuroimage* (2019) 187:145–53. doi:10.1016/j.neuroimage.2018.03.068

46. Wang Z, Aguirre GK, Rao H, Wang J, Fernández-Seara MA, Childress AR, et al. Empirical optimization of ASL data analysis using an ASL data processing toolbox: ASLtbx. *Magn Reson Imaging* (2008) 26:261–9. doi:10.1016/j.mri.2007.07.003

47. Ashburner J, Barnes G, Chen C-C, Daunizeau J, Flandin G, Friston K, et al. *SPM12 manual*. London, UK: Wellcome Trust Centre for Neuroimaging (2014). p. 2464.

48. Jenkinson M, Beckmann CF, Behrens TE, Woolrich MW, Smith SM. Fsl. *Neuroimage* (2012) 62:782–90. doi:10.1016/j.neuroimage.2011.09.015

49. Hernandez-Garcia L, Aramendía-Vidaurreta V, Bolar DS, Dai W, Fernández-Seara MA, Guo J, et al. Recent technical developments in ASL: A review of the state of the art. *Magnet Reson Med* (2022) 88:2021–42. doi:10.1002/mrm.29381

50. Lu H, Hua J, van Zijl PC. Noninvasive functional imaging of cerebral blood volume with vascular-space-occupancy (VASO) MRI. *NMR Biomed* (2013) 26:932–48. doi:10.1002/nbm.2905

51. Schmid F, Barrett MJ, Jenny P, Weber B. Vascular density and distribution in neocortex. *Neuroimage* (2019) 197:792–805. doi:10.1016/j.neuroimage.2017.06.046

52. Hua J, Liu P, Kim T, Donahue M, Rane S, Chen JJ, et al. MRI techniques to measure arterial and venous cerebral blood volume. *Neuroimage* (2019) 187:17–31. doi:10.1016/j.neuroimage.2018.02.027

53. Xu F, Uh J, Brier MR, Hart J, Jr, Yezhuvath US, Gu H, et al. The influence of carbon dioxide on brain activity and metabolism in conscious humans. *J Cereb Blood Flow Metab* (2011) 31:58–67. doi:10.1038/jcbfm.2010.153

frontiers | Frontiers in Physics

TYPE Original Research
PUBLISHED 10 October 2023
DOI 10.3389/fphy.2023.1233059

OPEN ACCESS

EDITED BY
Thomas Beyer,
Medical University of Vienna, Austria

REVIEWED BY
Paul Cumming,
University of Bern, Switzerland
Miho Shidahara,
Tohoku University, Japan

*CORRESPONDENCE
Supatporn Tepmongkol,
supatporn.t@chula.ac.th

RECEIVED 01 June 2023
ACCEPTED 25 September 2023
PUBLISHED 10 October 2023

CITATION
Khamwan K, Sukprakun C, Limotai C, Jirasakuldej S, Jantarato A, Hemachudha T and Tepmongkol S (2023), Dynamic ^{18}F-FDG-PET kinetic parameters for epileptogenic zone localization in drug-resistant epilepsy. *Front. Phys.* 11:1233059. doi: 10.3389/fphy.2023.1233059

Dynamic ^{18}F-FDG-PET kinetic parameters for epileptogenic zone localization in drug-resistant epilepsy

Kitiwat Khamwan[1,2], Chanan Sukprakun[1], Chusak Limotai[3,4], Suda Jirasakuldej[3,4], Attapon Jantarato[5], Thiravat Hemachudha[6] and Supatporn Tepmongkol[1,2,4,7]*

[1]Division of Nuclear Medicine, Department of Radiology, Faculty of Medicine, Chulalongkorn University, Bangkok, Thailand, [2]Chulalongkorn University Biomedical Imaging Group, Department of Radiology, Faculty of Medicine, Chulalongkorn University, Bangkok, Thailand, [3]Department of Medicine, Faculty of Medicine, Chulalongkorn University, Bangkok, Thailand, [4]Chulalongkorn Comprehensive Epilepsy Center of Excellence (CCEC), King Chulalongkorn Memorial Hospital, Bangkok, Thailand, [5]National Cyclotron and PET Centre, Chulabhorn Hospital, Chulabhorn Royal Academy, Bangkok, Thailand, [6]Department of Medicine (Neurology), Neuroscience Centre for Research and Development, Thai Red Cross Emerging Infectious Disease-Health Science Centre, Faculty of Medicine, Chulalongkorn University, Bangkok, Thailand, [7]Cognitive Impairment and Dementia Research Unit, Faculty of Medicine, Chulalongkorn University, Bangkok, Thailand

Objective: Precisely localizing the seizure onset zone remains a challenging task in drug-resistant epilepsy (DRE) patients especially given its critical role in successful surgery and effective management. This study aimed to investigate the kinetic parameters of regional ^{18}F-fluorodeoxyglucose (FDG) uptake in DRE patients, aiming to identify the kinetic parameters best enabling the identification of the epileptogenic region.

Methods: Consecutive DRE patients with clinically mandated interictal ^{18}F-FDG PET/CT were recruited from October 2019 to September 2020 for pre-surgical evaluation. Immediately after injecting ^{18}F-FDG of 112–179 MBq, dynamic data were acquired for 90 min. The motion correction and resampling to the Montreal atlas was performed in order to generate a transformation matrix. 116 volume of interests (VOIs) and regional time-activity curves (TACs) were generated by employing the automated anatomical labeling (AAL) template using PMOD software. Kinetic parameters of FDG unidirectional blood-brain clearance (K_1), efflux (k_2), phosphorylation (k_3), and net metabolic flux (K_i) were derived using irreversible 2-tissue-compartment model with an image-derived input function (IDIF). The kinetic parameters values obtained from all regions were ranked and compared with the presumed epileptogenic zone (EZ).

Results: Eleven DRE patients (5 males, 6 females, mean age 35.1 $\pm$ 10.2 years) were analyzed. We found that the region with the lowest values of K_i provided correct lateralization in 7/7 (100%) of patient with temporal lobe epilepsy (TLE) and the region with the lowest K_i and k_3 parameters showed concordance with the EZ in 100% and 71.4% of patients, respectively.

Conclusion: The present parametric approach to the evaluation of FDG-PET may be more sensitive than semi-quantitative approaches for the detection of

pathophysiology in the EZ of patients with medically unresponsive TLE in addition to the routine clinical investigations.

KEYWORDS

drug-resistant epilepsy, pharmacokinetic modeling, compartmental modeling, dynamic-PET, PMOD software, epileptogenic zone localization

1 Introduction

Epilepsy is a prevalent neurological disorder that affects millions worldwide, and about one-third of patients with epilepsy become medically intractable, often requiring surgery for achievable management [1]. Precisely localizing the epileptogenic zone (EZ) is essential for successful surgical intervention. Functional imaging techniques such as ^{99m}Tc-ethyl cysteinate dimer (ECD) ictal-interictal single photon emission computed tomography (SPECT) and ^{18}F-fluorodeoxyglucose-positron emission tomography (FDG-PET) play a crucial role in identifying EZ and differentiating them from non-epileptogenic regions, particularly in patients with drug-resistant epilepsy (DRE) or discordant cases where conventional magnetic resonance imaging (MRI) has limited sensitivity [2–5]. ^{18}F-FDG PET is typically used in interictal studies for presurgical evaluation since ictal studies are difficult to obtain due to slow brain glucose uptake and the short decomposition time of ^{18}F. The main advantage of interictal ^{18}F-FDG PET over interictal ^{99m}Tc-ECD SPECT is that ^{18}F-FDG PET provides a better spatial resolution, thus results in higher diagnostic sensitivity for EZ localization [6].

In epilepsy, it was known that there is mutation of gene controlling oxidative phosphorylation affecting mitochondrial function [7–11]. Since the structure of mitochondria is disrupted in neuropathological study, the utilization of glucose in this area is less. This results in the focally reduced FDG uptake or the known relative hypometabolism in the EZ. However, the limitations of static FDG-PET (sFDG-PET) in accurately defining the surgical margin pose a significant challenge [12, 13]. Overcoming these limitations and achieving accurate localization of the seizure origin remain the greatest challenges for epilepsy pre-surgical evaluation.

Pharmacokinetic (PK) modeling plays a critical role in studying radiotracer kinetics in the human body, particularly in the field of nuclear medicine, which includes neuroimaging [14–16]. Applying kinetic models and quantifying PET data is of great interest for accurately localizing seizure onset zones in difficult epilepsy cases. While some studies have shed light on local cerebral FDG metabolism during epilepsy, our understanding of this phenomenon is limited, and most previous studies have investigated FDG kinetics in healthy adults or animals [17–22]. Their applicability to epilepsy has yet to be ascertained. As such, the establishment of PK models specific to epilepsy is a critical need, and would help optimize treatment for patients with DRE.

To achieve accurate localization of EZ, it is crucial to understand the differences in FDG kinetics and transfer rate between EZ and normal human brain areas. Therefore, the present study aimed to investigate the kinetic parameters for regional FDG uptake in DRE patients utilizing interictal dynamic FDG-PET (dFDG-PET) PK models. Quantitative analysis in terms of PK models that provide transfer rates and quantification in each region of the brain derived in this study can improve the localization of EZ for intractable epilepsy, ultimately leading to better management and outcomes for patients.

2 Materials and methods

2.1 Subjects

This study was conducted in accordance with the guidelines and regulations of our institutional review board (IRB) and obtained approval prior to patient recruitment. Consecutive DRE patients who underwent a prolonged video-electroencephalography (EEG) monitoring for presurgical evaluation and required ^{18}F-FDG PET/CT study during October 2019 to September 2020 were scanned in this study. Written informed consent was obtained from all patients prior to the examination. Patients were received anti-seizure medications as per their usual regimen at the time of scanning procedure in order to control the seizure condition. All patients underwent MRI brain epilepsy protocol with T1-weighted and T2-weighted sequences. Patients who had last seizure within 48 h prior to the examination, or lacked EEG data were excluded from the study.

2.2 Dynamic PET/CT image acquisition

To conduct the kinetic modeling, PET/CT imaging was performed using a Siemens Biograph Vision 64-slice digital PET/CT system. All patients fasted for at least 6 h before the study. Prior to injection, blood glucose levels were checked to ensure the level below 120 mg/dL. Each patient was intravenously injected with 2.6 MBq/kg of ^{18}F-FDG (half-dose protocol) and immediately followed by a 90-min dynamic PET scan. List-mode data were acquired and binned into 31 frames: 6 × 10 s, 8 × 30 s, and 17 × 300 s. PET image series for each frame was reconstructed using time-of-flight ordered subset expectation maximization (OSEM) algorithm with 8 iterations and 5 subsets, and matrix size of 440 × 440. Corrections for radioactivity decay, attenuation, model-based scatter, random events, and 5 mm Gaussian filtering of convolution kernel were applied to all PET image reconstructions. A low-dose CT scan protocol was used for attenuation correction and localization.

In this study, a non-invasive method, image-derived input function (IDIF) was utilized for alternative invasive arterial blood sampling [13, 23, 24]. The regions of interest (ROIs) were drawn by iso-contour (3D iso-contouring VOI tools using region-growing) inside the right internal carotid artery (ICA) in order to generate time-activity curve (TAC) input function for the kinetic modeling. Figure 1 shows the dFDG-PET images varying over time, which were used for generating the TAC at the internal carotid artery region as a non-invasive input function.

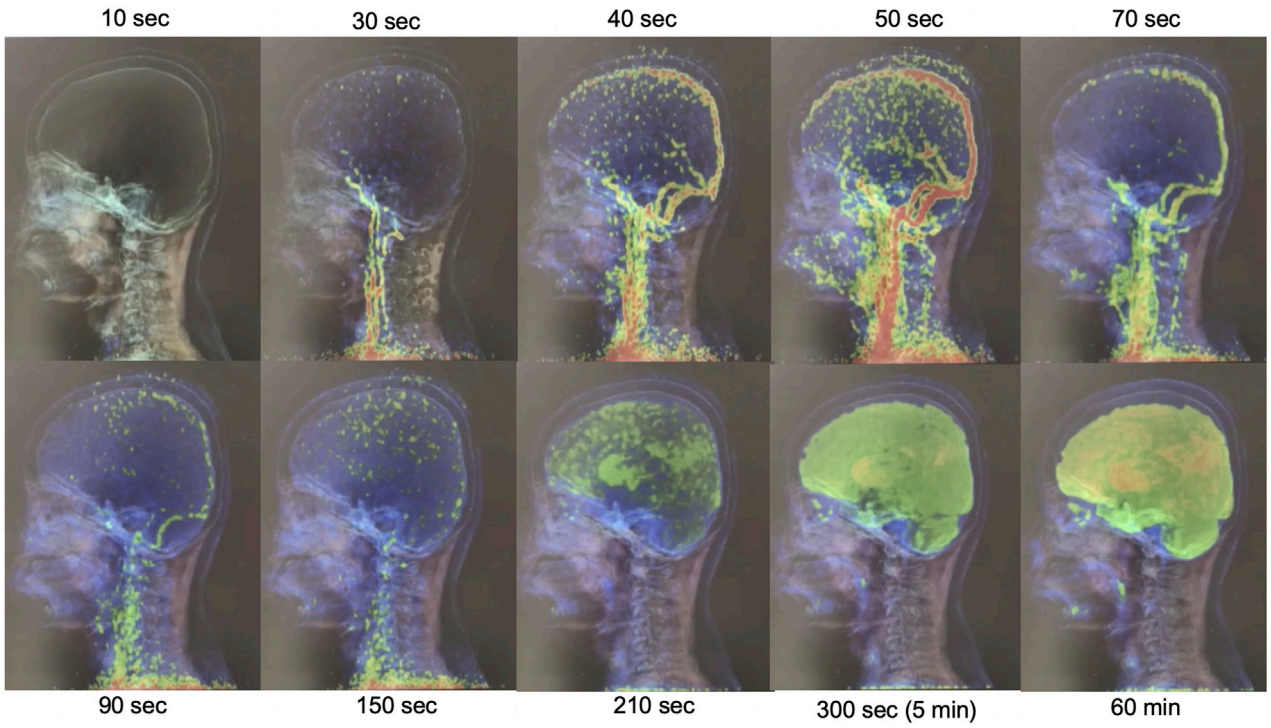

FIGURE 1
Illustration of dynamic-FDG PET images changing over-time for measuring the input function at the internal carotid artery region.

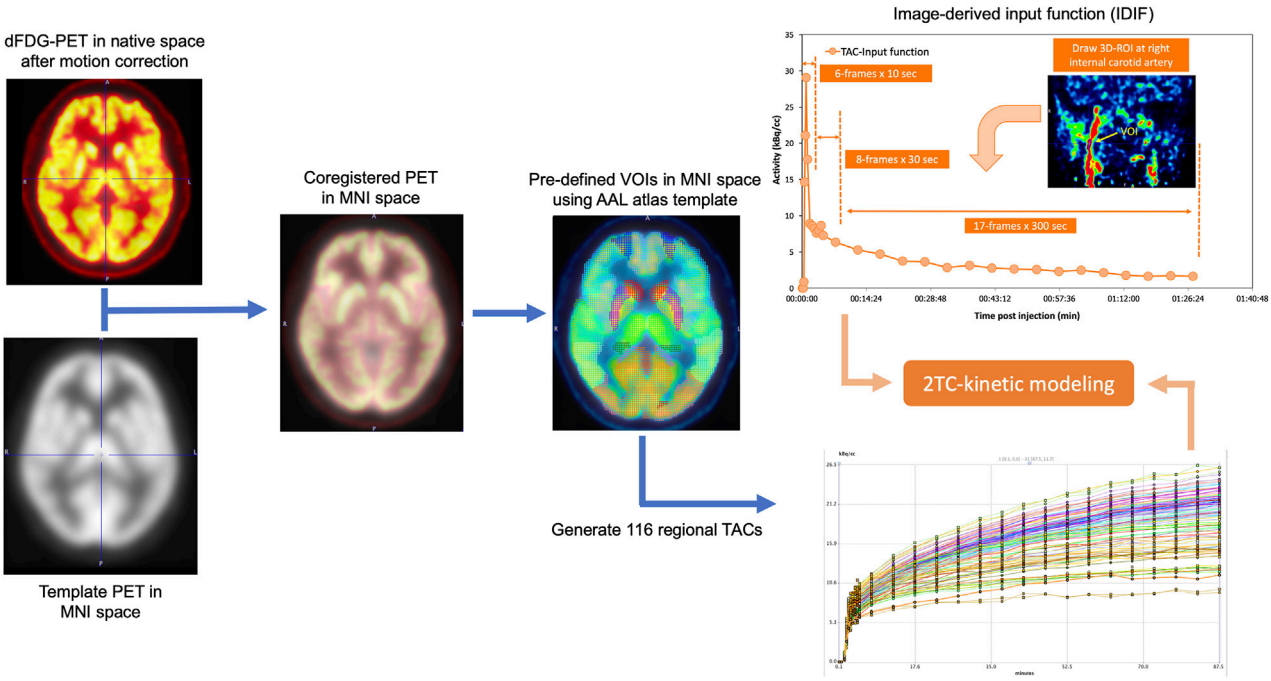

FIGURE 2
Overall workflow for PK model based on 2-tissue compartment (2TC) utilizing image-derived input function measured from dFDG-PET.

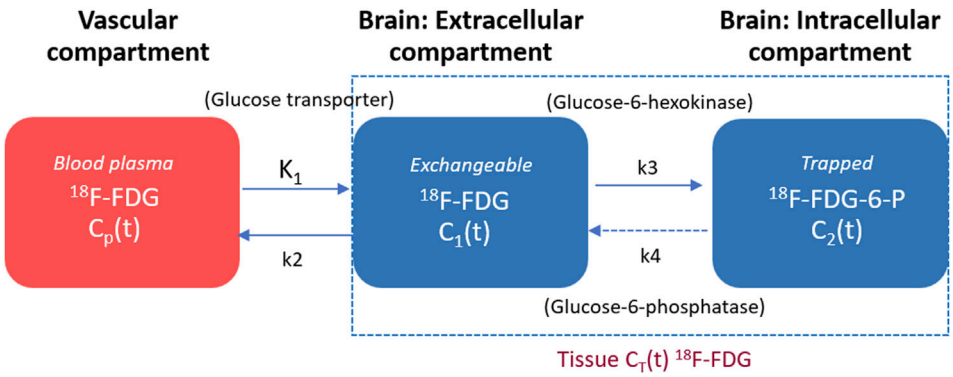

FIGURE 3
Two-tissue irreversible compartment model used for kinetic modeling of ^{18}F-FDG.

2.3 Regional tissue time-activity curves

In this study, 31 time-frames of dynamic PET images were transferred to the PMOD software (PMOD 4.101, PMOD Technologies Ltd.) to determine the FDG kinetic parameters in each patient. Image pre-processing was initiated with motion correction for the 90-min acquisition for the deformation process. PET data were averaged across the early 5 time-frames series to create a reference, which was used to perform a rigid body transform across all 31 frames of the dynamic PET. The motion-corrected PET frames were then re-sliced and co-registered with a PET template in the Montreal Neurological Institute (MNI) space using a non-rigid transform to generate a transformation matrix. The transformation information was then used to reorient the dynamic image into the MNI space. The resulting transformation matrix was inverted and applied to all ROIs to move them from the standard MNI template into the patient PET. A set of predefined volume of interests (VOIs) utilizing an automated anatomical labeling (AAL) template atlas was used to generate 58 VOIs per hemisphere, creating a total of 116 regional TACs for calculating the kinetic parameters. The overview workflow for spatial normalization, AAL atlas, which was used to automatically extract the VOIs and TACs for 116 local brain regions, and the IDIF for PK model, which was obtained using dynamic PET scan, is illustrated in Figure 2.

2.4 Compartmental modeling

By employing dFDG-PET measurements, the irreversible two-tissue compartment (2TC) model was used to develop the kinetic modeling for the dFDG-PET data utilizing the PKIN kinetic modeling module. The compartmental model used to describe the behaviors of FDG in brain tissue is depicted in Figure 3. The left compartment represents the vascular space for FDG, the center compartment represents the tissue space for free FDG, and the right compartment represents the tissue space for ^{18}F-FDG-6-phosphate (FDG-6-P). The transfer rate constants between compartmental tissues are represented by K_1 (FDG unidirectional blood-brain clearance), k_2 (efflux), and k_3 (phosphorylation). The corresponding ordinary differential equation of 2TC FDG kinetic modeling of each compartment can be expressed using Eq. 1 as follows [25, 26]:

$$\frac{d}{dt}\begin{bmatrix} C_1(t) \\ C_2(t) \end{bmatrix} = \begin{bmatrix} -(k_2+k_3) & 0 \\ k_3 & 0 \end{bmatrix}\begin{bmatrix} C_1(t) \\ C_2(t) \end{bmatrix} + \begin{bmatrix} K_1 \\ k_4 = 0 \end{bmatrix} C_{wb}(t), \quad (1)$$

where $C_{wb}(t)$ represents the ^{18}F-FDG activity concentration in whole blood derived from IDIF, $C_1(t)$ represents the activity concentration of free ^{18}F-FDG, and $C_2(t)$ represents the activity concentration of metabolized or trapped ^{18}F-FDG in the tissue space at time t. The constant K_1 (unit: mL/min/cm^3) is the rate of ^{18}F-FDG delivery from the whole blood to the tissue space, k_2 (unit: min^{-1}) is the rate constant of tracer leaving the tissue space, whereas k_3 (unit: min^{-1}) is the rate constant of ^{18}F-FDG being phosphorylated by hexokinase. Typically, this irreversible model widely assumes that the dephosphorylation process is negligible, therefore, FDG k_4 rate constant can be considered to be zero (i.e., $k_4 = 0$) for the majority of tissues. As a result, the irreversible FDG model using PMOD in this study includes 3 fittable parameters (i.e., K_1, k_2, k_3). With regard to non-linear fitting of kinetic parameters, the initial values of K_i, K_1, k_2, *and* k_3 were set to 0.05, 0.1, 0.01, and 0.01, respectively. The lower bound and the upper bound were set from zero to eight for all mentioned parameters.

The macro parameter K_i representing the net metabolic influx rate of ^{18}F-FDG consumption can be calculated using Eq. 2 as follows [26, 27]:

$$K_i = \frac{K_1 k_3}{k_2 + k_3} \quad (2)$$

The total radioactivity concentration in the tissue compartment as a function of time ($C_{PET}(t)$) that can be measured by PET is the sum of the time courses of ^{18}F-FDG in the vascular, intravascular and extravascular spaces, which can be written using Eq. 3 as follows [25–27]:

$$C_{PET}(t) = C_{wb}(t) \otimes \left(\frac{K_1 k_2}{k_2 + k_3} e^{[-(k_2+k_3)t]} + \frac{K_1 k_3}{k_2 + k_3} \right), \quad (3)$$

TABLE 1 Patient demographics data.

Id	Age/ Sex	Injected activity (MBq)	Blood glucose level (mg/dL)	Clinical localization/ lateralization	EEG location	MRI brain	Interictal PET/CT
1	26/M	150	91	Rt. temporal	Rt. mesial temporal	Probably right hippocampal sclerosis	Hypometabolism at antero-lateral right temporal lobe
2	47/F	125	77	Lt. temporal	Intermittent slow Lt. cerebral hemisphere with Lt. temporal lobe predominance	Left hippocampal sclerosis	Hypometabolism at left medial temporal lobe
3	22/F	140	81	Rt. parietal	IED spike C_z P_z, C_4, ictal EEG: repetitive spike C_z C_2 C_4	Relatively small gyri at superior aspect of anterior right temporal lobe	Suspicious of a small area of subtle mild hypometabolism at right inferomedial temporal lobe
4	38/M	125	109	Lt. hemisphere	Rt. temporal (ictal EEG Rt. temporal, IED bilateral R > L)	Left hippocampal sclerosis, Traumatic brain injury Lt. frontal and bilateral superior temporal	Hypometabolic focus at anterior left temporal lobe
5	35/M	110	85	Lt. temporal	Lt. temporal-occipital-parietal	Negative	Suspicious area of functional deficit zone at left temporal lobe (lateral, anterior and mesial)
6	31/F	112	89	Rt. temporal	Ictal EEG 4/4 Rt. (Rt frontal or Rt. Insula), IED—Rt. temporal, Lt. temporal, Lt. frontotemporal	Negative	Bilateral temporal metabolism is quite equal except area of relatively lower at left temporal pole
7	38/M	179	88	Rt. temporal	Ictal EEG: Rt. temporal 3/3, interictal EEG: Rt. temporal	Right occipital cortical-based tumor	Hypometabolism at the whole right temporal cortex
8	19/F	132	79	Rt. hemisphere	Ictal EEG → Rt. temporal-occipital-parietal 2/3 and 1/3 Lt. temporal Interictal EEG → Rt. PTO > Rt. frontal > bilat. occipital (Rt > Lt)	Left frontal focal cortical dysplasia (FCD), ± Right occipital FCD	Relatively hypometabolism at bilateral posterior parietal regions
9	41/F	132	75	Rt. temporal	Ictal EEG → Rt. temporal 8/8, interictal EEG → Rt. & Lt. temporal	Few hyperintense foci without restricted diffusion in right temporal stem. Brain atrophy	No evidence of focal hypometabolism
10	53/F	140	107	Lt. temporal	Lt temporal	Ill-defined internal architecture in posterior left hippocampal body	Hypometabolism at left lateral temporal lobe
11	36/M	145	79	Lt. hemisphere	Ictal EEG →Lt. 4/7, Rt. 3/7, interictal EEG → Lt. temporal, Lt. frontal	Few small non-specific white matter changes	Hypometabolism at the left temporal lobe

where ⊗ is the convolution operation symbol, K_1 is the rate of ^{18}F-FDG entry into the tissue, while $k_3/(k_2+k_3)$ represents how much ^{18}F-FDG is metabolized or trapped as mentioned previously. For model fitting, the fraction of blood volume (vB, unit: mL/mL) is fixed at a physiologic value of approximately 5% to reduce the number of fitted parameters [15, 18, 19, 26, 28].

2.5 Potential epileptogenic zone verification

The consensus of the area of potential EZ was made by the multidisciplinary epilepsy team which consisted of epileptogists, neurosurgeons, diagnostic radiologists and nuclear medicine physicians. At the time of this study, results of the kinetic ^{18}F-FDG study were not as part of information used for consensus decision.

2.6 Data analysis

The kinetic parameters of K_i, K_1, k_2, and k_3 derived from kinetic modeling of 116 regions in each patient were analyzed. All rate constants among these regions were ranked and the lowest value of kinetic parameters was chosen, and compared with the

TABLE 2 Summary of suspected epileptogenic zone by pre-surgical workups and associated kinetic parameter findings.

Id	Suspected epileptogenic area		Lowest K_i	Lowest K_1	Lowest k_2	Lowest k_3	Associated kinetic parameter findings
1	Rt. temporal	TLE	Rt. hippo	Temporal_Inf_l	Occipital_Inf_l	Rt. hippo	K_i, k_3
2	Lt. temporal	TLE	Lt. hippo	Parietal_Sup_l	Parietal_Sup_l	Lt. hippo	K_i, k_3
3	Inconclusive	-	Rt. hippo	Frontal_Inf_Oper_l	Frontal_Inf_Oper_l	Frontal_Sup_Orb_l	*n/a*
4	Lt. temporal	TLE	Lt. hippo	Frontal_Sup_l	Occipital_Sup_l	Lt. hippo	K_i, k_3
5	Lt. temporal	TLE	Lt. hippo	Parietal_Sup_l	Occipital_Inf_r	Occipital_Sup_r	K_i
6	Inconclusive	-	Temporal_Pole_Sup_l	Frontal_Sup_r	Precentral_l	Lt. hippo	n/a
7	Rt. temporal	TLE	Rt. hippo	Temporal_Inf_l	Frontal_Sup_l	Rt. hippo	K_i, k_3
8	Inconclusive	-	Rt. hippo	Rt. hippo	Frontal_Sup_Orb_r	Rt. hippo	n/a
9	Rt. temporal	TLE	Rt. hippo	Temporal_Pole_Mid_r	Frontal_Sup_Orb_l	Temporal_Pole_Mid_l	K_i
10	Lt. temporal	TLE	Temporal_Pole_Mid_l	Temporal_Pole_Mid_l	Temporal_Pole_Mid_l	Temporal_Pole_Mid_l	K_i, k_1, k_2, k_3
11	Inconclusive	-	Parietal_Sup_r	Temporal_Pole_Sup_l	Temporal_Pole_Sup_l	Lt. hippo	n/a

Tem, temporal; TLE, temporal lobe epilepsy; Hippo, hippocampus; Sup, superior; Mid, middle; Inf, inferior; n/a, unable to associate kinetic parameter with the epileptogenic zone due to inconclusive epileptogenic area.

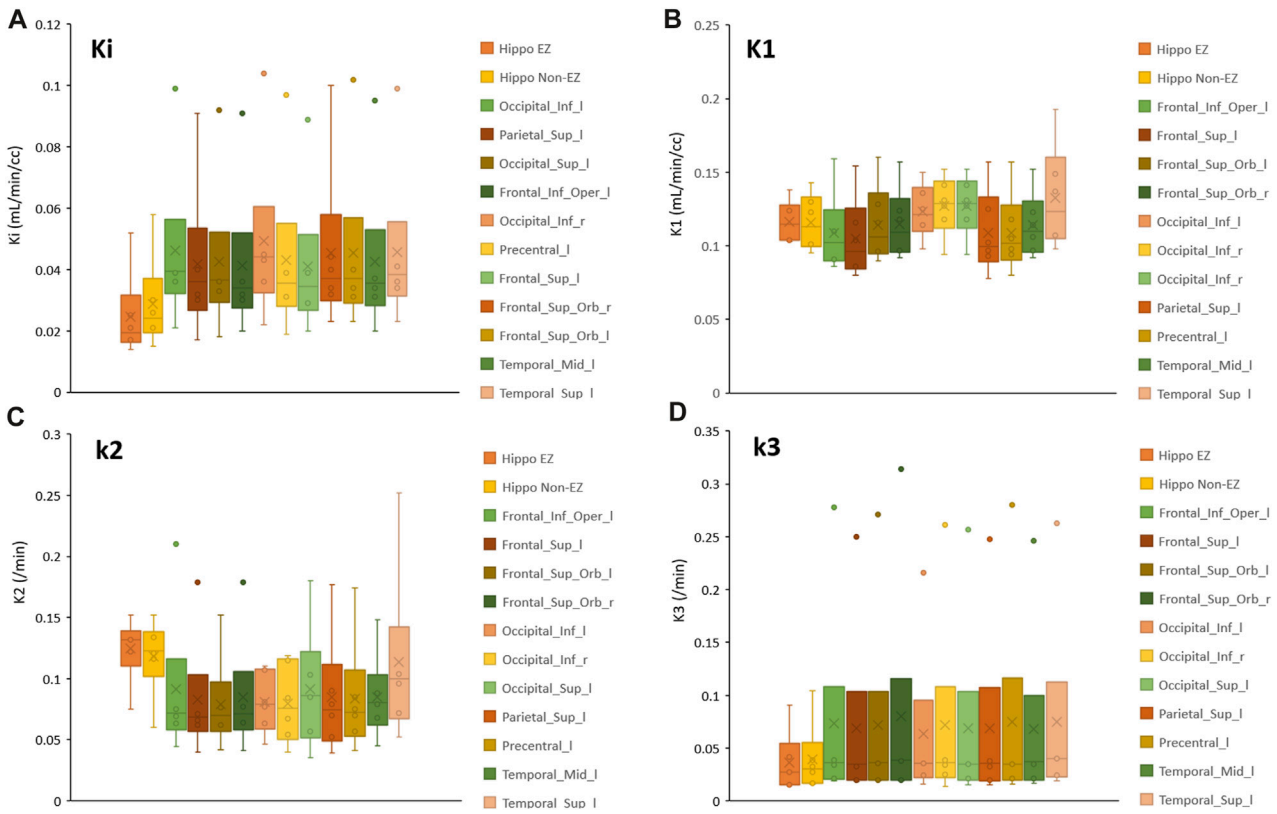

FIGURE 4
Box plot showing the rate constants in presumed EZ regions for **(A)** FDG net metabolic flux; K_i **(B)** FDG unidirectional blood-brain clearance; K_1 **(C)** efflux; k_2 and **(D)** phosphorylation; k_3.

presumed EZ identified by the concordance of at least 3 out of 4 pre-surgical workups, which are clinical semiology, scalp EEG, MRI, and static FDG-PET visual analysis results. The presumed EZ as established through the previously mentioned concordance was determined by assigning it to a specific region based on the AAL atlas.

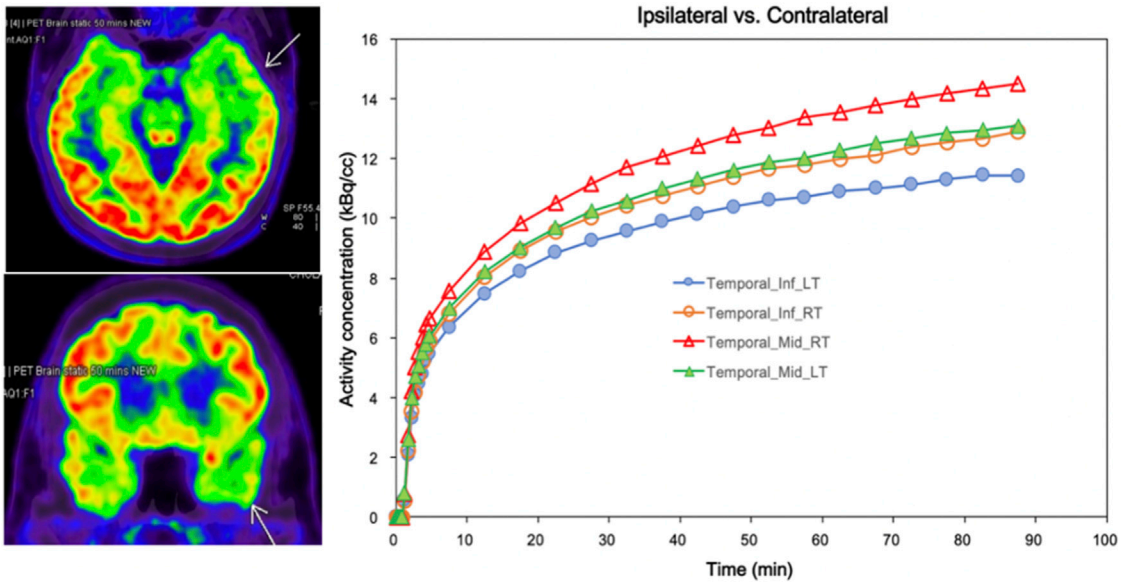

FIGURE 5
Comparison of biokinetic of ipsilateral and contralateral in patient who has suspected epileptic foci at Lt temporal lobe (Pt.10/F). The arrows on PET images indicate the hypometabolic areas at Lt temporal lobe corresponds to the lowest K_i (0.017) and k_3 (0.034) at Lt middle temporal pole. Time-activity curves of dynamic FDG PET were generated in both the epileptogenic foci and the counterpart homologous regions in the contralateral hemispheres for calculating the kinetic parameters.

3 Results

Eleven patients with DRE, aged 19–53 years (5 males, 6 females, mean age 35.1 ± 10.2 years) were carried out. Table 1 presents the characteristics of the study subjects with DRE referred to dFDG-PET in this study. The mean ^{18}F-FDG activity administered to the patients was 135.5 ± 19.2 MBq, ranging from 110–179 MBq, and all dynamic scans of the 11 DRE patients were successful. Negative MRI findings were found in 2 patients (patient 5 and patient 6). Table 2 lists the summary of suspected area of EZ and related kinetic parameter findings. In this study, the suspected areas for EZ were found at the left temporal lobe in 4 patients, right temporal lobe in 3 patients, and inconclusive in 4 patients (patients 3, 6, 8, and 11). We thus excluded the patients who had inconclusive EZ due to the discordance of clinical, EEG, MRI, and PET/CT interpretation from the analysis of this study. When the lowest value of kinetic parameters was chosen and compared with the presumed EZ, we found that the net metabolic flux K_i and the rate constant k_3 kinetic parameters provided high association with the suspected EZ in all patients. The lowest K_i values were concordance with the suspected EZ in all the remaining EZ identifiable 7 patients, while the lowest k_3 values were found concordance in 5 out of 7 patients (71.7%).

Figure 4 illustrates the box plots of the rate constants of K_i, K_1, k_2 and k_3 in presumed EZ regions found in this study. The plots indicated that the values of K_i and k_2 were significantly lower and higher, respectively, in the presumed EZ regions compared to other regions. The details of regional FDG kinetic parameters determined from 11 DRE patients are provided in Supplementary Material S1.

Figure 5 illustrates a comparison of the biokinetic in the presumed EZ and homologous regions in the contralateral hemisphere of a patient suspected to have presumed EZ in the left temporal region, showing hypometabolic areas at the left temporal lobe. The kinetic parameters were calculated from TAC generated from both the epileptogenic foci and counterpart homologous regions in the contralateral hemispheres. The lowest K_i values of 0.017 mL/min/cm^3 and k_3 of 0.034 min^{-1} were found in the left middle temporal pole region for this case, which were associated with the clinical diagnosis and EEG location.

4 Discussion

Improving the localization of epileptic foci in DRE is of great interest, as visualization of hypometabolic areas on FDG-PET is non-specific to the EZ [29, 30]. In recent years, there have been huge efforts in using nuclear medicine techniques, both by visual and by quantitative analysis, for better localizing EZ [30]. Among these, the study of FDG biokinetic pattern in epilepsy is a method that has potential to benefit patients in clinical settings by avoiding invasive diagnoses [13]. To address this, we further investigated the kinetic parameters of regional FDG uptake using a 2TC-PK model of dFDG-PET in DRE patients for pre-surgical evaluation to see if a single kinetic parameter or a combination would benefit in EZ localization or not. Based on our results, we found that the lowest net metabolic flux (K_i) values were concordance with all of the presumed EZ. In addition, the rate constant of ^{18}F-FDG phosphorylation (k_3) was also lowest in 5 of 7 patients. Thus, both of these kinetic parameters can be used in isolation without comparison to any other brain reference regions (e.g., contralateral homologous brain region, cerebellum, pons, *etc.*). Of note is that although some patients showed that there were other structural abnormalities on their MRI (patients 4 and 9) or even if there was a lesion not related

to epileptogenicity (patient 7), the lowest K_i and k_3 were still located at the epileptogenic region. So, the utilization of dFDG-PET imaging combined with pharmacokinetic modeling has a potential to provide important information for the assessment and characterization of epileptic foci in DRE patients with discordant pre-surgical investigation data in addition to the use of FDG-PET visual analysis alone.

According to distribution of the kinetic values in representative brain regions illustrated in Figure 4, we observed that K_i and k_3 showed decreasing trends, while k_2 showed higher values in the presumed EZ. We also found that K_i was the lowest in all seven EZs, k_3 was the lowest in 5 out of 7 patients, and k_2 was the highest in 4 out of 7 patients. According to these results, we suggested that k_3's low value and high k_2 might contribute to the low K_i. The high k_2 values could be due to the accumulation of radiotracer in the extracellular compartment in the EZ, resulting in a high flux of the radiotracer back into the bloodstream.

Reference [18] described a mathematical model based on blood sampling to determine a local cerebral metabolic rate of glucose in 13 healthy subjects. The average kinetic parameters of FDG (K_i, K_1, k_2 and k_3) in gray matter were 0.0334 ± 0.0058, 0.102 ± 0.028, 0.130 ± 0.066, and 0.062 ± 0.019 min^{-1} respectively, while in white matter were 0.0154 ± 0.0035, 0.054 ± 0.014, 0.109 ± 0.044, and 0.045 ± 0.019 min^{-1} respectively. Although the kinetic parameters K_i, K_1, k_2 and k_3 in the suspected EZ of our study, as depicted in Figure 4, closely matched those reported by Huang et al, there were notable exceptions in the hippocampus areas for both EZ and non-EZ regions. It is important to note that Huang et al. reported their kinetic parameters in gray matter and white matter regions. Consequently, direct comparisons between their findings and those of our study may not be comparable, as we have reported the kinetic parameters specific to each local region derived from the AAL atlas.

In comparison to our study, Ref. [13] assessed the use of asymmetry indexes (ASYM) derived from dFDG-PET and from static FDG PET to identify the pathophysiology of metabolism in intractable epilepsy. They found that hypometabolism within epileptic foci may be related to reduced glucose phosphorylation (k_3) compared to capillary influx (K_1). This is in line with our study, in which k_3 was usually lowest in the presumed EZ. This was also proven in a study of patients with temporal lobe epilepsy, in which the oxidative metabolism of glucose was reduced in the area of epileptogenicity, not the decrease of neuronal density [31]. The lowest net flux (K_i) in our study may be the result of low k_3 as it is frequently the lowest parameter in the EZ. This finding corresponds with the previous genetic and pathological studies mentioned earlier in the introduction that the affecting pathology in epilepsy focused on phosphorylation, aka hexokinase activity or k_3 in kinetic modeling. However, there might also be other factors causing low K_i because some of the presumed EZ did not show lowest k_3 value.

The study by Ref. [12] utilized the parametric quantification from dFDG-PET imaging to locate hypometabolic foci in patients with no MRI evidence of focal epilepsy. The lowest negative z-scores were identified as hypometabolic. Their study found that dFDG-PET was able to detect focal regions of altered metabolism in all cases where standard clinical FDG-PET found no abnormalities. However, the authors suggest that further study is warranted to evaluate the specificity and sensitivity of dFDG-PET in larger cohorts to determine whether glucose dynamics can improve clinical utility for localization of epileptic foci over standard static PET techniques.

The reduced interictal uptake of ^{18}F-FDG in the temporal lobe ipsilateral to the seizure focus in temporal lobe epilepsy (TLE) patients was studied by Ref. [32]. They attributed this reduction to regional differences in the lumped constant (lambda), indicative of altered glucose metabolism. Our study aligns with this finding by demonstrating altered glucose metabolism in DRE patients, emphasizing the importance of accurate metabolic assessments for epilepsy evaluation. The study by Ref. [33] focused on the coupling between regional cerebral glucose metabolism (rCMRGlc) and blood flow (rCBF) in TLE patients. They found a mismatch between metabolism and blood flow in the temporomesial structures, indicating that alterations in glucose metabolism might not always correspond to changes in blood flow. Their study resonnates with our findings, as we observed a specific kinetic parameter, the K_i and k_3 to be a more reliable indicator of EZ compared to traditional static measures.

The use of PET templates instead of T1-weighted MRI in the MNI space for generating the transformation matrix allowed the results of automated AAL segmentation comparable to the T1-weighted MRI templates. In this study, we opted for an alternative approach for invasive arterial blood sampling in patients by extracting the IDIF from the ICA instead. This non-invasive method has demonstrated its robustness through a number of studies [13, 23, 24, 27, 34, 35]. Furthermore, it can offer relative simplicity and appropriateness for clinical implementation especially for patients with DRE. Unfortunately, this study did not correct the partial volume effect (PVE) for the IDIF, as outlined in previously mentioned literature. Consequently, the measured activity concentration employed to generate the IDIF may potentially be underestimated due to this effect, especially in smaller vessels. This underestimation could influence the peak of the IDIF TAC and the fitting of the kinetic model, potentially leading to an overestimation of the kinetic parameters. We acknowledge this limitation in our study. Another limitation is the number of studied subjects was relatively small. Since only one patient proceeded with epilepsy surgery, the localization of epileptic foci was not uniformly confirmed through the standard outcome of seizure remission following the resection of the identified regions. Therefore, further studies with larger cohorts and follow-up data after epilepsy surgery are merited to validate the findings.

5 Conclusion

This study investigated whether kinetic modeling approach has a potential to improve FDG-PET localization of epileptic foci in DRE patients. The findings from this study demonstrated that the net metabolic flux (K_i) and phosphorylation (k_3) of ^{18}F-FDG, as investigated using 2-tissue irreversible compartment model in dFDG-PET, were concordance with suspected epileptogenic regions with K_i as the most reliable parameter for identifying EZ. The presumed kinetic parameters obtained from this study provide non-invasive indicators and complement clinical setting to define the potential epileptic foci in addition to the other clinical

information. This approach could contribute to more effective treatment options for DRE patients.

Data availability statement

The original contributions presented in the study are included in the article/Supplementary Material, further inquiries can be directed to the corresponding author.

Ethics statement

The studies involving humans were approved by the Faculty of Medicine, Chulalongkorn University. The studies were conducted in accordance with the local legislation and institutional requirements. The participants provided their written informed consent to participate in this study.

Author contributions

KK contributed the concept, methods, patient data collection and analysis, kinetic modeling, and manuscript drafting. CS contributed the concept, image analysis, and manuscript editing. CL contributed the patient recruitment, EEG data analysis, and manuscript editing. SJ contributed the patient recruitment. AJ contributed the image acquisition and patient data collection. TH contributed the concept. ST contributed the concept, methods, data analysis and interpretation, and manuscript drafting. All authors contributed to the article and approved the submitted version.

Funding

This work was supported by the Thailand Research Fund, Thailand Science Research and Innovation (grant number MRG6180141), and the Ratchadapiseksompotch Fund, Chulalongkorn University (grant number GB-A_61_006_30_02).

Acknowledgments

The authors would like to express their gratitude to epilepsy monitoring unit (EMU) team for taking care of the patients and sending patients for recruitment. We also thank to all Nuclear Medicine technologists at King Chulalongkorn Memorial Hospital, and at National Cyclotron and PET center Chulabhorn Hospital, Chulabhorn Royal Academy, for their help in patient data collection and image acquisition.

Conflict of interest

The authors declare that the research was conducted in the absence of any commercial or financial relationships that could be construed as a potential conflict of interest.

Publisher's note

All claims expressed in this article are solely those of the authors and do not necessarily represent those of their affiliated organizations, or those of the publisher, the editors and the reviewers. Any product that may be evaluated in this article, or claim that may be made by its manufacturer, is not guaranteed or endorsed by the publisher.

Supplementary material

The Supplementary Material for this article can be found online at: https://www.frontiersin.org/articles/10.3389/fphy.2023.1233059/full#supplementary-material

References

1. Kwan P, Brodie MJ. Early identification of refractory epilepsy. *New Engl J Med* (2000) 342:314–9. doi:10.1056/NEJM200002033420503

2. Kim S, Mountz JM. SPECT imaging of epilepsy: an overview and comparison with F-18 FDG PET. *Int J Mol Imaging* (2011) 2011:e1–e9. doi:10.1155/2011/813028

3. Nasrallah I, Dubroff J. An overview of PET neuroimaging. *Semin Nucl Med* (2013) 43:449–61. doi:10.1053/j.semnuclmed.2013.06.003

4. Tepmongkol S, Srikijvilaikul T, Vasavid P. Factors affecting bilateral temporal lobe hypometabolism on ^{18}F-FDG PET brain scan in unilateral medial temporal lobe epilepsy. *Epilepsy Behav* (2013) 29:386–9. doi:10.1016/j.yebeh.2013.08.017

5. Sarikaya I. PET studies in epilepsy. *Am J Nucl Med Mol Imaging* (2015) 5:416–30.

6. Alabart NB, Parego XS. Imaging in epilepsy: functional studies. *Radiología* (2012) 54:124–36. doi:10.1016/j.rxeng.2012.06.002

7. Naviaux RK, Nguyen KV. POLG mutations associated with Alpers' syndrome and mitochondrial DNA depletion. *Ann Neurol Official J Am Neurol Assoc Child Neurol Soc* (2004) 55:706–12. doi:10.1002/ana.20079

8. Shoffner JM, Lott MT, Lezza AM, Seibel P, Ballinger SW, Wallace DC. Myoclonic epilepsy and ragged-red fiber disease (MERRF) is associated with a mitochondrial DNA tRNALys mutation. *Cell* (1990) 61:931–7. doi:10.1016/0092-8674(90)90059-n

9. Zsurka G, Hampel K, Nelson I, Jardel C, Mirandola S, Sassen R, et al. Severe epilepsy as the major symptom of new mutations in the mitochondrial tRNAPhe gene. *Neurology* (2010) 74:507–12. doi:10.1212/WNL.0b013e3181cef7ab

10. Kunz WS, Kudin AP, Vielhaber S, Blümcke I, Zuschratter W, Schramm J, et al. Mitochondrial complex I deficiency in the epileptic focus of patients with temporal lobe epilepsy. *Ann Neurol* (2000) 48:766–73. doi:10.1002/1531-8249(200011)48:5<766::aid-ana10>3.0.co;2-m

11. Meldrum BS. Excitotoxicity and selective neuronal loss in epilepsy. *Brain Pathol* (1993) 3:405–12. doi:10.1111/j.1750-3639.1993.tb00768.x

12. Seshadri V, Zarroli KA, Schetlick RS, Massey JC, Reyes JM, Eluvathingal Muttikal TJ, et al. Dynamic FDG-PET in localization of focal epilepsy: A pilot study. *Epilepsy Behav* (2021) 122:108204. doi:10.1016/j.yebeh.2021.108204

13. Tang Y, Liow J-S, Zhang Z, Li J, Long T, Li Y, et al. The evaluation of dynamic FDG-PET for detecting epileptic foci and analyzing reduced glucose phosphorylation in refractory epilepsy. *Front Neurosci* (2019) 12:993. doi:10.3389/fnins.2018.00993

14. Buratachwatanasiri W, Chantadisai M, Onwanna J, Chongpison Y, Rakvongthai Y, Khamwan K. Pharmacokinetic modeling of ^{18}F-FDOPA PET in the human brain for early Parkinson's disease. *Mol Imaging Radionuclide Ther* (2021) 30:69–78. doi:10.4274/mirt.galenos.2021.08831

15. Khamwan K, Plyku D, O'Reilly SE, Goodkind A, Cao X, Fahey FH, et al. Pharmacokinetic modeling of [^{18}F] fluorodeoxyglucose (FDG) for premature infants, and newborns through 5-year-olds. *EJNMMI Res* (2016) 6:28–11. doi:10.1186/s13550-016-0179-6

16. Sgouros G, Frey EC, Bolch WE, Wayson MB, Abadia AF, Treves ST. An approach for balancing diagnostic image quality with cancer risk: application to pediatric

diagnostic imaging of ^{99m}Tc-dimercaptosuccinic acid. *J Nucl Med* (2011) 52:1923–9. doi:10.2967/jnumed.111.092221

17. Eberlein U, Bröer JH, Vandevoorde C, Santos P, Bardiès M, Bacher K, et al. Biokinetics and dosimetry of commonly used radiopharmaceuticals in diagnostic nuclear medicine–a review. *Eur J Nucl Med Mol Imaging* (2011) 38:2269–81. doi:10.1007/s00259-011-1904-z

18. Huang SC, Phelps ME, Hoffman EJ, Sideris K, Selin CJ, Kuhl DE. Noninvasive determination of local cerebral metabolic rate of glucose in man. *Am J Physiology-Endocrinology Metab* (1980) 238:E69–E82. doi:10.1152/ajpendo.1980.238.1.E69

19. Loessner A, Alavi A, Lewandrowski KU, Mozley D, Souder E, Gur R. Regional cerebral function determined by FDG-PET in healthy volunteers: normal patterns and changes with age. *J Nucl Med* (1995) 36:1141–9.

20. Löscher W. Critical review of current animal models of seizures and epilepsy used in the discovery and development of new antiepileptic drugs. *Seizure* (2011) 20:359–68. doi:10.1016/j.seizure.2011.01.003

21. Mirrione MM, Tsirka SE. Neuroimaging in animal seizure models with ^{18}F-FDG-PET. *Epilepsy Res Treat* (2011) 2011:e1–e8. doi:10.1155/2011/369295

22. Van Bogaert P, Wikler D, Damhaut P, Szliwowski H, Goldman S. Regional changes in glucose metabolism during brain development from the age of 6 years. *Neuroimage* (1998) 8:62–8. doi:10.1006/nimg.1998.0346

23. Zanotti-Fregonara P, Liow J-S, Fujita M, Dusch E, Zoghbi SS, Luong E, et al. Image-derived input function for human brain using high resolution PET imaging with [^{11}C](R)-rolipram and [^{11}C] PBR28. *PLoS One* (2011) 6:e17056. doi:10.1371/journal.pone.0017056

24. Croteau E, Lavallée É, Labbe SM, Hubert L, Pifferi F, Rousseau JA, et al. Image-derived input function in dynamic human PET/CT: methodology and validation with ^{11}C-acetate and ^{18}F-fluorothioheptadecanoic acid in muscle and ^{18}F-fluorodeoxyglucose in brain. *Eur J Nucl Med Mol Imaging* (2010) 37:1539–50. doi:10.1007/s00259-010-1443-z

25. Wang G, Nardo L, Parikh M, Abdelhafez YG, Li E, Spencer BA, et al. Total-body PET multiparametric imaging of cancer using a voxelwise strategy of compartmental modeling. *J Nucl Med* (2022) 63:1274–81. doi:10.2967/jnumed.121.262668

26. Rahmim A, Lodge MA, Karakatsanis NA, Panin VY, Zhou Y, McMillan A, et al. Dynamic whole-body PET imaging: principles, potentials and applications. *Eur J Nucl Med Mol Imaging* (2019) 46:501–18. doi:10.1007/s00259-018-4153-6

27. Fahrni G, Karakatsanis NA, Di Domenicantonio G, Garibotto V, Zaidi H. Does whole-body Patlak ^{18}F-FDG PET imaging improve lesion detectability in clinical oncology? *Eur Radiol* (2019) 29:4812–21. doi:10.1007/s00330-018-5966-1

28. Hays MT, Segall GM. A mathematical model for the distribution of fluorodeoxyglucose in humans. *J Nucl Med* (1999) 40:1358–66.

29. Tepmongkol S, Tangtrairattanakul K, Lerdlum S, Desudchit T. Comparison of brain perfusion SPECT parameters accuracy for seizure localization in extratemporal lobe epilepsy with discordant pre-surgical data. *Ann Nucl Med* (2015) 29:21–8. doi:10.1007/s12149-014-0905-y

30. Sukprakun C, Limotai C, Khamwan K, Pasawang P, Tepmongkol S. A novel method of seizure onset zone localization by serial Tc-99m ECD brain perfusion spect clearance patterns. *Brain Imaging Behav* (2022) 16:1646–56. doi:10.1007/s11682-022-00640-x

31. Vielhaber S, Von Oertzen JH, Kudin AF, Schoenfeld A, Menzel C, Biersack H, et al. Correlation of hippocampal glucose oxidation capacity and interictal FDG-PET in temporal lobe epilepsy. *Epilepsia* (2003) 442:193–9. doi:10.1046/j.1528-1157.2003.38102.x

32. Reutens DC, Gjedde AH, Meyer E. Regional lumped constant differences and asymmetry in fluorine-18-FDG uptake in temporal lobe epilepsy. *J Nucl Med* (1998) 39:176–80.

33. Fink G, Pawlik G, Stefan H, Pietrzyk U, Wienhard K, Heiss WD. Temporal lobe epilepsy: evidence for interictal uncoupling of blood flow and glucose metabolism in temporomesial structures. *J Neurol Sci* (1996) 137:28–34. doi:10.1016/0022-510x(95)00323-t

34. Hammers A, Panagoda P, Heckemann RA, Kelsch W, Turkheimer FE, Brooks DJ, et al. [^{11}C] flumazenil PET in temporal lobe epilepsy: do we need an arterial input function or kinetic modeling? *J Cereb Blood Flow Metab* (2008) 28:207–16. doi:10.1038/sj.jcbfm.9600515

35. Bertrán M, Martínez N, Carbajal G, Fernández A, Gómez Á. An open tool for input function estimation and quantification of dynamic PET FDG brain scans. *Int J Comput Assist Radiol Surg* (2016) 11:1419–30. doi:10.1007/s11548-015-1307-x

frontiers | Frontiers in Physics

TYPE Brief Research Report
PUBLISHED 15 December 2023
DOI 10.3389/fphy.2023.1303690

OPEN ACCESS

EDITED BY
Thomas Beyer,
Medical University of Vienna, Austria

REVIEWED BY
Siddesh V. Hartimath,
Institute of Bioengineering and Bioimaging (IBB), A*STAR, Singapore
Roberto Francischello,
University of Pisa, Italy

*CORRESPONDENCE
Thomas Wanek,
thomas.wanek@meduniwien.ac.at

RECEIVED 28 September 2023
ACCEPTED 20 November 2023
PUBLISHED 15 December 2023

CITATION
Wanek T, Mairinger S, Filip T, Löbsch M, Stanek J and Kuntner C (2023), Multi-organ comparison and quantification parameters of [18F]THK-5317 uptake in preclinical mouse models of tau pathology.
Front. Phys. 11:1303690.
doi: 10.3389/fphy.2023.1303690

Multi-organ comparison and quantification parameters of [^{18}F]THK-5317 uptake in preclinical mouse models of tau pathology

Thomas Wanek[1,2]*, Severin Mairinger[2,3], Thomas Filip[2,4], Mathilde Löbsch[2,5], Johann Stanek[1,2] and Claudia Kuntner[1,2,6]

[1]Department of Biomedical Imaging and Image-guided Therapy, Medical University of Vienna, Vienna, Austria, [2]Preclinical Molecular Imaging, AIT Austrian Institute of Technology GmbH, Seibersdorf, Austria, [3]Department of Clinical Pharmacology, Medical University of Vienna, Vienna, Austria, [4]Institute of Animal Breeding and Genetics and Biomodels Austria, University of Veterinary Medicine, Vienna, Austria, [5]Core Facility Laboratory Animal Breeding and Husbandry (CFL), Medical University of Vienna, Vienna, Austria, [6]Medical Imaging Cluster, Medical University of Vienna, Vienna, Austria

Introduction: Current small-animal PET instrumentation provides sufficient resolution, sensitivity, and quantitative accurate information on the radiotracer distribution within the whole body. However, most preclinical imaging studies focus on the disease-related organ of interest and do not use the total body information provided by small-animal PET. In this study, we investigated the distribution of [^{18}F]THK-5317 (also referred to as (*S*)-[^{18}F]THK-5117), a radiotracer initially developed to visualize tau deposits in the brain, in two transgenic mouse models of tau overexpression and littermate controls at different ages and of both sexes. We compared multiple quantitative parameters of radiotracer uptake in multiple organs of mice to investigate sex, age, or strain-related differences.

Methods: After intravenous administration, 60-min dynamic PET scans were acquired, followed by venous blood sampling, organ harvesting, and metabolite analysis by radio-thin-layer chromatography.

Results: Blood pharmacokinetics and metabolism of [^{18}F]THK-5317 significantly differed between males and females across all strains. Sex-related differences in organ V_Ts were identified from two-way ANOVA analysis. Organ-to-blood concentration ratios correlated well with organ V_Ts in all investigated organs.

Conclusion: Following our workflow, a straightforward multiple-organ analysis of [^{18}F]THK-5317 uptake in mice was easily achievable. From the derived quantitative parameters, the organ-to-blood values correlate best with the calculated V_Ts. Given the active incorporation of 3R principles into preclinical quantitative imaging, we propose that this workflow might be suitable to select novel radiotracer candidates before more complex kinetic models, comprising invasive methods such as full arterial blood sampling, for radiotracer quantification are applied.

KEYWORDS

[^{18}F]THK-5317, small-animal PET, tauopathy, sex-difference, tracer metabolism, brain uptake parameters

1 Introduction

Quantitative, non-invasive imaging technologies utilizing small laboratory animals are essential for research on the biodistribution of new drugs, disease progression, or response to novel therapeutic approaches. The availability of specifically bred or genetically modified mouse disease models, as well as technological advances in small-animal imaging instrumentation and methodologies, have led to significant discoveries on the molecular origins of these illnesses and triggered research on various novel therapeutic approaches [1–4].

Among the non-invasive imaging modalities, especially positron emission tomography (PET), utilizing radiolabeled compounds (radiotracers) offers considerable versatility in studying diseases from multiple perspectives and at different disease stages. Despite numerous species differences between rodents and humans, PET studies usually enable a high degree of translatability as many correlative and longitudinal study designs utilized in basic research can be modified to match current clinical safety requirements with reasonable effort [5–8].

Current small-animal PET instrumentation offers sufficient spatial resolution, high sensitivity for dynamic imaging, and, provided sufficient efforts are directed toward standardized protocols, a high degree of quantitative accuracy for rodent brain studies. Moreover, multimodal preclinical PET/CT scanners are available with an axial field of view (FOV) large enough to acquire whole-body mouse images in a single scan. As such, total-body positron emission tomography (TB-PET) scans, which are now increasingly emerging in clinical imaging, are easily achievable in mice. Such total-body scans provide holistic and dynamic information on radiotracer distribution within the scanned subject during the whole acquisition time. However, most preclinical imaging studies only focus on the disease-related organ of interest and do not use total body information. This is especially true for neurological diseases or disorders, where the brain is the focus [9–13].

TB-PET enables the quantification of radiotracer pharmacokinetics throughout the entire body or multiple organ systems in a single scan acquisition. These data form the basis for subsequent kinetic modeling where the distribution of radioactivity in the target organ and the input function (the time course of the radiotracer in the blood or plasma) are used to determine the local tissue concentration(s). Further graphical evaluation methods to quantify the organ uptake in terms of the distribution volume (V_T) provide non-invasive, quantitative measures that can then be observed in a systems biology approach [14–17].

The challenge in using whole-organ (blood/plasma-based) kinetic modeling in small-animal imaging lies in the requirement for an arterial blood input function and the determination of radioactive metabolites. In mice, however, arterial blood sampling is often impossible and limited by the small total blood volume. Even when arterial blood sampling is performed, the study design is limited to non-recovery imaging procedures, rendering longitudinal studies in aged animals or comparative studies of different therapeutic interventions in the same animal impossible. Closed-loop systems to avoid blood loss during such imaging procedures require long pre-scan preparation times, surgically skilled personnel, and are not feasible in a high-throughput manner [18]. Alternatively, a whole-blood based, non-invasive image-derived input function (IDIF), derived from small-animal total-body images, can be obtained, an approach that has been shown to be feasible in multiple preclinical radiotracer evaluations [19]. Using modern small-animal PET scanners, IDIF can be accurately derived by measuring the time–radioactivity concentration curves (TACs) in the left ventricle or a major vessel in mice [20]. For certain radiotracers, using population-based IFs and metabolization data has shown to be feasible in rodents [21–23].

Another aspect of adding total body information to small-animal PET might be the identification of sex differences in radiotracer pharmacokinetics, response to therapies, or metabolic changes during disease progression. Consequently, putative sex differences may be identified and addressed accordingly. It is commonly recognized that organ size and function change during aging and are sex-dependent. However, such differences are not reflected by changes in the whole-body weight of the respective animals [24]. This is particularly relevant for the excretory organs such as the liver and the kidneys, which directly influence radiotracer metabolism and elimination kinetics.

We recently reported one such sex difference in an APP/h Tau rat model so far as the plasma pharmacokinetics and metabolism of the putative tau radiotracer [^{18}F]THK-5317 (also referred to as (*S*)-[^{18}F]THK-5117) were different between male and female rats [22].

In the present study, our goal is to investigate the multi-organ distribution of [^{18}F]THK-5317 in the brain and peripheral tissues in two transgenic mouse models of tau overexpression, as well as their littermate controls, across various age groups and both sexes. Peripheral tau accumulation has been reported recently and has not yet been explored with dynamic PET [25,26]. We further aim to introduce a systematic workflow for performing quantitative analysis on multiple organs in mice. Lastly, we compared different quantification measures other than the Logan volume of distribution (V_T) as outcome parameters for [^{18}F]THK-5317 uptake.

2 Materials and methods

2.1 Chemicals

Chemicals were purchased from Sigma-Aldrich Handels GmbH (Vienna, Austria) and used without further purification. Radiosynthesis of [^{18}F]THK-5317 was performed, following the established protocols [22,27]. For this study, [^{18}F]THK-5317 (n = 15) was synthesized with a decay-corrected radiochemical yield of 12% ± 4% and a radiochemical purity of 95% ± 3% in a synthesis time of 76 ± 4 min. Molar activity at the end of synthesis was 498 ± 281 GBq/μmol.

2.2 Animals

We examined hTau (B6.Cg-*Mapt*$^{tm1(EGFP)Klt}$ Tg(MAPT)8cPdav/J) [28] and TMHT (Thy-1-mutated human tau) [29], as well as non-transgenic hTau littermates (as ntg-control), in this study. In total, 86 mice purchased from QPS Austria GmbH (Grambach, Austria) were used. Mice were scanned at 20, 44, or 68 weeks of age, including both sexes. A detailed study summary is provided in Supplementary

Table S1. Mice were housed in a temperature- and humidity-controlled facility under a cycle of 12/12 h of light/dark with free access to standard laboratory animal diet (ssniff R/M-H, ssniff Spezialdiäten GmbH, Soest, Germany) and water *ad libitum*. An acclimatization period of at least 1 week was allowed before animals were used in the experiments. Of the 86 mice, 14 mice, especially of the 44- and 68-week age groups, were lost during imaging (e.g., technical problems with the scanner and breathing arrest under anesthesia while scanning), yielding 72 PET datasets available for analysis. In one mouse, blood sampling and tissue harvesting were not possible. The study was approved by the national authorities (LF1-TVG-48/028-2016; Amt der Niederösterreichischen Landesregierung, Austria), and study procedures followed the European Communities Council Directive 2010/63/EU. The animal experimental data reported in this study comply with the ARRIVE (Animal Research: Reporting of *in Vivo* Experiments) guidelines 2.0 [30].

2.3 Small-animal PET imaging

PET imaging was performed on a small-animal PET scanner (Focus 220™, Siemens Healthineers, Knoxville, TN, United States) with 7.6 cm axial and 19 cm transaxial field-of-view [31]. Two mice (side by side) were imaged during one PET acquisition using a dual-mouse imaging cradle (m2m Imaging Corp, Cleveland, OH, United States). Before initiating PET acquisitions, anesthesia was induced in an induction box with isoflurane [concentration: 1.5%–3.0% (v/v)] in medical air as carrier gas. Afterward, animals were positioned on the dual-mouse imaging cradle, and isoflurane concentration levels were adjusted [range: 0.8%–1.5% (v/v)] to maintain the respiratory rate of the animals between 60 and 80 breaths/minute during the scan procedure. Then, the lateral tail veins were catheterized after warming the tails using pre-heated (~38°C) pads. Animals were warmed throughout the experiment, and the body temperature and respiratory rate were constantly monitored (SA Instruments Inc., Stony Brook, NY, United States). All animals underwent a 60-min dynamic [^{18}F]THK-5317 scan. Data acquisition was initiated at the start of intravenous injection (0.15 mL as slow bolus over ~ 40 sec), and list-mode data were acquired with an energy window of 250–750 keV and a 6-ns timing window. A 10-min transmission scan was performed using a rotating ^{57}Co-point source before each PET scan for attenuation correction. At the end of the scan, a blood sample was collected into a small tube (Microvette CB 300 LH, Sarstedt AG & Co, Nümbrecht, Germany) by puncture of the retrobulbar plexus, and animals were euthanized by cervical dislocation under deep anesthesia. Afterward, the organs of interest were extracted for gamma counting.

2.4 *Ex vivo* analysis of samples

Blood was centrifuged to obtain plasma (17,000 g, 4°C, 1 min), and radioactivity concentrations in blood, plasma samples, and organs were measured in a gamma counter (HIDEX AMG automatic gamma counter, Turku, Finland). Data from the gamma counter were decay-corrected to the time of radiotracer injection. Then, data were corrected by animals' injected activity, and expressed as percentage of injected dose per gram (%ID/g). Individual plasma-to-blood concentration ratios (P/B ratio) at 60 min after [^{18}F]THK-5317 administration were calculated by dividing the radioactivity concentration measured in the plasma by the radioactivity measured in the blood of the respective animal.

2.5 Metabolite analysis

The percentage of unchanged (unconjugated) [^{18}F]THK-5317 was analyzed by radio-thin-layer chromatography (radio-TLC). Blood was centrifuged to obtain plasma, and proteins were precipitated with acetonitrile (1 µL per µL plasma). Tissues were homogenized using an Ultra Turrax T10 instrument (IKA Laboratory Equipment, Staufen, Germany), and proteins were precipitated with acetonitrile (0.2 mL per brain). All solutions were vortexed and centrifuged (12,000 × g, 1 min, 21°C). Approximately 5 µL of the supernatant and diluted radiotracer solution as references were spotted on silica gel 60F 254-nm TLC plates (10 × 20 cm; Merck, Darmstadt, Germany), and plates were developed in dichloromethane/methanol (95/5, v/v). Detection was performed by exposing the TLC plates to multi-sensitive phosphor screens overnight. The screens were then scanned at 300 dpi resolution using a phosphor imager (Cyclone® Plus, PerkinElmer, Waltham, MA, United States). The retardation factor (Rf) of [^{18}F]THK-5317 was 0.58, as assessed using unlabeled reference standards.

2.6 PET image analysis

Dynamic list-mode data from the 60-min scans were sorted into three-dimensional sinograms, according to the following frame sequence: 8 × 5 s, 2 × 10 s, 2 × 30 s, 3 × 60 s, 2 × 150 s, 2 × 300 s, and 4 × 600 s. PET images were reconstructed by Fourier rebinning of 3D sinograms, followed by two-dimensional filtered back projection with a ramp filter, resulting in a voxel size of 0.4 × 0.4 × 0.8 mm^3. The standard data correction protocol was applied to the data, including normalization, attenuation, and decay correction. Before each measurement series, the PET scanner was cross-calibrated with the activimeter by imaging a phantom with a known activity concentration of an ^{18}F-radiotracer solution.

On the dynamic PET images, organs of interest (the brain, heart, lung, liver, left kidney, and muscle) were defined by delineating pre-defined volumes of interest (VOIs) using the software program AMIDE [32]. Then, TACs of these VOIs were extracted, and the area under the curves (AUCs) from 0 to 60 min were calculated.

The heart curve was used as an IDIF. First, the heart curve was scaled to the blood curve using the blood activity from the gamma counter. Then, a sex-specific (male or female) plasma-to-blood ratio (P/B ratio) was applied to obtain the plasma input function. For metabolite correction, a simple linear regression was performed, assuming a parent fraction of 1 (100%) at 0 s and the measured parent fraction at 3,600 s, separate for the male and female animals. The sex-specific plasma input function was then corrected by the resulting linear equation. The final obtained metabolite-corrected plasma input function $C_p(t)$ was used for calculating the volumes of

distribution (V_T) for different organs derived from the slope of the linearized Logan graphical analysis [33]:

$$\frac{\int_0^T C_{ROI}(t)dt}{C_{ROI}(T)} = V_T \times \frac{\int_0^T C_p(t)dt}{C_{ROI}(T)} + Int,$$

where AUC_{ROI} for each organ from 0-T was used as a measure of $\int_0^T C_{ROI}(t)dt$. For all assessed organs, the plot became linear after 10 min.

In addition, radiotracer clearance from the plasma was performed on decay- and metabolite-corrected plasma radioactivity data from all animals. Plasma clearance was calculated as the quotient of the injected activity divided by the AUC and corrected by the body weight of the animal [34]:

$$Clearance\left[mL/h/g\,BW\right] = \frac{Inj\,Activity\left[kBq\right]}{AUC\left[\frac{kBq}{mL}*h\right]} * BW^{-1}\left[g^{-1}\right].$$

Moreover, we calculated the organ-to-blood ratio by dividing the organ activity values derived from the last PET frame (50–60 min) by the corresponding blood activity values measured with the gamma counter of the respective animal.

2.7 Statistics

Statistical testing was performed using GraphPad Prism 9.1.0 software (GraphPad Software, La Jolla, CA, United States). Differences between groups were analyzed by two-way ANOVA using a full model for assessing the effects of sex, strain and age, and the interaction between them, followed by Tukey's multiple comparison test. Alternatively, two-tailed, unpaired t-tests were used to compare groups in the biodistribution experiments. The level of statistical significance was set to $p < 0.05$. Unless stated otherwise, all values are given as mean ± standard deviation (SD).

3 Results

VOI-based analysis of the dynamic small-animal PET data was performed to determine the brain, liver, lung, kidney, and muscle retention of [^{18}F]THK-5317. PET images, as well as the derived organ TACs for the investigated mouse strains, are shown in Supplementary Figures S1–S7. In all investigated organs, [^{18}F]THK-5317 showed a peak uptake within the first 5–10 min after intravenous administration, followed by a fast washout from the organs until the end of the PET scan. The highest organ uptake (%ID/g) was observed in the liver and kidney, followed by the lungs and brain, and was lowest in muscle tissue. No distinct differences in radiotracer pharmacokinetics were observed in TACs, irrespective of the mouse strain, age group, and sex, except for the kidney.

Biodistribution performed at the end of the PET scans showed no significant age dependency of [^{18}F]THK-5317 uptake in the investigated organs (Supplementary Tables S2–S4). Data from different age groups within the investigated mouse strains were pooled to further focus on sex-related issues. After data pooling, blood pharmacokinetics of [^{18}F]THK-5317 showed significant differences between male and female individuals across all strains (Table 1). In general, female mice showed higher blood radioactivity at 60 min after radiotracer injection (0.50 ± 0.21; 0.43 ± 0.15; 0.36 ± 0.09 %ID/g in ntg-control, hTau, and TMHT mice, respectively) compared to male mice (0.29 ± 0.15; 0.25 ± 0.08; 0.27 ± 0.07 %ID/g in ntg-control, hTau, and TMHT mice). In addition, in plasma, female mice showed higher radioactivity concentration levels at 60 min after radiotracer injection (0.62 ± 0.25; 0.51 ± 0.01; 0.50 ± 0.13 %ID/g in ntg-control, hTau, and TMHT mice, respectively) when compared to male mice (0.45 ± 0.24; 0.37 ± 0.12; 0.35 ± 0.09 %ID/g in ntg-control, hTau, and TMHT mice). The derived plasma/blood ratios at 60 min, however, were not different between males and females. Radiotracer clearance from plasma was not significantly different between the investigated age, strain, or sex groups (Supplementary Figure S8). Further significant sex-related uptake differences were found for the liver, which was higher in female ntg-control (2.39 ± 0.92 vs. 1.33 ± 0.65 %ID/g) and hTau (2.53 ± 1.53 vs. 1.52 ± 0.41 %ID/g) mice but lower in TMHT mice (0.26 ± 0.36 vs. 0.93 ± 0.69 %ID/g) compared to male mice. Additional significant differences in the organ uptake between male and female ntg-control and hTau mice but not in TMHT mice were found in the urinary bladder and bone (*Os femoris*) (Table 1).

For the plasma and brain, no significant differences in metabolism of [^{18}F]THK-5317 were identified between ntg-control, hTau, and TMHT mice, regardless of age. However, a trend of more extensive metabolism in female compared to male mice was observed (Supplementary Table S5). When pooled, female mice showed a significantly higher fraction of radiometabolites of [^{18}F]THK-5317 in plasma (22.1% ± 5.9% unchanged parent) compared to male mice (26.0% ± 7.7% unchanged parent). Additionally, in some animals, liver metabolization of [^{18}F]THK-5317 was assessed, showing a higher fraction of radiometabolites (2.2% ± 0.6% vs. 3.9% ± 1.9% unchanged parent) in female vs. male mice. In the brain, the percentage of the unchanged radiotracer did not differ between female and male mice (Table 2). For the determination of brain V_Ts as the outcome parameter for [^{18}F]THK-5317 distribution, we generated an image-derived blood input function (IDIF) by placing a spherical VOI over the heart of the individual animals. For validation, we compared such derived PET blood radioactivity measurements in the last PET frame (50–60 min after radiotracer administration) with the radioactivity measured in the venous blood sample taken at the end of the PET scan in the gamma counter. In line with our previous experiences [35], heart radioactivity concentrations measured in PET showed a good correlation with the respective gamma counter values ($r = 0.704$, $p < 0.0001$, Supplementary Figure S9).

Based on individual blood IDIFs and the population-based metabolite correction, we derived the organ uptake of [^{18}F]THK-5317, expressed as Logan V_T in the investigated mouse groups (Figure 1). In the brain, two-way ANOVA analysis revealed a statistically significant effect of sex on brain V_Ts ($F_{1,54} = 7.462$, $p = 0.009$, $\eta^2 = 0.123$) and an effect of strain and age ($F_{8,54} = 3.302$, $p = 0.004$, $\eta^2 = 0.333$). In contrast, in the liver, no significant effect between the investigated study groups was found. Further significant sex-related differences in organ V_Ts were identified from the two-way ANOVA analysis in the lung ($F_{1,54} = 4.662$, $p = 0.035$, $\eta^2 = 0.079$), kidney ($F_{1,54} = 16.52$, $p = 0.002$, $\eta^2 = 0.169$), and muscle

TABLE 1 Biodistribution of [^{18}F]THK-5317 in male and female (pooled over the investigated age groups) non-transgenic hTau littermates (ntg-control), hTau (B6.Cg-Mapt$^{tm1(EGFP)Klt}$ Tg(MAPT)8cPdav/J), and TMHT (Thy-1 mutated human tau) mice obtained at 60 min after intravenous administration. Data are presented as mean percent of injected dose per gram tissue (%ID/g) ± standard deviation. Significance indicates differences between male and female individuals of the respective study groups.

Study group	ntg-control			hTau			TMHT		
	Male	*Female*	*Significant**	*Male*	*Female*	*Significant**	*Male*	*Female*	*Significant**
	n = 11	*n = 11*		*n = 13*	*n = 11*		*n = 11*	*n = 14*	
Blood	0.29 ± 0.15	0.50 ± 0.21	*p = .004*	0.25 ± 0.08	0.43 ± 0.15	*p = .028*	0.27 ± 0.07	0.36 ± 0.09	*p = .011*
Plasma	0.45 ± 0.24	0.62 ± 0.25	*p = .031*	0.37 ± 0.12	0.51 ± 0.1	*p = .033*	0.35 ± 0.09	0.50 ± 0.13	*p = .003*
Brain	0.27 ± 0.08	0.29 ± 0.14	*n.s.*	0.24 ± 0.10	0.24 ± 0.06	*n.s.*	0.24 ± 0.09	0.28 ± 0.09	*n.s.*
Heart	0.34 ± 0.13	0.47 ± 0.15	*n.s.*	0.39 ± 0.17	0.38 ± 0.04	*n.s.*	0.32 ± 0.08	0.37 ± 0.08	*n.s.*
Lung	0.52 ± 0.22	0.68 ± 0.25	*n.s.*	0.67 ± 0.32	0.54 ± 0.22	*n.s.*	0.53 ± 0.15	0.55 ± 0.13	*n.s.*
Liver	1.33 ± 0.65	2.39 ± 0.92	*p = .011*	1.52 ± 0.41	2.53 ± 1.53	*p = .044*	0.93 ± 0.69	0.26 ± 0.36	*p = .028*
Kidney	0.72 ± 0.26	0.86 ± 0.26	*n.s.*	0.88 ± 0.33	0.77 ± 0.15	*n.s.*	1.25 ± 0.89	0.95 ± 0.28	*n.s.*
Spleen	0.52 ± 0.22	0.52 ± 0.13	*n.s.*	0.53 ± 0.27	0.67 ± 0.42	*n.s.*	1.33 ± 0.79	1.40 ± 0.78	*n.s.*
Stomach	2.07 ± 1.44	2.25 ± 1.37	*n.s.*	2.39 ± 1.34	1.46 ± 0.24	*n.s.*	2.12 ± 0.88	1.52 ± 0.41	*n.s.*
Small intestine	2.37 ± 1.64	2.36 ± 1.53	*n.s.*	5.46 ± 5.20	3.58 ± 2.5	*n.s.*	-	-	-
Large intestine	0.82 ± 0.36	1.17 ± 0.38	*n.s.*	1.49 ± 2.28	0.89 ± 0.21	*n.s.*	1.48 ± 0.65	1.24 ± 0.36	*n.s.*
Gall bladder	83.08 ± 50.6	83.57 ± 61.02	*n.s.*	102.77 ± 83.78	58.69 ± 58.09	*n.s.*	80.27 ± 79.87	41.76 ± 44.19	*n.s.*
Urine	17.74 ± 13.5	21.11 ± 20.93	*n.s.*	15.89 ± 10.39	10.47 ± 5.51	*n.s.*	17.00 ± 18.69	19.72 ± 12.95	*n.s.*
Urinary bladder	5.21 ± 1.54	1.25 ± 0.78	*n.s.*	6.22 ± 2.38	3.39 ± 1.58	*p = .021*	6.02 ± 3.37	5.24 ± 3.34	*n.s.*
Bone	*0.33 ± 0.12*	0.15 ± 0.11	*p = .008*	0.20 ± 0.12	0.19 ± 0.08	*p = .044*	0.22 ± 0.06	0.20 ± 0.04	*n.s.*
Muscle	*0.26 ± 0.08*	0.30 ± 0.13	*n.s.*	0.23 ± 0.09	0.22 ± 0.05	*n.s.*	0.21 ± 0.05	0.23 ± 0.06	*n.s.*

*Statistical significance was determined using a two-tailed, unpaired t-test. The level of significance was set to $p < 0.05$. n.s. : not significant.

TABLE 2 Levels of the unchanged parent of [^{18}F]THK-5317 determined at 60 min after radiotracer injection in male and female individuals of the investigated mouse study groups. Data show pooled values for male and female individuals, irrespective of the age group or strain.

Study group			
	Male	*Female*	*Significant**
	n = 35	*n = 36*	
Plasma	26.00 ± 7.67	22.08 ± 5.94	*p = .032*
Brain	47.26 ± 12.35	48.90 ± 11.77	*n.s.*
Liver	3.86 ± 1.94 #	2.19 ± 0.60 #	*p = .020*

the number was lower for the liver analysis; *n* = 8 for male and *n* = 10 for female.
Statistical significance was determined using a two-tailed, unpaired t-test. The level of significance was set to $p < 0.05$. n.s. : not significant.

($F_{1,54} = 4.923$, $p = 0.031$, $\eta^2 = 0.084$). Alternative organ analysis given as organ-to-blood ratios revealed similar effects of sex in the identical organs such as the brain/blood ($F_{1,54} = 12.02$, $p = 0.001$, $\eta^2 = 0.182$), lung/blood ($F_{1,54} = 13.37$, $p = 0.001$, $\eta^2 = 0.198$), kidney/blood ($F_{1,54} = 6.399$, $p = 0.014$, $\eta^2 = 0.106$), and muscle/blood ($F_{1,54} = 8.052$, $p = 0.006$, $\eta^2 = 0.130$) but not in the liver/blood ($F_{1,54} = 0.562$, $p = 0.457$). Interestingly, organ AUC values exhibited a significant effect of sex on the brain ($F_{1,54} = 12.68$, $p = 0.0008$, $\eta^2 = 0.190$), liver ($F_{1,54} = 42.29$, $p < 0.0001$, $\eta^2 = 0.439$), and lung ($F_{1,54} = 9.482$, $p = 0.033$, $\eta^2 = 0.149$) but not on the other organs. The individual organ AUC values, as well as organ-to-blood ratios for ntg-control, hTau, and TMHT mice, are shown in Supplementary Figures S10, S11. Individual comparisons obtained with Tukey's multiple comparisons test showed significant differences between certain individual groups for some organs (e.g., the kidney). However, these differences did not follow a general trend and varied between the organs.

Correlation analysis of different organ uptake measures of [^{18}F]THK-5317 such as AUC_{organ}, organ-to-blood ratio, and measured concentration in the last PET frame (%ID/g) to the respective V_Ts is shown in Figure 2. Organ-to-blood ratios showed a statistically significant correlation to the respective organ V_Ts for all analyzed

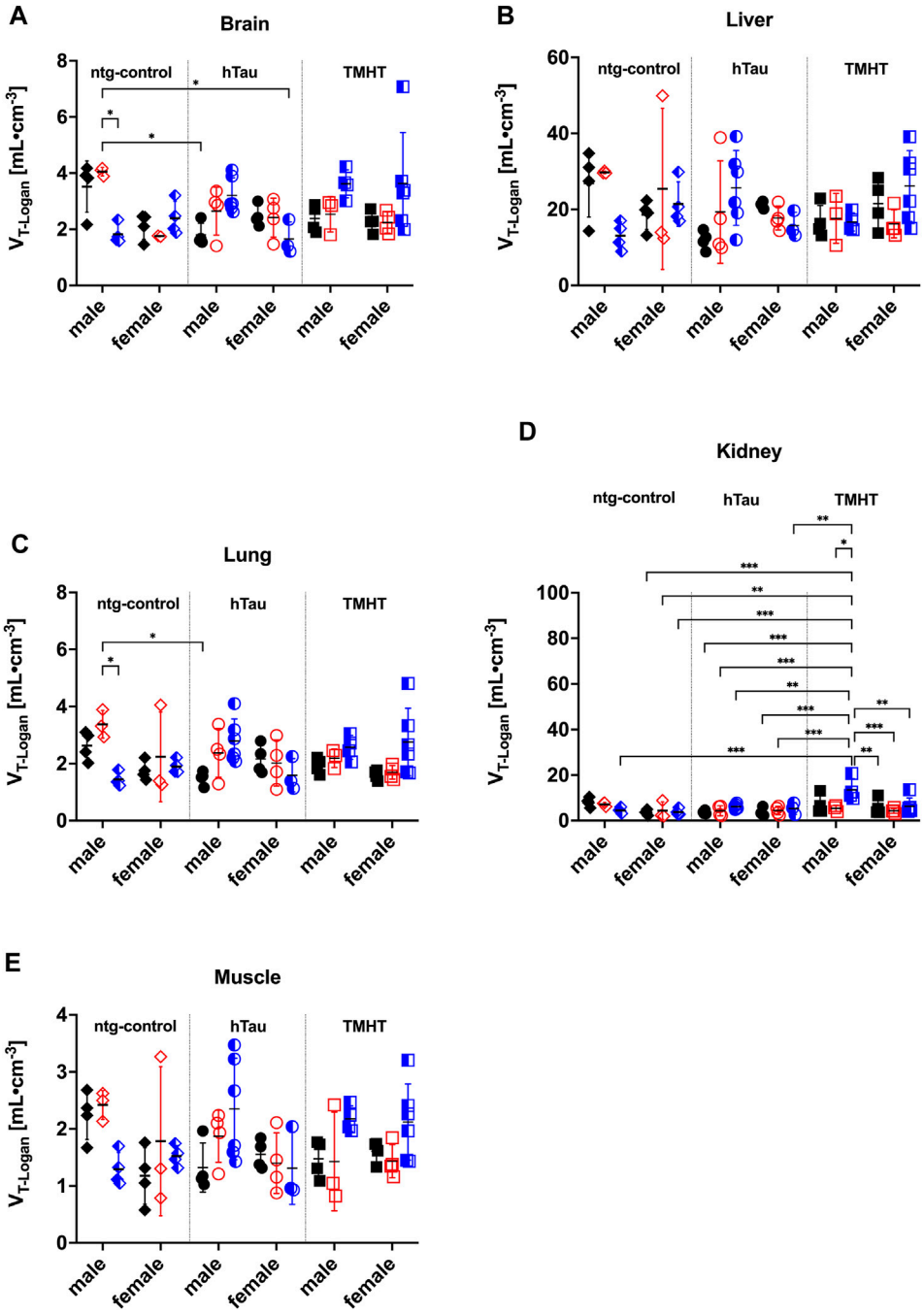

FIGURE 1
Whole-organ volume of distribution (V_T) of [^{18}F]THK-5317 obtained with Logan graphical analysis in the **(A)** brain, **(B)** liver, **(C)** lung, **(D)** kidney, and **(E)** muscle in male and female non-transgenic hTau littermates (ntg-control), hTau (B6.Cg-Mapt$^{tm1(EGFP)Klt}$ Tg(MAPT)8cPdav/J), and TMHT (Thy-1 mutated human tau) mice aged 20 weeks (black, closed symbols), 44 weeks (red, open symbols), and 68 weeks (blue, half-open symbols). *$p < 0.05$, **$p < 0.01$, and ***$p < 0.001$; two-way ANOVA followed by Tukey's multiple comparison test.

organs: the brain ($r = 0.707$, $p < 0.0001$), liver ($r = 0.798$, $p < 0.0001$), lung ($r = 0.751$, $p < 0.0001$), kidney ($r = 0.337$, $p = 0.0038$), and muscle ($r = 0.679$, $p < 0.0001$). In addition, a positive correlation between kidney V_T and AUC_{kidney} ($r = 0.4655$, $p < 0.0001$), and kidney %ID/g at 60 min after radiotracer administration ($r = 0.2527$, $p = 0.0322$) was identified.

4 Discussion

We were interested in identifying the sex, age, or strain-related differences in the distribution and kinetics of tau-radiotracer [^{18}F]THK-5317 on a whole-organ level. We, therefore, quantitatively analyzed PET images obtained in three different mice strains at three

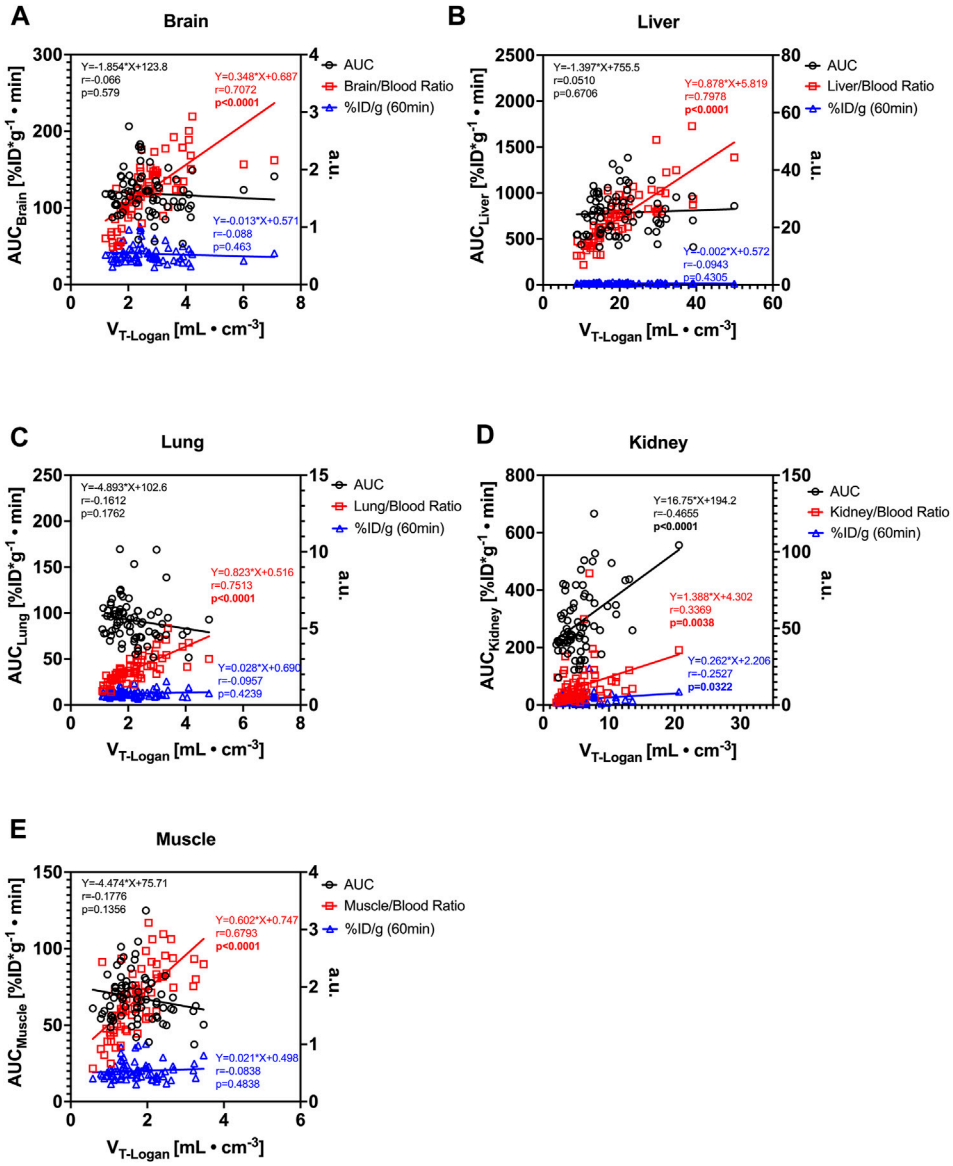

FIGURE 2
Comparison of measures of the [^{18}F]THK-5317 uptake in the **(A)** brain, **(B)** liver, **(C)** lung, **(D)** kidney, and **(E)** muscle and correlation analysis of whole-organ area under the concentration curve (AUC_{Organ}), organ-to-blood ratio at the end of the PET scan, and PET-derived percent of injected dose per gram tissue (%ID/g) at 60 min after the administration with the volume of distribution (V_T) obtained with Logan graphical analysis. (a.u. = arbitrary units either %ID/g or organ-to-blood ratio; *r* = Pearson correlation coefficient; p = *p*-value for Pearson correlation; linear regression formula shows the slope and intercept of the respective simple linear regression fit.)

different ages using both sexes in terms of percent of injected dose per gram tissue (%ID/g). Moreover, we were interested if alternative quantitative parameters such as AUC values, or organ-to-blood ratios, which are easier to obtain in mice, can be used as a surrogate for the volume of distribution (V_T) obtained by Logan graphical analysis. In line with previous observations in rats [22], we observed sex-related differences in the [^{18}F]THK-5317 uptake in the studied mice. In all strains, we observed significant differences in blood and plasma uptake between male and female mice. Contrary to rats, in the studied mice, the female values were overall higher. Biodistribution values agree with values published previously by [36] in male ICR mice. Apart from blood and plasma, we additionally obtained a sex-related difference in the liver (all strains), bone (ntg-control and hTau), and urinary bladder (hTau).

It is broadly recognized that drug pharmacokinetics are largely affected by hepatic drug-metabolizing enzymes (DME) and that their function is highly variable between species, strains, and sex [37]. Our observation suggests different retention/metabolization of [^{18}F]THK-5317 in these animals by phase I/II DME or other DME-regulating factors. Interestingly, in the liver, [^{18}F]THK-5317 uptake was higher in female ntg-control and hTau mice compared to male mice, whereas in TMHT mice, it was the opposite. As ntg-control and hTau mice share an identical genetic background in contrast to TMHT mice, the probable involvement of additional strain-dependent co-factors in

DME expression and function is likely. We, therefore, speculate that the differences observed in this study are related to sex- and strain-dependent hepatic processes which require further studies.

Surprisingly, we obtained a small but statistically higher amount of unchanged parent at 60 min post-injection in plasma in male mice (26%) compared to female mice (22%). Irrespective of sex, the obtained values were in good agreement with values reported in other mouse strains [38]. Yet, the unchanged parent in the brain was comparable between the sexes (47% male vs. 49% female), and the obtained values were significantly lower than that reported by Alzghool et al. (95% unchanged parent in the brain tissue of APP/PS1-21 mice), as well as our findings in rats at the same sampling time [22]. These findings emphasize the importance of radiometabolite analysis within the respective study setup and that the rate of tracer metabolism can differ not only between species but also between individual mouse strains. Furthermore, this supports our previous observations [22] showing that mice seem to metabolize [^{18}F]THK-5317 much faster than rats.

Whole-organ V_Ts of [^{18}F]THK-5317 were highest for the liver, followed by the kidney, brain, lung, and muscle. The rank order of organ V_Ts generally followed previous reports on tau retention, but further correlation studies are required [26].

Our attempt to identify an alternative approach to derive alternative quantitative parameters has shown that the organ-to-blood values exhibited the best correlation to the calculated V_Ts. This is not surprising as both parameters are based on organ-to-blood activity ratios. Yet, we believe that this approach might be a good base for the evaluation of new radiotracers as blood samples at the end of the PET scan are easy to obtain. In addition, it also offers the possibility to examine plasma and radioactive metabolites. When a new radiotracer shows promising parameters using this approach, a more complex kinetic model and specifically a full arterial IF could be planned for subsequent preclinical evaluation. This strategy might aid in decreasing severity and the number of research animals used, and further facilitates candidate selection, following this low-complexity setup in preclinical PET studies.

However, we have identified the following limitations from our study. First, [^{18}F]THK-5317 is metabolically unstable, not exclusively tau-selective, and has been shown to bind to Aß plaques and monoamine oxidase B (MAO-B) in mouse models [38,39]. Although hTau and TMHT mice used in this study clearly showed the absence of ß-amyloid, cerebral MAO-B expression has not been investigated. Furthermore, MAO-B expression increases as part of the neuroinflammatory response to tau accumulations, as well as during aging [40,41]. It cannot be excluded that the sex differences identified in the whole-brain uptake of [^{18}F]THK-5317 solely reflects changes in MAO-B expression patterns as sex-dependency of MAO-isoform expression has been confirmed in the human brain [42]. Second, our initial assumption about the estimated effect size for sample size calculation for different study groups was incorrect. We, therefore, pooled the acquired data over age and strain groups to increase the respective group sizes, which ultimately revealed statistically significant differences. Conclusively, this study highlights the importance of preliminary, pilot studies from which effect sizes and, ultimately, sample size calculations can be based on real-world data obtained in the own research environment and not solely based on the published data. Third, the heart input function suffered from spillover from the liver and gall bladder signals, especially in the late time frames. We, therefore, carefully positioned the heart VOI to minimize this influence. Fourth, for the calculation of the liver V_T, we only used a single input function and did not account for the dual blood supply (the portal vein and the hepatic artery). In PET-only images without anatomical guidance, the liver portal vein cannot be identified in mice. Fifth, the IDIF method was not validated to the ground truth, which would be the arterial sampling. This might add some additional bias to the results. Finally, the radiosynthesis process of [^{18}F]THK-5317 requires further optimization to consistently achieve radiochemical purities above 98%.

In conclusion, we presented a workflow for quantitative, multiple-organ analysis of the [^{18}F]THK-5317 uptake in mice, revealing sex-differences in the plasma concentration, the formation of radiometabolites, and uptake in various organs in mice. From the derived quantitative parameters, the organ-to-blood values correlate best with the calculated V_Ts. Given the active incorporation of 3R principles into preclinical quantitative imaging, we propose that following this workflow, comprising dynamic PET scans, concomitant blood sampling, subsequent metabolite analysis, and candidate selections based on organ-to-blood uptake parameters, might be suitable to select novel radiotracer candidates before more complex kinetic models, comprising invasive methods such as full arterial blood sampling, for radiotracer quantification are applied.

Data availability statement

The raw data supporting the conclusion of this article will be made available by the authors, without undue reservation.

Ethics statement

The animal study was approved by Intramural Committee for Animal Experimentation. The study was conducted in accordance with the local legislation and institutional requirements.

Author contributions

TW: conceptualization, formal analysis, investigation, methodology, project administration, resources, writing–original draft, and visualization. SM: conceptualization, investigation, and writing–review and editing. TF: conceptualization, investigation, methodology, project administration, and writing–review and editing. ML: investigation, methodology, and writing–review and editing. JS: investigation and writing–review and editing. CK: conceptualization, data curation, funding acquisition, methodology, project administration, resources, visualization, and writing–original draft.

Funding

The author(s) declare that financial support was received for the research, authorship, and/or publication of this article. Methodology used for research leading to these results has received funding from

the Austrian Research Promotion Agency (FFG) through project number 853256 awarded to CK.

Acknowledgments

The authors would like to acknowledge the efforts of the management teams at the Medical University of Vienna and at the AIT Austrian Institute of Technology GmbH to enable the successful transfer of the former AIT Preclinical Molecular Imaging Group to the Medical University of Vienna. The authors would also like to thank Michael Sauberer and Sarah Furtner for their help in conducting the experiments and analyzing data. We further thank our colleagues from Radiopharmaceuticals, Seibersdorf Labor GmbH, for their continuous support.

Conflict of interest

Authors TW, SM, TF, ML, JS, and CK were employed by AIT Austrian Institute of Technology GmbH.

The author(s) declared that they were an editorial board member of Frontiers, at the time of submission. This had no impact on the peer review process and the final decision.

Publisher's note

Supplementary material

The Supplementary Material for this article can be found online at: https://www.frontiersin.org/articles/10.3389/fphy.2023.1303690/full#supplementary-material

References

1. Myers A, Mcgonigle P. Overview of transgenic mouse models for alzheimer's disease. *Curr Protoc Neurosci* (2019) 89:e81. doi:10.1002/cpns.81

2. Busche MA, Hyman BT. Synergy between amyloid-beta and tau in Alzheimer's disease. *Nat Neurosci* (2020) 23:1183–93. doi:10.1038/s41593-020-0687-6

3. Sanchez-Varo R, Mejias-Ortega M, Fernandez-Valenzuela JJ, Nunez-Diaz C, Caceres-Palomo L, Vegas-Gomez L, et al. Transgenic mouse models of alzheimer's disease: an integrative analysis. *Int J Mol Sci* (2022) 23:5404. doi:10.3390/ijms23105404

4. Chavan RS, Supalkar KV, Sadar SS, Vyawahare NS. Animal models of Alzheimer's disease: an origin of innovative treatments and insight to the disease's etiology. *Brain Res* (2023) 1814:148449. doi:10.1016/j.brainres.2023.148449

5. Cao L, Kong Y, Ji B, Ren Y, Guan Y, Ni R. Positron emission tomography in animal models of tauopathies. *Front Aging Neurosci* (2021) 13:761913. doi:10.3389/fnagi.2021.761913

6. Van Camp N, Lavisse S, Roost P, Gubinelli F, Hillmer A, Boutin H. TSPO imaging in animal models of brain diseases. *Eur J Nucl Med Mol Imaging* (2021) 49:77–109. doi:10.1007/s00259-021-05379-z

7. Chen B, Marquez-Nostra B, Belitzky E, Toyonaga T, Tong J, Huang Y, et al. PET imaging in animal models of alzheimer's disease. *Front Neurosci* (2022) 16:872509. doi:10.3389/fnins.2022.872509

8. Syvänen S, Meier SR, Roshanbin S, Xiong M, Faresjö R, Gustavsson T, et al. PET imaging in preclinical anti-aβ drug development. *Pharm Res* (2022) 39:1481–96. doi:10.1007/s11095-022-03277-z

9. Mannheim JG, Mamach M, Reder S, Traxl A, Mucha N, Disselhorst JA, et al. Reproducibility and comparability of preclinical PET imaging data: a multicenter small-animal PET study. *J Nucl Med* (2019) 60:1483–91. doi:10.2967/jnumed.118.221994

10. Herfert K, Mannheim JG, Kuebler L, Marciano S, Amend M, Parl C, et al. Quantitative rodent brain receptor imaging. *Mol Imaging Biol* (2020) 22:223–44. doi:10.1007/s11307-019-01368-9

11. Mcdougald W, Vanhove C, Lehnert A, Lewellen B, Wright J, Mingarelli M, et al. Standardization of preclinical PET/CT imaging to improve quantitative accuracy, precision, and reproducibility: a multicenter study. *J Nucl Med* (2020) 61:461–8. doi:10.2967/jnumed.119.231308

12. Miyaoka RS, Lehnert AL. Small animal PET: a review of what we have done and where we are going. *Phys Med Biol* (2020) 65:24TR04. doi:10.1088/1361-6560/ab8f71

13. Du J, Jones T. Technical opportunities and challenges in developing total-body PET scanners for mice and rats. *EJNMMI Phys* (2023) 10:2. doi:10.1186/s40658-022-00523-6

14. Patlak CS, Blasberg RG. Graphical evaluation of blood-to-brain transfer constants from multiple-time uptake data. Generalizations. *J Cereb Blood Flow Metab* (1985) 5:584–90. doi:10.1038/jcbfm.1985.87

15. Logan J, Fowler JS, Volkow ND, Wolf AP, Dewey SL, Schlyer DJ, et al. Graphical analysis of reversible radioligand binding from time-activity measurements applied to [N-11C-methyl]-(-)-cocaine PET studies in human subjects. *J Cereb Blood Flow Metab* (1990) 10:740–7. doi:10.1038/jcbfm.1990.127

16. Hood L, Heath JR, Phelps ME, Lin B. Systems biology and new technologies enable predictive and preventative medicine. *Science* (2004) 306:640–3. doi:10.1126/science.1104635

17. Innis RB, Cunningham VJ, Delforge J, Fujita M, Gjedde A, Gunn RN, et al. Consensus nomenclature for *in vivo* imaging of reversibly binding radioligands. *J Cereb Blood Flow Metab* (2007) 27:1533–9. doi:10.1038/sj.jcbfm.9600493

18. Alf MF, Wyss MT, Buck A, Weber B, Schibli R, Krämer SD. Quantification of brain glucose metabolism by 18F-FDG PET with real-time arterial and image-derived input function in mice. *J Nucl Med* (2013) 54:132–8. doi:10.2967/jnumed.112.107474

19. Bini J, Lattin CR, Toyonaga T, Finnema SJ, Carson R. Optimized methodology for reference region and image-derived input function kinetic modeling in preclinical PET. *IEEE Trans Radiat Plasma Med Sci* (2022) 6:454–62. doi:10.1109/trpms.2021.3088606

20. Lanz B, Poitry-Yamate C, Gruetter R. Image-derived input function from the vena cava for 18F-FDG PET studies in rats and mice. *J Nucl Med* (2014) 55:1380–8. doi:10.2967/jnumed.113.127381

21. Meyer M, Le-Bras L, Fernandez P, Zanotti-Fregonara P. Standardized input function for 18F-fdg PET studies in mice: a cautionary study. *PLoS One* (2017) 12:e0168667. doi:10.1371/journal.pone.0168667

22. Mairinger S, Filip T, Sauberer M, Flunkert S, Wanek T, Stanek J, et al. Plasma pharmacokinetic and metabolism of [(18)F]THK-5317 are dependent on sex. *Nucl Med Biol* (2020) 84-85:28–32. doi:10.1016/j.nucmedbio.2020.01.001

23. Filip T, Mairinger S, Neddens J, Sauberer M, Flunkert S, Stanek J, et al. Characterization of an APP/tau rat model of Alzheimer's disease by positron emission tomography and immunofluorescent labeling. *Alz Res Ther* (2021) 13:175. doi:10.1186/s13195-021-00916-2

24. Jin J, Yang X, Gong H, Li X. Time- and gender-dependent alterations in mice during the aging process. *Int J Mol Sci* (2023) 24:12790. doi:10.3390/ijms241612790

25. Gu Y, Oyama F, Ihara Y. Tau is widely expressed in rat tissues. *J Neurochem* (1996) 67:1235–44. doi:10.1046/j.1471-4159.1996.67031235.x

26. Solorzano A, Brady M, Bhatt N, Johnson A, Burgess B, Leyva H, et al. *Central and peripheral tau retention modulated by an anti-tau antibody* (2023). bioRxiv.

27. Tago T, Furumoto S, Okamura N, Harada R, Ishikawa Y, Arai H, et al. Synthesis and preliminary evaluation of 2-arylhydroxyquinoline derivatives for tau imaging. *J Labelled Comp Radiopharm* (2014) 57:18–24. doi:10.1002/jlcr.3133

28. Andorfer C, Kress Y, Espinoza M, De Silva R, Tucker KL, Barde YA, et al. Hyperphosphorylation and aggregation of tau in mice expressing normal human tau isoforms. *J Neurochem* (2003) 86:582–90. doi:10.1046/j.1471-4159.2003.01879.x

29. Flunkert S, Hierzer M, Löffler T, Rabl R, Neddens J, Duller S, et al. Elevated levels of soluble total and hyperphosphorylated tau result in early behavioral deficits and distinct changes in brain pathology in a new tau transgenic mouse model. *Neurodegener Dis* (2013) 11:194–205. doi:10.1159/000338152

30. Percie Du Sert N, Ahluwalia A, Alam S, Avey MT, Baker M, Browne WJ, et al. Reporting animal research: explanation and elaboration for the ARRIVE guidelines 2.0. *PLoS Biol* (2020) 18:e3000411. doi:10.1371/journal.pbio.3000411

31. Tai YC, Ruangma A, Rowland D, Siegel S, Newport DF, Chow PL, et al. Performance evaluation of the microPET focus: a third-generation microPET scanner dedicated to animal imaging. *J Nucl Med* (2005) 46:455–63.

32. Loening AM, Gambhir SS. AMIDE: a free software tool for multimodality medical image analysis. *Mol Imag* (2003) 2:131–7. doi:10.1162/153535003322556877

33. Logan J. Graphical analysis of PET data applied to reversible and irreversible tracers. *Nucl Med Biol* (2000) 27:661–70. doi:10.1016/s0969-8051(00)00137-2

34. Schneider D, Oskamp A, Holschbach M, Neumaier B, Bauer A, Bier D. Relevance of *in vitro* metabolism models to PET radiotracer development: prediction of *in vivo* clearance in rats from microsomal stability data. *Pharmaceuticals (Basel)* (2019) 12:57. doi:10.3390/ph12020057

35. Traxl A, Mairinger S, Filip T, Sauberer M, Stanek J, Poschner S, et al. Inhibition of ABCB1 and ABCG2 at the mouse blood-brain barrier with marketed drugs to improve brain delivery of the model ABCB1/ABCG2 substrate [(11)C]erlotinib. *Mol Pharmaceutics* (2019) 16:1282–93. doi:10.1021/acs.molpharmaceut.8b01217

36. Harada R, Okamura N, Furumoto S, Furukawa K, Ishiki A, Tomita N, et al. 18F-THK5351: a novel PET radiotracer for imaging neurofibrillary pathology in alzheimer disease. *J Nucl Med* (2016) 57:208–14. doi:10.2967/jnumed.115.164848

37. Waxman DJ, Holloway MG. Sex differences in the expression of hepatic drug metabolizing enzymes. *Mol Pharmacol* (2009) 76:215–28. doi:10.1124/mol.109.056705

38. Alzghool OM, Rokka J, Lopez-Picon FR, Snellman A, Helin JS, Okamura N, et al. (S)-[18F]THK5117 brain uptake is associated with Aβ plaques and MAO-B enzyme in a mouse model of Alzheimer's disease. *Neuropharmacology* (2021) 196:108676. doi:10.1016/j.neuropharm.2021.108676

39. Murugan NA, Chiotis K, Rodriguez-Vieitez E, Lemoine L, Agren H, Nordberg A. Cross-interaction of tau PET tracers with monoamine oxidase B: evidence from *in silico* modelling and *in vivo* imaging. *Eur J Nucl Med Mol Imaging* (2019) 46:1369–82. doi:10.1007/s00259-019-04305-8

40. Saura J, Richards JG, Mahy N. Differential age-related changes of mao-a and mao-b in mouse brain and pe peripheral organs. *Neurobiol Aging* (1994) 15:399–408. doi:10.1016/0197-4580(94)90071-x

41. Carter SF, Scholl M, Almkvist O, Wall A, Engler H, Langstrom B, et al. Evidence for astrocytosis in prodromal Alzheimer disease provided by 11C-deuterium-L-deprenyl: a multitracer PET paradigm combining 11C-Pittsburgh compound B and 18F-FDG. *J Nucl Med* (2012) 53:37–46. doi:10.2967/jnumed.110.087031

42. Sanfilippo C, Castrogiovanni P, Imbesi R, Lazzarino G, Di Pietro V, Li Volti G, et al. Sex-dependent monoamine oxidase isoforms expression patterns during human brain ageing. *Mech Ageing Dev* (2021) 197:111516. doi:10.1016/j.mad.2021.111516

frontiers | Frontiers in Physics

TYPE Review
PUBLISHED 19 December 2023
DOI 10.3389/fphy.2023.1246973

OPEN ACCESS

EDITED BY
Ewald V. Moser,
Medical University of Vienna, Austria

REVIEWED BY
Giovanni Di Domenico,
University of Ferrara, Italy
Christian Nasel,
University Hospital Tulln, Austria

*CORRESPONDENCE
Ting-Yim Lee,
tlee@uwo.ca

RECEIVED 25 June 2023
ACCEPTED 27 November 2023
PUBLISHED 19 December 2023

CITATION
Chung KJ, De Sarno D and Lee T-Y (2023), Quantitative functional imaging with CT perfusion: technical considerations, kinetic modeling, and applications.
Front. Phys. 11:1246973.
doi: 10.3389/fphy.2023.1246973

Quantitative functional imaging with CT perfusion: technical considerations, kinetic modeling, and applications

Kevin J. Chung[1,2], Danny De Sarno[2] and Ting-Yim Lee[1,2,3]*

[1]Department of Medical Biophysics, The University of Western Ontario, London, ON, Canada, [2]Robarts Research Institute and Lawson Health Research Institute, London, ON, Canada, [3]Department of Medical Imaging, The University of Western Ontario, London, ON, Canada

CT perfusion (CTP)-derived quantitative maps of hemodynamic parameters have found important clinical applications in stroke, cancer, and cardiovascular disease. Blood flow, blood volume, transit time, and other perfusion parameters are sensitive markers of pathophysiology with impaired perfusion. This review summarizes the basic principles of CTP including image acquisition, tracer kinetic modeling, deconvolution algorithms, and diagnostic interpretation. The focus is on practical and theoretical considerations for accurate quantitative parametric imaging. Recommended CTP scan parameters to maintain CT number accuracy and optimize radiation dose *versus* image noise are first reviewed. Tracer kinetic models, which describe how injected contrast material is distributed between blood and the tissue microenvironment by perfusion and bidirectional passive exchange, are then derived. Deconvolution algorithms to solve for hemodynamic parameters of kinetic models are discussed and their quantitative accuracy benchmarked. The applications and diagnostic interpretation of CTP in stroke, cancer, and cardiovascular disease are summarized. Finally, we conclude with a discussion of future directions for CTP research, including radiation dose reduction, new opportunities with novel CT hardware, and emerging diagnostic applications.

KEYWORDS

perfusion imaging, computed tomography, tracer kinetic modeling, deconvolution, radiation dose reduction, acute ischemic stroke, cancer, cardiovascular disease

1 Introduction

CT perfusion (CTP) is a functional imaging technique used to generate quantitative maps of hemodynamic parameters such as blood flow, blood volume, and mean transit time. Normal vascular perfusion underpins normal tissue function, and its disruption may be an indicator of underlying disease. Since the first demonstration of brain CTP by Leon Axel in 1980 [1], the field has rapidly grown to encompass specific diagnostic applications in various diseases such as acute ischemic stroke, cancer, and cardiovascular disease. Specifically, CTP may be used to non-invasively diagnose and characterize diseases with impaired tissue perfusion, monitor disease progression, and distinguish viable from non-viable tissue. Decisions on the management and treatment of patients can be informed by CTP.

A notable diagnostic application of CTP is in acute ischemic stroke. CTP was used to select patients with large vessel ischemic stroke for endovascular stroke treatment in multiple randomized controlled trials [2–4]. Post-processing and analysis of brain CTP imaging was

fully automated, and imaging-based assessment of treatment eligibility was available within minutes of acquisition. Patients who received endovascular stroke treatment based on a favorable CTP profile had greatly improved 90-day functional outcomes compared to those not receiving treatment. The therapeutic benefit persisted beyond the 6-h onset-to-treatment time window normally recommended for patients selected without perfusion imaging. CTP is a validated and automated treatment decision assistance tool in acute ischemic stroke and played an important role in demonstrating that endovascular stroke treatment was safe and effective beyond the standard therapeutic time window.

A CTP study is normally performed as follows. An iodinated contrast agent is intravenously injected into the patient, and following a short delay (<10 s) for the contrast agent to arrive at the organ of interest, CT scans are serially acquired for ≈1 to 3 min. Time–density (attenuation) curves (TDCs) derived from the acquired serial (dynamic) contrast-enhanced CT images describe how the contrast agent washes in and out from tissue by blood flow. Hemodynamic parameters such as blood flow (F), blood volume (V_b), mean transit time (MTT), artery-to-tissue contrast delay time (T0), and time-to-maximum of the residue function (Tmax, a composite index of delay, dispersion, and MTT) [5] can be estimated by analyzing the acquired TDCs. Specifically, the arterial TDC, which estimates the arterial contrast concentration, is deconvolved from tissue TDCs to estimate an impulse residue function (IRF). The perfusion parameters of interest are derived from the IRF, which describes the hemodynamic response if a unit mass of contrast was injected into the arterial inlet of the tissue. Calculation of the IRF for each tissue voxel leads to quantitative maps of perfusion parameters from which regional impairment of perfusion can be visualized.

This review summarizes the basic principles of CTP, methods to estimate perfusion parameters, diagnostic applications, and emerging research, with a focus on quantitative parametric imaging.

2 The quantitative capability of CT

CT images are cross-sectional, quantitative maps of the linear attenuation coefficient (expressed as CT number) of tissue. Due to the small differences in the linear attenuation coefficient between water, blood, and soft tissue in the diagnostic X-ray energy range (≤150 keV) [6, 7], blood cannot be distinguished from soft tissue with CT to estimate perfusion. In contrast, iodine has a much greater attenuation coefficient than that of soft tissue [6, 7]. Intravenous injection of an iodine contrast agent allows the contrast agent to circulate throughout the organ of interest. If the patient is scanned serially with fixed CT protocols as in a CTP study, the contrast-induced changes in CT number reflect the same in iodine concentration in vessels and tissue in a linear fashion and can be quantified as TDCs. Furthermore, an iodine contrast agent is inert, extracellular, and does not bind to any target nor does it enter a cell; it remains either in the intravascular or interstitial space [8]. As such, contrast transport principles, which are described in Section 3, can be applied to describe TDCs obtained from CTP.

The linear relationship between CT number and contrast concentration is a notable advantage of CTP compared to perfusion magnetic resonance imaging (MRI). In dynamic susceptibility contrast perfusion MRI, a tissue-dependent scaling factor must be accounted to convert T2* signal change to gadolinium concentration [9, 10]. As such, absolute measurements of blood flow and blood volume cannot be obtained without knowledge of these tissue-dependent scaling factors. The relative blood flow and volume obtained by normalizing by mean blood flow or volume in a reference region are used for perfusion MRI in clinical practice due to this limitation. While perfusion imaging with positron emission tomography and flow-specific radiotracers is the clinical gold standard for absolute perfusion measurements, it is often impractical due to its long scan time and high resource requirement (e.g., availability of a cyclotron and flow-specific radiotracers such as ^{15}O-water or ^{13}N-NH_3, which are short-lived tracers with additional logistical problems, unlike off-the-shelf stable contrast agents used in CTP).

2.1 CT perfusion scan protocol

In designing a CTP scan protocol, the goal is to balance the radiation dose to the patient *versus* the signal-to-noise ratio (SNR) of TDCs required to generate diagnostic quality perfusion maps. The following scan parameters are of significance in CTP: X-ray tube voltage, tube current-exposure time, scan interval, contrast injection volume and rate, axial coverage, and scan duration.

Tube voltage determines the energy spectrum of the incident X-ray beam and sensitivity to the iodine contrast agent. For CTP, to balance the iodine contrast-to-noise ratio and radiation dose, a tube voltage of 80 kV is used for most diagnostic applications [11, 12], though higher tube voltages (100 or 120 kV) may be appropriate in thoracic and abdominal CTP, where there may be greater attenuation of X-rays due to the larger scan object.

At a fixed tube voltage, photon fluence is determined by the tube current-exposure time product (referred to by its unit, mAs). Photon fluence and radiation dose are linearly proportional to mAs, and the noise level is inversely proportional to the square root of the mAs. The mAs is an important factor, besides kV, in determining the TDC SNR. The recommended mAs for brain CTP ranges between 100 mAs and 200 mAs per dynamic image at a tube voltage of 80 kV [13, 14]. The optimal mAs for other anatomical applications has not yet been established, but can range from tens of mAs to up to 200 mAs per dynamic image. The choice of mAs also depends on the number of dynamic CTP images acquired to balance the radiation dose.

The recommended CTP temporal resolution is ≤ 3 s between dynamic images [13–16]. This range has mainly been determined empirically and depends on other scan parameters such as contrast volume and injection rate, patient cardiac output, desired brain coverage *versus* scanner axial coverage, and radiation dose [17, 18]. A uniform scan interval of 3 s with a 40-mL bolus injection at 4 mL/s was found to balance the radiation dose and perfusion parameter accuracy [17]. Non-uniform scan intervals have also been used to sample the slower venous/wash-out phase of TDCs at prolonged intervals to assess blood–brain barrier permeability [19] or to optimize the radiation dose [15, 20].

The minimum scan interval can also be limited by the desired anatomical coverage *versus* the axial coverage provided by the scanner. In CT scanners with less whole organ coverage

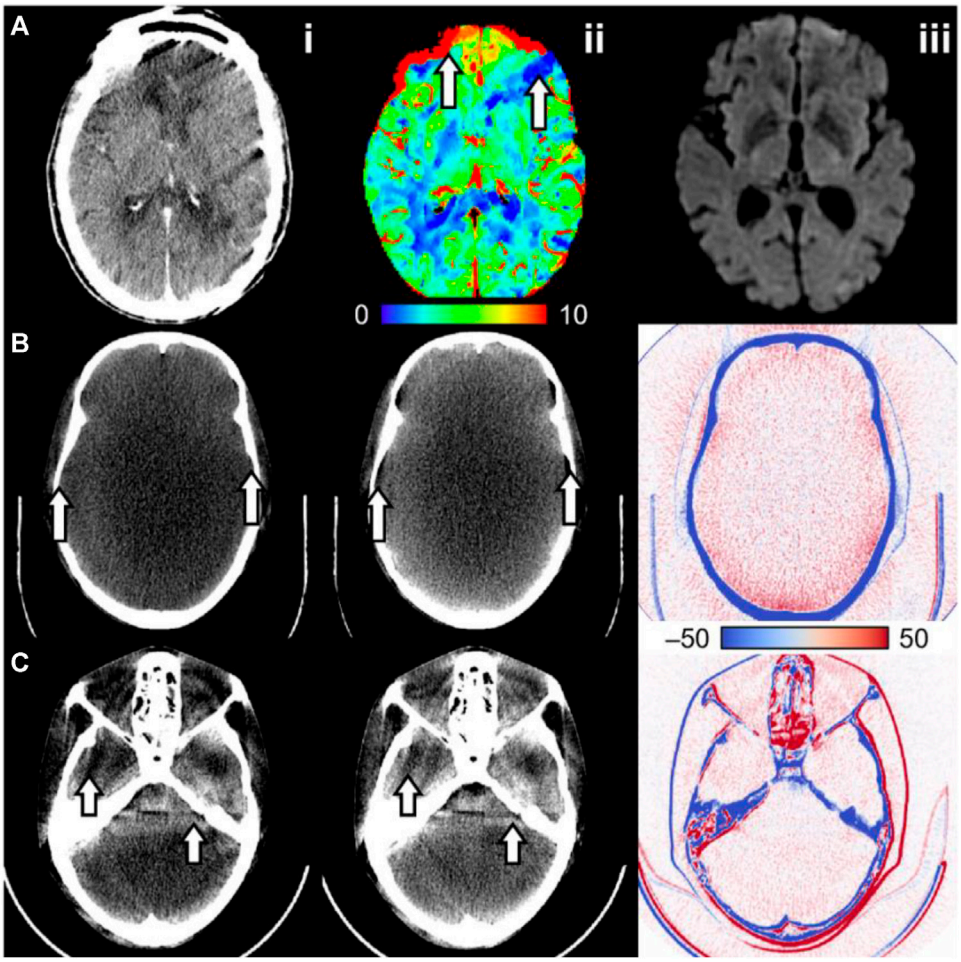

FIGURE 1
Examples of CT artifacts that may affect CT number consistency in CT perfusion. **(A)** Intra-scan motion artifact in a CT perfusion dynamic image. **(A.ii)** The cerebral blood volume map shows regions of increased and decreased blood volume (arrows), where the decrease suggests an ischemic core. **(A.iii)** Follow-up diffusion-weighted imaging does not show an infarct in that region. **(B)** An anthropomorphic head phantom reconstructed **(B.i)** with and **(B.ii)** without beam hardening correction and **(B.iii)** the difference image (without minus with correction). The image without beam hardening correction has cupping artifacts and a poor bone–brain interface (arrows). **(C)** An anthropomorphic head phantom scanned at **(C.i)** 20 mm and **(C.ii)** 40 mm beam collimation width. **(C.iii)** The difference image (40 mm minus 20 mm) shows increased intracranial CT number at 40 mm relative to 20 mm collimation width, possibly due to scattering overcorrection. The arrows also show beam hardening shading artifacts due to the different attenuation characteristics of bone compared to the intracranial material.

(<8 cm axially), a toggling table [21, 22] or periodic spiral [23] technique is often used to increase coverage. The toggling table technique (also called step-and-shoot or shuttle mode) increases the axial coverage by acquiring two "slabs" of the object at two "toggled" table positions. Here, the table is stopped during the scan, and this process is repeated over the prescribed scan duration [21, 22]. In the periodic spiral technique, the object is scanned continuously while the patient table smoothly moves in and out of the gantry (*i.e.*, a continuous helical or spiral CT scan). The scan interval is therefore limited by the inter-scan time required due to table movement and the desired axial coverage.

CTP scan duration should be chosen such that at least the first pass of contrast through the vasculature is fully captured, which normally takes 45–60 s after contrast injection [24]. Following the first pass of contrast (the intravascular phase), the TDC signal is mainly from the influx and efflux of contrast through the blood–tissue barrier by passive diffusion (interstitial phase). Therefore, a longer scan duration of 120–150 s may be prescribed to assess vessel permeability and other kinetic parameters with model-dependent deconvolution [15, 19, 25]. Scan duration must otherwise be balanced against radiation dose. If a CTP study is too short, the full wash-out phase of the contrast agent may not be sampled, especially in diseased regions where the transit time may be prolonged. This so-called truncation of TDCs is known to cause an underestimation of CBV, MTT, and Tmax and, accordingly, may lead to an inaccurate diagnosis [26]. Tolerance to TDC truncation may depend on the deconvolution algorithm used to generate perfusion parametric maps [27]. Of note, an iodinated contrast material is diffusion-limited with respect to perfusion in blood–tissue exchange, particularly in the case of an intact blood–brain barrier. This contrasts with xenon, which is not diffusion-limited in all tissues. Tracers that are not diffusion-limited are freely diffusible.

2.2 CT artifacts

A select number of relevant CT artifacts that affect the estimation of perfusion are reviewed here. The key idea is to mitigate CT artifacts such that the linear relationship between the change in CT number and the change in iodine concentration is maintained. As such, for CTP, the consistency of the CT number between images is arguably more important than absolute CT number accuracy. Representative examples of CT artifacts discussed in this article are illustrated in Figure 1.

2.2.1 Patient motion

Two types of patient motion can be identified for CTP: (1) inter-scan motion, which misaligns tissue voxels between dynamic images, and (2) intra-scan motion, or motion during the scanning of an image, which often causes dark shading artifacts. Moderate-to-severe patient motion may be seen in up to 25% of patients receiving brain CTP [28]. A secondary analysis of a randomized clinical trial of endovascular stroke treatment revealed that ≈10% of patients who received brain CTP had motion artifacts, which rendered the CTP study unanalyzable [29]. Inter-scan motion can mostly be corrected by co-registering (spatially aligning) all dynamic images to a reference dynamic image in the CTP study [30]. Motion correction by image registration is automated and available in all commercial CTP software. Intra-scan motion artifact is difficult to correct retrospectively, and dynamic images showing severe intra-scan motion artifacts may need to be selectively excluded from CTP post-processing. Motion artifacts can cause both erroneous increases and decreases in estimated perfusion depending on the context. For example, intra-scan motion shading may decrease the amplitude of TDCs and erroneously introduce a low-blood flow region. In contrast, inter-scan motion may cause blurring of inter-organ boundaries (*e.g.*, the bone–brain interface) and cause artificial increases or decreases in the measured TDC value. Motion is a major challenge for myocardial CTP imaging in which the beating heart undergoes nonrigid movement. These challenges are mitigated by electrocardiogram gating, fast gantry rotation time to minimize intra-scan motion, and nonrigid motion correction post-reconstruction [31]. Figure 1A illustrates the effect of intra-scan motion on a CTP cerebral blood volume map.

2.2.2 Beam hardening

Beam hardening refers to an increase in mean X-ray energy ("hardening"). Generated X-rays are polyenergetic, and low-energy photons are disproportionately attenuated compared to high-energy photons when passing through an object [6, 32]. X-rays that pass through a greater length of the attenuating material will proportionally have greater hardening. Non-uniform energy attenuation results in inconsistent X-ray energy distributions between detectors and projections, which causes a shift in the CT number, wherein beams with greater hardening have a lower CT number. Furthermore, streaking and shading artifacts may occur at cross-sections with heterogenous bone structures, such as at the posterior fossa of the head [6, 32]. This occurs due to inconsistent levels of beam hardening between projections. All commercial CT systems have methods to correct for these artifacts, but the discussion of specific methods is outside the scope of this review. Without proper correction, the linear relationship between CT number and iodine concentration is not maintained, thereby compromising the accuracy of perfusion parameter estimations. Beam hardening artifacts are illustrated in Figure 1B and Figure 1C.

2.2.3 X-ray scattering

Compton scattering is one of the main modes of interaction between X-ray photons and tissue at diagnostic X-ray energy levels [6]. As a result, the measured CT detector signal can be from primary photons (directly from the incident X-ray) or a scattered photon (deflected at a random angle from within the scanned object). Scattering increases with greater beam collimation width as the volume of the irradiated material and detector coverage are increased. Scattering can be modeled as a low-frequency additive bias to the true primary detector signal, which may cause streaking artifacts and CT number bias in the reconstructed image [6]. Because scattering induces a greater measured detector signal, the projections are seemingly less attenuated, causing a reduction in CT number [33]. Software correction methods [34, 35] or a post-patient collimator that rejects scattered photons [36] can reduce the effects of scattering. However, suboptimal scattering correction or scattering overcorrection may result in increased CT number [36]. In CTP, an inconsistent level of scattering between dynamic images may cause CT number inconsistency, which would invalidate the linear relationship between CT number and iodine concentration. The accuracy of estimated perfusion parameters would accordingly be affected. Figure 1C illustrates how CT number consistency may be impacted by differing levels of scattering due to protocols using different beam collimation widths.

2.3 CT perfusion radiation dose

2.3.1 CT perfusion dose reduction

Radiation dose levels used for CTP imaging likely do not increase the risk of cancer mortality substantially, relative to the natural prevalence rate. Concerns with CTP radiation dose are, therefore, with respect to the potential diagnostic benefit that is provided and whether the same diagnostic information can be reliably abstracted from a lower scan dose. Given a low enough scan dose, radiation risk-to-diagnostic benefit criteria may be favorable for CTP.

The most straightforward dose reduction technique is to reduce the mAs or kV. Dose scales linearly with mAs and by a power law with kV [6]. CTP image and TDC SNR suffer with lower mAs as noise increases proportionally to the inverse square root of mAs. The estimated blood flow becomes overestimated at lower mAs than at higher mAs, and similar biases are observed for other estimated CTP parameters [37]. The relationship between kV and the TDC SNR is more complex: while noise increases with lower kV by a power law [6], the sensitivity to iodine concentration also increases due to a greater proportion of the X-ray energy spectrum being closer to the K edge of iodine.

Dose reduction by reducing mAs and kV has mainly been investigated empirically. Murphy et al. found no significant differences in CBF, CBV, and Tmax estimated from brain CTP studies of patients with acute ischemic stroke acquired at 50 mAs

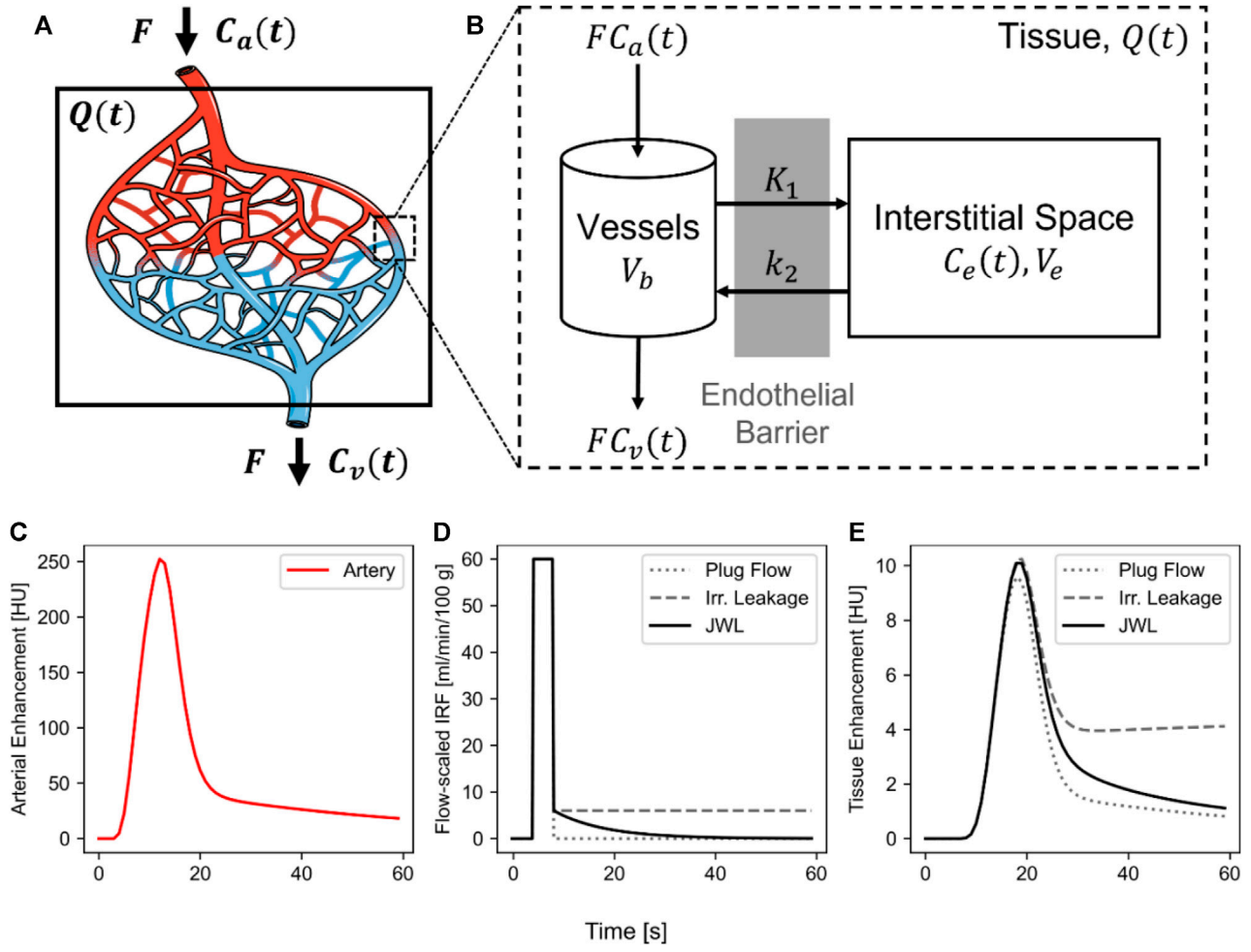

FIGURE 2
Contrast transport in CT perfusion. **(A)** Schematic of a tissue volume, ***Q***, comprising a network of capillaries with an arterial inlet time-contrast concentration (density), $C_a(t)$, supplied by blood flow ***F*** and a venous outlet time-contrast concentration, $C_v(t)$, drained similarly by ***F***. **(B)** Schematic of the Johnson–Wilson–Lee (JWL) model of contrast transport. **(C)** Arterial time–density curve, **(D)** JWL-based impulse residue functions, and **(E)** corresponding tissue time curves. **(A)** was adapted and modified with permission from Servier Medical Art, licensed under a Creative Commons Attribution 3.0 unported license.

versus 100 mAs at otherwise fixed protocols, potentially offering dose reduction by 50% [38]. Li et al. demonstrated that low-dose CTP acquired at 70 kV did not compromise the image quality of generated perfusion maps compared to 80 kV, resulting in a reduction of the effective dose from 4.7 to 3.0 mSv [39]. A low-dose 70 kV and 120 mAs CTP protocol was also superior to an 80 kV and 100 mAs protocol for CTP imaging of the pancreas, resulting in a lower effective dose of 3.60 *versus* 4.88 mSv [40]. The minimum image and TDC SNR required for reliable detection of disease at CTP is not yet known. A model relating the TDC SNR to lesion detectability may help determine the minimum required scan dose for the diagnosis.

3 Theory of contrast transport

This section describes the principles of contrast transport used to estimate perfusion parameters with dynamic contrast-enhanced CT imaging.

3.1 Fick principle

We begin with the Fick principle, which considers a control volume, Q, with an arterial inlet contrast concentration, $C_a(t)$, and a venous outlet contrast concentration, $C_v(t)$. A schematic is provided in Figure 2A. By conservation of mass, the concentration of contrast that accumulates in $Q(t)$ over time is related to C_a and C_v by:

$$Q(t) = F\int_0^t [C_a(\tau) - C_v(\tau)]\, d\tau, \tag{3.1}$$

where F is the blood flow (in units of mL/g per unit time, but often reported in mL/min/100 g) delivering contrast into and draining contrast out of the tissue volume. Eq. 3.1 is the integral form of the Fick principle and is the basis of the peak enhancement method for determination of perfusion: under the assumption of no venous outflow ($C_v(t) = 0$) in the period $[0, t_{max}]$, where t_{max} is the time when $Q(t)$ attains its maximum (peak) value. Eq. 3.1 can be rewritten as

$$F = \frac{[Q(t)]_{max}}{\int_0^{t_{max}} C_a(\tau)\, d\tau}, \tag{3.2}$$

which states that perfusion is the ratio of the maximum tissue TDC value and the area of the arterial curve until t_{max}. Alternatively, differentiating Eq. 3.1 while assuming no venous outflow results in

$$F = \frac{\left[\frac{d}{dt}Q(t)\right]_{max}}{C_{a,max}}. \tag{3.3}$$

Eq. 3.3, the differential form of the Fick principle, is the basis for the maximum front slope method [41], which states that blood flow is the quotient of the maximum slope of $Q(t)$ and the maximum value of the arterial curve. While this model simply describes blood flow, it relies on the assumption that there is no venous outflow of contrast agent during the measurement period, which is likely violated in regions such as the brain, where the artery-to-venous transit time of the contrast may be only 4–6 s. If this assumption is violated, the measured $Q(t)$ will change slower over time compared to no venous outflow, and blood flow will be underestimated as a result. Nonetheless, Eq. 3.3 highlights a key relationship between the slope of $Q(t)$, $C_a(t)$, and blood flow. Alternatively, F can be computed as the linear regression ($y = mx$) slope when taking $x = \int_0^t C_a(\tau)\, d\tau$ and $y = Q(t)$.

3.2 Impulse residue function

Meier and Zierler [42] formalized the work by Stewart [43] to describe an alternative impulse residue function (IRF)-based formulation to contrast transport. Consider a network of capillaries with contrast delivery via blood flow by an arterial inlet and a venous outlet (Figure 2A). The transit time of contrast from the arterial inlet to the venous outlet can be modeled by a probability distribution function or a transit time spectrum, $h(t)$, where $\int_0^\infty h(\tau)\, d\tau = 1$. If the transit time spectrum is time-invariant (does not change over the measurement time; *i.e.*, contrast transport can be modeled as a stationary system) and CT number is linear with contrast concentration, then by the principle of linear superposition, the TDC at the venous outlet is related to that at the arterial inlet as follows:

$$C_v(t) = C_a(t) \otimes h(t), \tag{3.4}$$

where $\otimes$ is the convolution operator defined as

$$f(t) \otimes g(t) = \int_{-\infty}^{\infty} f(\tau) g(t-\tau)\, d\tau. \tag{3.5}$$

Defining the IRF, $R(t)$, as the fraction of the contrast agent remaining in tissue at time t, results in

$$R(t) = 1 - \int_0^t h(\tau)\, d\tau. \tag{3.6}$$

Eq. 3.1 can be reformulated using (3.4) and (3.6) to arrive at the form:

$$\begin{aligned} Q(t) &= F \int_0^t C_a(\gamma) R(t-\gamma)\, d\gamma \\ &= F C_a(t) \otimes R(t) \end{aligned}. \tag{3.7}$$

The tissue TDC is the convolution of the arterial curve and the IRF scaled by blood flow. A flow-scaled IRF, $R_F(t)$, can be defined as $R_F(t) = FR(t)$ for convenience. Since $\int_0^t h(\tau)\, d\tau$ is a monotonically increasing function that ranges from 0 to 1, $R(t)$ also ranges from 0 to 1 and monotonically decreases between time 0 and t. This agrees with the definition that the IRF is the fraction of contrast remaining in the system at time t. F can then be estimated as the maximum value of the flow-scaled IRF.

The IRF describes a theoretical tissue response function if a unit mass of bolus was instantaneously injected into the arterial inlet (*i.e.*, $C_a(t) = \delta(t)$, a Dirac delta function). In practice, directly measuring the IRF non-invasively is infeasible. Imaging modalities such as CT, magnetic resonance imaging, or positron emission tomography are used to non-invasively measure $Q(t)$ and $C_a(t)$, and $R_F(t)$ is calculated by inverting the convolution, i.e., deconvolution. Deconvolution algorithms are discussed in Section 4.

3.3 Central volume principle

The central volume principle [42] describes the relationship between blood flow (F), blood volume (V_b), and the mean transit time (MTT) of blood through the tissue vasculature (both macro- and micro-vasculature). Consider that a bolus of the contrast agent is injected into the arterial inlet of the tissue, i.e., $F\int_0^{0+}\delta(t)dt = F$. At time t, by definition, the fraction of the contrast agent leaving the system is $h(t)\, dt$. If contrast agent and blood are uniformly mixed, the fraction of tissue blood volume leaving via the venous outlet at this time is $h(t)dt$. However, this fraction would have 'traced' a blood volume of $dV_b = Fh(t)tdt$. The total blood volume, V_b is obtained by integrating over time or

$$V_b = \int_0^\infty F\, th(t)\, dt = F\int_0^\infty th(t)\, dt.$$

$\int_0^\infty th(t)\, dt$ is recognized as the expected value of $h(t)$. The MTT of blood through the tissue vasculature (both macro and micro) is

$$MTT = \int_0^\infty th(t)\, dt.$$

Therefore, the central volume principle states that the blood volume is the product of the blood flow and the MTT:

$$V_b = F \cdot MTT. \tag{3.8}$$

Meier and Zierler also showed that the area underneath $R(t)$ is equal to the MTT [42]:

$$MTT = \int_0^\infty R(t)\, dt. \tag{3.9}$$

Of note, the central volume principle made no assumptions on the shape of $h(t)$, and thus is generally applicable, independent of the hemodynamic model of intravascular contrast transport.

3.4 Tracer kinetic modeling

So far, the properties of the contrast agent were not considered, and no assumptions were made about underlying hemodynamic processes that determine the functional form of the transit time

spectrum, $h(t)$, and therefore the IRF, $R(t)$. X-ray contrast is inert, does not bind to any target in blood or tissue, and does not enter cells [8]. Therefore, the contrast agent remains extracellular and distributes in the intravascular blood space and interstitial space. The magnitude of distribution in the interstitial space depends on the permeability of local capillaries. For example, an intact blood–brain barrier prevents the contrast agent from entering the interstitial space; however, if this barrier is disturbed, contrast can leak into the extravascular (interstitial) space and efflux from there back into the blood space by bidirectional passive diffusion depending on the concentration gradient. Without a tracer kinetic model, the distribution of the tracer in the intravascular and extravascular spaces cannot be described mathematically by the $R(t)$.

The Johnson–Wilson–Lee (JWL) model is a kinetic model that can describe the equilibration of contrast through the blood–tissue barrier between intra- and extra-vascular space [12, 44, 45], which accounts for the perfusion of contrast through the vasculature as well as its bidirectional permeation across the blood–tissue barrier. Note that because both perfusion and permeation are explicitly accounted for, the JWL model is valid independent of the relative rates of perfusion (F) and blood–tissue permeation (characterized by the permeability surface product (PS) of the barrier). A schematic of the JWL model is shown in Figure 2B. The JWL model IRF and its special cases (plug flow and irreversible leakage) are discussed in the following sections and are illustrated in Figure 2D. Corresponding tissue curves after convolving with the arterial curve in Figure 2C are shown in Figure 2E.

3.4.1 Johnson–Wilson–Lee model

The flow-scaled IRF of the JWL model is given by

$$\begin{aligned} R_F^{JWL}(t) &= \begin{cases} 0 & 0 \le t < T_0 \\ F & T_0 \le t < T_0 + W \\ FEe^{-k_2(t-T_0-W)} & t \ge T_0 + W \end{cases} \\ &= F[U(t-T_0) - U(t-T_0-W)] \\ &\quad + FEe^{-k_2(t-T_0-W)}U(t-T_0-W), \end{aligned} \tag{3.10}$$

where T_0 is the delay time between the arrival of the contrast agent at the artery and tissue; W is the minimum transit time for the contrast to pass through the tissue vasculature; FE is the flow-extraction product, where E is the fraction of the contrast that is extracted to the interstitial space by unidirectional passive diffusion ($0 \le E \le 1$), and k_2 is the efflux rate constant. $U(t)$ is the Heaviside step function:

$$U(t-\tau) = \begin{cases} 0 & t < \tau \\ 1 & t \ge \tau \end{cases}.$$

For the JWL model, St Lawrence and Lee showed that [45]

$$\begin{aligned} K_1 &= FE, \\ E &= 1 - e^{-PS/F}, \\ k_2 &= \frac{K_1}{V_e}, \end{aligned} \tag{3.11}$$

where K_1 is the influx rate constant of the extracted contrast agent to the extravascular space, PS is the permeability surface area product of the endothelial barrier and gives the permeation rate through passive diffusion, k_2 is the efflux rate constant of the contrast leaking back to the intravascular space, and V_e is the distribution volume of the extravascular space.

By using Eq. 3.10 and (3.7), a closed-form solution to $Q(t)$ can be derived:

$$\begin{aligned} Q^{JWL}(t) &= F[D(t-T_0) - D(t-T_0-W)] \\ &\quad + FEC_a(t-T_0-W) \otimes e^{-k_2 t}U(t-T_0-W), \end{aligned} \tag{3.12}$$

where $D(t-\gamma) = \int_\gamma^t C_a(\tau-\gamma)U(\tau-\gamma)\,d\tau$ and the time integral of $C_a(t)$ shifted by γ.

The standard interpretation of the JWL model is that all vessels in a tissue volume are fused into a single tube and, therefore, has a uniform transit time. In this case, the minimum transit time W is equal to the MTT. This is the so-called "plug flow" model in which the contrast agent passes through vessels without dispersion. In the case of a permeable vessel, a fraction of flowing contrast is initially extracted from the vessels into the extravascular space and then leaks back to the intravascular space at the efflux rate constant. Here, the exponential decay component of the JWL IRF is fully attributed to the wash-out of the extracted contrast from the extravascular space.

A modified interpretation of the JWL model may instead consider the exponential decay as a measure of dispersion due to varying vessel path lengths. In this interpretation, the contrast fully remains in the intravascular space and E represents the fraction of contrast with transit time > W such that the $MTT = W + E/k$ (*i.e.*, the mean vascular transit time is the total area underneath the JWL IRF). A mixed interpretation, one in which both heterogeneous vascular transit time and leakage of the endothelial barrier are accounted for, may be possible, but the two processes must be alternatively modeled or partitioned heuristically. The JWL model of contrast transport is, therefore, highly flexible depending on its interpretation and how the distribution of the contrast is partitioned between the intra- and extra-vascular space.

3.4.2 Special case of the Johnson–Wilson–Lee model: irreversible leakage ($k_2 = 0$)

A special case of the JWL model arises when the contrast leaks into the extravascular space but does not leak back into the intravascular space ($k_2 = 0$). The resulting flow-scaled IRF, $R_F^{FE}(t)$, for this special case is

$$\begin{aligned} R_F^{FE}(t) &= \begin{cases} 0 & 0 \le t < T_0 \\ F & T_0 \le t < T_0 + W \\ FE & t \ge T_0 + W \end{cases}, \\ &= F[U(t-T_0) - U(t-T_0-W)] \\ &\quad + FE\,U(t-T_0-W) \end{aligned} \tag{3.13}$$

and the closed-form solution, $Q^{FE}(t)$, is simplified to

$$Q^{FE}(t) = F[D(t-T_0) - D(t-T_0-W)] + FE\,D(t-T_0-W). \tag{3.14}$$

As with the JWL model, this special case can also be interpreted such that E represents the extraction of the contrast into the extravascular space from endothelial barrier leakage or the fraction of contrast with vascular transit time > W (heterogenous vascular transit time). MTT and V_b therefore depend on the interpretation of the model: in the former case, $MTT = W$, whereas in the latter case, $MTT = W + E(T_D - T_0)$, where T_D is the duration of the CTP study. A width $(T_D - T_0)$ is

enforced such that MTT is clipped to a finite value. $V_b = F \cdot MTT$ is the same as in Eq. 3.8 but depends on the adopted definition of MTT.

3.4.3 Patlak graphical analysis

The special case of the JWL model with irreversible leakage is similar to the Patlak graphical analysis method when taking $W \to 0$ in $R_F^{FE}(t)$ (i.e., a Dirac delta function in place of a finite-width boxcar) [46]. The Patlak flow-scaled IRF is therefore:

$$R_F^{Patlak}(t) = V_b\,\delta(t - T_0) + K_1 U(t - T_0), \tag{3.15}$$

where the area underneath the Dirac delta function is V_b. By evaluating Eq. 3.7 with (3.15), the tissue TDC can be expressed as

$$Q^{Patlak}(t) = V_b C_a(t - T_0) + K_1 \int_{T_0}^{t} C_a(\tau - T_0)\,d\tau. \tag{3.16}$$

Dividing both sides by $C_a(t - T_0)$ results in

$$\frac{Q^{Patlak}(t)}{C_a(t - T_0)} = V_b + K_1 \frac{\int_{T_0}^{t} C_a(\tau - T_0)\,d\tau}{C_a(t - T_0)}. \tag{3.17}$$

The Patlak parameters V_b and K_1 can then be estimated linearly taking $y = Q^{Patlak}(t)/C_a(t - T_0)$ and $x = \int_{T_0}^{t} C_a(\tau - T_0)\,d\tau / C_a(t - T_0)$ for assumed values of T_0 (e.g., by a grid search of T_0 values).

3.4.4 Special case of the Johnson–Wilson–Lee model: intravascular plug flow ($FE = 0$, $k_2 = 0$)

Another special case arises when there is no leakage of contrast to the extravascular space (*i.e.*, the contrast fully remains in the intravascular space) and the vascular transit time is uniform. As mentioned previously, this is the so-called "plug flow" model. The resulting IRF, $R_F^{plug}(t)$, for this special case is

$$\begin{aligned} R_F^{plug}(t) &= \begin{cases} 0 & 0 \le t < T_0 \\ F & T_0 \le t < T_0 + W \\ 0 & t \ge T_0 + W \end{cases} \\ &= F[U(t - T_0) - U(t - T_0 - W)] \end{aligned}, \tag{3.18}$$

and the closed-form solution, $Q^{plug}(t)$, is

$$Q^{plug}(t) = F[D(t - T_0) - D(t - T_0 - W)]. \tag{3.19}$$

Here, $W = MTT$ as the contrast is entirely intravascular. The significance of the two special cases of the JWL model will be elaborated in Section 4.2 when discussing model-dependent deconvolution methods.

4 Deconvolution methods

Deconvolution aims to "invert" the convolution in Eq. 3.7 to recover the flow-scaled IRF from the measured arterial ($C_a(t)$) and tissue TDCs ($Q(t)$). Methods can be broadly categorized into model-independent and model-dependent deconvolution. Model-independent methods make no assumption about the functional form of $R_F(t)$ which is non-parametrically recovered from the measured $Q(t)$ and $C_a(t)$. Conversely, model-dependent methods parameterize $R_F(t)$ based on tracer kinetic models (e.g., equations 3.9; 3.12; 3.14) and use the parametric form of $Q(t)$ (e.g., equations 4.11; 4.13; 4.15; 4.16) to estimate the model parameters of $R_F(t)$. It has been extensively shown that different deconvolution methods can produce different estimates of perfusion parameters [47–50].

4.1 Model-independent deconvolution

First, the convolution in Eq. 3.7 can be discretized as

$$\boldsymbol{q}[j] = \Delta t \sum_{i=0}^{N-1} \boldsymbol{c_a}[i]\boldsymbol{r_F}[j - i], \tag{4.1}$$

where

$$\begin{aligned} \boldsymbol{q} &= [Q(t_0), Q(t_1), \cdots, Q(t_{N-1})]^T \\ \boldsymbol{c_a} &= [C_a(t_0), C_a(t_1), \cdots, C_a(t_{N-1})]^T \\ \boldsymbol{r} &= [R_F(t_0), R_F(t_1), \cdots, R_F(t_{N-1})]^T \end{aligned}$$

are vectorized forms of $Q(t)$, $C_a(t)$, and $R_F(t)$, respectively, over measurement times $t_0, t_1, \ldots, t_{N-1}$ at Δt uniformly spaced intervals. i and j are integer vector indices, and N is the number of vector elements. Vectors and matrices are denoted by emboldened characters.

The discrete convolution in Eq. 3.14 can be formulated as a matrix multiplication:

$$\boldsymbol{q} = \Delta t\, \boldsymbol{A}\boldsymbol{r}, \tag{4.2}$$

where $\boldsymbol{A}$ is a Toeplitz matrix formed by the elements of $\boldsymbol{c_a}$:

$$\boldsymbol{A} = \begin{bmatrix} C_a(t_0) & 0 & \cdots & 0 \\ C_a(t_1) & C_a(t_0) & \cdots & 0 \\ \vdots & \vdots & \ddots & \vdots \\ C_a(t_{N-1}) & C_a(t_{N-2}) & \cdots & C_a(t_0) \end{bmatrix}. \tag{4.3}$$

Model-independent deconvolution methods therefore aim to non-parametrically recover $\boldsymbol{r}$ from the measured $\boldsymbol{q}$ and $\boldsymbol{c_a}$.

4.1.1 Singular value decomposition

One of the most commonly used approaches to recover $\boldsymbol{r}$ in perfusion imaging is with singular value decomposition (SVD) [49, 51]. The SVD factorizes an $m \times n$ matrix, $\boldsymbol{M}$, into the form:

$$\boldsymbol{M} = \boldsymbol{U}\Sigma\boldsymbol{V}^{\boldsymbol{T}} = \sum_{i=1}^{k} \sigma_i \boldsymbol{u_i}\boldsymbol{v_i}^T,$$

where $\boldsymbol{U} = [\,\boldsymbol{u_1}\ \ldots\ \boldsymbol{u_m}\,]$ and $\boldsymbol{V}^T = [\,\boldsymbol{v_1}\ \ldots\ \boldsymbol{v_n}\,]^T$ are real orthogonal matrices for a real matrix $\boldsymbol{M}$, comprising left and right singular vectors $\boldsymbol{u_i}$ and $\boldsymbol{v_i}$, respectively, and Σ is an $m \times n$ diagonal matrix with non-negative real singular values $\sigma_i = \Sigma_{ii}$ on its diagonal. Singular values by convention are arranged in descending order such that $\sigma_1 \ge \sigma_2 \ge \ldots \ge \sigma_k$, where k is the rank of $\boldsymbol{M}$. Knowing that the inverse of an orthogonal matrix is its transpose, the pseudoinverse of $\boldsymbol{M}$ can be obtained by

$$\boldsymbol{M}^{+} = \boldsymbol{V}\Sigma^{+}\boldsymbol{U}^{T} = \sum_{i=1}^{k} \frac{\boldsymbol{v_i}\boldsymbol{u_i}^T}{\sigma_i},$$

where $^+$ indicates the pseudoinverse and Σ^+ is obtained by taking the reciprocal of each singular value:

$$\Sigma_{ii}^{+} = \begin{cases} 1/\sigma_i & \sigma_i > 0 \\ 0 & \sigma_i = 0 \end{cases}.$$

Eq. 3.14 can then be solved by the pseudoinverse with the SVD:

$$\hat{\boldsymbol{r}} = \frac{1}{\Delta t}\boldsymbol{V}\Sigma^{+}\boldsymbol{U}^{T}\boldsymbol{q} = \frac{1}{\Delta t}\sum_{i=1}^{k}\frac{\boldsymbol{u}_i^{T}\boldsymbol{q}}{\sigma_i}\boldsymbol{v}_i, \tag{4.4}$$

where $\hat{\boldsymbol{r}}$ is the pseudoinverse-estimated flow-scaled IRF and $\boldsymbol{U}$,Σ,$\boldsymbol{V}$ are from the SVD of $\boldsymbol{A}$. The pseudoinverse returns the least-squares solution [49, 52, 53]:

$$\hat{\boldsymbol{r}} = \underset{\boldsymbol{r}}{\operatorname{argmin}} \|\boldsymbol{q} - \boldsymbol{A}\boldsymbol{r}\|_2^2.$$

However, since Σ^{+} comprises reciprocals of σ_i, small singular values will cause the solution $\hat{\boldsymbol{r}}$ to be unstable [53]. Small singular values arise when columns of $\boldsymbol{A}$ are collinear, that is, columns of $\boldsymbol{A}$ can be expressed as a linear combination of its other columns [54]. A simple method to combat this problem is to truncate small singular values below a prescribed threshold [49, 55]:

$$f_{i,\lambda_r}^{trunc} = \begin{cases} 1 & \sigma_i > \lambda \\ 0 & \sigma_i \le \lambda \end{cases}, \tag{4.5}$$

where f_{i,λ_r}^{trunc} is a regularization filter and $\lambda = \lambda_r\sigma_1$ is the singular value threshold for truncating singular values below a fraction λ_r of the largest singular value σ_1. Commonly used values for λ_r range between 10% and 20% [48–50]. Alternatively, small singular values can be rolled off more smoothly with a Tikhonov/Wiener weighting filter [56]:

$$f_{i,\lambda_r}^{Tikh} = \frac{\sigma_i^2}{\sigma_i^2 + \lambda^2}.$$

These filters can be incorporated into Eq. 4.4:

$$\hat{\boldsymbol{r}} = \frac{1}{\Delta t}\sum_{i=1}^{k} f_{i,\lambda_r}\frac{\boldsymbol{u}_i^{T}\boldsymbol{q}}{\sigma_i}\boldsymbol{v}_i,$$

where f_{i,λ_r} is either f_{i,λ_r}^{trunc} or f_{i,λ_r}^{Tikh}. Of note, the solution $\hat{\boldsymbol{r}}$ obtained after applying the Tikhonov/Wiener filter is equivalent to the least-squares solution with Tikhonov (2-norm) regularization [56, 57]:

$$\hat{\boldsymbol{r}} = \underset{\boldsymbol{r}}{\operatorname{argmin}} \|\boldsymbol{q} - \boldsymbol{A}\boldsymbol{r}\|_2^2 + \lambda^2\|\boldsymbol{I}\boldsymbol{r}\|_2^2,$$

where $\boldsymbol{I}$ is the identity matrix. More advanced constraints, such as non-negativity and regularizing the second derivative of $\boldsymbol{r}$ (by replacing $\boldsymbol{I}$ with a second-order finite difference matrix) to reduce spurious oscillations [58, 59], may be further applied to produce more physiologically reasonable solutions, but is outside the scope of this review.

Standard SVD deconvolution is considered delay-sensitive; that is, $\hat{\boldsymbol{r}}$ is erroneous when there is a time interval between contrast arrival at $C_a(t)$ and at $Q(t)$. This time interval is T_0. There are two cases to consider: (1) when the contrast arrives at $Q(t)$ earlier than at $C_a(t)$ and, conversely, (2) when the contrast arrives at $Q(t)$ later than at $C_a(t)$. The first case is arguably more problematic as it violates the causality assumption of the contrast transport theory formulated in Eq. 4.2, where tissue enhancement, $Q(t)$, is expected to be "driven" by the arterial contrast concentration, $C_a(t)$. $Q(t)$ and $R(t)$ must therefore be 0 between $0 \le t < T_0$ as the contrast has not yet arrived in the tissue from the artery. However, this assumption may not hold in practice if $C_a(t)$ was obtained from a distal artery relative to the local artery supplying $Q(t)$. Alternatively, $C_a(t)$ may have been selected in an ischemic region where arterial contrast arrival is delayed relative to that of normal brain. In such cases, $T_0 < 0$ and the first non-zero element of $Q(t)$ and $R(t)$ occur at $t < 0$. Smith et al. [60] reformulated the standard SVD deconvolution to enforce causality by deconvolving a shifted $Q(t)$ such that it lags $C_a(t)$. Without shifting $Q(t)$, standard SVD substantially overestimated true blood flow, but after reformulation, SVD blood flow was equivalent to that of delay-insensitive deconvolution [60].

The second case, in which the contrast arrives at $Q(t)$ later than that at $C_a(t)$, is common in acute ischemic stroke and may lead to an underestimation of blood flow [61, 62]. $C_a(t)$ is often selected at a proximal large artery, and $Q(t)$ is downstream of an occlusion, so the contrast arrival in tissue is delayed. In these cases, $T_0 > 0$, and $Q(t)$ and $R(t)$ should theoretically be 0 between $0 \le t < T_0$ as no contrast has arrived at $t < T_0$. As this criterion is not enforced by the formulation in Eq. 4.2, $\hat{\boldsymbol{r}}$ may not be 0 between $0 \le t < T_0$. True blood flow is underestimated as a result of SVD deconvolution when $T_0 > 0$ [61, 62]. Ibaraki et al. proposed estimating T_0 for each tissue curve until the arterial peak time by a least-squares fitting to $Q(t)$ with a shifted $C_a(t)$ convolved with an exponential decay kernel. Alternatively, a more thorough but computationally expensive method would be to iteratively shift $Q(t)$ for a range of T_0 and compute an $\hat{\boldsymbol{r}}_{T_0}$ by SVD for each T_0-shifted $Q(t)$, $\boldsymbol{q}_{T_0}$ [58]. The optimal delay time and deconvolved IRF would be the $\hat{\boldsymbol{r}}_{T_0}$ producing the least-squares difference between $\boldsymbol{q}_{T_0}$ and $\boldsymbol{A}\hat{\boldsymbol{r}}_{T_0}$. By including both negative and positive delays in the iterative search of T_0, this method can address both delay sensitivity problems of standard SVD in which the contrast can arrive at $Q(t)$ either earlier or later than at the selected $C_a(t)$.

4.1.2 Block-circulant singular value decomposition

Wu et al. described a delay-insensitive deconvolution method by performing the SVD with a block-circulant matrix of $\boldsymbol{c_a}$ [50]. The matrix multiplication in Eq. 4.2 becomes a circular convolution when replacing $\boldsymbol{A}$ with the circulant matrix, $\boldsymbol{A_c}$:

$$\boldsymbol{A}_c = \begin{bmatrix} C_a(t_0) & 0 & \cdots & 0 & 0 & C_a(t_{N-1}) & \cdots & C_a(t_1) \\ C_a(t_1) & C_a(t_0) & \cdots & 0 & 0 & 0 & \cdots & C_a(t_2) \\ \vdots & \vdots & \ddots & \vdots & \vdots & \vdots & \ddots & \vdots \\ C_a(t_{N-1}) & C_a(t_{N-2}) & \cdots & C_a(t_0) & 0 & C_a(t_{N-2}) & \cdots & 0 \\ 0 & C_a(t_{N-1}) & \cdots & C_a(t_1) & C_a(t_0) & 0 & \cdots & 0 \\ 0 & 0 & \cdots & C_a(t_2) & C_a(t_1) & C_a(t_0) & \cdots & 0 \\ \vdots & \vdots & \ddots & \vdots & \vdots & \vdots & \ddots & \vdots \\ 0 & C_a(t_{N-2}) & \cdots & 0 & C_a(t_{N-1}) & C_a(t_{N-2}) & \cdots & C_a(t_0) \end{bmatrix} = \begin{bmatrix} \boldsymbol{A} & \boldsymbol{A}' \\ \boldsymbol{A}' & \boldsymbol{A} \end{bmatrix},$$

where

$$\boldsymbol{A}' = \begin{bmatrix} 0 & C_a(t_{N-1}) & \cdots & C_a(t_1) \\ 0 & 0 & \cdots & C_a(t_2) \\ \vdots & \vdots & \ddots & \vdots \\ 0 & C_a(t_{N-2}) & \cdots & 0 \end{bmatrix}.$$

Block-circulant SVD deconvolution can be performed using $\boldsymbol{A_c}$ in Eq. 4.2 and using the pseudoinverse method with regularization as described in the previous section. Circular convolution is equivalent to linear convolution with time aliasing [63]. Time aliasing can be avoided by appending $\boldsymbol{c_a}$ with zeroes to have a total length $\ge 2N$, which is already considered in the above notation. Note that this is equivalent to applying a rectangular window function of width t_{N-1}; unless $\boldsymbol{c_a}$ decays to 0 at $t = t_{N-1}$, the sharp change from $C_a(t_{N-1})$ to 0 will result in Gibbs ringing artifact in the deconvolved IRF $\hat{\boldsymbol{r}}$.

Ringing can be mitigated in part by regularizing the solution with an oscillation index as described by Gobbel and Fike [50, 64]. Regularizing the second derivative of $\hat{\boldsymbol{r}}$ as briefly alluded in the previous section may also be effective in this context.

4.1.3 Fourier transform deconvolution

The Fourier transform-based method of deconvolution utilizes the convolution theorem, which states that a convolution in the time domain is a product in the frequency domain. Applying the Fourier transform to both sides of Eq. 3.7 results in

$$\tilde{Q}(f) = \tilde{C}_a(f) \cdot \tilde{R}_F(f),$$

where ~ indicates the Fourier transform of a function and f is the frequency variable in units of inverse time. $R_F(t)$ can then be obtained by taking the inverse Fourier transform ($\mathcal{F}^{-1}$) of the quotient of the tissue and arterial curve frequency spectra:

$$R_F(t) = \mathcal{F}^{-1}\left\{\frac{\tilde{Q}(f)}{\tilde{C}_a(f)}\right\}.$$

The Fourier transform method of deconvolution is mathematically equivalent to the block-circulant SVD method [50, 53]. It follows that $Q(t)$ and $C_a(t)$ should also be zero-padded in this method to have a total length $\geq 2N$ prior to taking the Fourier transform to avoid time aliasing. As with SVD methods, the Fourier transform method is also highly sensitive to noise and must be regularized with a filter, $\tilde{g}(f)$:

$$R_F(t) = \mathcal{F}^{-1}\left\{\tilde{g}(f)\,\frac{\tilde{Q}(f)}{\tilde{R}_F(f)}\right\}.$$

$\tilde{g}(f)$ could be a rectangular low-pass filter defined as

$$\tilde{g}^{lp}(f) = \begin{cases} 1 & -\lambda \leq R_F(f) \leq \lambda \\ 0 & |f| > \lambda \end{cases},$$

where $\lambda = \lambda_r \tilde{R}_F(0)$ is a fractional threshold of the zero-frequency $\tilde{R}_F(0)$ and would be equivalent to block-circulant SVD with truncated singular values of the same relative threshold. Alternatively, Straka et al. proposed a Wiener-like filter to roll off high-frequency components more smoothly [65]:

$$\tilde{g}^{Wiener}(f) = \begin{cases} \dfrac{\tilde{C}_a^2(f) - N^2}{\tilde{C}_a^2(f)} & \tilde{C}_a(f) > N, f \neq 0 \\ 1 & f = 0 \\ 0 & else \end{cases}, \tag{4.6}$$

where $N = \frac{\lambda_r}{2}\max|\tilde{C}_a(f)|$. Wiener-like filtering is effectively similar to Tikhonov regularization in block-circulant SVD. Note that the filter value at zero frequency is 1, and thus the zero frequency of the filtered $\tilde{R}_F(f)$ remains unchanged. The significance of the zero frequency of $\tilde{R}_F(f)$ is that it is the area underneath $R_F(t)$, which is equal to the blood volume. This can be shown by evaluating the Fourier transform integral at $f = 0$:

$$\tilde{R}_F(0) = \int_{-\infty}^{\infty} R_F(t)\,dt = F\int_0^t R(\tau)\,d\tau = F \cdot MTT = V_b.$$

As such, with careful filtering to not modify the zero-frequency value during Fourier transform deconvolution, blood volume estimates will be unaffected by regularization.

4.1.4 Bayesian deconvolution

Applying Bayesian deconvolution to estimate hemodynamic parameters in patients starts with the assumption that each patient can be specified by two types of events (characteristics)—CTP TDCs and the model represented by the flow-scaled IRF, $R_F(t)$, to generate $Q(t)$ according to Eq. 3.7. The *a* posteriori probability of $R_F(t)$ given a measured $Q(t)$, or $P(R_F(t)|Q(t))$, can be factored using the Bayes Theorem [66] as follows:

$$P(R_F(t)|Q(t)) = \frac{P(Q(t)|R_F(t))P(R_F(t))}{P(Q(t))}, \tag{4.7}$$

where $P(Q(t)|R_F(t))$ is the probability (likelihood) of observing $Q(t)$ given a specific $R_F(t)$, $P(R_F(t))$ is the *a priori* probability of $R_F(t)$, and $P(Q(t))$ is the probability of observing $Q(t)$. The Bayesian deconvolution for $R_F(t)$ then maximizes the *a posteriori* probability $P(R_F(t)|Q(t))$ or

$$\underset{R_F(t)}{\operatorname{argmax}}\, P(R_F(t)|Q(t)) = \underset{R_F(t)}{\operatorname{argmax}}\, \frac{P(Q(t)|R_F(t))P(R_F(t))}{P(Q(t))}. \tag{4.8}$$

$P(Q(t))$ can also be written as

$$P(Q(t)) = \int P(Q(t)|R_F(t))P(R_F(t))dR_F(t). \tag{4.9}$$

Eq. 4.9 shows that $P(Q(t))$ gives the probability (evidence) that the measured $Q(t)$ can be modeled by $R_F(t)$ using Eq. 3.7. Unless there are biases or artifacts in the CTP study, every $Q(t)$ is equally likely; therefore, $P(Q(t))$ is uniform and Eq. 4.8 simplifies to

$$\underset{R_F(t)}{\operatorname{argmax}}\, P(R_F(t)|Q(t)) = \underset{R_F(t)}{\operatorname{argmax}}\, P(Q(t)|R_F(t))P(R_F(t)). \tag{4.10}$$

If $P(R_F(t))$ is uniform (i.e., ~1), i.e., we do not have prior knowledge of which $R_F(t)$ is more likely, Eq. 4.10 simplifies to

$$\underset{R_F(t)}{\operatorname{argmax}}\, P(R_F(t)|Q(t)) = \underset{R_F(t)}{\operatorname{argmax}}\, P(Q(t)|R_F(t)). \tag{4.11}$$

Eq. 4.11 shows that the Bayesian deconvolution or maximum *a posteriori* (MAP) is equivalent to the maximum likelihood estimation of $R_F(t)$ under the assumption that both $P(R_F(t))$ and $P(Q(t))$ are uniform. In addition, because an $R_F(t)$ that maximizes $P(R_F(t)|Q(t))$ and $P(Q(t)|R_F(t))$ also maximizes their logarithms, Eq. 4.11 can also be written as

$$\underset{R_F(t)}{\operatorname{argmax}}\, \log P(R_F(t)|Q(t)) = \underset{R_F(t)}{\operatorname{argmax}}\, \log P(Q(t)|R_F(t)). \tag{4.12}$$

Assuming that the measured $Q(t)$ has a Gaussian noise of equal variance, σ^2, distributed around the true value and the noise between samples is independent (IID Gaussian noise), then the likelihood, $P(R_F(t)|Q(t))$, can be written as

$$P(R_F(t)|Q(t)) = \prod_{n=1}^{N} \frac{1}{\sqrt{2\pi\sigma^2}} e^{-\frac{1}{2}\left(\frac{Q(t_n) - [C_a(t) \otimes R_F(t)]_{t=t_n}}{\sigma}\right)^2}. \tag{4.13}$$

Substituting Eq. 4.13 into (4.12) results in

$$\underset{R_F(t)}{\operatorname{argmax}}\, \log P(R_F(t)|Q(t)) = \underset{R_F(t)}{\operatorname{argmin}} \sum_{n=1}^{N} \frac{1}{2\sigma^2}\left(Q(t_n) - [C_a(t) \otimes R_F(t)]_{t=t_n}\right)^2 + \sum_{n=1}^{N} \frac{1}{2} log\left(\sqrt{2\pi\sigma^2}\right).$$

Therefore, the MAP $R_F(t)$ estimate is equivalent to the traditional least-squares estimate. That is, under the assumptions of (1), $P(R_F(t))$ and $P(Q(t))$ are uniform (i.e., ~1) and (2) $Q(t)$ has IID Gaussian noise:

$$\underset{R_F(t)}{\operatorname{argmax}} P(R_F(t)|Q(t)) = \underset{R_F(t)}{\operatorname{argmin}} \sum_{n=1}^{N} \left(Q(t_n) - [C_a(t) \otimes R_F(t))]_{t=t_n}\right)^2. \tag{4.14}$$

When *a priori* knowledge of $R_F(t)$ is available, the MAP $R_F(t)$ estimate for uniform $P(Q(t))$ is given by the log transformation of Eq. 4.10:

$$\underset{R_F(t)}{\operatorname{argmax}} \log P(R_F(t)|Q(t)) = \underset{R_F(t)}{\operatorname{argmax}} \left[\log P(Q(t)|R_F(t)) + \log P(R_F(t))\right]. \tag{4.15}$$

If $Q(t)$ has IID Gaussian noise, Eq. 4.15 can be rewritten as (ignoring constant term) follows:

$$\underset{R_F(t)}{\operatorname{argmax}} \log P(R_F(t)|Q(t)) \sim \underset{R_F(t)}{\operatorname{argmax}} \sum_{n=1}^{N} -\frac{1}{2\sigma^2}\left(Q(t_n) - [C_a(t) \otimes R_F(t)]_{t=t_n}\right)^2 + \underset{R_F(t)}{\operatorname{argmax}} \log P(R_F(t)). \tag{4.16}$$

One useful *a priori* constraint on $R_F(t)$ is smoothness as measured by the integral of the square of the curvature. Boutelier et al. formally expressed the smoothness of $R(t)$ as a probability distribution and solved for the MAP distribution, $\hat{P}(R_F(t)|Q(t))$, using Eq. 4.16 [67]. The hemodynamic parameters can then be obtained as the means of different marginal distributions of $\hat{P}(R_F(t)|Q(t))$.

The marginal *a posteriori* distribution of F, $\hat{P}(F|Q(t))$, is obtained by evaluating the following multiple definite integrals (noting $R_F(t) = FR(t)$):

$$\hat{P}(F|Q(t)) = \int_{R(t)} \hat{P}(R_F(t)|Q(t))dR(t),$$

which is a definite integral in the N-dimensional space (as $R(t)$ is discretized into a vector of N elements, see Eq. 4.1). The Bayesian deconvolution-estimated blood flow, $\hat{F}$, is the mean of $\hat{P}(F|Q(t))$:

$$\hat{F} = \int F\hat{P}(F|Q(t))dF.$$

The marginal *a posteriori* distribution of $R(t)$, $\hat{P}(R(t)|Q(t))$, is obtained by evaluating the following multiple definite integrals:

$$\hat{P}(R(t)|Q(t)) = \int_{F} \hat{P}(R_F(t)|Q(t))dF.$$

The Bayesian deconvolution-estimated IRF, $\hat{R}(t)$, is the mean of $\hat{P}(R(t)|Q(t))$:

$$\hat{R}(t) = \int_{R(t)} R(t)\,\hat{P}(R(t)|Q(t))dR(t),$$

which is a definite integral in the N-dimensional space. The estimated mean transit time, $\widehat{MTT}$, is calculated as

$$\widehat{MTT} = \sum_{n=1}^{N} R(t_n)\Delta t,$$

where Δt is the sampling interval of $Q(t)$. Finally, the estimated fit to $Q(t)$ is evaluated by Eq. 3.7 with $\hat{F}\hat{R}(t)$.

However, calculations of both marginal distributions and their means can be time-consuming as they involve evaluating up to N definite integrals, where N is the number of samples of $Q(t)$ and $R(t)$, which can be as many as 90 depending on the sampling interval. Approximate analytical rather than more exact numerical integration can speed up the calculation but lead to oscillating and negative $R(t)$ at certain times [66], both of which are non-physiological.

The right side of Eq. 4.16 suggests that Bayesian deconvolution with *a priori* knowledge of $P(R(t))$ can be cast as an optimization problem. If a least-squares criterion is used for IID Gaussian noise in $Q(t)$, then the cost function $\mathbb{C}(R(t),\lambda)$ to be minimized is

$$\mathbb{C}(R(t),\lambda) = \sum_{n=1}^{N}\left(Q(t_n) - [C_a(t) \otimes R_F(t)]_{t=t_n}\right)^2 + \lambda\int_{R(t)}\left(\frac{d^2R(t)}{dt^2}\right)^2 dR(t) \tag{4.17}$$

for imposing *a priori* smoothness constraint on $R(t)$, where λ is the Lagrange multiplier to control the importance of $R(t)$ smoothness relative to the least-squares criterion. $\mathbb{C}(\mathcal{R}(t),\lambda)$ is linear with respect to $R(t)$ and λ and, therefore, is amenable to non-negative linear least-squares (NNLS) techniques described by Lawson and Hanson [52]. Lee extended the optimization to include time causality (i.e., $Q(t)$ must start later than $C_a(t)$ or $Q(t)$ lags behind $C_a(t)$ by $\tau > 0$) and monotonicity (i.e., $R(t)$ starts with a maximal plateau for a duration equal to the minimum transit time and thereafter decreases monotonically to baseline without oscillations) [58].

4.2 Johnson–Wilson–Lee model-dependent deconvolution

Model-dependent deconvolution based on the JWL model will be described in this section. The special cases of the JWL model as described previously simplify parameter estimation by reducing the number of unknowns.

The closed-form solution of the JWL tissue curve, $Q^{JWL}(t)$, is shown in Eq. 3.12. This equation can be discretized as

$$\boldsymbol{q} = \boldsymbol{D}\boldsymbol{f}, \tag{4.18}$$

where $\boldsymbol{f} = [\,F \;\; FE\,]^T$ and $\boldsymbol{D}$ is an $N\times 2$ matrix given by

$$\boldsymbol{D} = \begin{bmatrix} D(t_0 - T_0) - D(t_0 - T_0 - W) & G(t_0 - T_0 - W) \\ D(t_1 - T_0) - D(t_1 - T_0 - W) & G(t_1 - T_0 - W) \\ \vdots & \vdots \\ D(t_{N-1} - T_0) - D(t_{N-1} - T_0 - W) & G(t_{N-1} - T_0 - W) \end{bmatrix}. \tag{4.19}$$

$D(t-\gamma) = \int_{\gamma}^{t} C_a(\tau-\gamma)\,U(\tau-\gamma)\,d\tau$ is the time integral of the arterial TDC, and $G(t-\gamma) = C_a(t-\gamma) \otimes e^{-k_2 t}\,U(t-\gamma)$ is the convolution of the arterial TDC with an exponential decay function.

Note that $D(t)$ can be computed numerically with the measured $C_a(t)$, and evaluating $G(t)$ requires an estimate of k_2. Therefore, there are five unknown parameters: F,FE,T_0,W,k_2. Estimating the five parameters of the JWL model requires solving a nonlinear optimization problem. This is computationally intensive, requires a

reliable initial guess, and is susceptible to returning solutions of local minima. To solve for the parameters in the JWL model, Bennink et al. [68] used parameter estimates from a simplified model as initial guesses to a nonlinear regression of Eq. 3.12. It is unclear whether these initial guesses may have biased the nonlinear regression to unsatisfactory local minimum solutions.

Alternatively, the estimation of $\boldsymbol{f}$ can be linearized by performing a grid search of the nonlinear parameters T_0,W,*and* k_2. With assumed values of T_0,W, and k_2, $D(t)$ and $G(t)$ can be numerically evaluated and $\boldsymbol{f}$ can be estimated by an NNLS algorithm to enforce physiological positive values of blood flow and the flow-extraction product [52]. For example, a grid search may comprise 25 values of T_0 from 0 to 24 s at 1-s intervals, 25 values of W between 2 and 26 s at 1-s intervals, and 25 logarithmically spaced values of k_2 between 10^{-3} and 1 s^{-1}, leading to 15,625 grid search combinations. The optimal set of estimated parameters, $\hat{\boldsymbol{f}}$,$\hat{T}_0$, $\hat{W}$, and $\hat{k}_2$ would be the set that minimizes the squared differences between $\boldsymbol{q}$ and $\boldsymbol{Df}$:

$$\hat{\boldsymbol{f}},\hat{T}_0,\hat{W},\hat{k}_2 = \underset{\hat{\boldsymbol{f}},\hat{T}_0,\hat{W},\hat{k}_2}{\arg\min} \left\|\boldsymbol{q}-\boldsymbol{Df}\right\|_2^2 s.t. \boldsymbol{f} \geq 0. \tag{4.20}$$

As can be seen, the number of NNLS required can be large depending on the number of grid search combinations. Advanced optimization methods, such as using a dynamic grid search step size, may be required to reduce the grid search combinations for efficient application in practice. Alternatively, the grid search can be greatly accelerated by assuming a simplified model as described in Section 3.4.2 and Section 3.4.4.

Using the irreversible leakage model described in Section 3.4.2, it is assumed that k_2= 0. The exponential function with a decay rate constant of 0 evaluates to 1, so the convolution term $G(t-T_0-W)$ is simply the shifted time integral of the arterial TDC ($G(t-T_0-W) = D(t-T_0-W)$ when k_2= 0). By excluding k_2 from the grid search, the number of grid search combinations greatly decreases (e.g., 25 × 25 = 625 in the above example), resulting in a more manageable computation time. The four model parameters are estimated as described for the JWL model with the aforementioned simplifications.

A further simplification is to assume no leakage and a uniform vascular transit time as in the plug flow model described in Section 3.4.4. Here, FE= 0, so there are three model parameters to be estimated: $\boldsymbol{f}$ = [F], T_0, and W. As such, only the first column of $\boldsymbol{D}$ is required in Eq. 4.19. A fast method of calculating a normalized form of the residuals is as follows. Knowing that the areas underneath the left and right sides of Eq. 3.19 are equal, we can normalize both sides to have an unit area as follows:

$$\frac{Q(t)}{\int_0^T Q(t)\,dt} = \frac{D(t-T_0)-D(t-T_0-W)}{\int_0^T D(t-T_0)-D(t-T_0-W)\,dt},$$

where T is the total measurement time. Areas of $Q(t)$ and $D(t-T_0)-D(t-T_0-W)$ can both be computed numerically. Note that F is eliminated on the right-hand side after normalizing the area and eliminates the need to estimate $\boldsymbol{f}^{\boldsymbol{plug}}$ to compute the normalized residuals. Defining $\boldsymbol{q}'$ and $\boldsymbol{D}'$ as $\boldsymbol{q}^{\boldsymbol{plug}}$ and $\boldsymbol{D}^{\boldsymbol{plug}}$ normalized by their respective areas, the residuals become $\|\boldsymbol{q}'-\boldsymbol{D}'\boldsymbol{1}\|_2^2$, where $\boldsymbol{1}$ is a vector of 1. The set of $\hat{T}_0$,$\hat{W}$ that produce the minimum residual can be quickly determined, and only a single NNLS needs to be computed to determine the corresponding optimal $\hat{\boldsymbol{f}}$ for the TDC. A similar approach without T_0-delay estimation was described by Axel [69].

While the appeal of the simplified models is their fast computation, their assumptions may not hold in general, especially in highly diseased conditions.

4.3 Comparison of deconvolution methods

We compared the quantitative accuracy of five deconvolution algorithms: two model-independent (SVD and Fourier transform) and three model-dependent (plug flow, irreversible leakage, and JWL) deconvolution methods. Block-circulant SVD was omitted as it produced the same results as the Fourier transform method when using equivalent regularization filters. Details of the methods are provided in Section 4.1 and Section 4.2. Specifically, SVD was not delay-corrected and regularized by truncating the smallest 15% of the largest singular value as described in Eq. 4.5. Fourier transform deconvolution used a Wiener-like regularization filter with 15% regularization as described in Eq. 4.6. The plug flow and irreversible leakage model deconvolution methods were the simplified cases of the JWL model as described in Section 4.2 and used a grid search of $T_0 \in [0, 1, \ldots, 20]$ s and $W \in [2, 3, \ldots, 24]$ s. A research version of commercial CTP software (CT Perfusion 4D, GE Healthcare) was used to solve for the full JWL model parameters. The remaining four methods were implemented in-house using a custom Python script. Details on the simulation of CTP data are provided in the Supplementary Materials.

4.3.1 Ground truth *versus* deconvolution-estimated blood flow

Correlation plots comparing ground truth *versus* mean estimated blood flow over 1,024 trials for each deconvolution method are shown in Figure 3. Simulation of routine-dose noise (σ= 2.5 HU) and low-dose noise (σ= 5.0 HU) is shown in the left and right columns, respectively. Linear lines of best fit are indicated by the solid red lines, while the dashed black line is the identity line. The linear regression slope is an indicator of parametric contrast (i.e., magnitude of difference between high and low estimated blood flow values), and the intercept can be loosely interpreted as an indicator of bias at low ground truth blood flow values. The linear regression line of an ideal method would be the identity line, indicating a one-to-one agreement between the ground truth and estimated blood flow values.

As shown in the correlation plots, all deconvolution methods have a positive vertical axis intercept that is similar in value and overestimates very low true blood flow values (e.g., <8 mL/min/100 g). The regression intercept has greater deviation from the origin at the low-dose noise level compared to the routine-dose noise level. Notably, the model-independent methods have shallower regression slopes that substantially underestimate higher true blood flow values, whereas the regression slopes of model-dependent methods are closer to 1. This indicates that despite the difference in the simulated model IRF *versus* those used in model-dependent deconvolution methods, (1) the model-dependent deconvolution methods investigated here are better able to estimate

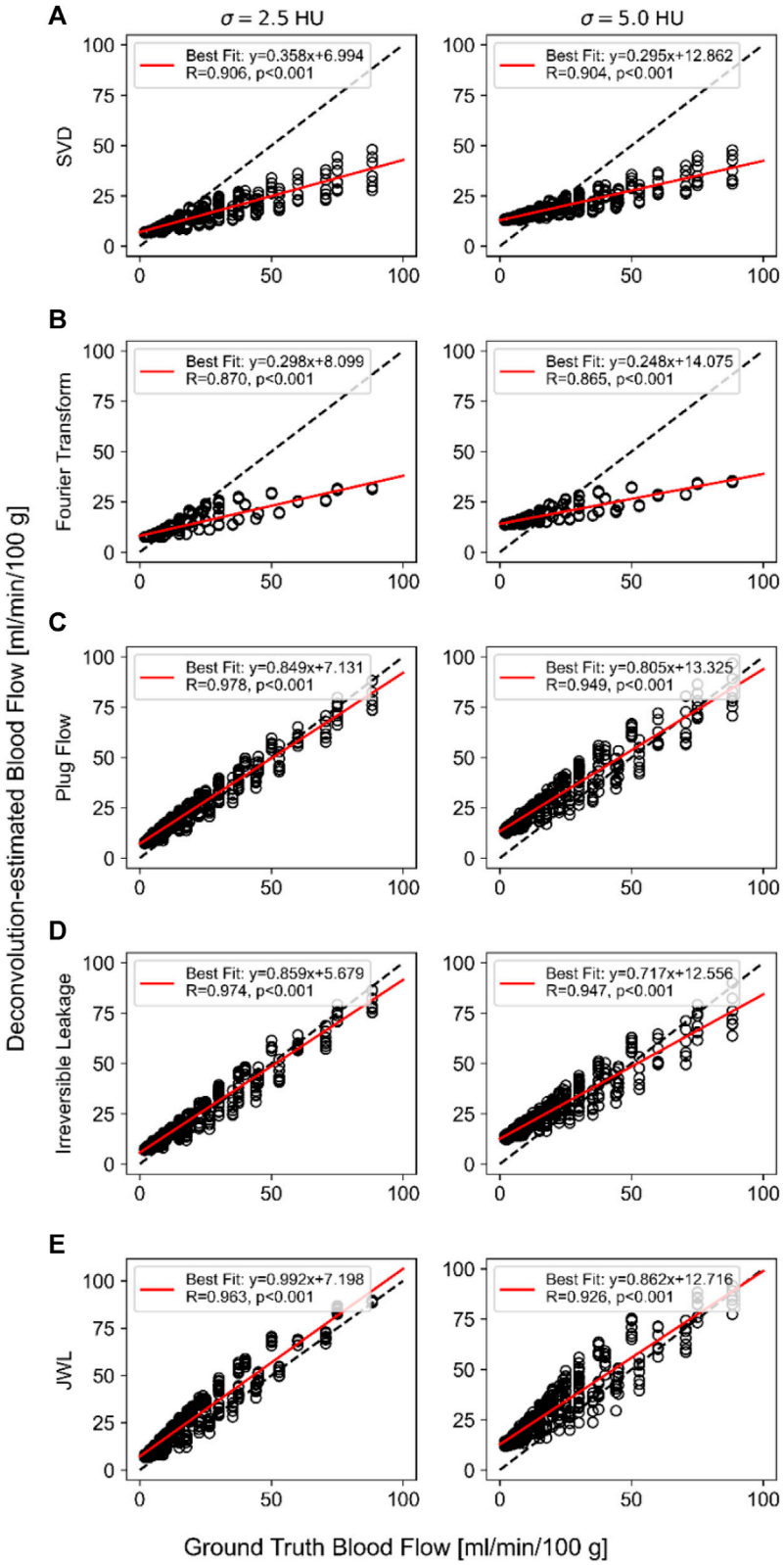

FIGURE 3
Ground truth *versus* deconvolution-estimated blood flow using **(A)** singular value decomposition (SVD), **(B)** Fourier transform, **(C)** plug flow, and **(D)** irreversible leakage. **(E)** Johnson–Wilson–Lee (JWL) model deconvolution at routine-dose noise (σ = 2.5 HU; left) and low-dose noise (σ = 5.0 HU; right) levels. The linear regression equation and Pearson's correlation are indicated in the inset of each plot.

TABLE 1 Mean and standard deviation of deconvolution-estimated perfusion parameters over 1,024 noise trials for a set of ground truth perfusion parameters.

Method	F [mL/min/100 g]	V_b [ml/100 g]	MTT [s]	T0 [s]
Ground truth	60	4	4	4
SVD	21.7 ± 0.2	3.7 ± 0.2	10.3 ± 0.5	N/A
Fourier transform	26.0 ± 0.2	3.7 ± 0.2	8.6 ± 0.4	N/A
Plug flow	59.9 ± 5.2	4.0 ± 0.1	4.0 ± 0.5	4.0 ± 0.4
Irreversible leakage	61.5 ± 3.1	4.0 ± 0.1	4.0 ± 0.3	4.2 ± 0.2
JWL	65.5 ± 1.7	4.3 ± 0.1	3.9 ± 0.1	4.4 ± 0.1

F, blood flow; V_b, blood volume; MTT, mean transit time; T0, delay time between contrast arrival at the artery and tissue; SVD, singular value decomposition; JWL, Johnson–Wilson–Lee.

absolute blood flow than model-independent methods and (2), as a result, can better quantify differences between low and high ground truth blood flow values. In addition, the regression slope became shallower with greater noise for all methods, indicating that blood flow quantification worsens with greater noise.

The trade-off for better absolute agreement (lower bias) between ground truth and estimated blood flow with model-dependent methods is that they have higher variance than model-independent methods. The mean and standard deviation of deconvolution-estimated perfusion parameters over 1,024 trials for a single set of ground truth parameters at routine-dose noise levels (σ= 2.5 HU) are tabulated in Table 1. Reflecting the correlation plots, the model-independent methods underestimate the true blood flow value on average, whereas the model-dependent methods better agree with the true value on average. However, the model-independent methods have smaller standard deviations compared to model-dependent methods. Note that for this set of ground truth parameters, the mean SVD blood flow is less than that of the Fourier transform method despite the latter having a shallower regression slope. This is due to the positive T0 (i.e., the tissue TDC and the artery TDC), which is described in Section 4.1.1, which causes a reduction in estimated blood flow, whereas the Fourier transform method is delay-insensitive.

Figure 4 shows a comparison of the mean deconvolution-estimated flow-scaled IRF and their corresponding fitted tissue TDCs overlaid on their respective ground truths for the parameter set listed in Table 1. For the model-independent methods, the estimated flow-scaled IRFs were averaged and the fitted TDC was then computed with Eq. 4.2. For the model-dependent methods, the means of the estimated model parameters were first computed and then substituted into Equation 3.10 and 4.18 to evaluate the mean estimated flow-scaled IRFs and fitted TDCs, respectively. Despite applying regularization and averaging over 1,024 trials, the model-independent flow-scaled IRFs are oscillatory and fail to recover the sharp initial peak in the true flow-scaled IRF. The corresponding fitted tissue TDCs also contain oscillations, indicating that the model-independent deconvolution methods overfitted to noise. While the flow-scaled IRFs for the model-dependent methods did not match the shape of the ground truth, they better reproduced the sharp peak required for accurately estimating blood flow. The fitted tissue TDCs do not show oscillations and arguably agree better with those of the ground truth in this example.

The rightmost column of Figure 4 shows the distribution of blood flow values estimated over 1,024 trials with each deconvolution method. All methods produced approximately a unimodal normal distribution of estimated blood flow values. The model-independent methods produced a very narrow distribution, whereas the model-dependent methods had a broader distribution. The standard deviations of estimated blood flow values are accordingly greater with model-dependent deconvolution. However, the mean of the distribution better converges to the true value with the model-dependent methods. As such, model-independent deconvolution methods are more precise at the expense of accuracy, whereas model-dependent methods are more accurate but are less precise.

Though not investigated in this experiment, model-dependent methods can also provide hemodynamic parameters that are unavailable with model-independent methods, such as those related to vessel permeability.

5 Applications of CT perfusion

5.1 Acute ischemic stroke

Acute ischemic stroke is mainly caused by a clot that limits blood flow to the brain. Reperfusion treatments including intravenous thrombolysis (IV-tPA) and endovascular thrombectomy (EVT) are highly effective if administered early after stroke onset (<4.5 h for IV-tPA and <6 h for EVT). However, randomized controlled trials demonstrated that the therapeutic time window can be extended up to 9 h after stroke onset for IV-tPA and 16–24 h for EVT with selection by CTP [2–4, 70]. Treatment selection was based on a target mismatch profile defined as a small volume of irreversible brain injury (infarct or ischemic core) relative to a large salvageable region (penumbra). Specifically, the target mismatch profile in the DEFUSE-3 late-window EVT trial (6–16 h after stroke onset) was defined as an ischemic core volume <70 mL, penumbra volume ≥15 mL, and a mismatch ratio (quotient of penumbra and core volume) ≥ 1.8 [4]. Anterior large vessel ischemic stroke patients receiving late-window EVT based on this target mismatch profile had significantly greater rates of good 90-day functional outcome compared to best medical therapy [4]. As of 2022, CTP is one of two imaging-based selection methods (alongside diffusion-weighted imaging and perfusion magnetic resonance imaging) approved by the American Heart Association best practice

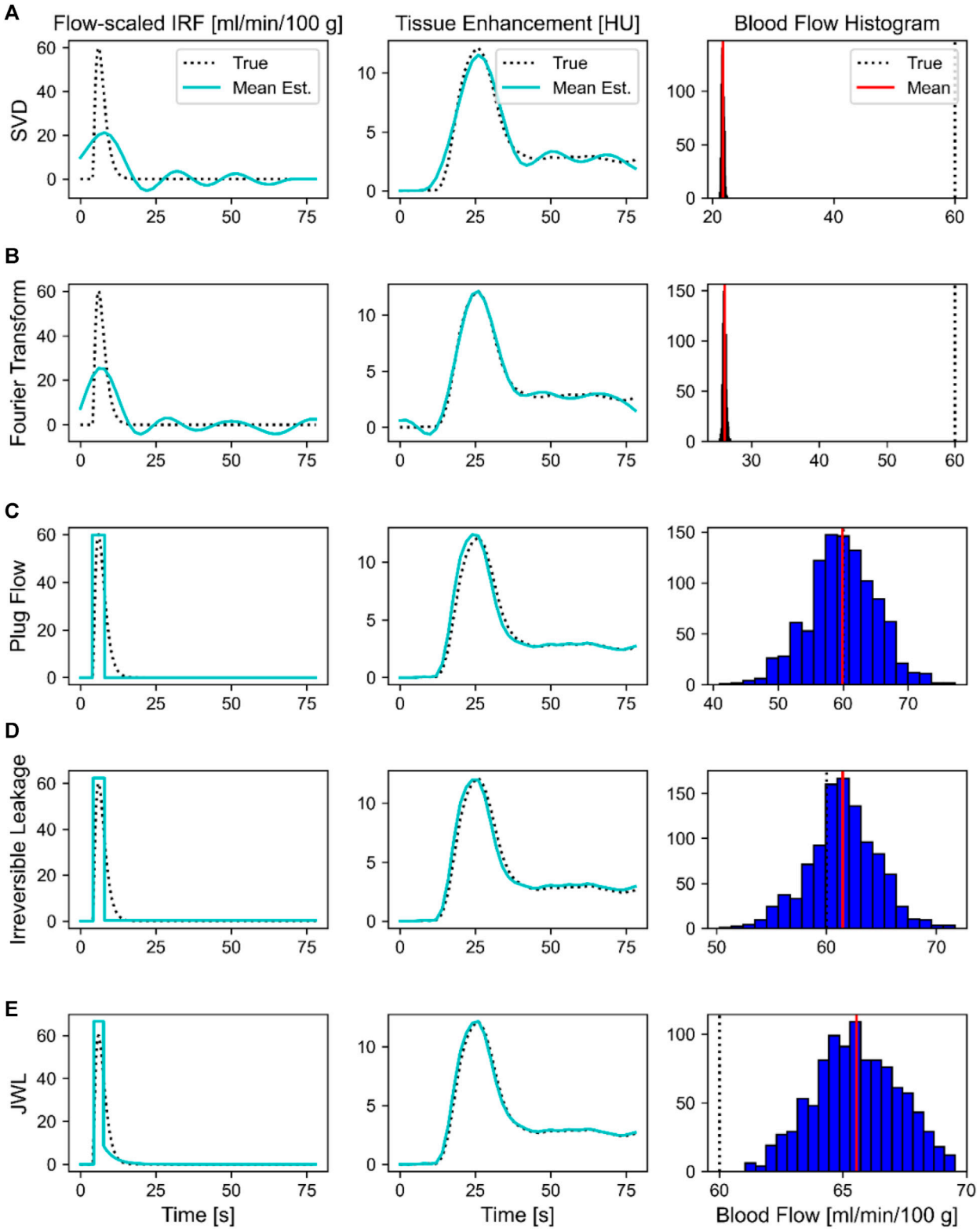

FIGURE 4
Comparison of deconvolution methods for a single set of ground truth parameters: blood flow, 60 mL/min/100 g; blood volume, 4 mL/100 g; mean transit time, 4 s; T0, 4 s. Deconvolution methods were **(A)** singular value decomposition (SVD), **(B)** Fourier Transform, **(C)** plug flow, **(D)** irreversible leakage, and **(E)** Johnson-Wilson-Lee (JWL) model. The mean deconvolution-estimated flow-scaled impulse residue function (IRF) and fitted tissue time–density curve over 1,024 trials are overlaid on their respective ground truths in the left and middle columns, respectively. Histograms showing the distribution of deconvolution-estimated blood flow values over 1,024 trials are shown in the rightmost column, where the solid red line indicates the mean and the dotted black line is the ground truth.

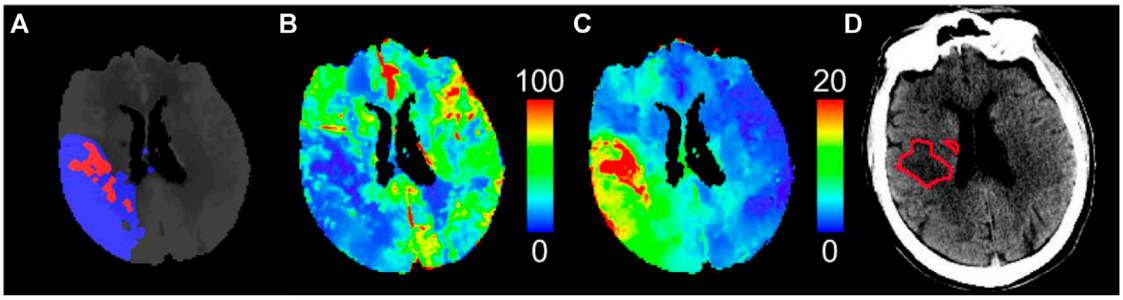

FIGURE 5
CT perfusion study of a patient with large vessel ischemic stroke who achieved early quality recanalization at endovascular thrombectomy. **(A)** Predicted pre-treatment ischemic core (red) and penumbra (blue) by thresholding **(B)** cerebral blood flow and **(C)** Tmax maps, respectively, using the optimal thresholds for this software package (CT Perfusion 4D, GE Healthcare). The small ischemic core relative to the large penumbra indicates a target mismatch profile suitable for endovascular thrombectomy. **(D)** Follow-up infarct (red outline) delineated on non-contrast CT shows good agreement with the ischemic core predicted by pre-treatment CT perfusion. Cerebral blood flow is in units of mL/min/100 g, and Tmax is in units of seconds.

guidelines for EVT selection between 6 and 16 h after stroke onset [71]. CTP played a major role in demonstrating that the therapeutic window of reperfusion treatments can be extended based on tissue status rather than strict time thresholds. An example CTP study of a patient with large vessel ischemic stroke is shown in Figure 5.

As such, the main role of CTP is to measure the ischemic core and penumbral volumes and quantify mismatch profiles. Modern CTP software is automated and can provide diagnostic information within minutes of image acquisition [72]. Ischemic core and penumbra volumes are mainly measured by thresholding perfusion parameters. CBF is often used to detect the ischemic core, and Tmax is often used for the penumbra [73–75]. The randomized controlled trials that validated the diagnostic utility of CTP used a single software package (RAPID CTP, RapidAI, Menlo Park, CA), which used CBF<30% relative to that in the normal tissue to detect the ischemic core and Tmax>6 s for the penumbra [2–4, 70]. Of note, RAPID perfusion imaging software uses Fourier Transform deconvolution as described by Straka et al. [65], which may have limited absolute agreement with ground truth blood flow, as we have shown in Section 4.3.1. This demonstrates that absolute accuracy and quantification of blood flow may not be required specifically for determining target mismatch profiles, which may have implications for CTP scan protocol design and radiation dose reduction.

Optimal stroke lesion thresholds, however, differ between CTP software packages, which has raised doubts about its widespread deployment across institutions using different software platforms [76]. One of the potential reasons that stroke lesion thresholds differ between CTP software is that each software may use different deconvolution algorithms. As shown in Section 4.3, each deconvolution algorithm has different biases and variances in estimating blood flow, and optimal lesion thresholds may accordingly differ. Chung et al. found that linear regression relationships of ground truth *versus* estimated perfusion parameters determined from simulated CTP data (as in Section 4.3.1) may help guide the calibration of optimal stroke lesion thresholds between software packages [77]. Threshold calibration and demonstration of equivalence between other CTP software and RAPID CTP have also been shown empirically [78–81]. Nonetheless, CTP requires better standardization between software packages such that reliable diagnostic criteria can be deployed between institutions using different platforms.

CTP has also demonstrated potential for detecting hemorrhagic transformation in ischemic stroke [19, 82]. Hemorrhagic transformation is a brain bleed caused by a complete breakdown of the blood–brain barrier due to sustained severe ischemia and is associated with high rates of mortality when symptomatic [83, 84]. According to the Heidelberg Bleeding Classification [85], there are two main types of hemorrhagic transformation following ischemia: hemorrhagic infarct (HI1 and HI2) and parenchymal hemorrhage (PH1 and PH2). Symptomatic hemorrhage, which causes an increase in the National Institutes of Health Stroke Scale (NIHSS), is usually associated with PH and not HI.

Measures of vessel permeability as determined with model-dependent deconvolution methods have been found to identify patients likely to undergo hemorrhagic transformation. Aviv et al. found that patients with larger permeability surface area products (PS, Eq. 3.11) within the ischemic region at admission CTP were associated with hemorrhagic transformation [19]. In a voxel-wise analysis of CTP maps of 1,407 patients with acute ischemic stroke, Bivard et al. found that an extraction fraction (E, Eq. 3.11) threshold of 30% relative to the contralateral hemisphere optimally distinguished between patients who did and did not develop any form of hemorrhagic transformation [82]. Both studies by Bivard et al. and Aviv et al. showed that increased PS or E is associated with hemorrhagic transformation, but differentiation of PH from HI is an ongoing research issue. Nonetheless, Bivard et al. showed that the severity of hemorrhage increased with larger volumes of tissue with E > 30%.[82] Neither study included patients treated with EVT and only included patients who were considered for IV-tPA. CTP measures of vessel permeability may therefore help identify patients at risk of hemorrhagic transformation. Validation of CTP permeability measures in predicting hemorrhagic transformation after EVT is still required. Specifically, a useful application may be to predict hemorrhagic transformation in large vessel ischemic stroke patients presenting with a large ischemic core or beyond 24 h after stroke onset, who have been found to have high rates of hemorrhage after EVT [86, 87].

5.2 Solid tumor

Tumor angiogenesis fosters the microenvironment required for tumor growth and metastasis [88]. Tumor perfusion and vessel permeability are therefore associated with tumor grades, prognosis, and treatment response [89, 90]. Therefore, the main role of CTP in evaluating solid tumors is to supplement histological assessment of the tumor with non-invasive imaging of tumor perfusion and vessel permeability.

5.2.1 Brain tumors

Gliomas are highly heterogeneous brain tumors that are the most common type of neoplasm in adults [91]. The malignancy of glioma is graded according to WHO tumor classification using a tumor sample taken from a brain biopsy or surgery [92]. However, the acquisition and utility of sampling the tumor is problematic due to the highly heterogeneous nature of glioma cells and the limited obtainable samples, meaning that the histopathological results may be under-graded [93, 94]. An alternative to this invasive and limited procedure is *in vivo* perfusion imaging, such as CTP. Perfusion parameters such as blood volume, blood flow, and PS are associated with angiogenesis, which underpins tumor growth. In current practice, perfusion imaging supplements histological evaluation of tumor grading, prognosis, and monitoring treatment response. Histological assessment is nonetheless still required as CTP lacks the spatial resolution required for assessing tumor microenvironments (i.e., CT resolution is approximately 0.5 mm, whereas microvasculature is on the order of μm) [89].

Perfusion parameters such as blood volume, blood flow, and PS are associated with the tumor vasculature and have demonstrated predictive value in glioma grading, prognosis, and treatment response [89, 90]. Studies have suggested that blood volume may potentially be a good biomarker for microvascular density (MVD), which is associated with angiogenesis and, therefore, the aggressiveness of the tumor [95–98]. Vascular endothelial growth factor (VEGF) is an additional biomarker that shows a positive correlation with hypoxic and hypoglycemic permeable blood vessels. It is used to judge the potential for neoangiogenesis, aiding in the histological grading process [99]. CTP PS could replace the need to sample for VEGF as well as be used to study treatment response [100]. This may help design more effective therapies based on the underlying mechanisms of permeability and the blood–brain barrier [99]. Jain et al. reported that in a study of 23 brain tumor patients with various tumor grades, CBV and PS showed a significant positive correlation with MVD (Pearson's correlation, r = 0.596, $p < 0.001$) and microvascular cellular proliferation (MVCP) (r = 0.546, $p = 0.001$), respectively, as well as a significant correlation with WHO-defined tumor grade for CBV (r = 0.373, $p = 0.031$) and PS (r = 0.452, $p = 0.039$) [95]. Ellika et al. found that in a cohort of 19 patients with glioma, CTP had higher sensitivity and specificity than conventional MRI in classifying patients into low-grade and high-grade glioma (92.9% and 100% for CTP *versus* 85.7% and 60% for MRI, respectively) [90]. Therefore, CTP-derived parameters can be used in combination with biopsy to non-invasively differentiate tumor grades and elucidate different characteristics of tumor proliferation. Overall, CTP may have the potential to non-invasively track relevant biomarkers for tumor grading and angiogenesis associated with treatment planning and response.

5.3 Cardiovascular disease

The main role of CTP in cardiovascular disease is to determine regions of ischemic myocardial tissue using functional information on blood flow, blood volume, MTT, and other hemodynamic parameters.

5.3.1 Ischemic heart disease

Although coronary CT angiography (CCTA) is the main imaging tool used to define coronary artery disease (CAD) that causes myocardial ischemia, invasive fractional flow reserve (FFR) is currently the gold standard for the identification of significant CAD requiring revascularization [101–104]. CCTA provides morphological information on the degree of stenosis but lacks functional information on myocardial perfusion, leading to suboptimal positive predictive value and specificity for significant CAD [104–106]. FFR is a diagnostic measure that assesses the relative pressure difference across stenotic coronary arteries, providing guidance for revascularization decisions. It exhibits a diagnostic accuracy of over 90% when using a relative pressure threshold of ≤0.8 [102]. Treatment for significant CAD involves either enlarging the narrowed artery by percutaneous transluminal coronary angioplasty or stenting or bypassing blockages by grafts [103].

Despite diagnostically validated non-invasive FFR_{CT} technology [107–110], FFR_{CT} still does not provide quantitative data in the myocardium, such as with CTP. The principal role of CTP in CAD is non-invasively providing functional information on ischemic myocardial tissue while maintaining a similar diagnostic value to FFR_{CT}. Using CTP-derived functional maps of blood flow, blood volume, and mean transit time, occluded major vessels can be determined by referencing ischemic regions segmented according to the AHA 17 segment model [111]. CTP, either dynamic or static, has been shown to have utility in isolation [104, 112] but has the most impact when combined with other modalities such as CCTA [113, 114]. Using their PERFECTION study data with CCTA-derived FFR_{CT}, Pontone et al. showed that CCTA + CTP had similar diagnostic performance per vessel determination of significant CAD as CCTA + FFR_{CT} in terms of the area under its receiver operating characteristic curve (CCTA + CTP AUC = 0.876 with 95% confidence interval: 0.832 to 0.919, and CCTA + FFR_{CT} AUC = 0.878 with 95% confidence interval: 0.833–0.923) [113].

5.3.2 Cardiac sarcoidosis

Sarcoidosis is a disease where a number of granuloma cells accumulate within the tissue of any organ in the body, and in 2011, it was reported to affect about 10–40 in 100,000 Americans [115]. Cardiac sarcoidosis (CS) accounts for approximately 20%–30% of all sarcoidosis cases in the United States and can lead to sudden death without any admissible symptoms [115]. Silverman et al. found that there were a significant number of CS patients who were clinically silent [116]. Diagnostic imaging via ^{18}F-FDG PET or gadolinium-based cardiac MRI has substantially improved the detection of sarcoidosis. Corticosteroid therapy is currently the only treatment for CS, though its benefit requires validation in randomized controlled trials [117]. Imaging may guide the management of CS symptoms and potentially decisions for corticosteroid treatment, but this requires validation in future studies [118]. So et al. demonstrated the potential utility of CTP to identify scar tissue in a CS patient using myocardial blood flow and extravascular contrast distribution volume

imaging [119]. More studies are needed to validate the diagnostic potential of CTP in identifying CS patients, but if successful, myocardial CTP may prove to be a more accessible imaging modality than cardiac MRI and ^{18}F-FDG PET for diagnosing CS.

6 Discussion

6.1 Radiation dose reduction

6.1.1 Low-dose CT perfusion denoising

Dose reduction by reducing mAs comes at the expense of lower CTP image SNRs and TDC SNRs. The lower limit for recommended mAs has mainly been established empirically. Further dose reduction may be possible with post-processing or advanced CT reconstruction techniques that improve image and TDC SNRs. In simulation studies, spatiotemporal filtering of dynamic CTP images demonstrated potential for dose reduction by leveraging spatial and temporal relationships between CTP TDCs to improve TDC SNRs [120–123]. An ultra-low-dose brain CTP protocol (effective dose: 1.2 mSv) with statistical iterative reconstruction (ASIRv, GE Healthcare) allowed the evaluation of blood–brain barrier permeability in thrombotic thrombocytopenic purpura [124]. Statistical iterative reconstruction has also been applied for 20 × dose reduction myocardial CTP imaging in a porcine model of coronary artery occlusion [125]. More recently, deep learning-based image reconstruction and denoising techniques have been proposed, potentially offering greater improvements in CTP imaging and TDC SNRs [126–128]. These methods have mainly been evaluated in terms of quantitative image fidelity metrics and require clinical validation. In addition, the strength of these noise reduction methods needs to be increased at lower doses, which often comes at the expense of spatial resolution. A balance between a perfusion map SNR and spatial resolution is required for reliable diagnostic application [73], though this has not been investigated in detail.

6.1.2 Low-temporal resolution CT perfusion

Radiation dose can be reduced by acquiring fewer dynamic CTP images at the expense of temporal resolution or scan duration. Van Ommen et al. demonstrated that certain deconvolution methods for brain CTP tolerated a scanning interval of up to 5 s while still adequately distinguishing between ischemic and normal brain tissue [129]. Chung et al. found that tailored sampling of four dynamic CTP images (pre-contrast baseline, arterial peak, and two additional delayed images at 8-s intervals) had diagnostic potential in identifying mismatch profiles in acute ischemic stroke [130]. While the quantitative accuracy of estimated perfusion parameters may decrease with fewer acquired dynamic images, perfusion map quality may be sufficient for diagnosis. Deep learning methods to interpolate missing dynamic images or directly predict perfusion maps from low-temporal resolution CTP studies may also be viable [131, 132].

6.1.3 Future outlook

Demonstration of low-dose CTP has mainly been with simulation studies or animal models. Prospective acquisition of low-dose CTP in humans has been hampered by ethical and safety considerations or concerns of diagnostic reliability. Studies reporting the prospective application of low-dose CTP are required. These data may then support the wider deployment of low-dose CTP in practice. In addition, a theoretical model relating the radiation dose and image/TDC SNR to the detectability of disease in CTP parametric maps may be helpful in guiding the selection of low-dose protocols. Future studies should also consider diagnostic task-based metrics rather than intermediate measures, such as the accuracy of estimated perfusion parameters. Absolute agreement between regular-dose and low-dose CTP parameters may not be important so long as diagnosis is reliable. For better inter-study comparison, dose reduction studies should also report dosage in more comparable absolute measures, such as the dose-length product (mGy cm), $CTDI_{100}$ dose (mGy), or effective dose (mSv), in addition to relative measures of dose reduction compared to routine levels.

Ongoing work in CTP dose reduction may facilitate its broader clinical application. For example, perfusion imaging of pediatric stroke patients is garnering interest to validate the translation of diagnostic and therapeutic stroke paradigms from adults to children [133], but pediatric perfusion imaging studies have mainly used MRI in part due to the lack of ionizing radiation [134]. Therefore, ultra-low-dose CTP protocols may provide a broad opportunity to better characterize pediatric cerebrovascular disease and identify pediatric-specific imaging profiles suitable for stroke reperfusion therapies.

6.2 New CT technology

6.2.1 Photon-counting detector CT

Current clinical CT scanners use energy-integrating detectors (EIDs), which comprise scintillators to convert X-rays to light and light to electrical signals via photodiodes. The generated electrical signal is proportional to the sum of energies of all transmitted X-rays. Photon-counting detector (PCD) CT is an emerging technology that instead uses semiconductors to produce an electrical signal directly proportional to the energy of each incident X-ray photon. Electronic noise, which may be prevalent at low-fluence scans with EIDs, can therefore be minimized by setting an energy floor required for photon detection [135, 136]. PCD elements are much smaller than EID elements, ranging from 0.11 × 0.11 to 0.5 × 0.5 mm^2 and 1 × 1 mm^2, respectively [135], allowing for higher spatial resolution.

PCDs provide several advantages over EIDs: (1) spectral energy resolution from a single X-ray source, (2) higher spatial resolution, (3) beam hardening and metal artifact reduction, and (4) radiation dose efficiency. These have meaningful implications for PCD-CT perfusion. First, multi-energy resolution may improve the iodine contrast-to-noise ratio [135] and thus improve the CTP TDC SNR. Radiation dose reduction may be possible if sufficient TDC SNRs can be achieved at lower doses with spectral imaging. Second, smaller perfusion deficits, such as lacunar or watershed infarcts [137], may be better visualized with the higher spatial resolution afforded by PCD-CT. Last, artifact reduction may improve perfusion map quality in previously problematic anatomical locations and scan conditions. For example, CTP is less reliable in quantifying stroke lesion volumes for posterior circulation ischemic strokes compared to anterior circulation [30]. This may be in part due to beam hardening and photon starvation artifacts at the posterior fossa obscuring CTP TDCs.

6.3 New applications

6.3.1 Lung perfusion CT

In contrast to brain perfusion imaging, where deconvolution techniques are commonly employed, lung perfusion imaging predominantly utilizes either the peak enhancement method (Eq. 3.2) or the maximum front slope method (Eq. 3.3) [138–141]. These methods are applied under the assumption of no venous outflow and have the advantage that the numerical computation is simpler to implement. Nevertheless, the requirement of no venous outflow means the perfusion values will be dependent on injection rate and the viscosity of the contrast agent, as investigated by Xin et al. [141] They found that compared to invasive measurement of cardiac output by thermal dilution at the pulmonary artery, applying Eq. 3.3 to data acquired with diluted contrast (Isovue-370 and saline in the ratio of 3:2) calculated more accurate lung perfusion than applying Eq. 3.2. In contrast to Equation 3.2, Equation 3.3 also provided more comparable lung perfusion values when comparing the rapid injection rate (8 mL/s) with the slower rate (4 mL/s) of diluted contrast.

To circumvent the assumption of zero venous outflow, two approaches have been employed. The first approach involved utilizing the irreversible leakage model, as outlined in Section 3.4.3 and Eq. 3.16 [142]. The second approach used the model-independent regularized deconvolution method, as described in Section 4.1 [143]. The justification for irreversible leakage lies in the fact that CTP acquisition for lung perfusion usually lasts less than 20–30 s, primarily due to the necessity of breath holding. Consequently, any potential backflux of leaked contrast from tissue to blood can be disregarded. Nonetheless, as discussed in Section 3.4.1, the value of K_1 obtained through the irreversible leakage model does not directly represent lung perfusion. Rather, it represents the product of lung perfusion and the contrast extraction efficiency by the lung tissue. Consistent with this interpretation, lung perfusion calculated with Eq. 3.3 with the no venous outflow assumption had better potential for the diagnosis of pulmonary nodules than K_1 from the irreversible leakage model [144]. The deconvolution approach demonstrated a significant reduction in lung perfusion downstream of a stenosed pulmonary artery, surpassing 50% occlusion. The threshold for stenosis, leading to a decrease in lung blood volume, was higher at 76%. This higher threshold is likely due to autoregulation, wherein at lower degrees of stenosis, the microvasculature undergoes vasodilation to compensate for the decrease in perfusion pressure, resulting in an increase in lung blood volume.

Due to tumor-associated angiogenesis, the blood supply to lung cancer transitions from a single input solely from the pulmonary artery to a dual input from both the pulmonary and bronchial arteries. To account for this change, Yabuuchi et al. [145] expanded the application of the maximum front slope method to accommodate dual-input scenarios. By utilizing the dual-input maximum front slope method, Ohno et al. [146] demonstrated that dual-input total perfusion outperformed pulmonary arterial perfusion and the single-input perfusion obtained through the single-input maximum slope method in predicting treatment response and recurrence following chemo-radiotherapy for non-small-cell lung cancer.

The requirement of breath holding during lung CT perfusion restricts the acquisition time to a maximum of 20–30 s. Consequently, the analysis of lung CTP studies is currently limited to the simple models discussed above, namely, peak enhancement and maximum front slope, operating under the assumptions of no venous outflow or irreversible leakage. To advance lung CTP techniques, future developments can explore acquiring studies with shallow breathing and subsequently employing non-rigid registration to align the images. This approach has the potential to extend the acquisition time to 2–3 min. With these extended data, in addition to perfusion and blood volume, parameters such as PS can be determined as in solid tumors (Section 5.2).

7 Conclusion

CTP has demonstrated diagnostic utility in numerous clinical applications due to its relative accessibility and low cost compared to other perfusion imaging modalities. This review provided a summary of CTP scan protocols, theory of contrast transport, deconvolution methods, applications, and future opportunities for research and application. With further reductions to radiation dose and improvements in hardware and software methods to acquire and generate perfusion maps, CTP is poised to become an integral component of the diagnosis and management of patients with perfusion injuries.

Author contributions

KJC: conceptualization, data collection and analysis, investigation, methodology, software, validation, visualization, and writing. DDS: conceptualization, investigation, and writing. T-YL: conceptualization, investigation, methodology, project administration, and writing. All authors contributed to the article and approved the submitted version.

Funding

This work was supported by the Canadian Institutes of Health Research (CIHR, Grant Number 168945), the Canada Foundation for Innovation (CFI, Project Number 30954), the Ontario Research Fund (ORF, Project Number 30954), and the Heart and Stroke Foundation of Canada (Grant # G-19-0024345). KJC was supported in part by a CIHR Canada Graduate Scholarship–Doctoral Research Award.

Conflict of interest

T-YL licenses CT Perfusion software to GE HealthCare and Neusoft (Shenyang, China).

The remaining authors declare that the research was conducted in the absence of any commercial or financial relationships that could be construed as a potential conflict of interest.

Publisher's note

organizations, or those of the publisher, the editors, and the reviewers. Any product that may be evaluated in this article, or claim that may be made by its manufacturer, is not guaranteed or endorsed by the publisher.

Supplementary material

The Supplementary Material for this article can be found online at: https://www.frontiersin.org/articles/10.3389/fphy.2023.1246973/full#supplementary-material

References

1. Axel L. Cerebral blood flow determination by rapid-sequence computed tomography: theoretical analysis. *Radiology* (1980) 137(3):679–86. doi:10.1148/radiology.137.3.7003648

2. Campbell BCV, Mitchell PJ, Kleinig TJ, Dewey HM, Churilov L, Yassi N, et al. Endovascular therapy for ischemic stroke with perfusion-imaging selection. *N Engl J Med* (2015) 372(11):1009–18. doi:10.1056/NEJMoa1414792

3. Nogueira RG, Jadhav AP, Haussen DC, Bonafe A, Budzik RF, Bhuva P, et al. Thrombectomy 6 to 24 hours after stroke with a mismatch between deficit and infarct. *N Engl J Med* (2018) 378(1):11–21. doi:10.1056/NEJMoa1706442

4. Albers GW, Marks MP, Kemp S, Christensen S, Tsai JP, Ortega-Gutierrez S, et al. Thrombectomy for stroke at 6 to 16 hours with selection by perfusion imaging. *N Engl J Med* (2018) 378(8):708–18. doi:10.1056/NEJMoa1713973

5. Calamante F, Christensen S, Desmond PM, Østergaard L, Davis SM, Connelly A. The physiological significance of the time-to-maximum (tmax) parameter in perfusion MRI. *Stroke* (2010) 41(6):1169–74. doi:10.1161/STROKEAHA.110.580670

6. Hsieh J. *Computed tomography: principles, design, artifacts, and recent advances*. 2. Hoboken: Wiley Interscience; SPIE Press (2009).

7. Seltzer S. *Tables of X-ray mass attenuation coefficients and mass energy-absorption coefficients, NIST standard reference database 126* (1995). Published online 1995. doi:10.18434/T4D01F

8. Christiansen C. X-ray contrast media—an overview. *Toxicology* (2005) 209(2):185–7. doi:10.1016/j.tox.2004.12.020

9. Copen WA, Schaefer PW, Wu O. MR perfusion imaging in acute ischemic stroke. *Neuroimaging Clin N Am* (2011) 21(2):259–83. doi:10.1016/j.nic.2011.02.007

10. Boxerman JL, Hamberg LM, Rosen BR, Weisskoff RM. MR contrast due to intravascular magnetic susceptibility perturbations. *Magn Reson Med* (1995) 34(4):555–66. doi:10.1002/mrm.1910340412

11. Wintermark M, Maeder P, Verdun FR, Thiran JP, Valley JF, Schnyder P, et al. Using 80 kVp versus 120 kVp in perfusion CT measurement of regional cerebral blood flow. *AJNR Am J Neuroradiol* (2000) 21 (10):1881–1884.

12. Lee TY, Yang DM, Li F, Marants R. CT perfusion techniques and applications in stroke and cancer. In: Samei E, Pelc NJ, editors. *Computed tomography: approaches, applications, and operations*. Springer International Publishing (2020). p. 347–65. doi:10.1007/978-3-030-26957-9_19

13. Wintermark M, Albers GW, Alexandrov AV, Alger JR, Bammer R, Baron JC, et al. Acute stroke imaging research roadmap. *Stroke* (2008) 39(5):1621–8. doi:10.1161/STROKEAHA.107.512319

14. The Alliance for Quality Computed Tomography. *Adult brain perfusion CT protocols* (2016). Available at: https://www.aapm.org/pubs/CTProtocols/documents/AdultBrainPerfusionCT.pdf (Accessed January 1, 2023).

15. Kim SH, Kamaya A, Willmann JK. CT perfusion of the liver: principles and applications in oncology. *Radiology* (2014) 272(2):322–44. doi:10.1148/radiol.14130091

16. Patel AR, Bamberg F, Branch K, Carrascosa P, Chen M, Cury RC, et al. Society of cardiovascular computed tomography expert consensus document on myocardial computed tomography perfusion imaging. *J Cardiovasc Comput Tomogr* (2020) 14(1):87–100. doi:10.1016/j.jcct.2019.10.003

17. Wintermark M, Smith WS, Ko NU, Quist M, Schnyder P, Dillon WP. Dynamic perfusion CT: optimizing the temporal resolution and contrast volume for calculation of perfusion CT parameters in stroke patients. *AJNR Am J Neuroradiol* (2004) 25 (5):720–729.

18. Wiesmann M, Berg S, Bohner G, Klingebiel R, Schöpf V, Stoeckelhuber BM, et al. Dose reduction in dynamic perfusion CT of the brain: effects of the scan frequency on measurements of cerebral blood flow, cerebral blood volume, and mean transit time. *Eur Radiol* (2008) 18(12):2967–74. doi:10.1007/s00330-008-1083-x

19. Aviv RI, d'Esterre CD, Murphy BD, Hopyan JJ, Buck B, Mallia G, et al. Hemorrhagic transformation of ischemic stroke: prediction with CT perfusion. *Radiology* (2009) 250(3):867–77. doi:10.1148/radiol.2503080257

20. Lin L, Bivard A, Krishnamurthy V, Levi CR, Parsons MW. Whole-brain CT perfusion to quantify acute ischemic penumbra and core. *Radiology* (2016) 279(3):876–87. doi:10.1148/radiol.2015150319

21. Roberts HC, Roberts TPL, Smith WS, Lee TJ, Fischbein NJ, Dillon WP. *Multisection dynamic CT perfusion for acute cerebral ischemia: the "'Toggling-table"' technique* (2001). p. 4. Published online.

22. Youn SW, Kim JH, Weon YC, Kim SH, Han MK, Bae HJ. Perfusion CT of the brain using 40-mm-Wide detector and toggling table technique for initial imaging of acute stroke. *Am J Roentgenol* (2008) 191(3):W120–6. doi:10.2214/AJR.07.2519

23. Haberland U, Klotz E, Abolmaali N. Performance assessment of dynamic spiral scan modes with variable pitch for quantitative perfusion computed tomography. *Invest Radiol* (2010) 45(7):378–86. doi:10.1097/RLI.0b013e3181dfda9f

24. Miles K, Eastwood JD, König M. *Multidetector computed tomography in cerebrovascular disease: CT perfusion imaging*. London, United Kingdom: Informa Healthcare (2007).

25. Yeung TPC, Yartsev S, Bauman G, He W, Fainardi E, Lee TY. The effect of scan duration on the measurement of perfusion parameters in CT perfusion studies of brain tumors. *Acad Radiol* (2013) 20(1):59–65. doi:10.1016/j.acra.2012.08.013

26. Copen WA, Deipolyi AR, Schaefer PW, Schwamm LH, González RG, Wu O. Exposing hidden truncation-related errors in acute stroke perfusion imaging. *Am J Neuroradiol* (2015) 36(4):638–45. doi:10.3174/ajnr.A4186

27. Bennink E, Oosterbroek J, Kudo K, Viergever MA, Velthuis BK, de Jong HWAM. Fast nonlinear regression method for CT brain perfusion analysis. *J Med Imaging* (2016) 3(2):026003. doi:10.1117/1.JMI.3.2.026003

28. Fahmi F, Beenen LFM, Streekstra GJ, Janssen N, de Jong H, Riordan A, et al. Head movement during CT brain perfusion acquisition of patients with suspected acute ischemic stroke. *Eur J Radiol* (2013) 82(12):2334–41. doi:10.1016/j.ejrad.2013.08.039

29. Borst J, Berkhemer OA, Roos YBWEM, van Bavel E, van Zwam WH, van Oostenbrugge RJ, et al. Value of computed tomographic perfusion–based patient selection for intra-arterial acute ischemic stroke treatment. *Stroke* (2015) 46(12):3375–82. doi:10.1161/STROKEAHA.115.010564

30. Vagal A, Wintermark M, Nael K, Bivard A, Parsons M, Grossman AW, et al. Automated CT perfusion imaging for acute ischemic stroke: pearls and pitfalls for real-world use. *Neurology* (2019) 93:888–98. Published online. doi:10.1212/WNL.0000000000008481

31. So A. CT myocardial perfusion imaging. In: Samei E, Pelc NJ, editors. *Computed tomography*. Cham: Springer International Publishing (2020). p. 367–93. doi:10.1007/978-3-030-26957-9_20

32. Barrett JF, Keat N. Artifacts in CT: recognition and avoidance. *RadioGraphics* (2004) 24(6):1679–91. doi:10.1148/rg.246045065

33. Siewerdsen JH, Jaffray DA. Cone-beam computed tomography with a flat-panel imager: magnitude and effects of x-ray scatter. *Med Phys* (2001) 28(2):220–31. doi:10.1118/1.1339879

34. Ning R, Tang X, Conover D. X-ray scatter correction algorithm for cone beam CT imaging. *Med Phys* (2004) 31(5):1195–202. doi:10.1118/1.1711475

35. Siewerdsen JH, Daly MJ, Bakhtiar B, Moseley DJ, Richard S, Keller H, et al. A simple, direct method for x-ray scatter estimation and correction in digital radiography and cone-beam CT: X-ray scatter correction. *Med Phys* (2005) 33(1):187–97. doi:10.1118/1.2148916

36. Endo M, Mori S, Tsunoo T, Miyazaki H. Magnitude and effects of x-ray scatter in a 256-slice CT scanner: X-ray scatter in a 256-slice CT. *Med Phys* (2006) 33(9):3359–68. doi:10.1118/1.2239366

37. Murase K, Nanjo T, Ii S, Miyazaki S, Hirata M, Sugawara Y, et al. Effect of x-ray tube current on the accuracy of cerebral perfusion parameters obtained by CT perfusion studies. *Phys Med Biol* (2005) 50(21):5019–29. doi:10.1088/0031-9155/50/21/005

38. Murphy A, So A, Lee TY, Symons S, Jakubovic R, Zhang L, et al. Low dose CT perfusion in acute ischemic stroke. *Neuroradiology* (2014) 56(12):1055–62. doi:10.1007/s00234-014-1434-z

39. Li Zlin, Li H, Zhang K, Li W, Chen X, Wu B, et al. Improvement of image quality and radiation dose of CT perfusion of the brain by means of low-tube voltage (70 KV). *Eur Radiol* (2014) 24(8):1906–13. doi:10.1007/s00330-014-3247-1

40. Li Hou, Sun C, Xu Zdong, Miao F, Zhang D, Chen J, et al. Low-dose whole organ CT perfusion of the pancreas: preliminary study. *Abdom Imaging* (2014) 39(1):40–7. doi:10.1007/s00261-013-0045-1

41. Klotz E, König M. Perfusion measurements of the brain: using dynamic CT for the quantitative assessment of cerebral ischemia in acute stroke. *Eur J Radiol* (1999) 30(3):170–84. doi:10.1016/S0720-048X(99)00009-1

42. Meier P, Zierler KL. On the theory of the indicator-dilution method for measurement of blood flow and volume. *J Appl Physiol* (1954) 6(12):731–44. doi:10.1152/jappl.1954.6.12.731

43. Stewart GN. Researches on the circulation time in organs and on the influences which affect it: parts I.-III. *J Physiol* (1893) 15(1-2):1–89. doi:10.1113/jphysiol.1893.sp000462

44. Johnson J, Wilson T. A model for capillary exchange. *Am J Physiol-leg Content* (1966) 210(6):1299–303. doi:10.1152/ajplegacy.1966.210.6.1299

45. Lawrence KSS, Lee TY. An adiabatic approximation to the tissue homogeneity model for water exchange in the brain: II. Experimental validation. *J Cereb Blood Flow Metab* (1998) 18(12):1378–85. doi:10.1097/00004647-199812000-00012

46. Patlak CS, Blasberg RG. Graphical evaluation of blood-to-brain transfer constants from multiple-time uptake data. Generalizations. *J Cereb Blood Flow Metab* (1985) 5(4):584–90. doi:10.1038/jcbfm.1985.87

47. Kudo K, Christensen S, Sasaki M, Østergaard L, Shirato H, Ogasawara K, et al. Accuracy and reliability assessment of CT and MR perfusion analysis software using a digital phantom. *Radiology* (2013) 267(1):201–11. doi:10.1148/radiol.12112618

48. Kudo K, Sasaki M, Ogasawara K, Terae S, Ehara S, Shirato H. Difference in tracer delay–induced effect among deconvolution algorithms in CT perfusion analysis: quantitative evaluation with digital phantoms. *Radiology* (2009) 251(1):241–9. doi:10.1148/radiol.2511080983

49. Østergaard L, Weisskoff RM, Chesler DA, Gyldensted C, Rosen BR. High resolution measurement of cerebral blood flow using intravascular tracer bolus passages. Part I: mathematical approach and statistical analysis. *Magn Reson Med* (1996) 36(5):715–25. doi:10.1002/mrm.1910360510

50. Wu O, Østergaard L, Weisskoff RM, Benner T, Rosen BR, Sorensen AG. Tracer arrival timing-insensitive technique for estimating flow in MR perfusion-weighted imaging using singular value decomposition with a block-circulant deconvolution matrix: technique for Estimating CBF in PWI. *Magn Reson Med* (2003) 50(1):164–74. doi:10.1002/mrm.10522

51. Østergaard L, Sorensen AG, Kwong KK, Weisskoff RM, Gyldensted C, Rosen BR. High resolution measurement of cerebral blood flow using intravascular tracer bolus passages. Part II: experimental comparison and preliminary results. *Magn Reson Med* (1996) 36(5):726–36. doi:10.1002/mrm.1910360511

52. Lawson CL, Hanson RJ. *Solving least squares problems*. Philadelphia, United States: SIAM (1995).

53. Golub GH, Van Loan CF. *Matrix computations*. 3. Maryland, United States: Johns Hopkins University Press (1996).

54. Gill PE, Murray W, Wright MH. *Practical optimization*. Massachusetts, United States: Academic Press (1981).

55. Fieselmann A, Kowarschik M, Ganguly A, Hornegger J, Fahrig R. Deconvolution-based CT and MR brain perfusion measurement: theoretical model revisited and practical implementation details. *Int J Biomed Imaging* (2011) 2011:1–20. doi:10.1155/2011/467563

56. Tikhonov AN. On the solution of ill-posed problems and the method of regularization. *Proc USSR Acad Sci* (1963) 151(3):501–4.

57. Li K, Chen G. Statistical properties of cerebral CT perfusion imaging systems. Part II. Deconvolution-based systems. *Med Phys* (2019) 46(11):4881–97. doi:10.1002/mp.13805

58. Lee TY. Method And Apparatus For Calculating Blood Flow Parameters. *Published online May* (2005) 24:18.

59. Lee TY, Murphy B. Implementing deconvolution analysis for perfusion CT. In: *Multidetector computed tomography in cerebrovascular disease*. Florida, United States: CRC Press (2007). p. 29–45. Available at: https://www.taylorfrancis.com/books/9780203008584/chapters/10.3109/9780203008584-7 (Accessed January 1, 2023).

60. Smith MR, Lu H, Trochet S, Frayne R. Removing the effect of SVD algorithmic artifacts present in quantitative MR perfusion studies: SVD Deconvolution Artifacts. *Magn Reson Med* (2004) 51(3):631–4. doi:10.1002/mrm.20006

61. Calamante F, Gadian DG, Connelly A. Delay and dispersion effects in dynamic susceptibility contrast MRI: simulations using singular value decomposition. *Magn Reson Med* (2000) 44(3):466–73. doi:10.1002/1522-2594(200009)44:3<466::AID-MRM18>3.0.CO;2-M

62. Ibaraki M, Shimosegawa E, Toyoshima H, Takahashi K, Miura S, Kanno I. Tracer delay correction of cerebral blood flow with dynamic susceptibility contrast-enhanced MRI. *J Cereb Blood Flow Metab* (2005) 25(3):378–90. doi:10.1038/sj.jcbfm.9600037

63. Oppenheim AV, Schafer RW, Buck JR. *Discrete-time signal processing*. 2. Hoboken, New Jersey: Prentice Hall (1999).

64. Gobbel GT, Fike JR. A deconvolution method for evaluating indicator-dilution curves. *Phys Med Biol* (1994) 39(11):1833–54. doi:10.1088/0031-9155/39/11/004

65. Straka M, Albers GW, Bammer R. Real-time diffusion-perfusion mismatch analysis in acute stroke. *J Magn Reson Imaging* (2010) 32(5):1024–37. doi:10.1002/jmri.22338

66. Gershenfeld NA. *The nature of mathematical modeling*. Cambridge: Cambridge University Press (1999).

67. Boutelier T, Kudo K, Pautot F, Sasaki M. Bayesian hemodynamic parameter estimation by bolus tracking perfusion weighted imaging. *IEEE Trans Med Imaging* (2012) 31(7):1381–95. doi:10.1109/TMI.2012.2189890

68. Bennink E, Riordan AJ, Horsch AD, Dankbaar JW, Velthuis BK, de Jong HW. A fast nonlinear regression method for estimating permeability in CT perfusion imaging. *J Cereb Blood Flow Metab* (2013) 33(11):1743–51. doi:10.1038/jcbfm.2013.122

69. Axel L. Tissue mean transit time from dynamic computed tomography by a simple deconvolution technique. *Invest Radiol* (1983) 18(1):94–9. doi:10.1097/00004424-198301000-00018

70. Ma H, Campbell BCV, Parsons MW, Churilov L, Levi CR, Hsu C, et al. Thrombolysis guided by perfusion imaging up to 9 hours after onset of stroke. *N Engl J Med* (2019) 380(19):1795–803. doi:10.1056/NEJMoa1813046

71. Powers WJ, Rabinstein AA, Ackerson T, Adeoye OM, Bambakidis NC, Becker K, et al. Guidelines for the early management of patients with acute ischemic stroke: 2019 update to the 2018 guidelines for the early management of acute ischemic stroke: a guideline for healthcare professionals from the American Heart Association/American Stroke Association. *Stroke* (2019) 50(12):e344–e418. doi:10.1161/STR.0000000000000211

72. Campbell BCV, Yassi N, Ma H, Sharma G, Salinas S, Churilov L, et al. Imaging selection in ischemic stroke: feasibility of automated CT-perfusion analysis. *Int J Stroke* (2015) 10(1):51–4. doi:10.1111/ijs.12381

73. Campbell BCV, Christensen S, Levi CR, Desmond PM, Donnan GA, Davis SM, et al. Cerebral blood flow is the optimal CT perfusion parameter for assessing infarct core. *Stroke* (2011) 42(12):3435–40. doi:10.1161/STROKEAHA.111.618355

74. Cereda CW, Christensen S, Campbell BC, Mishra NK, Mlynash M, Levi C, et al. A benchmarking tool to evaluate computer tomography perfusion infarct core predictions against a DWI standard. *J Cereb Blood Flow Metab* (2016) 36(10):1780–9. doi:10.1177/0271678X15610586

75. Olivot JM, Mlynash M, Thijs VN, Kemp S, Lansberg MG, Wechsler L, et al. Optimal tmax threshold for predicting penumbral tissue in acute stroke. *Stroke* (2009) 40(2):469–75. doi:10.1161/STROKEAHA.108.526954

76. Kamalian S, Kamalian S, Maas MB, Goldmacher GV, Payabvash S, Akbar A, et al. CT cerebral blood flow maps optimally correlate with admission diffusion-weighted imaging in acute stroke but thresholds vary by postprocessing platform. *Stroke* (2011) 42(7):1923–8. doi:10.1161/STROKEAHA.110.610618

77. Chung KJ, De Sarno D, Lee TY. CT perfusion stroke lesion threshold calibration between deconvolution algorithms. *Sci Rep* (Forthcoming 2023). doi:10.1038/s41598-023-48700-6

78. Koopman MS, Berkhemer OA, Geuskens RREG, Emmer BJ, van Walderveen MAA, Jenniskens SFM, et al. Comparison of three commonly used CT perfusion software packages in patients with acute ischemic stroke. *J Neurointerventional Surg* (2019) 11(12):1249–56. doi:10.1136/neurintsurg-2019-014822

79. Rava RA, Snyder KV, Mokin M, Waqas M, Allman A, Senko J, et al. Assessment of a bayesian vitrea CT perfusion analysis to predict final infarct and penumbra volumes in patients with acute ischemic stroke: a comparison with rapid. *Am J Neuroradiol* (2020) 41(2):206–12. doi:10.3174/ajnr.A6395

80. Rava RA, Snyder KV, Mokin M, Waqas M, Zhang X, Podgorsak AR, et al. Assessment of computed tomography perfusion software in predicting spatial location and volume of infarct in acute ischemic stroke patients: a comparison of Sphere, Vitrea, and RAPID. *J Neurointerventional Surg* (2021) 13(2):130–5. doi:10.1136/neurintsurg-2020-015966

81. Muehlen I, Sprügel M, Hoelter P, Hock S, Knott M, Huttner HB, et al. Comparison of two automated computed tomography perfusion applications to predict the final infarct volume after thrombolysis in cerebral infarction 3 recanalization. *Stroke* (2022) 53(5):1657–64. doi:10.1161/STROKEAHA.121.035626

82. Bivard A, Kleinig T, Churilov L, Levi C, Lin L, Cheng X, et al. Permeability measures predict hemorrhagic transformation after ischemic stroke. *Ann Neurol* (2020) 88(3):466–76. doi:10.1002/ana.25785

83. Simard JM, Kent TA, Chen M, Tarasov KV, Gerzanich V. Brain oedema in focal ischaemia: molecular pathophysiology and theoretical implications. *Lancet Neurol* (2007) 6(3):258–68. doi:10.1016/S1474-4422(07)70055-8

84. Seet RCS, Rabinstein AA. Symptomatic intracranial hemorrhage following intravenous thrombolysis for acute ischemic stroke: a critical review of case definitions. *Cerebrovasc Dis* (2012) 34(2):106–14. doi:10.1159/000339675

85. Von Kummer R, Broderick JP, Campbell BCV, Demchuk A, Goyal M, Hill MD, et al. The Heidelberg bleeding classification: classification of bleeding events after ischemic stroke and reperfusion therapy. *Stroke* (2015) 46(10):2981–6. doi:10.1161/STROKEAHA.115.010049

86. Yoshimura S, Sakai N, Yamagami H, Uchida K, Beppu M, Toyoda K, et al. Endovascular therapy for acute stroke with a large ischemic region. *N Engl J Med* (2022) 386(14):1303–13. doi:10.1056/NEJMoa2118191

87. Sarraj A, Kleinig TJ, Hassan AE, Portela PC, Ortega-Gutierrez S, Abraham MG, et al. Association of endovascular thrombectomy vs medical management with functional and safety outcomes in patients treated beyond 24 hours of last known

well: the SELECT late study. JAMA Neurol *Published Online December* (2022) 27:172. doi:10.1001/jamaneurol.2022.4714

88. Folkman J. The role of angiogenesis in tumor growth. *Semin Cancer Biol* (1992) 3(2):65–71.

89. Jain R, Gutierrez J, Narang J, Scarpace L, Schultz L, Lemke N, et al. *In vivo* correlation of tumor blood volume and permeability with histologic and molecular angiogenic markers in gliomas. *Am J Neuroradiol* (2011) 32(2):388–94. doi:10.3174/ajnr.A2280

90. Ellika SK, Jain R, Patel SC, Scarpace L, Schultz L, Rock J, et al. Role of perfusion CT in glioma grading and comparison with conventional MR imaging features. *Am J Neuroradiol* (2007) 28(10):1981–7. doi:10.3174/ajnr.A0688

91. McFaline-Figueroa JR, Lee EQ. Brain tumors. *Am J Med* (2018) 131(8):874–82. doi:10.1016/j.amjmed.2017.12.039

92. Louis DN, Perry A, Wesseling P, Brat DJ, Cree IA, Figarella-Branger D, et al. The 2021 WHO classification of tumors of the central nervous system: a summary. *Neuro-Oncol.* (2021) 23(8):1231–51. doi:10.1093/neuonc/noab106

93. Chandrasoma PT, Smith MM, Apuzzo MLJ. Stereotactic biopsy in the diagnosis of brain masses: comparison of results of biopsy and resected surgical specimen. *Neurosurgery* (1989) 24(2):160–5. doi:10.1227/00006123-198902000-00002

94. Jackson RJ, Fuller GN, Abi-Said D, Lang FF, Gokaslan ZL, Shi WM, et al. Limitations of stereotactic biopsy in the initial management ofgliomas. *Neuro-Oncol* (2001) 3(3):193–200. doi:10.1093/neuonc/3.3.193

95. Jain R. Perfusion CT imaging of brain tumors: an overview. *Am J Neuroradiol* (2011) 32(9):1570–7. doi:10.3174/ajnr.A2263

96. Leon SP, Folkerth RD, Black PML. Microvessel density is a prognostic indicator for patients with astroglial brain tumors. *Cancer* (1996) 77(2):362–72. doi:10.1002/(SICI)1097-0142(19960115)77:2<362::AID-CNCR20>3.0.CO;2-Z

97. Li VW, Yu ABC, Folkman J, Yu C, Rupnick M, Barnes P, et al. Microvessel count and cerebrospinal fluid basic fibroblast growth factor in children with brain tumours. *The Lancet* (1994) 344(8915):82–6. doi:10.1016/S0140-6736(94)91280-7

98. Weidner N. Intratumor microvessel density as a prognostic factor in cancer. *Am J Pathol* (1995) 147(1):9–19.

99. Provenzale JM, Mukundan S, Dewhirst M. The role of blood-brain barrier permeability in brain tumor imaging and therapeutics. *Am J Roentgenol* (2005) 185(3):763–7. doi:10.2214/ajr.185.3.01850763

100. Ma SH, Le HB, Jia Bhui, Wang ZX, Xiao ZW, Cheng XL, et al. Peripheral pulmonary nodules: relationship between multi-slice spiral CT perfusion imaging and tumor angiogenesis and VEGF expression. *BMC Cancer* (2008) 8(1):186. doi:10.1186/1471-2407-8-186

101. Tonino PAL, Fearon WF, De Bruyne B, Oldroyd KG, Leesar MA, Ver Lee PN, et al. Angiographic versus functional severity of coronary artery stenoses in the FAME study. *J Am Coll Cardiol* (2010) 55(25):2816–21. doi:10.1016/j.jacc.2009.11.096

102. Tonino PAL, De Bruyne B, Pijls NHJ, Siebert U, Ikeno F, van `t Veer M, et al. Fractional flow reserve versus angiography for guiding percutaneous coronary intervention. *N Engl J Med* (2009) 360(3):213–24. doi:10.1056/NEJMoa0807611

103. Virani SS, Alonso A, Benjamin EJ, Bittencourt MS, Callaway CW, Carson AP, et al. Heart disease and stroke statistics—2020 update: a report from the American heart association. *Circulation* (2020) 141(9):e139–e596. doi:10.1161/CIR.0000000000000757

104. Yun CH, Hung CL, Wen MS, Wan YL, So A. CT assessment of myocardial perfusion and fractional flow reserve in coronary artery disease: a review of current clinical evidence and recent developments. *Korean J Radiol* (2021) 22(11):1749. doi:10.3348/kjr.2020.1277

105. Budoff MJ, Dowe D, Jollis JG, Gitter M, Sutherland J, Halamert E, et al. Diagnostic performance of 64-multidetector row coronary computed tomographic angiography for evaluation of coronary artery stenosis in individuals without known coronary artery disease: results from the prospective multicenter ACCURACY (Assessment by Coronary Computed Tomographic Angiography of Individuals Undergoing Invasive Coronary Angiography) trial. *J Am Coll Cardiol* (2008) 52(21):1724–32. doi:10.1016/j.jacc.2008.07.031

106. Meijboom WB, Meijs MFL, Schuijf JD, Cramer MJ, Mollet NR, van Mieghem CAG, et al. Diagnostic accuracy of 64-slice computed tomography coronary angiography: a prospective, multicenter, multivendor study. *J Am Coll Cardiol* (2008) 52(25):2135–44. doi:10.1016/j.jacc.2008.08.058

107. Min JK, Taylor CA, Achenbach S, Koo BK, Leipsic J, Nørgaard BL, et al. Noninvasive fractional flow reserve derived from coronary CT angiography. *JACC Cardiovasc Imaging* (2015) 8(10):1209–22. doi:10.1016/j.jcmg.2015.08.006

108. Cook CM, Petraco R, Shun-Shin MJ, Ahmad Y, Nijjer S, Al-Lamee R, et al. Diagnostic accuracy of computed tomography-derived fractional flow reserve: a systematic review. *JAMA Cardiol* (2017) 2(7):803–10. doi:10.1001/jamacardio.2017.1314

109. Fujimoto S, Kawasaki T, Kumamaru KK, Kawaguchi Y, Dohi T, Okonogi T, et al. Diagnostic performance of on-site computed CT-fractional flow reserve based on fluid structure interactions: comparison with invasive fractional flow reserve and instantaneous wave-free ratio. *Eur Heart J - Cardiovasc Imaging* (2019) 20(3):343–52. doi:10.1093/ehjci/jey104

110. Siogkas PK, Anagnostopoulos CD, Liga R, Exarchos TP, Sakellarios AI, Rigas G, et al. Noninvasive CT-based hemodynamic assessment of coronary lesions derived from fast computational analysis: a comparison against fractional flow reserve. *Eur Radiol* (2019) 29(4):2117–26. doi:10.1007/s00330-018-5781-8

111. Cerqueira M. Standardized myocardial segmentation and nomenclature for tomographic imaging of the heart: a statement for healthcare professionals from the Cardiac Imaging Committee of the Council on Clinical Cardiology of the American Heart Association. *J Nucl Cardiol* (2002) 9(2):240–5. doi:10.1067/mnc.2002.123122

112. Mushtaq S, Conte E, Pontone G, Baggiano A, Annoni A, Formenti A, et al. State-of-the-art-myocardial perfusion stress testing: static CT perfusion. *J Cardiovasc Comput Tomogr* (2020) 14(4):294–302. doi:10.1016/j.jcct.2019.09.002

113. Pontone G, Baggiano A, Andreini D, Guaricci AI, Guglielmo M, Muscogiuri G, et al. Dynamic stress computed tomography perfusion with a whole-heart coverage scanner in addition to coronary computed tomography angiography and fractional flow reserve computed tomography derived. *JACC Cardiovasc Imaging* (2019) 12(12):2460–71. doi:10.1016/j.jcmg.2019.02.015

114. Pontone G, Baggiano A, Andreini D, Guaricci AI, Guglielmo M, Muscogiuri G, et al. Stress computed tomography perfusion versus fractional flow reserve CT derived in suspected coronary artery disease. *JACC Cardiovasc Imaging* (2019) 12(8):1487–97. doi:10.1016/j.jcmg.2018.08.023

115. Sekhri V, Sanal S, DeLorenzo LJ, Aronow WS, Maguire GP. Cardiac sarcoidosis: a comprehensive review. *Arch Med Sci* (2011) 4:546–54. doi:10.5114/aoms.2011.24118

116. Silverman KJ, Hutchins GM, Bulkley BH. Cardiac sarcoid: a clinicopathologic study of 84 unselected patients with systemic sarcoidosis. *Circulation* (1978) 58(6):1204–11. doi:10.1161/01.CIR.58.6.1204

117. Sadek MM, Yung D, Birnie DH, Beanlands RS, Nery PB. Corticosteroid therapy for cardiac sarcoidosis: a systematic review. *Can J Cardiol* (2013) 29(9):1034–41. doi:10.1016/j.cjca.2013.02.004

118. Youssef G, Beanlands RSB, Birnie DH, Nery PB. Cardiac sarcoidosis: applications of imaging in diagnosis and directing treatment. *Heart* (2011) 97(24):2078–87. doi:10.1136/hrt.2011.226076

119. So A, Lee TY, Tzemos N. Myocardial perfusion and scar assessment in cardiac sarcoidosis with functional computed tomography imaging. *Circ Cardiovasc Imaging* (2020) 13(4):e010046. doi:10.1161/CIRCIMAGING.119.010046

120. Mendrik AM, Vonken Ejan, van Ginneken B, de Jong HW, Riordan A, van Seeters T, et al. TIPS bilateral noise reduction in 4D CT perfusion scans produces high-quality cerebral blood flow maps. *Phys Med Biol* (2011) 56(13):3857–72. doi:10.1088/0031-9155/56/13/008

121. Pisana F, Henzler T, Schönberg S, Klotz E, Schmidt B, Kachelrieß M. Noise reduction and functional maps image quality improvement in dynamic CT perfusion using a new k-means clustering guided bilateral filter (KMGB). *Med Phys* (2017) 44(7):3464–82. doi:10.1002/mp.12297

122. Yeung TPC, Dekaban M, De Haan N, Morrison L, Hoffman L, Bureau Y, et al. Improving quantitative CT perfusion parameter measurements using principal component analysis. *Acad Radiol* (2014) 21(5):624–32. doi:10.1016/j.acra.2014.01.015

123. Zhao C, Martin T, Shao X, Alger JR, Duddalwar V, Wang DJJ. Low dose CT perfusion with K-space weighted image average (KWIA). *IEEE Trans Med Imaging* (2020) 39(12):3879–90. doi:10.1109/TMI.2020.3006461

124. Huang SHS, Pavenski K, Lee TY, Jurkiewicz MT, Bharatha A, Thiessen JD, et al. Blood–brain barrier permeability in survivors of immune-mediated thrombotic thrombocytopenic purpura: a pilot study. *Blood Adv* (2021) 5(20):4211–8. doi:10.1182/bloodadvances.2021005317

125. Tao Y, Chen GH, Hacker TA, Raval AN, Van Lysel MS, Speidel MA. Low dose dynamic CT myocardial perfusion imaging using a statistical iterative reconstruction method: low dose myocardial perfusion CT using SIR. *Med Phys* (2014) 41(7):071914. doi:10.1118/1.4884023

126. Wu D, Ren H, Li Q. Self-supervised dynamic CT perfusion image denoising with deep neural networks. *IEEE Trans Radiat Plasma Med Sci* (2021) 5(3):350–61. doi:10.1109/TRPMS.2020.2996566

127. Kadimesetty VS, Gutta S, Ganapathy S, Yalavarthy PK. Convolutional neural network-based robust denoising of low-dose computed tomography perfusion maps. *IEEE Trans Radiat Plasma Med Sci* (2019) 3(2):137–52. doi:10.1109/TRPMS.2018.2860788

128. Li S, Zeng D, Bian Z, Li D, Zhu M, Huang J, et al. Learning non-local perfusion textures for high-quality computed tomography perfusion imaging. *Phys Med Biol* (2021) 66(11):115007. doi:10.1088/1361-6560/abfc90

129. Ommen F, Kauw F, Bennink E, Dankbaar JW, Viergever MA, Jong HWAM. Effect of prolonged acquisition intervals for CT-perfusion analysis methods in patients with ischemic stroke. *Med Phys* (2019) 46(7):3156–64. doi:10.1002/mp.13559

130. Chung KJ, Khaw AV, Pandey SK, Lee DH, Mandzia JL, Lee TY. Feasibility of deconvolution-based multiphase CT angiography perfusion maps in acute ischemic stroke: simulation and concordance with CT perfusion. *J Stroke Cerebrovasc Dis* (2022) 31(12):106844. doi:10.1016/j.jstrokecerebrovasdis.2022.106844

131. Wang C, Shi Z, Yang M, Huang L, Fang W, Jiang L, et al. Deep learning-based identification of acute ischemic core and deficit from non-contrast CT and CTA. *J Cereb Blood Flow Metab* (2021) 41(11):3028–38. doi:10.1177/0271678X211023660

132. Qiu W, Kuang H, Ospel JM, Hill MD, Demchuk AM, Goyal M, et al. Automated prediction of ischemic brain tissue fate from multiphase computed tomographic angiography in patients with acute ischemic stroke using machine learning. *J Stroke* (2021) 23(2):234–43. doi:10.5853/jos.2020.05064

133. Lee S, Jiang B, Heit JJ, Dodd RL, Wintermark M. Cerebral perfusion in pediatric stroke: children are not little adults. *Top Magn Reson Imaging* (2021) 30(5):245–52. doi:10.1097/RMR.0000000000000275

134. Lee S, Mlynash M, Christensen S, Jiang B, Wintermark M, Sträter R, et al. Hyperacute perfusion imaging before pediatric thrombectomy: analysis of the save ChildS study. *Neurology* (2023) 100(11):e1148–58. doi:10.1212/WNL.0000000000201687

135. Willemink MJ, Persson M, Pourmorteza A, Pelc NJ, Fleischmann D. Photon-counting CT: technical principles and clinical prospects. *Radiology* (2018) 289(2): 293–312. doi:10.1148/radiol.2018172656

136. Danielsson M, Persson M, Sjölin M. Photon-counting x-ray detectors for CT. *Phys Med Biol* (2021) 66(3):03TR01. doi:10.1088/1361-6560/abc5a5

137. Sotoudeh H, Bag AK, Brooks MD. "Code-Stroke" CT perfusion; challenges and pitfalls. *Acad Radiol* (2019) 26(11):1565–79. doi:10.1016/j.acra.2018.12.013

138. Sun H, Gao F, Li N, Liu C. An evaluation of the feasibility of assessment of volume perfusion for the whole lung by 128-slice spiral CT. *Acta Radiol* (2013) 54(8): 921–7. doi:10.1177/0284185113490151

139. Mirsadraee S, Reid JH, Connell M, MacNee W, Hirani N, Murchison JT, et al. Dynamic (4D) CT perfusion offers simultaneous functional and anatomical insights into pulmonary embolism resolution. *Eur J Radiol* (2016) 85(10):1883–90. doi:10.1016/j.ejrad.2016.08.018

140. Zhao Y, Hubbard L, Malkasian S, Abbona P, Molloi S. Dynamic pulmonary CT perfusion using first-pass analysis technique with only two volume scans: validation in a swine model. *PLOS ONE* (2020) 15(2):e0228110. doi:10.1371/journal.pone.0228110

141. Xin Y, Kim T, Winkler T, Brix G, Gaulton T, Gerard SE, et al. Improving pulmonary perfusion assessment by dynamic contrast-enhanced computed tomography in an experimental lung injury model. *J Appl Physiol* (2023) 134(6): 1496–507. doi:10.1152/japplphysiol.00159.2023

142. Sitartchouk I, Roberts HC, Pereira AM, Bayanati H, Waddell T, Roberts TP. Computed tomography perfusion using first pass methods for lung nodule characterization. *Invest Radiol* (2008) 43(6):349–58. doi:10.1097/RLI.0b013e3181690148

143. Jimenez-Juan L, Mehrez H, Dey C, Homampour S, Salazar-Ferrer P, Granton JT, et al. Quantitative assessment of pulmonary artery occlusion using lung dynamic perfusion CT. *Sci Rep* (2021) 11(1):483. doi:10.1038/s41598-020-80177-5

144. Ohno Y, Nishio M, Koyama H, Fujisawa Y, Yoshikawa T, Matsumoto S, et al. Comparison of quantitatively analyzed dynamic area-detector CT using various mathematic methods with FDG PET/CT in management of solitary pulmonary nodules. *Am J Roentgenol* (2013) 200(6):W593–W602. doi:10.2214/AJR.12.9197

145. Yabuuchi H, Kawanami S, Iwama E, Okamoto I, Kamitani T, Sagiyama K, et al. Prediction of therapeutic effect of chemotherapy for NSCLC using dual-input perfusion CT analysis: comparison among bevacizumab treatment, two-agent platinum-based therapy without bevacizumab, and other non-bevacizumab treatment groups. *Radiology* (2018) 286(2):685–95. doi:10.1148/radiol.2017162204

146. Ohno Y, Koyama H, Fujisawa Y, Yoshikawa T, Seki S, Sugihara N, et al. Dynamic contrast-enhanced perfusion area detector CT for non-small cell lung cancer patients: influence of mathematical models on early prediction capabilities for treatment response and recurrence after chemoradiotherapy. *Eur J Radiol* (2016) 85(1):176–86. doi:10.1016/j.ejrad.2015.11.009

frontiers | Frontiers in Physics

TYPE Original Research
PUBLISHED 18 January 2024
DOI 10.3389/fphy.2023.1299522

OPEN ACCESS

EDITED BY
Ewald V. Moser,
Medical University of Vienna, Austria

REVIEWED BY
Marcos Wolf,
Medical University of Vienna, Austria
Jon-Fredrik Nielsen,
University of Michigan, United States

*CORRESPONDENCE
Anne Slawig,
anne.slawig@uk-halle.de

RECEIVED 22 September 2023
ACCEPTED 19 December 2023
PUBLISHED 18 January 2024

CITATION
Bibiano J, Kleineisel J, Schad O, Weng AM, Köstler H and Slawig A (2024), No-wait inversion—a novel model for T1 mapping from inversion recovery measurements without the waiting times.
Front. Phys. 11:1299522.
doi: 10.3389/fphy.2023.1299522

No-wait inversion—a novel model for T1 mapping from inversion recovery measurements without the waiting times

Juliana Bibiano[1], Jonas Kleineisel[1], Oliver Schad[1], Andreas Max Weng[1], Herbert Köstler[1] and Anne Slawig[1,2]*

[1]Department of Diagnostic and Interventional Radiology, University Hospital of Würzburg, Würzburg, Germany, [2]Department for Radiation Medicine, Section Medical Physics, University Clinic and Outpatient Clinic for Radiology, University Hospital Halle (Saale), Halle (Saale), Germany

Introduction: Quantification of longitudinal relaxation time T1 gained interest as an important MR-inducible tissue property for tissue characterization. Standard inversion recovery (IR) measurements for T1 determination take a prohibitively long time, and signal models assume a perfect inversion. Acceleration is possible by using the Look–Locker (LL) technique or other accelerated, model-based algorithms. However, the calculation of real T1 values from LL acquisitions necessitates the knowledge of equilibrium magnetization M0. Thus, usually, a waiting time to allow for free relaxation between global inversion pulses must be implemented. This study aims to introduce a novel model-based fitting approach for T1 mapping without the need for such waiting times.

Methods: Single-inversion spiral LL spoiled gradient echo acquisitions were performed in a phantom and eight healthy volunteers using a 1.5T magnetic resonance imaging (MRI) scanner. The measurements comprised two parts, one without magnetization preparation and a second featuring a global inversion pulse preparation before each of the 35 slices. Acquisition was performed without any waiting time in between slices, i.e., before the inversion pulses. T1 maps were calculated based on an iterative model-based reconstruction algorithm which combines the information from these two measurements, with and without inversion.

Results: Accurate T1 maps were obtained in phantom and volunteer measurements. ROI-based mean T1 values differ by an average of 1.5% in the phantom and 5% *in vivo* between reference measurements and the proposed method. The combined fit benefits from both the information obtained in the inversion prepared and the unprepared measurements. The former provides a large dynamic range for accurate model-based fitting of the relaxation process, while the latter provides equilibrium magnetization M0, necessary to obtain accurate T1 values from a LL-like acquisition.

Conclusion: The proposed model of a combined fit of an inversion-prepared and an unprepared measurement allows for robust fast T1 mapping, even in cases of imperfect inversion due to skipped waiting times for magnetization recovery. Thus, it can render long waiting times in between inversion pulses redundant.

KEYWORDS

T1 mapping, quantitative MRI, model-based reconstruction, inversion recovery, non-Cartesian trajectory, brain

1 Introduction

Quantitative magnetic resonance imaging (MRI) allows obtaining maps of specific physical parameters in MRI. When compared to qualitative MRI (or weighted imaging), it additionally allows

- comparison of different tissues within the same individual from different locations or points in time;
- comparison between images from different individuals; and
- achievement of disease-specificity, with studies correlating abnormalities in the absolute values of certain MR-inducible tissue properties and health conditions [1–4].

The quantification of longitudinal relaxation time T1 gained interest for tissue characterization, and T1 mapping is already used in cardiac [1, 2, 5] and brain MRI [3, 4, 6]. Conventional techniques for T1 determination are based on tracking magnetization after a suitable magnetization preparation, e.g., inversion recovery (IR) measurements. Following an inversion pulse, an image is acquired for a fixed delay after the inversion pulse. Typically, the k-space is filled in a segmented fashion. Consequently, for each repetition, magnetization must be restored to the original state, requiring a waiting interval to ensure full recovery of the signal before every new magnetization preparation. Repetitions of these measurements, to acquire images at different delays after the inversion pulse, are necessary to trace the relaxation of magnetization. Thus, standard IR measurements have a prohibitively long duration and are hardly feasible for clinical application [6–8]. The Look–Locker (LL) technique [9] came as a milestone for accelerated T1 quantification. Typically, an IR magnetization preparation pulse is applied, followed by a series of low-angle radiofrequency (RF) pulses used for spoiled gradient echo imaging. Data acquired after one inversion is sorted into different k-spaces, corresponding to the different delays after the inversion. Thus, the number of necessary repetitions can be reduced compared to conventional IR T1 mapping. However, the problem of the long waiting periods, on the order of 5*T1max, still exists for the LL technique [2, 10]. Although LL techniques are much faster than conventional IR T1 mapping, the RF pulses used for data acquisition affect the T1 recovery. Thus, the longitudinal relaxation process is not the same as for an undisturbed IR experiment, resulting in an apparent T1 (termed T1*). The longitudinal relaxation time T1 can be calculated from the apparent relaxation time T1* using the acquisition parameters repetition time and the local flip angle [11, 12]. Alternatively, T1 can be calculated from the measured quantities, T1*, equilibrium magnetization M0, and steady-state magnetization Mss [10, 12]: $T1/T1^* = M0/Mss$. To overcome the issue of long acquisition times, single shot techniques with a very restricted spatial or temporal resolution can be used. However, both can lead to a poor accuracy of the corresponding parameter maps. Alternatively, undersampled k-spaces can be used. Yet, these approaches require sophisticated reconstruction approaches to mitigate the effects of undersampled data sets [13, 14]. For example, the model-based acceleration of LL T1 mapping (MAP [10]) uses a single inversion to generate a series of undersampled images. Then, a pixel-wise fit of the undersampled dataset is performed using a model of monoexponential relaxation. This results in fully sampled k-spaces, leading to a series of images that cover the whole IR process. As a result, accurate parameter maps are calculated [10, 15].

Based on a novel model-based fitting approach, this study aims to introduce a technique for T1 mapping without the necessity of waiting times for free relaxation in between inversion pulses.

2 Materials and methods

2.1 Measurements

Measurements were performed on eight healthy volunteers. The study was approved by the local ethics committee, and informed consent was obtained from all volunteers before scanning. Experiments were performed on a 1.5T MRI scanner (Siemens MAGNETOM Avanto Fit) using a 20-channel head coil array. Table 1 gives an overview of all measurements performed. In general, reference measurements were performed using a turbo spin echo (TSE) sequence (Table 1, Nb 1 and 3), while acquisitions for the proposed method are based on a LL [9], spoiled gradient echo acquisition with a spiral trajectory (Table 1, Nb. 2A, 2B, 4A, 4B, 5A, and 5B).

For comparison, in each volunteer and the phantom examination, one slice was acquired using a TSE sequence using the following imaging parameters: flip angle = 150°, resolution = 0.5 × 0.5 mm^2, slice thickness = 5 mm, turbo factor = 10, measurement time = 22 min, and TE = 12 ms. Inversion times were as follows: TI = 30 ms, 100 ms, 250 ms, 500 ms, 1,000 ms, 1,600 ms, and 2,500 ms, and TR was TI + 1,000 ms and ranged between 1,030 and 3,500 ms. In the phantom, measurements at TI = 6,000 ms and 10,000 ms were added.

For all other acquisitions in each slice, 400 spoiled gradient echoes (GREs) using a variable-density spiral read-out trajectory were acquired. Consecutive spiral arms were spaced apart by a double golden angle. The trajectory was designed using the *variable-density spiral design function tool* [16, 17] by Brian Hargreaves and adjusted to observe a maximum gradient amplitude of 40 mT/m and a maximum gradient slew rate of 170 mT/m/s. The readout length of one spiral arm was 6.28 ms and extended in k-space to a maximum value of 0.625 1/

TABLE 1 Overview of measurements and their measurement parameters.

Nb	Object	Sequence	Magnetization preparation	Waiting time
1	Volunteers, 1 slice each	Turbo spin echo	Inversion-prepared	-
2A	Volunteers, 35 slices each	Spoiled GRE with spiral trajectory	Non	Non
2B	Volunteers, 35 slices each	Spoiled GRE with spiral trajectory	Inversion-prepared	Non
3	Phantom, 1 slice	Turbo spin echo	Inversion-prepared	-
4A	Phantom, 35 slices	Spoiled GRE with spiral trajectory	Non	Non
4B	Phantom, 35 slices	Spoiled GRE with spiral trajectory	Inversion-prepared	Non
5A	Phantom, 35 slices	Spoiled GRE with spiral trajectory	Non	Non
5B	Phantom, 35 slices	Spoiled GRE with spiral trajectory	Inversion-prepared	20s

Common parameters	
Spoiled GRE	TSE
TE = 0.61 ms	TE = 12 ms
	TI = 30 ms, 100 ms, 250 ms, 500 ms, 1,000 ms, 1,600 ms, and 2,500 ms
TR = 7.5 ms, flip angle = 10°	TR = TI + 1,000 ms, flip angle = 150°,
Resolution: 0.8 × 0.8 mm^2	Resolution = 0.5 × 0.5 mm^2
Slice thickness = 5 mm	Slice thickness = 5 mm
	Turbo factor = 10
Measurement time per slice = 3 s	Measurement time per slice = 22 min

TABLE 2 T1 values as determined in the phantom measurements.

Phantom	T1 values (mean ± SD) [ms]							
Measurement	Spiral acquisition with pause (Nb. 5)			Spiral acquisition with no pause (Nb. 4)			TSE (Nb. 3)	Handbook
Reconstruction model	a)	b)	c)	a)	b)	c)	Reference	
ROI 1	1,363 ± 263	1,929 ± 121	1,811 ± 131	1,377 ± 271	1,302 ± 79	1,801 ± 97	1,793 ± 35	1,724
ROI 2	1,058 ± 151	1,461 ± 67	1,392 ± 69	1,129 ± 222	1,147 ± 78	1,374 ± 81	1,402 ± 24	1,451
ROI 3	904 ± 138	1,127 ± 69	1,059 ± 60	866 ± 135	1,021 ± 71	1,043 ± 73	1,017 ± 21	1,010
ROI 4	631 ± 141	765 ± 35	703 ± 33	612 ± 116	742 ± 29	702 ± 41	688 ± 8	672
ROI 5	481 ± 167	524 ± 23	492 ± 35	481 ± 112	525 ± 22	493 ± 31	488 ± 5	467
ROI 6	329 ± 167	373 ± 16	346 ± 23	358 ± 180	377 ± 25	343 ± 20	347 ± 4	333
ROI 7	252 ± 84	272 ± 14	243 ± 18	274 ± 24	271 ± 17	246 ± 18	249 ± 4	235
ROI 8	326 ± 45	204 ± 12	181 ± 14	493 ± 72	200 ± 18	184 ± 19	181 ± 3	169

Model a): unprepared measurement only.
Model b): inversion-prepared measurement only.
Model c): combined fit of inversion-prepared and unprepared measurements.
Ref: TSE acquisition.

mm in order to achieve a spatial resolution of 0.8 × 0.8 mm^2. By design, a total of 70 equally spaced spiral arms could fully cover the k-space for a FOV of 300 mm. However, in this study, a continuous rotation of a double golden angle was chosen between consecutive spiral arms. Other imaging parameters include TE = 0.61 ms, TR = 7.5 ms, flip angle = 10°, slice thickness = 5 mm, and measurement time = 3s for

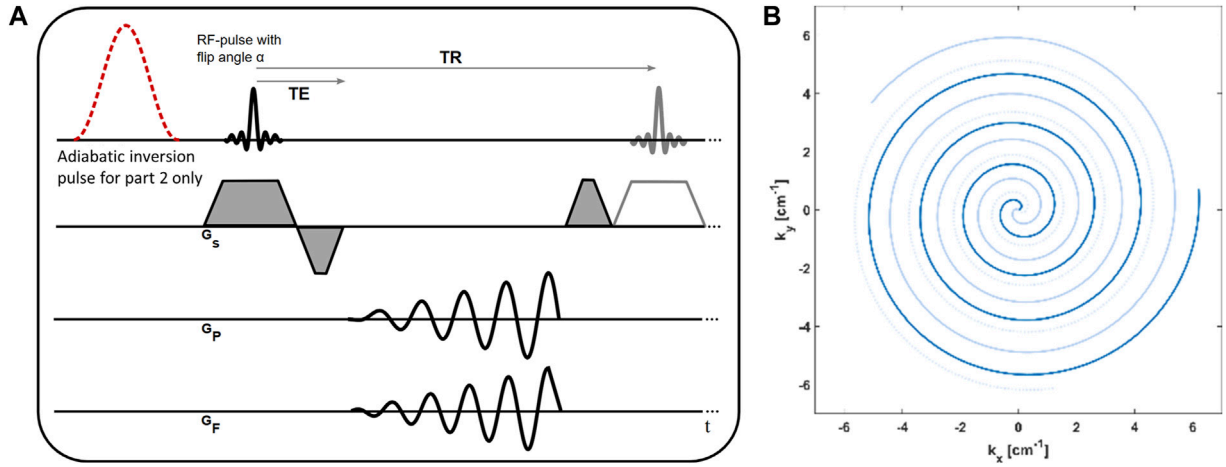

FIGURE 1
(A) Sequence diagram of the spoiled gradient echo acquisition with spiral trajectory. In part one of the measurement, no magnetization preparation is performed. In part two of the measurement, the nonselective adiabatic inversion pulse is played out before the acquisition of each slice. **(B)** Depiction of the spiral trajectory. Shown are the first three arms, and consecutive arms are continuously rotated by a double golden angle.

each slice. Each acquisition in a healthy volunteer comprised 35 slices in interleaved order and covered the whole brain.

These measurements comprised two LL-like acquisition parts: during the first part (Nb. 2A), no preparation and only slice-selective excitations were used. In the second part (Nb. 2B), a global adiabatic inversion pulse was applied before the acquisition of each slice (pulse length: 10.2 ms). No waiting time was heeded in between slices, and thus, starting magnetization was affected by the previous global inversion pulses. Both parts acquire the course of the receiver coil weighted magnetization from a starting point (M0 or −αM0) to the steady-state magnetization Mss.

The same protocol was used for phantom measurements (Nb. 4A and 4B) on an *Essential System Phantom Model 106* by CaliberMRI (Handbook T1 values are given in Table 2). Here, an additional measurement with a waiting time of 20 s in between slices, and thus in between successive inversion pulses, was performed (Nb. 5A, 5B). The value of more than 10*maximum T1 in the phantom was chosen to ensure full relaxation of all phantom compartments and no signal contamination by former inversion pulses. Additionally, reference T1 values for the different vials within the phantom are provided by the vendor in the phantom manual.

A depiction of the spoiled gradient echo pulse sequence and the spiral k-space trajectory is given in Figure 1.

2.2 Reconstruction

For all measurements, raw data was extracted from the scanner, and image reconstruction was performed offline in MATLAB. Reference TSE measurements (Table 1, Nb. 1 and 3) were reconstructed by 2D Fourier transform. Data reconstruction of spiral GRE acquisitions was performed by a modified model-based acceleration of LL T1 mapping (MAP) algorithm [10, 15]. First, the corrected spiral k-space trajectory was calculated based on the gradient system transfer function [18, 19]. Then, initial images were reconstructed by gridding the data of each spiral arm into separate k-spaces. All reconstructions were performed on a matrix of size 512 × 512 and with a field of view of 40.96 cm. After 2D Fourier transform, this results in a stack of highly undersampled images, which track the time course of T1* relaxation. As one spiral arm is gridded to each k-space, the temporal resolution equals TR. This was conducted separately for both parts of the spiral measurements, with and without the inversion pulse.

This initial step was followed by the iterative reconstruction algorithm consisting of alternating steps of pixel-wise model-based fitting and restoring data consistency. Data from the two parts of the measurement (Nb. 2A and B, 4A and B, and 5A and B) was either reconstructed together using a combined model (model (c)) or, for comparison, separately only for the unprepared part (model (a) for part A) or the inversion-prepared part (model (b) for part B).

This pixel-wise fitting of the reconstruction used the following fitting models:

(a) Unprepared:

The transient phase of unprepared magnetization in spoiled gradient echo acquisition only (Nb. 2A, 4A, and 5A) with three free parameters ($M0_{non}$, Mss, and T1*):

$$M_{non} = Mss + (M0_{non} - Mss)*e^{\left(-\frac{t}{T1^*}\right)}.$$

(b) Inversion-prepared:

Inversion recovery Look–Locker (IR-LL) acquisition only (Nb. 2B, 4B, and 5B) with three free parameters ($M0_{IR}$, Mss, and T1*):

$$M_{inv} = Mss - (M0_{IR} + Mss)*e^{\left(-\frac{t}{T1^*}\right)}.$$

(c) Combined:

A combination of unprepared GRE magnetization and magnetization of IR-LL acquisitions (Nb. 2A and B, 4A and B,

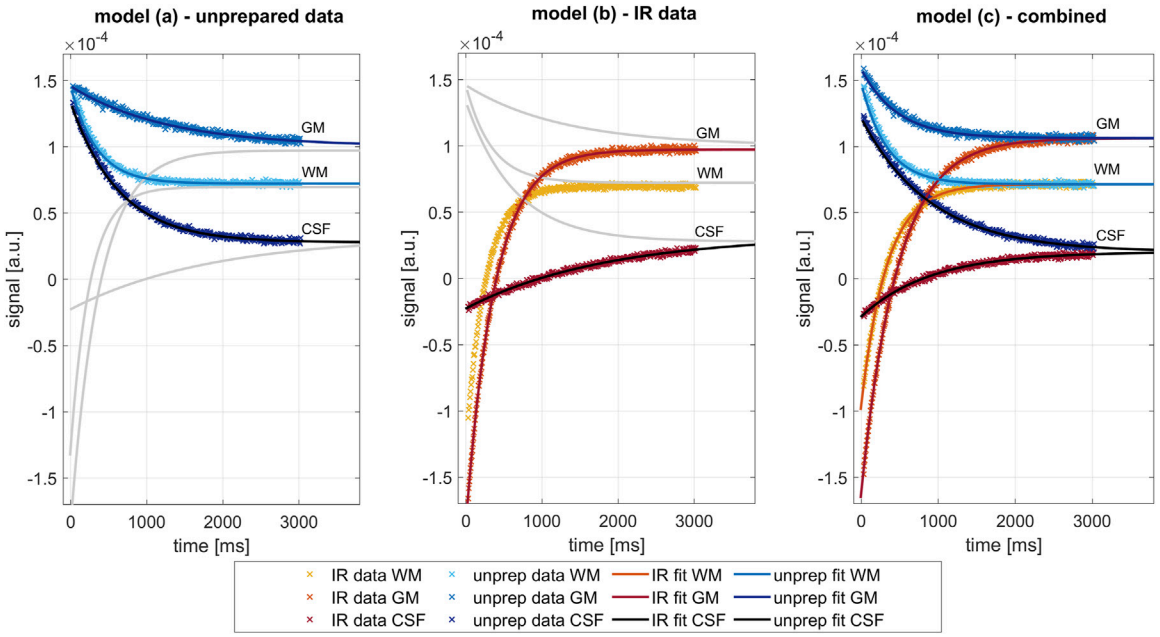

FIGURE 2
Comparison of the different fit models for three exemplary pixels in the white matter (WM), gray matter (GM), and cerebrospinal fluid (CSF), as performed in the last iteration. Data and fits of inversion prepared measurements are shown in shades of blue, from unprepared measurements in shades of red. Left: Fit of three parameters (Mss, $M0_{non}$, and T1*) on data on the unprepared measurement (part A of spiral LL acquisitions), as described by model (a). Center: Fit of three parameters (Mss, $M0_{IR}$, and T1*) on data on the inversion prepared measurement (part B of spiral LL acquisitions), as described by model (b). Right: combined fit of four parameters (Mss, $M0_{IR}$, $M0_{non}$, and T1*) on data on the unprepared and inversion-prepared measurement simultaneously, as described by model (c). Major difference lies in the constraint introduced by model (c), forcing Mss and T1* to be similar in both relaxation processes.

and 5A and B) with four free parameters ($M0_{IR}$, $M0_{non}$, Mss, and T1*):

$$\begin{pmatrix} M_{inv} = & Mss - (M0_{IR} + Mss) * e^{\left(-\frac{t}{T1*}\right)} \\ M_{non} = & Mss + (M0_{non} - Mss) * e^{\left(-\frac{t}{T1*}\right)} \end{pmatrix},$$

where Mss is steady-state magnetization, T1* is the LL relaxation time [9], $M0_{non}$ is equilibrium magnetization, and $M0_{IR}$ is magnetization directly after the inversion pulse. An illustration of the different models for data on representative voxels is given in Figure 2. Afterward, fitted images were transformed back to the k-space, and data consistency was enforced by reintroducing measured data points into these modeled k-spaces. As in the original MAP algorithm, we iteratively performed steps consisting of model-based fitting and data consistency until convergence to a solution was reached [15].

However, as this procedure converges rather slowly, we used a modified algorithm. The original MAP reconstruction algorithm can be seen as alternating projections onto two different subspaces: the data-consistent solutions and the subspace of exponential signal evolutions in all pixels. A combination of two MAP projections, either from the data-consistent solution subspace back onto the data-consistent solution subspace or from the exponential model subspace back to the model subspace, can be seen as steps into the right direction with a non-optimized step size. In other words, from two solutions in each of these subspaces, a one-dimensional (1D) consistency subspace and a 1D model subspace are defined. In the modified MAP algorithm, we calculate the point in the 1D data-consistent subspace, which is closest to the 1D model subspace, and use it as the starting points for two further MAP iterations. These MAP steps were used again to determine new 1D subspaces and a new step size estimate. If the reconstruction problem would be linear and the measured data without noise, the exact solution would be found after a single step size adjustment. Numerical experiments suggest that, for our data, this approach reduces the number of steps before convergence by a factor of approximately 50 compared to the original MAP approach while arriving at a similar solution. For the reconstructions presented below, we performed six MAP steps and two step size adjustments (after MAP steps 2 and 4) in total.

2.3 Calculation of parameter maps

From the results of the last iteration in the model-based subspace, absolute T1 values were calculated from the apparent relaxation time T1* in LL acquisitions as [10]: $T1 = \frac{T1^* * M0_{IR/non}}{Mss}$ using the latest fitting values. Additionally, the inversion efficiency was calculated as $InvEff = M0_{IR}/M0_{non}$ from the combined model (c).

Reference TSE data were reconstructed by 2D FFT, and an adaptive coil combination was performed [20]. The average phase of the last three measurements in each pixel was subtracted from all measurements, and subsequently, the real part of the data was fitted pixel-wise using the following equation (adapted from [21]):

$$S = M_0 * \left(1 - (1 - b) * e^{\left(-\frac{TI}{T1}\right)} + c * e^{\left(-\frac{TR}{T1}\right)}\right),$$

with $c = (e^{TE_{last}/T1})$,

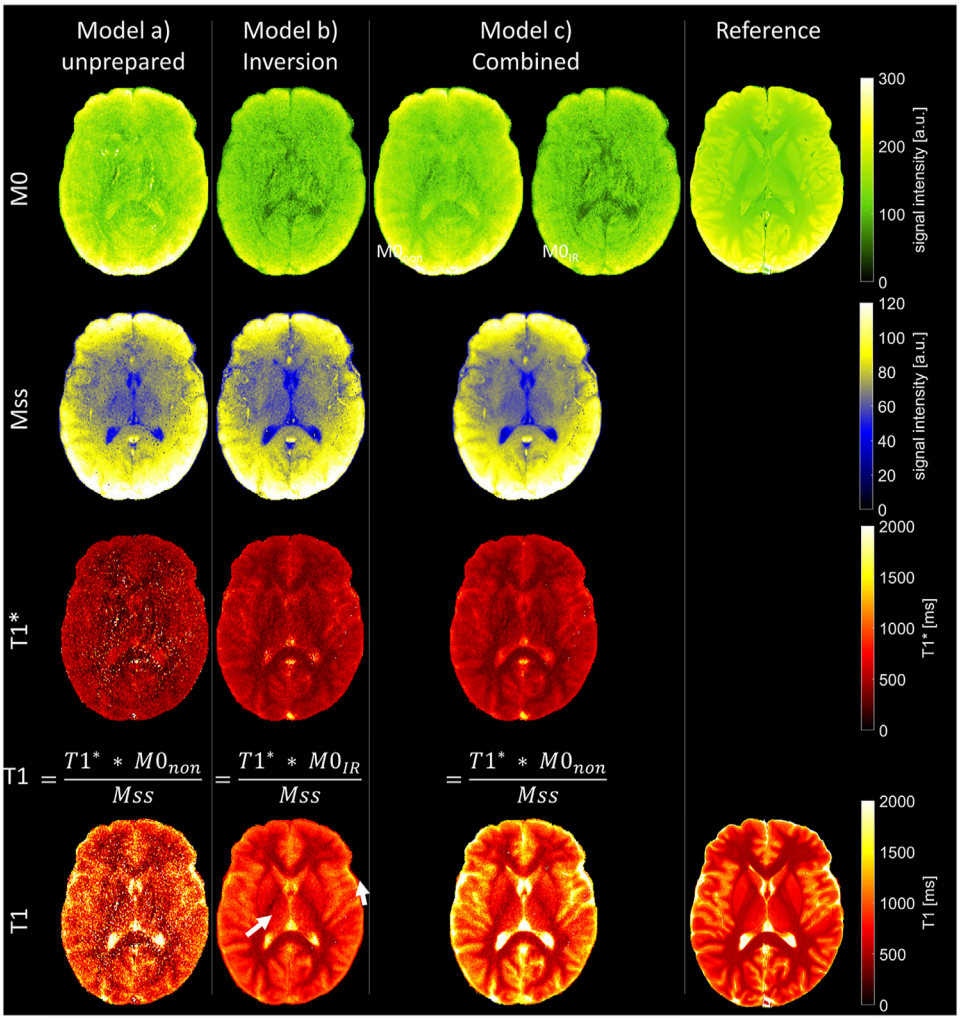

FIGURE 3
Parameter maps as determined by the three different fit models and from the reference measurement. Top: equilibrium magnetization (M0). In the combined fit, two independent parameters ($M0_{IR}$ and $M0_{non}$) are considered to allow for imperfect inversion. Center: steady-state magnetization (Mss) and apparent longitudinal relaxation times (T1*). Bottom: longitudinal relaxation times (T1), as calculated from fit parameters of unprepared acquisition only [model (a)], inversion-prepared data only [model (b)], and the combined fit of both parts of the measurements [model (c)]. Arrows point to areas of T1 underestimation.

where TR is the repetition time and TI is time after inversion. Parameters b and c account for a potential non-ideal inversion and a constant effect of the acquired multi-echo train, respectively.

2.4 ROI-based analysis

In each multi-slice measurement, the central slice was identified, which also corresponds to the slice chosen in single-slice reference measurements. ROIs were then manually placed in corresponding areas in all measurements. In the phantom, a total of eight circular ROIs were added to comprise each of the separate vials inside the phantom. These ROIs were labeled ROI 1 to ROI 8 in the order of decreasing T1 values. In each volunteer, three different polygonal ROIs were drawn within that selected slice. The first ROI is placed in the frontal white matter area, the second ROI in the gray matter in the sulci in the right posterior brain, and the third ROI inside the frontal part of one ventricle. For each ROI in the phantom, the mean T1 values and the standard deviation (SD) within the ROI are evaluated. In each volunteer mean T1 values and SD within the ROI are evaluated, as well as mean T1 values and SD in each tissue over the whole group of volunteers.

Additionally, equivalence testing was performed to assess whether the phantom measurements with and without the waiting time were statistically equivalent. Specifically, the two one-sided *t*-test (TOST) procedure was conducted to test whether the difference in means between two groups falls within a predefined equivalence margin [22]. The equivalence bounds were set to be 3% of the mean T1 value in the reference measurement (i.e., 59 ms in ROI 1, 44 ms in ROI 2, 32 ms in ROI 3, 21 ms in ROI 4, 15 ms in ROI 5, 10 ms in ROI 6, 7 ms in ROI 7, and 5 ms in ROI 8). Practically, the equivalence of the means was assessed by examining whether the 90% confidence interval fell entirely within the predetermined equivalence bounds. Values

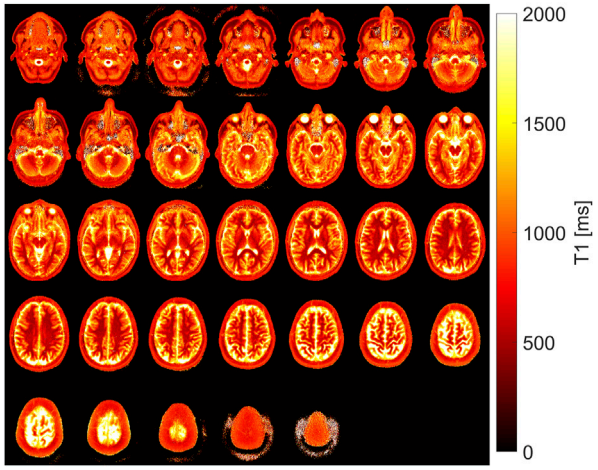

FIGURE 4
T1 maps as determined by the proposed combined fit model (c) in all slices of the whole head of one exemplary volunteer.

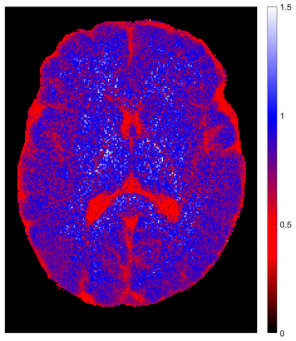

FIGURE 5
Inversion efficiency for one exemplary volunteer, as determined by the ratio of the two parameters $M0_{IR}$ and $M0_{non}$ in the combined fit model (c). Full inversion was not achieved in tissues with long relaxation time but worked fine in other areas.

within each ROI were considered as paired as the same ROIs were applied and pixel values were listed in the same order. The significance level was set at $\alpha = 0.05$.

3 Results

3.1 Signal evolution in the different models

Exemplarily, Figure 2 shows the signal evolution in three pixels located in the white matter area in the center of the brain, gray matter area, and cerebrospinal fluid (CSF) in the ventricle. Shown are the data points after data consistency was restored and the corresponding exponential curves fitted in the last iteration of each of the separate reconstruction processes (model (a), model (b), and model (c)). Note that the combined fitting, as proposed in model (c), forces Mss and T1* to be similar for both relaxation processes as data from identical tissue should feature identical tissue properties. Separate fitting of either inversion-prepared data (model (a)) or unprepared data (model (b)) imposes no such constraint, resulting in differing values.

3.2 Exemplary volunteer

Figure 3 shows parameter maps, as determined by the three different models after eight iteration steps. The combined model (c) yields two values for equilibrium magnetization $M0_{IR}$ and $M0_{non}$, from the inverted and unprepared relaxation processes respectively, while steady-state magnetization Mss and T1* times are preordained to be identical. Steady-state magnetization Mss (Figure 3 Mss) is comparable in all models. Maps of the equilibrium magnetization $M0_{IR/non}$ are shown in Figure 3 M0. Using model (b) for fitting of inversion-prepared data only (part B of LL measurements) enables robust fitting. Challenges to this model (b) arise in cases of imperfect inversion or altered magnetization due to the lack of waiting time between consecutive global inversions. The latter is especially apparent in areas with long relaxation times like in CSF, where the calculated values of $M0_{IR}$ are low. Low $M0_{IR}$ values are also determined by the combined model, but in contrast, it can robustly determine $M0_{non}$, and the resulting maps show a similar distribution as in the reference measurement.

T1* maps (Figure 3 T1*) are noisy when determined by model (a) from unprepared data only. The maps determined by model (b) or (c) show reduced tissue contrast as usual for T1* in LL acquisitions [23–26].

T1 maps, as calculated from these fitting parameters, are shown in Figure 3 T1. The calculation of T1 depends on the accurate determination of T1*, Mss, and M0. Although the first is challenging in model (a), the last poses a problem in model (b). In model (c), equilibrium magnetization is determined by $M0_{non}$, allowing robust T1 calculation, as reflected in the detailed T1 map (Figure 3 T1).

The results of all 35 slices in the exemplary volunteer are shown in Figure 4. Reasonable T1 maps were acquired at all positions in the head and were independent of the chronological position of the slice in the measurement setup and, therefore, independent of its history of inversion pulses.

The efficiency of the inversion preparation is shown in Figure 5. Clearly, the relaxation process does not start at 100% inversion of equilibrium magnetization M0 in tissues with long relaxation time but in many other areas.

3.3 Phantom measurements

Figure 6 shows the T1 maps, as determined in the phantom measurements with and without a deliberate waiting time in between slices and, therefore, before all global inversion pulses. Corresponding T1 values from the ROI-based analysis are collected in Table 2. The parameter maps (Mss, M0, T1*, and T1), as determined by the three different fit models after the eighth iteration step are presented in Supplementary Figure S1.

As in the volunteer, maps calculated from the unprepared measurement (Nb. 2A) with model (a) are noisy, while robust

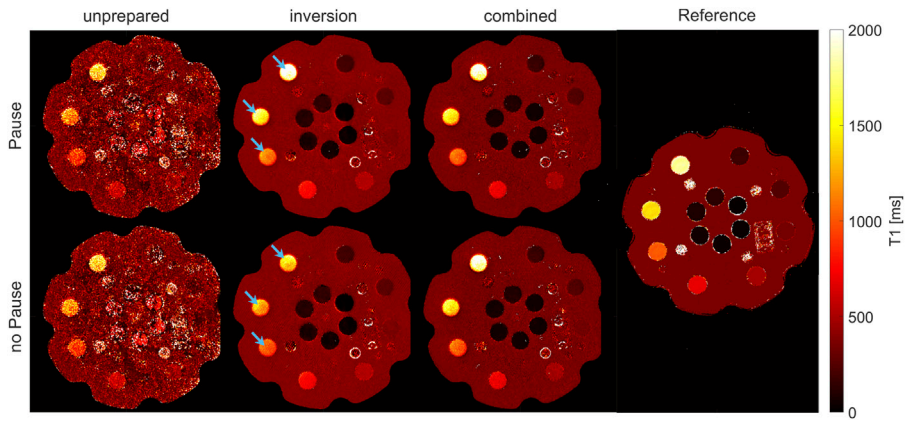

FIGURE 6
T1 maps of phantom measurement, with and without a waiting time to allow for free relaxation of magnetization. Maps calculated from the unprepared measurement by model (a) are noisy, while robust fitting was possible in the inversion-prepared case (model (b)) and with the proposed combined model (c). The major difference between measurements with and without waiting time emerges when regarding vials with long T1 values (indicated by arrows) and the inversion measurement only (model (b) for measurement part B). Measurements without waiting time result in a variable underestimation of absolute T1 values, which can be mitigated by either introducing the waiting time of 20 s or by using the combined model (c).

fitting was possible in the inversion-prepared case (Nb. 2B) with model (b) and with the proposed combined reconstruction (Nb. 2A and B) by model (c).

The statistical equivalence test for the combined reconstruction model (model (c)) revealed that the mean difference between T1 values from measurements with and without pause was below the equivalence bounds in all ROIs. Tests on the T1 values gained by model (b) from IR measurements showed that the mean difference was below the equivalent bounds in ROIs 5–8. T1 values in the ROIs 1–4, featuring the longest T1 values, cannot be considered equivalent within the given bounds. Tests for reconstruction model (a), unprepared measurement, revealed that the mean difference between T1 values from measurements with and without pause was outside the equivalence bounds in all ROIs, except for ROI 5.

Deviations of ROI-based mean T1 values between the combined fit model (c) and the TSE reference measurement were 0.4%, 2.0%, 2.5%, 2.0%, 1.0%, 1.2%, 1.2% and 1.6%, respectively, for the eight ROIs in the decreasing T1 order. Deviations to phantom manual values were 4.3%, 5.6%, 3.2%, 4.3%, 5.3%, 2.9%, 4.5%, 8.2%, respectively, for ROIs 1–8 (see also Supplementary Table S1).

3.4 Volunteer ensemble

T1 maps were calculated for all slices in all eight healthy volunteers and by all three reconstruction models. The T1 maps acquired from the TSE reference measurement and T1 maps calculated from the combined model (c) in a corresponding slice are shown in Supplementary Figure S2. Mean T1 and SD, as calculated by model (a), were 1,567 ± 139 ms in CSF, 967 ± 37 ms in the gray matter, and 529 ± 43 ms in the white matter. Mean T1 and SD, as calculated by model (b), were 2,278 ± 240 ms in CSF, 1,022 ± 44 ms in the gray matter, and 559 ± 84 ms in the white matter. For the combined model (c), mean T1 values and SD of 2,911 ± 240 ms in CSF, 1,198 ± 58 ms in the gray matter, and 557 ± 40 ms in the white matter were found. Separate results for each volunteer and area are collected in Table 3, relative deviations are collected in Supplementary Table S2. In general, model (a) underestimates T1 values and has high SD within the ROIs in each volunteer. Model (b) has lower SD within ROIs and shows underestimation of T1 values, especially in tissue with slow relaxation. The results from model (c) agree within the error bounds with the T1 times as determined by the reference measurement and are in good accordance with the literature values [27–29]. In addition, they feature low SD within each of the evaluated areas, indicating robust fitting.

4 Discussion

The proposed method aims to accomplish fast T1 mapping without the need for waiting times in between inversion pulses. Therefore, the combination of information from two parts of a measurement, with and without inversion, is proposed. To obtain T1 values from a LL acquisition, information on the apparent relaxation time T1* and on equilibrium magnetization M0 and steady-state magnetization Mss is necessary [9, 12]. Inversion-prepared measurements provide a large dynamic range for accurate model-based fitting of the relaxation process (and thus T1*), but without considering the necessary time for magnetization recovery, they cannot provide M0. In contrast, unprepared measurements can provide the equilibrium magnetization M0, but determination of T1* is challenging, due to the low dynamic range of the relaxation process. Information on M0 could, otherwise, be procured by considering long waiting times in between inversion pulses to allow full relaxation before each such pulse. The main advantage of the proposed approach is the omission of such waiting times, which significantly decreases acquisition time.

4.1 Sequence design

The design of the spiral trajectory was driven by two limitations. First, the desired resolution and second a limited readout length, in

TABLE 3 T1 values determined from ROIs placed in CSF, gray matter, and white matter for the three different fitting models.

Volunteer	T1 values (mean ± SD) [ms]											
ROI location	CSF				Gray matter				White matter			
Reconstruction model	a)	b)	c)	Reference	a)	b)	c)	Reference	a)	b)	c)	Reference
1	1,619 ± 60	2,549 ± 174	2,917 ± 55	2,387 ± 158	947 ± 34	969 ± 71	1,162 ± 57	989 ± 51	546 ± 33	664 ± 161	595 ± 62	571 ± 26
2	1,467 ± 55	1,751 ± 148	2,736 ± 88	2,434 ± 130	965 ± 33	1,019 ± 78	1,185 ± 55	1,065 ± 69	508 ± 18	547 ± 108	536 ± 25	527 ± 6
3	1,516 ± 118	2,199 ± 219	2,815 ± 104	2,723 ± 35	1,051 ± 39	1,094 ± 136	1,331 ± 63	1,129 ± 50	535 ± 20	596 ± 133	575 ± 27	547 ± 10
4	1,520 ± 69	2,228 ± 226	2,903 ± 59	2,908 ± 184	973 ± 21	979 ± 54	1,169 ± 22	1,122 ± 32	528 ± 25	597 ± 147	547 ± 30	539 ± 6
5	1,702 ± 103	2,306 ± 209	2,998 ± 5	3,130 ± 55	952 ± 25	1,008 ± 83	1,210 ± 34	1,176 ± 59	531 ± 16	478 ± 71	569 ± 24	546 ± 15
6	1,449 ± 98	2,406 ± 169	2,962 ± 35	2,699 ± 154	936 ± 24	1,022 ± 93	1,173 ± 35	1,241 ± 68	580 ± 21	484 ± 82	590 ± 30	565 ± 7
7	1,828 ± 93	2,413 ± 157	2,998 ± 6	2,781 ± 135	937 ± 25	1,007 ± 68	1,146 ± 28	1,063 ± 51	438 ± 19	659 ± 105	470 ± 19	519 ± 12
8	1,436 ± 102	2,369 ± 164	2,958 ± 49	2,677 ± 172	975 ± 29	1,079 ± 75	1,208 ± 51	1,122 ± 57	566 ± 23	445 ± 158	573 ± 27	560 ± 10
Mean	1,567 ± 139	2,278 ± 240	2,911 ± 92	2,717 ± 240	967 ± 37	1,022 ± 44	1,198 ± 58	1,113 ± 76	529 ± 43	559 ± 84	557 ± 40	547 ± 18

Model a): unprepared measurement only.
Model b): inversion-prepared measurement only.
Model c): combined fit of inversion-prepared and unprepared measurements.
Ref: TSE acquisition.

10.3389/fphy.2023.1299522

order to prevent strong effects of T2* relaxation along the readout. Furthermore, a variable density factor of two was chosen to optimize the acquisition of the k-space where most of the energy in an image is concentrated near the origin of the k-space [17]. Consecutive spiral arms were rotated in the spiral plane by a double golden angle. One advantage of golden angle sampling is the uniform coverage of the k-space along time. For optimized fitting of the exponential T1 relaxation, ideally, three full k-spaces are available at set points in time. For a fixed T1 value, the ideal position of these in time is known. For unknown multiple T1 values, golden angle sampling provides a good compromise. For center-out trajectory designs, the double golden angle (137.51° ≈ 360°–2*111.25°) features the same properties as the standard golden angle (111.25°) for full spoke acquisitions [30].

4.2 Reference measurement

Reference multi-inversion TSE measurements were performed in one slice in each volunteer and in the phantom. The settings were adjusted to minimize SAR in all acquisitions and to keep overall scan time within reasonable limits. A variable TR of TI+1,000 ms was chosen for each acquisition in order to realize equal relaxation time in between the last excitation for acquisition and the subsequent inversion pulse. A comprehensive overview of IR signal modeling can be found in MRI handbooks and online (e.g., [21, 31, 32]), including the signal dependencies on TR. In contrast, other measurement setups use constant long TR values (e.g., 5*T1) and include a long TR assumption in the fitting process.

4.3 Comparison of T1 measurements

In this study, T1 was determined by multi-inversion TSE measurements, as well as by inversion-prepared and unprepared spiral LL acquisitions in combination with three different fit models. Additionally, handbook values for the phantom are given.

Values given in the phantom handbook are generally lower than measured values (with the exception of ROI 2) independent of the acquisition type and fitting model. For our proposed fitting model (c), deviations are between 2.9% and 8.2%. Differences between the reference measurement and handbook values are in a similar range, between 0.7% and 7.1%. The main reason might be a difference in temperature as handbook values are stated at 20°C, whereas both reference and LL measurements were performed at 22°C–23°C. The temperature dependence of T1 is known to be between 1% and 3% per degree temperature change [33, 34]. Additionally, the reference measurement was performed as a TSE sequence, where the prolonged echo trains average signal around the set TI.

Reconstruction of LL acquisitions by model (a) has low mean T1 values and maps are very noisy, which is also reflected in the high SD within each ROI in the phantom and in all volunteers. Model (b) has lower SD within ROIs but also shows an underestimation of T1 values in comparison to reference measurements or other fitting models, especially in areas with slow relaxation (e.g., ROIs 1 and 2 in phantom or CSF and gray matter *in vivo*). Due to that, both are not considered a recommended technique.

T1 values, as determined by the proposed combined fit model (c), are in good agreement with reference values obtained by multiple inversion TSE measurements for phantom and *in vivo* cases. In *in vivo* measurements, T1 values deviate by 1.8% in the white matter, 7.1% in the gray matter, and 6.6% in CSF, and are in a range of literature values given for the evaluated tissues [27–29]. In the phantom, a T1 range of 150–2,000 ms is covered. Within these ROIs, T1 values deviate by no more than 2.5% from the reference measurement.

For very slow relaxing components (like CSF), inaccuracies can occur due to the short overall LL acquisition time per slice. Although main features of the relaxation process are covered within the 3 s acquisition, the magnetization level of very slow components has not necessarily reached the steady-state magnetization yet.

4.4 Model considerations

The main advantage of model-based reconstructions lies in the usage of prior knowledge. The MAP approach applied in this study combines prior knowledge about the relaxation behavior with the contrast information acquired using a spiral sampling scheme [10, 15]. The iterative reconstruction algorithm introduces more and more information about the relaxation process into the initial k-spaces, which originally contain only one spiral arm each. Although, for example, fingerprinting assumes that incoherent artifacts do not influence the fitting, MAP uses the information from other time points to consistently fill each k-space. Thus, over the iterations, the k-space of each point in time is filled and undersampling artifacts are eliminated. As a result, one complete image is generated for every time point TI of the relaxation process. Specifically, for the study presented here, a total of 400 full images spaced apart by TR were obtained.

The relaxation process from equilibrium magnetization (or inversion) into steady-state magnetization depends on T1* and can be fitted by corresponding exponential equations of T1* in inversion-prepared and unprepared measurements. The main advantage of the former is the large dynamic range of signal evolution, which benefits robust fitting, especially in accelerated methods. Unfortunately, to determine equilibrium magnetization M0, it also demands perfect inversion and, thus, a waiting time to allow free relaxation in between pulses. By combining the inversion acquisition with an unprepared measurement, M0 can be adequately recovered in a combined fit, as given by model (c). Thus, no waiting time is necessary. As an additional benefit, the combined fit model allows an investigation of the performance of the inversion pulse by comparing $M0_{non}$ and $M0_{IR}$.

The main advantage of such a model-based approach is the efficient use of information gathered in the shortest measurement times. Reconstructions can be performed on a fine temporal grid as no binning of phase-encoding steps is used, but each acquired spiral arm provides information on one time point along the relaxation curves. In combination with pixel-wise fitting, no spatial or temporal filtering is applied.

4.5 Inversion pulses

The presented study used a global inversion pulse to provide maximum insensitivity to B1 inhomogeneity [35]. The inversion was then followed by the acquisition of a single slice. Consequently, all slices are affected each time an inversion is played out. In other

words, all slices, but the first, have a history of multiple inversions. If no waiting time for free relaxation in between the inversion pulses is heeded, the inversion acts on an arbitrary magnetization vector and not on the equilibrium magnetization M0. Thus, the start point of the relaxation process shifts from –M0, as in a perfect inversion, to a different value, and M0 can no longer be determined. Loss of the M0 information subsequently prevents the necessary T1* correction for LL acquisitions [9, 10, 12].

An additional advantage of a global inversion is that it allows generalization of the method, for example, for segmented 3D [36–38] acquisitions or simultaneous multi-slice measurements [39].

4.6 Other T1 mapping techniques

T1 mapping is often included in multiparametric acquisition frameworks [40], like fingerprinting [41–44], the MR multitasking framework [45, 46], or SyMRI [47, 48], which can achieve clinically reasonable scan times below 10 min. Although the additional information gained might be a benefit, the faster acquisition in our proposed method is favorable for dedicated T1 mapping applications.

Another common technique to determine T1 is the variable flip angle method [49]. Several approaches were presented, which can acquire whole-head T1 maps under 10 min [3, 6, 50]. Although they are very fast, they require exact knowledge of the flip angle. Additionally, problems with the B1 inhomogeneity and slice profile may arise, especially for thin slices and fast pulses [51]. T1 values determined by the variable flip angle method are also dependent on the RF spoiling procedure [52].

In techniques based on IR-LL methods, T1 can be calculated from T1* either by using the acquisition parameters repetition time TR and the local flip angle or from the measured quantities, T1*, M0, and Mss [9, 12]. By choosing optimal settings for a given experiment and incorporating flip angle information, a bias from imperfect inversion can be minimized. Shin et al. [11] performed whole brain T1 mapping in approximately 4 min with a resolution of $1 \times 1 \times 4\ mm^3$. Within an optimized setup, an average error of T1 of 1.2% was achieved, without requiring a specific waiting time in between inversion pulses. In comparison to our approach, this study achieved comparable measurement times, albeit slightly lower in-plane resolution and volume coverage.

Other techniques based on IR-LL methods mostly rely on segmented acquisitions with multiple inversions, especially for 3D acquisitions, which require a high number of readout lines. For example, Henderson et al. [36] performed whole-head T1 mapping with a resolution of $1.4 \times 1.4 \times 6\ mm^3$ in 8 min. The volume was divided into 128 segments, each starting with an inversion pulse and a delay time of 2 s in between. Similar measurement times were achieved by Maier et al. [38] for 1-mm isotropic resolution by dividing the k-space into 60 segments. Building on that, interleaved slab-selective inversion preparations were proposed. The necessary delay times can there be used to acquire different slabs. For example, Li et al. [37] acquired whole-head T1 maps with 1-mm isotropic resolution within 4 min 21 s by separating the acquisition into six slabs.

The introduction of saturation pulses prior to the global inversion pulse of each segment can shorten necessary delay times. Such a setup was, for example, implemented by Deichmann et al. [53] to minimize waiting times from 15 s to 3 s in a segmented acquisition. The so-called TAPIR sequence [7, 54] uses a saturation pulse and a delay of 2–2.5 s before the inversion pulse. Similar to our technique, the relaxation process after the inversion does not start from inverted equilibrium magnetization. Although in TAPIR, the additional preparation step allows control over this start point, our approach assumes a random start point. The necessary information on equilibrium magnetization is then gained either by modeling (TAPIR) or by an additional part in the measurement (as proposed here). A 3D extension of the TAPIR algorithm was proposed by Claeser et al. [55] who acquired the whole head in five segments with a resolution of $0.94 \times 0.94 \times 2.5\ mm^3$ in 3 min 25 s. This method can achieve acquisition times similar to our proposed method.

The shortest scan times are generally achieved by single-shot, inversion-prepared LL techniques, with high undersampling rates in combination with a sophisticated reconstruction algorithm. Feng et al. [13] acquired 32 slices in the human head with a resolution of $1.25 \times 1.25 \times 3\ mm^3$ in 2 min 32 s and with a resolution of $0.875 \times 0.875 \times 3\ mm^3$ in 2 min 49 s. In addition, Müller et al. [56] achieved a resolution of $0.5 \times 0.5 \times 4\ mm^3$ or $0.5 \times 0.5 \times 3\ mm^3$ in 1 min 55 s and 2 min 36 s, respectively. Both methods provide in-plane resolutions similar to our proposed method ($0.8 \times 0.8 \times 5\ mm^3$). Measurement times are even shorter, albeit the total volume covered is also smaller ($280 \times 280 \times 96\ mm^3$ [13] and $192 \times 192 \times 115/117\ mm^3$ [56] vs $410 \times 410 \times 175\ mm^3$ in our method). Wang et al. [39] combined such an approach with a simultaneous multi-slice acquisition, thus allowing even further acceleration of whole-head acquisitions. A total of five stacks, comprising five slices each, were acquired in approximately 1 min. Out of the total time, 4 s each were spent on the acquisition of the five stacks, and in between those, a 10-s waiting period was heeded. Considering that, an evaluation of the combination of our proposed method without waiting times, with a simultaneous multi-slice acquisition, is a very interesting direction for future work.

Another recent study also aims at eliminating the waiting time in between inversion pulses, by using an AI-based reconstruction method to gain quantitative T1 values [57]. In comparison to our method, the main benefit is the extremely short reconstruction time once training of the data is accomplished. Nevertheless, our method does not require a matching training dataset and does not rely on specific acquisition parameters.

4.7 Measurement time

In this study, the whole brain was covered by acquiring 35 slices. As the acquisition of each slice only took 3 s, total measurement time for both inversion and unprepared measurement together resulted in 210 s. To the best of our knowledge, only few other techniques can provide T1 mapping in the whole head at submillimeter resolution in such short acquisition times [13, 39, 55, 56].

If the traditional waiting period of 5*T1 (e.g., approx. 1.2 s in the gray matter) after each inversion pulse was observed, total measurement time for an inversion prepared acquisition would have been 309 s, assuming a similar sequence setup. Over this reference, the proposed algorithm presents an acceleration, which is even more pronounced if longer T1 values are considered (e.g., in

CSF). In future implementations, further acceleration by shortening the unprepared acquisition might be possible and should be evaluated.

In the phantom, two sets of measurements were performed, with and without the waiting time, to evaluate the influence of the omission of waiting time for free relaxation on T1 values. Statistical equivalence testing revealed that the mean difference of T1 values, acquired from the combined reconstruction model (c), was below the equivalence bounds for the whole range of T1 values covered by the phantom (175–1900 ms). In contrast, the results from IR measurements without waiting time are not equivalent to the results from measurements with waiting time for free relaxation. In conclusion, by applying the combined reconstruction model, measurement time can be reduced without compromising T1 mapping.

4.8 Limitations

Common limitations of iterative reconstruction procedures are long reconstruction times and a high computational load. Although, here, the introduction of the step size adjustment into the reconstruction pipeline could significantly reduce the number of steps before convergence (approximately by a factor of 50), the offline implementation and overall time requirements do not yet allow an easy introduction into clinical practice. Further acceleration could be gained in future by using time-optimized fitting procedures, for example, by a reduced dimension nonlinear least-square fitting, as proposed in Barral et. al [58].

Furthermore, our approach is sensitive to model mismatches, which can occur, for example, due to motion, inflow, slice profile, partial volume effects, or multiple T1 components. Here, a rather simple straightforward exponential behavior is used as a model, which does not consider any such effects but, on the other hand, is very robust. Nevertheless, the introduction of such aspects into the model is possible [59].

The number of iterations and the setup of MAP steps and step size adjustments were empirically determined. The optimal settings might differ for different acquisition parameters. Then, other and maybe more flexible stop criteria could additionally be evaluated.

5 Conclusion

The proposed model of a combined fit of an inversion-prepared and unprepared measurement allows for robust fast T1 mapping, even in cases of insufficient magnetization relaxation before consecutive inversion pulses. It can thus render long waiting times in between inversion pulses redundant.

Data availability statement

The raw data supporting the conclusions of this article will be made available by the authors, without undue reservation. The reconstruction code developed for this study can be found here: https://github.com/expRad/nowaitinversion.

Ethics statement

The studies involving humans were approved by Klinische Ethikkomitee (KEK), University Hospital Würzburg. The studies were conducted in accordance with the local legislation and institutional requirements. The participants provided their written informed consent to participate in this study.

Author contributions

JB: conceptualization, data curation, formal analysis, investigation, methodology, software, validation, and writing–original draft. JK: formal analysis, investigation, methodology, software, writing–original draft, and writing–review and editing. OS: data curation, software, and writing–review and editing. AW: data curation, investigation, resources, and writing–review and editing. HK: conceptualization, data curation, methodology, project administration, resources, supervision, and writing–review and editing. AS: conceptualization, formal analysis, investigation, methodology, project administration, resources, software, supervision, validation, visualization, writing–original draft, and writing–review and editing.

Funding

The author(s) declare financial support was received for the research, authorship, and/or publication of this article. A PhD scholarship was granted to JB by Brazilian agency CAPES (program: DOUTORADO-CAPES-DAAD-CNPQ - Call No. 15/2017; process 88887.161448/2017-00). Open access publication was supported by the University and State Library of Saxony-Anhalt.

Conflict of interest

The authors declare that the research was conducted in the absence of any commercial or financial relationships that could be construed as a potential conflict of interest.

Publisher's note

Supplementary material

The Supplementary Material for this article can be found online at: https://www.frontiersin.org/articles/10.3389/fphy.2023.1299522/full#supplementary-material

References

1. Kim PK, Hong YJ, Im DJ, Suh YJ, Park CH, Kim JY, et al. Myocardial T1 and T2 mapping: techniques and clinical applications. *Korean J Radiol* (2017) 18:113–31. doi:10.3348/kjr.2017.18.1.113

2. Taylor AJ, Salerno M, Dharmakumar R, Jerosch-Herold M. T1 mapping: basic techniques and clinical applications. *JACC: Cardiovasc Imaging* (2016) 9:67–81. doi:10.1016/j.jcmg.2015.11.005

3. Eminian S, Hajdu SD, Meuli RA, Maeder P, Hagmann P. Rapid high resolution T1 mapping as a marker of brain development: normative ranges in key regions of interest. *PLoS One* (2018) 13:e0198250. doi:10.1371/journal.pone.0198250

4. Vrenken H, Geurts JJG, Knol DL, van Dijk LN, Dattola V, Jasperse B, et al. Whole-brain T1 mapping in multiple sclerosis: global changes of normal-appearing gray and white matter. *Radiology* (2006) 240:811–20. doi:10.1148/radiol.2403050569

5. Radunski UK, Lund GK, Stehning C, Schnackenburg B, Bohnen S, Adam G, et al. CMR in patients with severe myocarditis: diagnostic value of quantitative tissue markers including extracellular volume imaging. *JACC Cardiovasc Imaging* (2014) 7:667–75. doi:10.1016/j.jcmg.2014.02.005

6. Deoni SCL, Peters TM, Rutt BK. High-resolution T1 and T2 mapping of the brain in a clinically acceptable time with DESPOT1 and DESPOT2. *Magn Reson Med* (2005) 53:237–41. doi:10.1002/mrm.20314

7. Steinhoff S, Zaitsev M, Zilles K, Shah NJ. Fast T(1) mapping with volume coverage. *Magn Reson Med* (2001) 46:131–40. doi:10.1002/mrm.1168

8. Crawley AP, Henkelman RM. A comparison of one-shot and recovery methods in T1 imaging. *Magn Reson Med* (1988) 7:23–34. doi:10.1002/mrm.1910070104

9. Look DC, Locker DR. Time saving in measurement of NMR and EPR relaxation times. *Rev Scientific Instr* (2003) 41:250–1. doi:10.1063/1.1684482

10. Tran-Gia J, Wech T, Bley T, Köstler H. Model-based acceleration of look-locker T1 mapping. *PLOS ONE* (2015) 10:e0122611. doi:10.1371/journal.pone.0122611

11. Shin W, Gu H, Yang Y. Fast high-resolution T1 mapping using inversion-recovery look-locker echo-planar imaging at steady state: optimization for accuracy and reliability. *Magn Reson Med* (2009) 61:899–906. doi:10.1002/mrm.21836

12. Deichmann R. Fast high-resolution T1 mapping of the human brain. *Magn Reson Med* (2005) 54:20–7. doi:10.1002/mrm.20552

13. Feng L, Liu F, Soultanidis G, Liu C, Benkert T, Block KT, et al. Magnetization-prepared GRASP MRI for rapid 3D T1 mapping and fat/water-separated T1 mapping. *Magn Reson Med* (2021) 86:97–114. doi:10.1002/mrm.28679

14. Wang X, Roeloffs V, Merboldt KD, Voit D, Schätz S, Frahm J. Single-shot multi-slice T1 mapping at high spatial resolution – inversion-recovery FLASH with radial undersampling and iterative reconstruction. *Open Med Imaging J* (2015) 9:1–8. doi:10.2174/1874347101509010001

15. Tran-Gia J, Stäb D, Wech T, Hahn D, Köstler H. Model-based Acceleration of Parameter mapping (MAP) for saturation prepared radially acquired data. *Magn Reson Med* (2013) 70:1524–34. doi:10.1002/mrm.24600

16. Hargreaves Brian A. Variable-density spiral design functions (2023). Available at: http://mrsrl.stanford.edu/~brian/vdspiral/ (Accessed October 24, 2023).

17. Lee JH, Hargreaves BA, Hu BS, Nishimura DG. Fast 3D imaging using variable-density spiral trajectories with applications to limb perfusion. *Magn Reson Med* (2003) 50:1276–85. doi:10.1002/mrm.10644

18. Addy NO, Wu HH, Nishimura DG. Simple method for MR gradient system characterization and k-space trajectory estimation. *Magn Reson Med* (2012) 68:120–9. doi:10.1002/mrm.23217

19. Stich M, Wech T, Slawig A, Ringler R, Dewdney A, Greiser A, et al. Gradient waveform pre-emphasis based on the gradient system transfer function. *Magn Reson Med* (2018) 80:1521–32. doi:10.1002/mrm.27147

20. Walsh DO, Gmitro AF, Marcellin MW. Adaptive reconstruction of phased array MR imagery. *Magn Reson Med* (2000) 43:682–90. doi:10.1002/(SICI)1522-2594(200005)43:5<682::AID-MRM10>3.0.CO;2-G

21. Bernstein MA, King KF, Zhou XJ. *Handbook of MRI pulse sequences*. Burlington, MA: Elsevier Academic Press (2004).

22. Walker E, Nowacki AS. Understanding equivalence and noninferiority testing. *J Gen Intern Med* (2011) 26:192–6. doi:10.1007/s11606-010-1513-8

23. Stikov N, Boudreau M, Levesque IR, Tardif CL, Barral JK, Pike GB. On the accuracy of T1 mapping: searching for common ground. *Magn Reson Med* (2015) 73:514–22. doi:10.1002/mrm.25135

24. Scheffler K, Hennig J. T1 quantification with inversion recovery TrueFISP. *Magn Reson Med* (2001) 45:720–3. doi:10.1002/mrm.1097

25. Kellman P, Hansen MS. T1-mapping in the heart: accuracy and precision. *J Cardiovasc Magn Reson* (2014) 16:2. doi:10.1186/1532-429X-16-2

26. Slavin GS. On the use of the "look-locker correction" for calculating T1 values from MOLLI. *J Cardiovasc Magn Reson* (2014) 16:P55. doi:10.1186/1532-429X-16-S1-P55

27. Wright PJ, Mougin OE, Totman JJ, Peters AM, Brookes MJ, Coxon R, et al. Water proton T1 measurements in brain tissue at 7, 3, and 1.5T using IR-EPI, IR-TSE, and MPRAGE: results and optimization. *Magn Reson Mater Phy* (2008) 21:121–30. doi:10.1007/s10334-008-0104-8

28. Dieringer MA, Deimling M, Santoro D, Wuerfel J, Madai VI, Sobesky J, et al. Rapid parametric mapping of the longitudinal relaxation time T1 using two-dimensional variable flip angle magnetic resonance imaging at 1.5 tesla, 3 tesla, and 7 tesla. *PLoS One* (2014) 9:e91318. doi:10.1371/journal.pone.0091318

29. Morel B, Piredda GF, Cottier J-P, Tauber C, Destrieux C, Hilbert T, et al. Normal volumetric and T1 relaxation time values at 1.5 T in segmented pediatric brain MRI using a MP2RAGE acquisition. *Eur Radiol* (2021) 31:1505–16. doi:10.1007/s00330-020-07194-w

30. Feng L. Golden-angle radial MRI: basics, advances, and applications. *J Magn Reson Imaging* (2022) 56:45–62. doi:10.1002/jmri.28187

31. Hornak JP. The basics of MRI (2023). Available at: https://www.cis.rit.edu/htbooks/mri/inside.htm (Accessed August 8, 2023).

32. qMRLab. Signal modelling (2023). Available at: http://qMRLab.github.io/t1_book/01/ir_blog/IR_SignalModelling.html (Accessed November 9, 2023).

33. Rieke V, Pauly KB. MR thermometry. *J Magn Reson Imaging* (2008) 27:376–90. doi:10.1002/jmri.21265

34. Nelson TR, Tung SM. Temperature dependence of proton relaxation times *in vitro*. *Magn Reson Imaging* (1987) 5:189–99. doi:10.1016/0730-725x(87)90020-8

35. Kingsley PB, Ogg RJ, Reddick WE, Steen RG. Correction of errors caused by imperfect inversion pulses in MR imaging measurement of T1 relaxation times. *Magn Reson Imaging* (1998) 16:1049–55. doi:10.1016/s0730-725x(98)00112-x

36. Henderson E, McKinnon G, Lee T-Y, Rutt BK. A fast 3D Look-Locker method for volumetric T1 mapping. *Magn Reson Imaging* (1999) 17:1163–71. doi:10.1016/S0730-725X(99)00025-9

37. Li Z, Fu Z, Keerthivasan M, Bilgin A, Johnson K, Galons J-P, et al. Rapid high-resolution volumetric T1 mapping using a highly accelerated stack-of-stars Look Locker technique. *Magn Reson Imaging* (2021) 79:28–37. doi:10.1016/j.mri.2021.03.003

38. Maier O, Schoormans J, Schloegl M, Strijkers GJ, Lesch A, Benkert T, et al. Rapid T1 quantification from high resolution 3D data with model-based reconstruction. *Magn Reson Med* (2019) 81:2072–89. doi:10.1002/mrm.27502

39. Wang X, Rosenzweig S, Scholand N, Holme HCM, Uecker M. Model-based reconstruction for simultaneous multi-slice mapping using single-shot inversion-recovery radial FLASH. *Magn Reson Med* (2021) 85:1258–71. doi:10.1002/mrm.28497

40. Jara H, Sakai O, Farrher E, Oros-Peusquens A-M, Shah NJ, Alsop DC, et al. Primary multiparametric quantitative brain MRI: state-of-the-art relaxometric and proton density mapping techniques. *Radiology* (2022) 305:5–18. doi:10.1148/radiol.211519

41. Chen Y, Fang Z, Hung S-C, Chang W-T, Shen D, Lin W. High-resolution 3D MR Fingerprinting using parallel imaging and deep learning. *NeuroImage* (2020) 206:116329. doi:10.1016/j.neuroimage.2019.116329

42. Ma D, Jiang Y, Chen Y, McGivney D, Mehta B, Gulani V, et al. Fast 3D magnetic resonance fingerprinting for a whole-brain coverage. *Magn Reson Med* (2018) 79:2190–7. doi:10.1002/mrm.26886

43. Cao X, Ye H, Liao C, Li Q, He H, Zhong J. Fast 3D brain MR fingerprinting based on multi-axis spiral projection trajectory. *Magn Reson Med* (2019) 82:289–301. doi:10.1002/mrm.27726

44. Buonincontri G, Kurzawski JW, Kaggie JD, Matys T, Gallagher FA, Cencini M, et al. Three dimensional MRF obtains highly repeatable and reproducible multi-parametric estimations in the healthy human brain at 1.5T and 3T. *NeuroImage* (2021) 226:117573. doi:10.1016/j.neuroimage.2020.117573

45. Ma S, Nguyen CT, Han F, Wang N, Deng Z, Binesh N, et al. Three-dimensional simultaneous brain T1, T2, and ADC mapping with MR Multitasking. *Magn Reson Med* (2020) 84:72–88. doi:10.1002/mrm.28092

46. Cao T, Ma S, Wang N, Gharabaghi S, Xie Y, Fan Z, et al. Three-dimensional simultaneous brain mapping of T1, T2, and magnetic susceptibility with MR Multitasking. *Magn Reson Med* (2022) 87:1375–89. doi:10.1002/mrm.29059

47. Hagiwara A, Warntjes M, Hori M, Andica C, Nakazawa M, Kumamaru KK, et al. SyMRI of the brain. *Invest Radiol* (2017) 52:647–57. doi:10.1097/RLI.0000000000000365

48. Warntjes Jb. m., Leinhard OD, West J, Lundberg P. Rapid magnetic resonance quantification on the brain: optimization for clinical usage. *Magn Reson Med* (2008) 60:320–9. doi:10.1002/mrm.21635

49. Bottomley PA, Ouwerkerk R. The dual-angle method for fast, sensitive T1 measurement *in vivo* with low-angle adiabatic pulses. *J Magn Reson Ser B* (1994) 104:159–67. doi:10.1006/jmrb.1994.1070

50. Conte GM, Altabella L, Castellano A, Cuccarini V, Bizzi A, Grimaldi M, et al. Comparison of T1 mapping and fixed T1 method for dynamic contrast-enhanced MRI perfusion in brain gliomas. *Eur Radiol* (2019) 29:3467–79. doi:10.1007/s00330-019-06122-x

51. Boudreau M, Tardif CL, Stikov N, Sled JG, Lee W, Pike GB. B1 mapping for bias-correction in quantitative T1 imaging of the brain at 3T using standard pulse sequences. *J Magn Reson Imaging* (2017) 46:1673–82. doi:10.1002/jmri.25692

52. Zur Y, Wood ML, Neuringer LJ. Spoiling of transverse magnetization in steady-state sequences. *Magn Reson Med* (1991) 21:251–63. doi:10.1002/mrm.1910210210

53. Deichmann R, Hahn D, Haase A. Fast T1 mapping on a whole-body scanner. *Magn Reson Med* (1999) 42:206–9. doi:10.1002/(SICI)1522-2594(199907)42:1<206::AID-MRM28>3.0.CO;2-Q

54. Shah NJ, Zaitsev M, Steinhoff S, Zilles K. A new method for fast multislice T1 mapping. *NeuroImage* (2001) 14:1175–85. doi:10.1006/nimg.2001.0886

55. Claeser R, Zimmermann M, Shah NJ. Sub-millimeter T1 mapping of rapidly relaxing compartments with gradient delay corrected spiral TAPIR and compressed sensing at 3T. *Magn Reson Med* (2019) 82:1288–300. doi:10.1002/mrm.27797

56. Müller SJ, Khadhraoui E, Voit D, Riedel CH, Frahm J, Ernst M. First clinical application of a novel T1 mapping of the whole brain. *Neuroradiol J* (2022) 35:684–91. doi:10.1177/19714009221084244

57. Pei H, Xia D, Xu X, Yang Y, Wang Y, Liu F, et al. Rapid 3D T1 mapping using deep learning-assisted Look-Locker inversion recovery MRI. *Magn Reson Med* (2023) 90:569–82. doi:10.1002/mrm.29672

58. Barral JK, Gudmundson E, Stikov N, Etezadi-Amoli M, Stoica P, Nishimura DG. A robust methodology for *in vivo* T1 mapping. *Magn Reson Med* (2010) 64:1057–67. doi:10.1002/mrm.22497

59. Tran-Gia J, Wech T, Hahn D, Bley TA, Köstler H. Consideration of slice profiles in inversion recovery Look-Locker relaxation parameter mapping. *Magn Reson Imaging* (2014) 32:1021–30. doi:10.1016/j.mri.2014.05.012

frontiers | Frontiers in Physics

TYPE Original Research
PUBLISHED 04 April 2024
DOI 10.3389/fphy.2024.1378521

OPEN ACCESS

EDITED BY
Ciprian Catana,
Massachusetts General Hospital and Harvard Medical School, United States

REVIEWED BY
Charalampos Tsoumpas,
University Medical Center Groningen, Netherlands
Bo Zhou,
Yale University, United States

*CORRESPONDENCE
Daria Ferrara,
daria.ferrara@meduniwien.ac.at

RECEIVED 29 January 2024
ACCEPTED 18 March 2024
PUBLISHED 04 April 2024

CITATION
Ferrara D, Shiyam Sundar LK, Chalampalakis Z, Geist BK, Gompelmann D, Gutschmayer S, Hacker M, Kertész H, Kluge K, Idzko M, Langsteger W, Yu J, Rausch I and Beyer T (2024), Low-dose and standard-dose whole-body [18F]FDG-PET/CT imaging: implications for healthy controls and lung cancer patients. *Front. Phys.* 12:1378521.
doi: 10.3389/fphy.2024.1378521

Low-dose and standard-dose whole-body [18F]FDG-PET/CT imaging: implications for healthy controls and lung cancer patients

Daria Ferrara[1]*, Lalith Kumar Shiyam Sundar[1], Zacharias Chalampalakis[1], Barbara Katharina Geist[2], Daniela Gompelmann[3], Sebastian Gutschmayer[1], Marcus Hacker[2], Hunor Kertész[4], Kilian Kluge[2], Marco Idzko[3], Werner Langsteger[2], Josef Yu[2], Ivo Rausch[1] and Thomas Beyer[1]

[1]QIMP Team, Medical University of Vienna, Vienna, Austria, [2]Department of Biomedical Imaging and Image-Guided Therapy, Division of Nuclear Medicine, Medical University of Vienna, Vienna, Austria, [3]Division of Pulmonology, Department of Internal Medicine II, Medical University Vienna, Vienna, Austria, [4]Image X Institute, Faculty of Medicine and Health, The University of Sidney, Sidney, NSW, Australia

Aim: High-sensitivity hybrid positron emission tomography (PET) imaging using advanced whole-body (WB) or total-body PET/computed tomography (CT) systems permits reducing injected tracer activity while preserving diagnostic quality. Such approaches are promising for healthy control studies or exploring inter-organ communication in systemic diseases. This study assessed test/retest variations in the fluoro-2-deoxy-D-glucose (FDG) uptake in key organs from low-dose (LD) and standard-dose (STD) [18F]FDG-PET/CT imaging protocols in healthy controls and lung cancer patients.

Methods: A total of 19 healthy controls (19–62 years, 46–104 kg, 10 M/9 F) and 7 lung cancer patients (47–77 years, 50–88 kg, 4 M/3 F) underwent [18F]FDG-PET/CT imaging. All subjects were first injected ("test," LD) with 28 ± 2 MBq FDG and underwent a dynamic (0–67 min post-injection) WB imaging protocol with LD-CT. Then, 90 min post-LD injection, the subjects were repositioned and injected with 275 ± 16 MBq FDG ("retest," STD). Second LD-CT and STD-CT scans were acquired for healthy controls and patients, respectively. Static images (55–67 min post-injection) were considered for subsequent analysis. The CT images were used to automatically segment the target volumes of interest. Standardized uptake values normalized to the body weight (SUV_{BW}) were extracted for each volume of interest. The mean SUV_{BW} were compared for both LD/STD conditions with paired t-tests. In patients, FDG-avid lesions were manually delineated on LD and STD static images. Effective dose levels were estimated from both the CT and PET acquisitions.

Results: Organ-based mean SUV_{BW} were similar between the LD and STD (mean %difference ≤5%) in both healthy controls and cancer patients, except in the heart. Intra-control test/retest variability was significant in the brain, heart, and skeletal muscle ($p < 0.05$). While 17 lesions were delineated on the STD images of the patients, only 10/17 lesions were identified on the LD images due to increased image noise. Lesion-based mean SUV_{BW} were similar between LD and STD

acquisitions (p = 0.49, %difference = 10%). In patients, the effective doses were (1.9 ± 0.2) mSv (LD-CT), (16.6 ± 5.4) mSv (STD-CT), (0.5 ± 0.1) mSv (LD-PET), and (4.6 ± 0.3) mSv (STD-PET).

Conclusion: LD and STD [18F]FDG injections in healthy controls and lung cancer patients yielded comparable mean SUV_{BW}, except in the heart. Dose levels may be reduced for [18F]FDG-PET imaging without a loss in mean SUV_{BW} accuracy, promoting LD-PET/CT protocols for studying multi-organ metabolic patterns. In oncology patients, this approach may be hindered by a lower diagnostic quality in the presence of significant noise.

KEYWORDS

PET/CT, low-activity imaging, radiation exposure, [18F]fluoro-2-deoxy-D-glucose, standardized uptake values

Introduction

Since its inception in the late 1990s [1], hybrid positron emission tomography (PET) and computed tomography (CT), also referred to as dual-modality PET/CT, has become a well-established non-invasive imaging modality for a wide variety of clinical applications. In many oncology indications, PET/CT has been accepted as a standard imaging modality in patient management, providing both metabolic and anatomic information for diagnosis and treatment planning [2–4].

The technological innovations of recent years, culminating in the introduction of total-body (TB) PET/CT systems [5], have brought continuous improvements in system performance and sensitivity [6, 7] and consequently expanded PET/CT imaging to new research areas. For instance, the advent of extended axial field-of-view PET systems allows the simultaneous and quantitative imaging of multiple distant organs, thereby providing the possibility to investigate multi-organ metabolic information and detect potential anomalies from normal metabolic activity patterns [8, 9]. To visualize and quantify metabolic aberrations, it is necessary to establish a normative, organ- or voxel-wise, database based on the images derived from healthy controls. However, to create such a database, a significant amount of data must be collected first in light of the public concerns over ionizing radiation. Radiation exposure from PET/CT imaging, as measured by the effective dose to a subject, scales with the amount of injected PET tracer activity. The new PET/CT systems, with their increased sensitivity, allow for further reduction in injected tracer activity and, subsequently, reduction in radiation exposure [7, 10, 11].

Prior studies of low-dose PET/CT imaging have indicated potential for their adoption in clinical routine. For example, Calderón et al. demonstrated that decreasing levels of injected [18F]fluoro-2-deoxy-D-glucose (FDG) activity ranging from 3.0 MBq/kg to 0.125 MBq/kg affected the mean standardized uptake values (SUVs) by only 8% or less [11]. Kertész et al. investigated the effects of reducing the injected [18F]FDG activity in pediatric oncology patients undergoing whole-body PET/CT examinations and showed that the injected activity levels can be reduced to 75% of the original dose without compromising the PET image quality [12]. Prieto et al. evaluated the impact of a 30% FDG dose reduction on image quality, resulting in steady clinical reading confidence despite a slight reduction in image quality [13]. Taken together, these studies either focused solely on deriving low-count PET images from standard activity images via list-mode resampling rather than using actual low-activity injections or they relied on the improved sensitivity of TB-PET systems, which are not yet widely available in medical facilities. Adding to the above research, Tan et al. compared ultra-low-dose and half-dose [18F]FDG-TB-PET/CT imaging in a test–retest setup within a 72-h time frame [14]. However, this study focused primarily on parametric imaging and assessed SUVs exclusively in the liver, thereby neglecting other organs and the continuous predominance of semi-quantitative SUV evaluations over kinetic modeling in clinical routine [15].

Our study, preceding the installation of a TB-PET/CT system, assesses the impact of reduced PET tracer doses on quantitative organ-based SUV_{BW} measurements, especially in healthy controls. Focusing on [18F]FDG imaging, we seek to understand the effects of lowering injected tracer doses on healthy organ evaluations and

TABLE 1 Demographics of study participants.

Healthy controls	
n° participants	19
Median age (years, range)	32 (19–62)
Average age (years, mean ± SD)	35 ± 14
Height (cm, mean ± SD)	175 ± 12
Weight (kg, mean ± SD)	76 ± 17
BMI (kg/m^2, mean ± SD)	25 ± 5
Injected low dose (MBq, mean ± SD, “test”)	28 ± 2
Injected standard dose (MBq, mean ± SD, “retest”)	279 ± 14
Lung cancer patients	
n° participants	7
Median age (years, range)	65 (47–77)
Average age (years, mean ± SD)	62 ± 13
Height (cm, mean ± SD)	165 ± 11
Weight (kg, mean ± SD)	71 ± 14
BMI (kg/m^2, mean ± SD)	26 ± 4
Injected low dose (MBq, mean ± SD, “test”)	29 ± 3
Injected standard dose (MBq, mean ± SD, “retest”)	271 ± 17

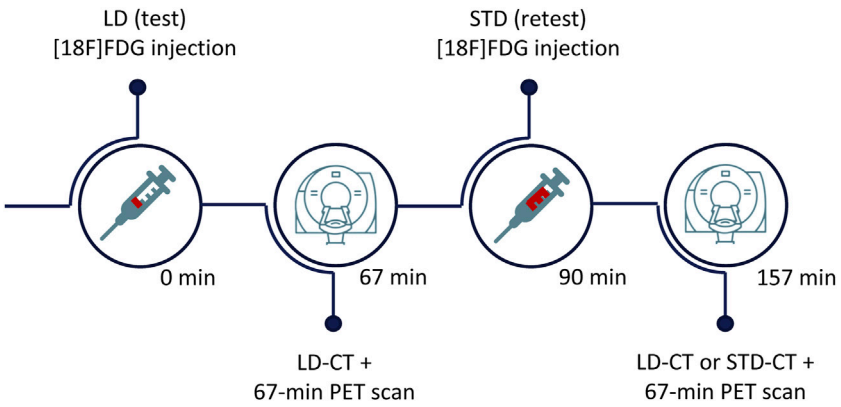

FIGURE 1
Visual description of the study protocol.

disease-related metabolic changes. Using serial [18F]FDG injections (test/retest), we examined intra-subject variabilities over 90 min and compared lesion uptake variations between low-dose (LD) and standard-dose (STD) PET scans in lung cancer patients. The goal was to create a standard organ-SUV_{BW} database for analyzing metabolic discrepancies due to diseases [9] and reduce radiation concerns from PET/CT scans.

Materials and methods

Participants

The study included 19 healthy controls (19–62 years, 46–104 kg, 10 M/9 F) and 7 lung cancer patients (47–77 years, 50–88 kg, 4 M/3 F). Here, "healthy" means the clinical absence of known systemic diseases. All data were acquired according to the Declaration of Helsinki (EK1907/2020) between July and December 2021. Written informed consent was obtained from all the subjects before examinations. The details of the participants' demographics are summarized in Table 1. Statistics are reported as the mean ± standard deviation (SD).

Imaging protocol

All participants were scanned on a Siemens Biograph Vision 600 PET/CT system with an axial field-of-view of 26.3 cm and time-of-flight (TOF) resolution of 220 ps [16]. The participants were asked to fast for 6 h before the examinations and were scanned in supine position with their arms down. Each subject first underwent a 67-min PET acquisition following an LD intravenous injection of [18F]FDG (28 ± 2 MBq, 10% of the National Diagnostic Reference Levels of Austria [17]). After completing the acquisition, the subjects were given a 20-min break to empty their bladder.

Then, 90 min post-LD injection, the subjects were repositioned and injected with a bolus of [18F]FDG (275 ± 16 MBq), followed by a 67-min acquisition (STD) (Figure 1). The first 6 min of both PET protocols were performed with the patient fixed to the table to cover the chest region, followed by 14 whole-body (WB) sweeps under continuous table motion, adding up to a total emission scan time of 61 min.

A CT scan (120 kVp, 35 mAs ref, CareDose tube current modulation enabled) was performed for the CT-based attenuation correction prior to each PET scan. Healthy controls were scanned using LD-CT (average dose length product, DLP = 133 ± 19 mGy*cm) for both the test (LD-PET) and retest (STD-PET). Lung cancer patients underwent an LD-CT (DLP = 121 ± 8 mGy*cm) for the test (LD-PET) and then STD-CT for standard clinical care (DLP = 1,144 ± 377 mGy*cm) in the retest scan (STD-PET). In the STD-CT protocol, dual-phase (venous and arterial phases) contrast-enhanced CT, including the entire body in the field-of-view, was used for both clinical reporting and attenuation correction.

PET images were reconstructed with a matrix size of 220 × 220 × 803 and a voxel size of 3.3 × 3.3 × 2 mm^3, using 3D PSF + TOF OSEM (4 iterations and 5 subsets) with all corrections applied and a 3-mm full-width at half-maximum (FWHM) Gaussian post-reconstruction filter.

Quantification of organs

In all acquisitions, LD-CT was used to automatically delineate different target volumes using the AI-based segmentation tool MOOSE [18]. The resulting segmentations included abdominal organs, bones, muscles, fat, and heart subregions. A complete list of the segmented regions is given in Supplementary Table S1 of Supplementary Materials. From the last 12 min of the static acquisitions (55–67 min post-injection) of both tracer activities, the mean SUVs normalized to the body weight (SUV_{BW}) were extracted for every volume of interest (VOI) and every participant. The mean SUV_{BW} extracted from the STD acquisitions were corrected according to Eq. 1, including the residual activity 90 min post-LD injection:

$$\text{Mean } SUV_{BW} = \frac{C_{VOI}\left[\frac{kBq}{mL}\right]}{A_{inj}[MBq] + A_{res}[MBq]} * BW[kg], \qquad (1)$$

where C_{VOI} is the activity concentration in the VOI, A_{inj} is the total injected activity, A_{res} is the residual activity 90 min post-LD

injection, and *BW* is the body weight [19]. The average SUV_{BW} and the corresponding standard deviations were evaluated for each VOI in both healthy controls and patients. Group averaged parameters were compared for both LD and STD conditions with %differences and unpaired sample t-tests. A p-value <0.05 was considered statistically significant. Intra-subject variability between the test–retest protocols was assessed with %differences and paired sample t-tests.

Lung cancer patients

The 3D Slicer [20] software was used to visualize the PET images of lung cancer patients. Otsu's method [21] was applied for image thresholding using the automatic option in 3D Slicer, highlighting regions in the images with pathologically increased signals (lesion). An experienced clinician manually fine-tuned lesion segmentations to visually refine lesion boundaries where necessary. FDG-avid lesions were first identified on LD-PET images and then on STD-PET images in order to prevent any potential bias caused by the improved image quality of the STD-PET data. The number of segmented lesions was compared to the clinical report of each patient.

The mean SUVs normalized for body weight were calculated for each lesion using data from the last 12 min of the PET acquisitions for both LD and STD. Corresponding volumes were extracted for both LD and STD acquisitions. The results were then compared using %differences and paired sample t-tests.

Literature comparison

The mean SUV_{BW} of organs in healthy controls undergoing STD-PET were compared to the SUV_{BW} ranges provided in [22], [23] (kidneys and skeletal muscle) and [24] (subcutaneous fat). References were chosen by ensuring that the study protocol (60 ± 10-min PET acquisitions with [18F]FDG) and participant demographics (age, sex, and weight distributions) were similar to those in the current study.

Effective dose estimations

Effective doses (EDs) were evaluated for both LD and STD protocols in healthy controls and lung cancer patients. Specifically, the radiation dose from the CT scans was estimated using the DLP multiplied by the conversion factor k, where k = 0.015 mSv/mGy*cm for whole-body CT examinations [25, 26]. The PET contribution to the effective dose was calculated by multiplying the injected activity with the dose coefficient Γ = 0.017 mSv/MBq for [18F]FDG [27]. The total effective doses were obtained by summing the individual CT and PET contributions, according to Eq. 2:

$$ED_{tot} = ED_{CT} + ED_{PET} = DLP[mGy^{*}cm]^{*}k\left[\frac{mSv}{mGy^{*}cm}\right] + A[MBq]^{*}\Gamma\left[\frac{mSv}{MBq}\right]. \quad (2)$$

The resulting effective doses for both LD and STD acquisitions were compared to dose estimates from the existing literature [28–31].

Results

Quantification of organs

Healthy controls

A complete list of the segmented regions, as well as the corresponding uptake values, is given in Supplementary Table S1 of Supplementary Materials. The mean SUV_{BW} of the target volumes ranged from 0.4 ± 0.1 (subcutaneous fat) to 6.4 ± 1.1 (brain) across healthy controls (Table 2). The mean SUV_{BW} from both LD and STD protocols were similar (absolute %difference ≤5%, Figure 2), except for the heart (absolute %difference = 14%). The group unpaired t-test underlined no statistical differences in any VOI ($p > 0.05$). In healthy controls, intra-subject variations in SUV_{BW} between test/retest scans were significant in the brain (average %difference = 5%, $p = 0.01$), heart (19%, $p = 0.04$), skeletal muscle (8%, $p = 0.01$), and adrenal glands (15%, $p = 0.03$) (Figure 3; Table 3).

Lung cancer patients

In lung cancer patients, the mean SUV_{BW} in the segmented regions varied, on average, from 0.4 ± 0.1 (subcutaneous fat) to 5.4 ± 1.0 (brain) (Table 4). In all the VOIs, the mean SUV_{BW} between test and retest scans were comparable (average absolute % difference ≤5%; Figure 4), except in the heart (20%). The group unpaired t-test indicated no statistical differences in any VOI ($p > 0.05$). Intra-patient changes in organ-based uptake values between test and retest scans were not significant (Figure 5; Table 5).

Lesion evaluation

A total of 10 FDG-avid lesions were observed and delineated on the LD images of the lung cancer patients. In contrast, 17 lesions were delineated on the STD images, a total number equivalent to the information provided in the clinical reports of the patients. Lesion volumes derived from LD images of the tumor were 41% smaller than those derived from the STD images (Supplementary Table S2). Seven lesions (<2 cm^3) were not detected on the LD-PET images (Figure 6). The mean SUV_{BW} values of correspondent lesions were similar in LD and STD acquisitions (10%, $p = 0.49$; Table 6). In patient #005, the lesion was visible only on the CT, and, therefore, no SUV was obtained.

Literature comparison

Organ-based mean SUV_{BW} values in the STD acquisitions of healthy controls were comparable to literature references (Figure 7). Across all organs, the assessed mean SUV_{BW} consistently fell within the ranges reported in previous studies [22–24]. Subcutaneous fat exhibited the least uptake values (0.4 ± 0.1), while the brain demonstrated the highest uptake (6.4 ± 1.1).

Effective dose estimations

For healthy controls, the average total effective dose was 2.5 ± 0.3 mSv for the test (LD-CT + LD-PET) and 6.7 ± 0.4 mSv for the

TABLE 2 Mean standardized uptake values normalized to the body weight (SUV_{BW}) group statistics for healthy controls.

Volume of interest	Test LD SUV_{BW}	Retest STD SUV_{BW}	Absolute difference (%)	Unpaired t-test
Brain	6.4 ± 1.1	6.6 ± 1.1	3	$p = 0.56$
Heart	3.0 ± 1.8	2.6 ± 1.5	14	$p = 0.46$
Kidneys	2.7 ± 0.5	2.8 ± 0.4	4	$p = 0.47$
Liver	2.0 ± 0.3	2.0 ± 0.3	1	$p = 0.85$
Pancreas	1.5 ± 0.2	1.5 ± 0.2	1	$p = 0.83$
Spleen	1.5 ± 0.2	1.5 ± 0.2	1	$p = 0.87$
Lung	0.6 ± 0.2	0.6 ± 0.1	5	$p = 0.49$
Skeletal muscle	0.6 ± 0.1	0.6 ± 0.1	5	$p = 0.25$
Subcutaneous fat	0.4 ± 0.1	0.4 ± 0.1	3	$p = 0.61$

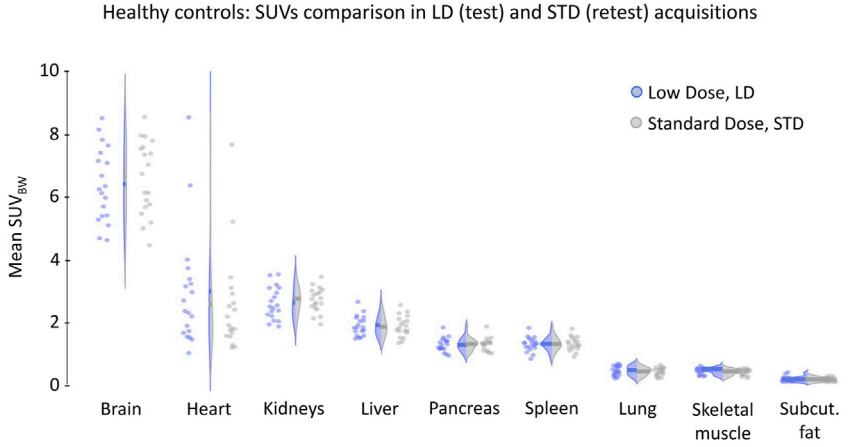

FIGURE 2
Comparison of the mean standardized uptake values normalized to the body weight (SUV_{BW}) in low-dose (LD) (blue, test) and standard-dose (STD) (gray, retest) acquisitions across 19 healthy controls.

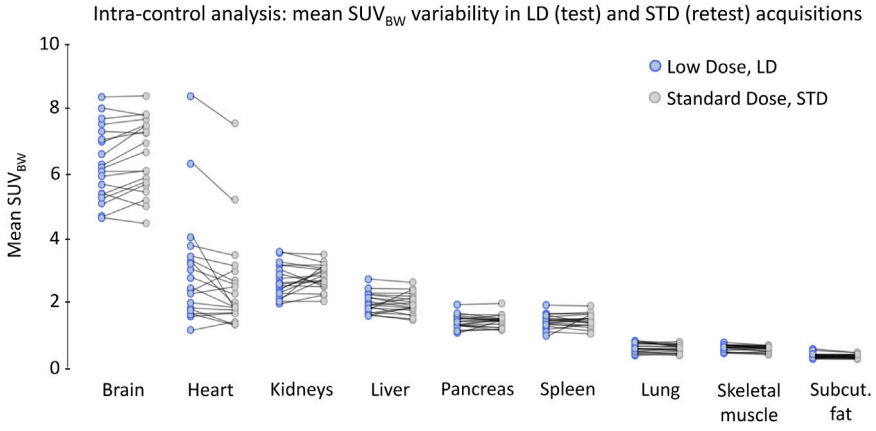

FIGURE 3
Intra-subject variability of the mean SUV_{BW} in LD (blue, test) and STD (gray, retest) acquisitions of 19 healthy controls.

TABLE 3 Intra-subject variability of the mean SUV_{BW} between LD/STD scans of healthy controls. Organs with statistically significant differences in LD/STD SUV are indicated in red.

Volume of interest	Absolute difference (%)	Paired t-test
Brain	5	$p = 0.01$
Heart	19	$p = 0.04$
Kidneys	10	$p = 0.21$
Liver	7	$p = 0.68$
Pancreas	7	$p = 0.63$
Spleen	8	$p = 0.77$
Lung	9	$p = 0.05$
Skeletal muscle	8	$p = 0.01$
Subcutaneous fat	8	$p = 0.24$

TABLE 4 Mean SUV_{BW} group statistics for lung cancer patients.

Volume of interest	Test LD SUV_{BW}	Retest STD SUV_{BW}	Absolute difference (%)	Unpaired t-test
Brain	5.3 ± 1.0	5.4 ± 0.9	2	$p = 0.79$
Heart	3.0 ± 1.8	3.0 ± 1.3	1	$p = 0.97$
Kidneys	2.9 ± 0.5	2.9 ± 0.3	1	$p = 0.85$
Liver	2.2 ± 0.4	2.3 ± 0.4	1	$p = 0.91$
Pancreas	1.5 ± 0.3	1.4 ± 0.2	3	$p = 0.74$
Spleen	1.6 ± 0.2	1.6 ± 0.1	2	$p = 0.74$
Lung	0.6 ± 0.2	0.6 ± 0.2	2	$p = 0.91$
Skeletal muscle	0.7 ± 0.1	0.6 ± 0.1	4	$p = 0.91$
Subcutaneous fat	0.4 ± 0.1	0.4 ± 0.1	3	$p = 0.91$

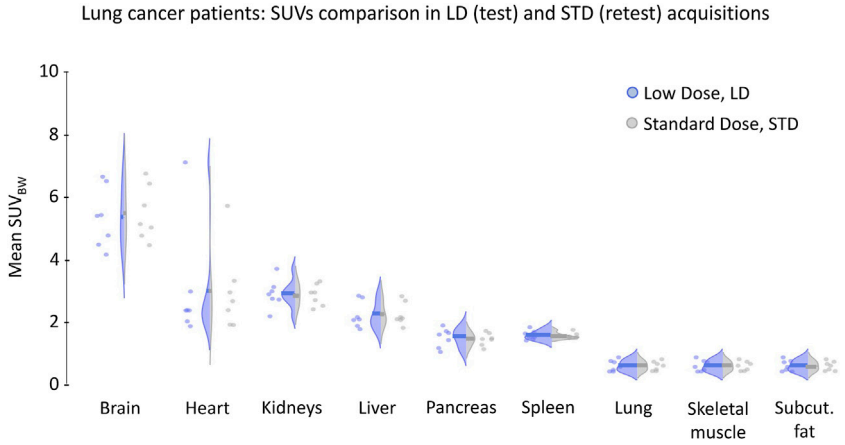

FIGURE 4
Comparison of the mean SUV_{BW} in LD (blue, test) and STD (gray, retest) acquisitions of seven lung cancer patients.

retest (LD-CT + STD-PET), respectively. The contribution from the PET scan to these total effective doses was 0.5 ± 0.1 mSv for the test (20%) and 4.8 ± 0.3 mSv for the retest acquisition (72%).

In cancer patients, the average effective dose contribution from the STD-CT was 16.6 ± 5.4 mSv (81%) to a total effective dose of 21.3 ± 5.4 mSv. With the LD-PET/CT protocol, the total effective

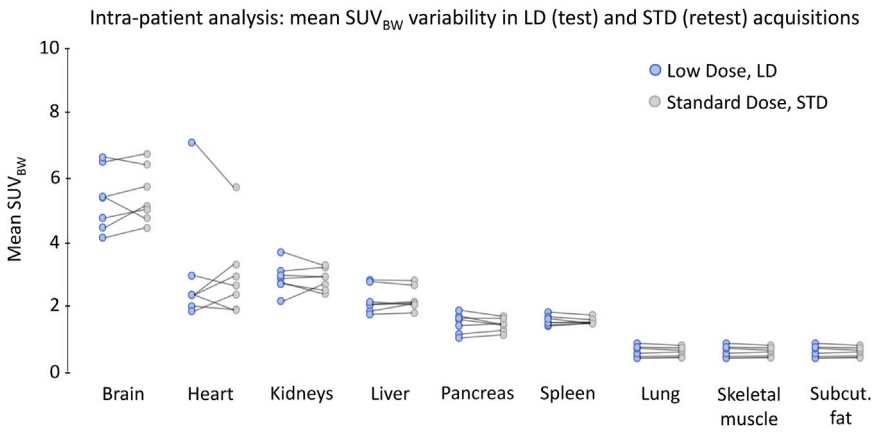

FIGURE 5
Intra-subject variability of the mean SUV_{BW} in LD (blue, test) and STD (gray, retest) acquisitions of seven lung cancer patients.

TABLE 5 Intra-subject variability of the mean SUV_{BW} between LD/STD scans of lung cancer patients.

Volume of interest	Absolute difference (%)	Paired t-test
Brain	7	$p = 0.44$
Heart	20	$p = 0.91$
Kidneys	8	$p = 0.74$
Liver	4	$p = 0.57$
Pancreas	8	$p = 0.42$
Spleen	4	$p = 0.47$
Lung	5	$p = 0.53$
Skeletal muscle	7	$p = 0.22$
Subcutaneous fat	4	$p = 0.16$

dose was reduced to 2.4 ± 0.1 mSv, while the relative contribution (1.9 ± 0.2 mSv) from the CT remained the same (79%). Table 7 summarizes the complete dose records in both groups of subjects.

Discussion

This study evaluated variations in organ uptake in [18F]FDG-PET/CT images of healthy controls and lung cancer patients undergoing a dual-injection, dual-scan protocol. We demonstrate similar uptake values in key organs for both LD- and STD-PET imaging, with an exception in the heart on a group-based level. Intra-subject variabilities were highest in the brain (7%), skeletal muscles (8%), and heart (20%). All mean SUV_{BW} were comparable with previously recorded literature values (Figure 7) [22–24]. While our study suggests equivalence of LD- and STD-PET imaging protocols for organ-based quantification in healthy controls, care must be taken when assessing patients since the LD protocol yielded a lower detection rate of actual lesions (Figure 6).

In the present study, test and retest [18F]FDG PET/CT scans were set apart by 90 min (Figure 1), without significant differences in the group mean SUV_{BW} in key organs (Figures 2, 4) in both healthy controls and lung cancer patients. The intra-subject variability in organ uptakes between LD and STD was also explored. Significant changes in the mean uptake values from test to retest scans of healthy controls were observed in the brain, heart, adrenal glands, and, to a lesser extent, in skeletal muscles (Figure 3; Table 3, Supplementary Table S1). Physiological changes in both the brain and heart can affect the SUVs measured from two PET scans acquired at different time points. This may include changes in blood flow, metabolism, and cardiac function [32–36], which are most likely to occur within the 90 min between the two scans. Notably, in all healthy controls, skeletal muscle uptake was somewhat higher in the test (LD) than in the retest (STD) acquisition (8%, Table 3). This decrease in muscle uptake during the retest protocol could indicate reduced stress and tension levels [37] in participants, who may have relaxed after undergoing the protocol once before. The intra-subject differences in brain, adrenal glands, and skeletal muscle SUVs for LD/STD acquisitions were found only in the healthy cohort (Figure 5; Table. 5), likely because of the increased variability provided by its larger cohort size than that of the patients (Table 1). Inaccurate segmentations may have altered some results as well. For example, adrenal gland uptakes might have been affected by segmentation errors due to their small

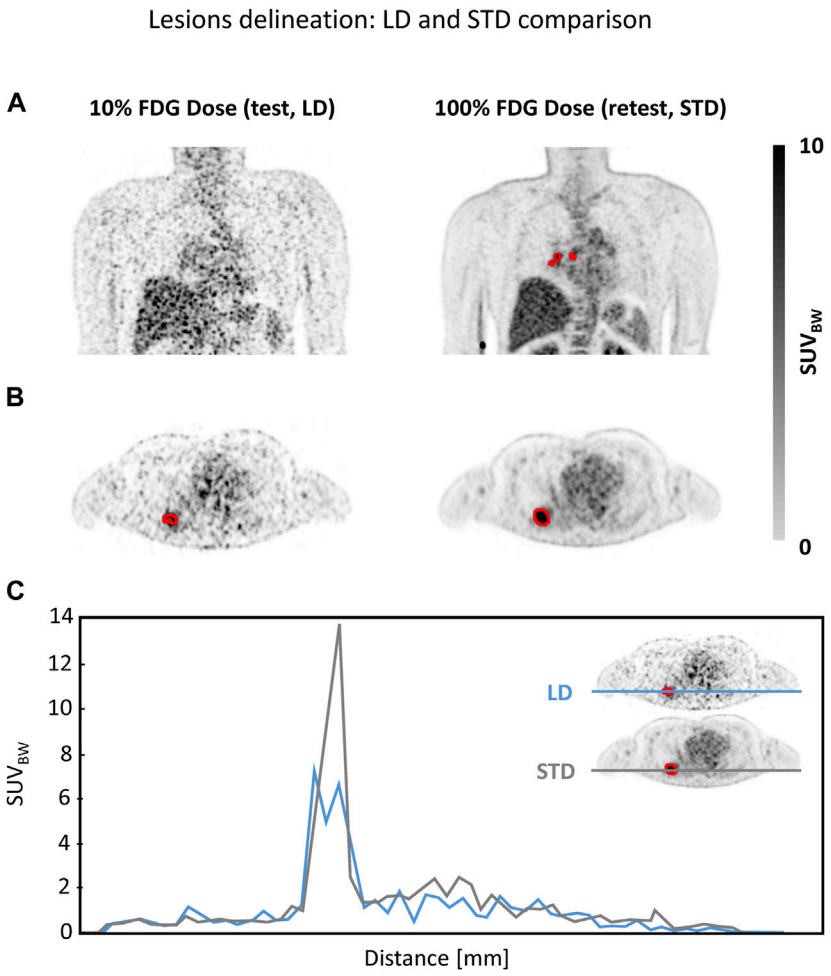

FIGURE 6
Visual comparison of lesion delineation on **(A)** coronal and **(B)** transverse images of LD and STD protocols of Pat-001. The LD images failed to detect the smallest fluoro-2-deoxy-D-glucose (FDG)-positive lesions. The primary lesion delineation in the LD image is smaller in volume and different in shape from the corresponding lesion delineation in the STD image. **(C)** Line profiles of the lesion segmented from the transverse LD (blue) and STD (gray) PET image of Pat-001.

size and low contrast with surrounding tissues, posing a challenge in distinguishing them from other structures, such as the kidneys and the liver [18], in the LD-CT image.

Imaging of lung cancer patients showed similar mean SUV_{BW} between LD and STD scans in all segmented organs. However, fewer FDG-avid lesions were identified on LD-PET images than on STD-PET images (Figure 6). Given the increased image noise levels in LD imaging, only 10 lesions were delineated from the LD images (at 10% activity injection), while 17 lesions were subsequently identified on the STD acquisitions. Specifically, delineations of seven smaller lesions (<2 cm^3) were not possible from LD images, given the increased noise level (Figure 6). In addition, the volumes of lesions were generally smaller in segmentations obtained from LD images due to reduced image quality. Nonetheless, the SUV_{BW} values of the corresponding lesions were similar in the LD and STD acquisitions, with a mean % difference equal to 10% (Table 6).

Overall, these findings suggest that low-dose FDG-PET/CT imaging may be a valuable option for reducing radiation exposure in FDG-PET/CT imaging for composing a normative database of healthy control values [9]. Our SUV_{BW} readouts for both STD and LD acquisitions were similar to published literature values [22–24]. Although variations in the mean SUV_{BW} values in organs with high metabolic activity and glucose turnover, such as the brain and the heart, were observed, the results were still consistent with the references in terms of both mean values and the minimum and maximum ranges of SUV_{BW} reported (Figure 7).

Effective doses from STD-PET were also consistent with established references for the standard clinical practice [28, 29]. Administering an activity that is 90% lower than that of the standard dose resulted in a 67% reduction in the total effective dose in healthy controls, thus effectively addressing concerns regarding radiation exposure in FDG-PET/CT imaging, particularly for non-clinical indications.

Exposure from CT plays a significant role in the overall effective dose during a standard examination. Using contrast-enhanced dual-phase CT (STD-CT) in cancer patients contributed 79% to their total effective dose, which, instead, was drastically reduced with the low-dose CT (2 mSv) protocol (Table 7). Mostafapour et al. demonstrated that the radiation dose in CT imaging could be further reduced from an effective dose of 2.6 mSv to less than 0.1 mSv by incorporating a tin filter for noise reduction [31].

10.3389/fphy.2024.1378521

TABLE 6 Mean SUV_{BW} statistics of delineated lesions. Average value and P value are indicated in bold.

Lesion ID	Test LD SUV_{BW}	Retest STD SUV_{BW}	Absolute difference
Pat-001_vol1	9.1 ± 1.6	5.9 ± 2.8	42%
Pat-001_vol2	-	6.0 ± 1.7	-
Pat-001_vol3	-	5.8 ± 1.4	-
Pat-001_vol4	-	3.6 ± 1.0	-
Pat-001_vol5	-	4.9 ± 0.6	-
Pat-002_vol1	2.6 ± 0.3	2.4 ± 0.4	9%
Pat-003_vol1	5.9 ± 0.6	6.4 ± 1.0	8%
Pat-003_vol2	-	2.6 ± 0.2	-
Pat-003_vol3	-	4.1 ± 1.0	-
Pat-003_vol4	-	3.1 ± 0.6	-
Pat-004_vol1	8.6 ± 2.6	8.5 ± 2.7	1%
Pat-006_vol1	8.0 ± 2.1	7.5 ± 2.3	7%
Pat-006_vol2	8.2 ± 2.3	7.5 ± 2.2	9%
Pat-006_vol3	7.1 ± 1.2	6.4 ± 1.4	10%
Pat-006_vol4	10.0 ± 2.8	8.0 ± 3.0	22%
Pat-006_vol5	6.5 ± 0.8	6.6 ± 1.4	1%
Pat-007_vol1	5.1 ± 0.6	4.9 ± 0.5	5%
Average			**(10 ± 14) %**
Paired T-test			**p = 0.49**

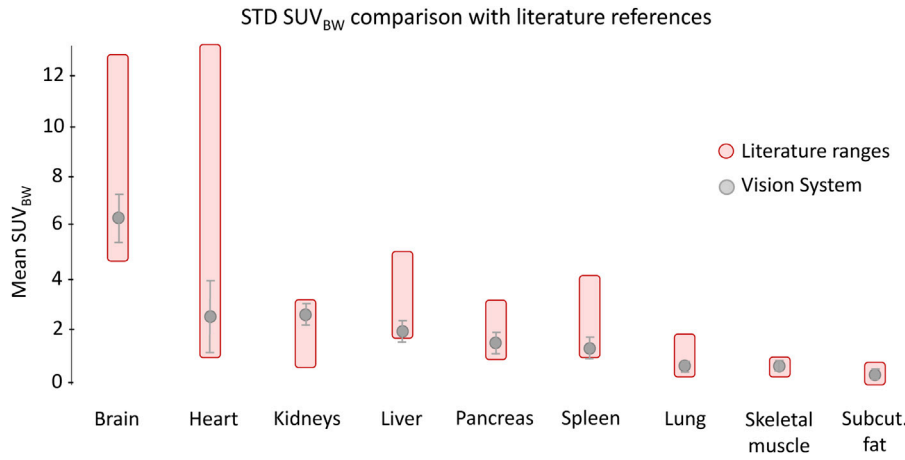

FIGURE 7
Mean SUV_{BW} comparison from STD acquisitions of healthy controls (Siemens Biograph Vision 600; gray). Red bars represent the literature ranges of minimum and maximum SUV_{BW} from [22–24].

However, potential artifacts from noise amplification during CT-based attenuation and scatter correction await further study.

Our study has several limitations. First, it was constrained by its small sample size. A larger cohort of participants could yield more reliable statistical results. Lesion delineation was performed by a single clinician, thus introducing a subjective bias into volume segmentations. The use of average delineations by multiple clinicians would offer a more precise reference. Next, LD PET imaging resulted in lower image quality, compromising its validity for clinical indications. Our study did not explore techniques to reduce noise in LD-PET images, such as AI-based image denoising methods [38, 39] or adjusted image reconstruction parameters for enhanced diagnostic accuracy [12, 40]. In our study, the

TABLE 7 Dose reports of participants in LD and STD acquisitions.

Test (LD acquisition)	ED_{CT} [mSv]	ED_{PET} [mSv]	ED_{TOT} [mSv]
Controls	2.0 ± 0.3	0.5 ± 0.1	2.5 ± 0.3
Patients	1.9 ± 0.2	0.5 ± 0.1	2.4 ± 0.1
Retest (STD acquisition)			
Controls	2.0 ± 0.3	4.8 ± 0.3	6.7 ± 0.4
Patients	16.6 ± 5.4	4.6 ± 0.3	21.3 ± 5.4

retest protocol started 90 min after the test injection, followed by an additional hour of dynamic acquisition before static reconstruction. During this period, a portion of LD activity remains undecayed and may exert a minor influence on the subsequent quantification of STD uptakes. Considering our initial injected LD activity of 28 MBq and the behavior of [18F]FDG kinetic signals at long uptake times [41–43], we anticipate an impact smaller than 5% at the time of STD static acquisition on our uptake quantifications. Last, the present study focused solely on the analysis of static images, neglecting the dynamic information of PET images. For instance, Liu et al. demonstrated that whole-body dynamic PET imaging with a 10-fold reduction in injected activity could provide relevant kinetic metrics of [18F]FDG and comparable image contrast to full-activity imaging [44]. The parametric assessment of LD-PET could contribute valuable information to the evaluation of a reference database of normal PET values in healthy controls.

Conclusion

The study demonstrated that a reduction of 90% in the administered [18F]FDG activity is feasible for semi-quantitative whole-body PET/CT imaging without loss of accuracy of organ-based SUV_{BW} assessment. LD and STD injections provided comparable mean SUV_{BW} of organs in both healthy controls and lung cancer patients, except in organs with fast a [18F]FDG turnover. However, LD images did not provide sufficient clinical quality for the diagnostic assessment of lung cancer patients. Thus, our study supports the general adoption of LD-PET/CT imaging data for imaging healthy controls for the purpose of building an organ-based normative database.

Data availability statement

The original contributions presented in the study are included in the article/Supplementary Material; further inquiries can be directed to the corresponding author.

Ethics statement

The studies involving humans were approved by the Ethics Committee of the Medical University of Vienna (EK1907/2020). The studies were conducted in accordance with the local legislation and institutional requirements. The participants provided their written informed consent to participate in this study.

Author contributions

DF: writing–original draft and writing–review and editing. LS: writing–original draft and writing–review and editing. ZC: writing–original draft and writing–review and editing. BG: writing–original draft and writing–review and editing. DG: writing–original draft and writing–review and editing. SG: writing–original draft and writing–review and editing. MH: writing–original draft and writing–review and editing. HK: writing–original draft and writing–review and editing. KK: writing–original draft and writing–review and editing. MI: writing–original draft and writing–review and editing. WL: writing–original draft and writing–review and editing. JY: writing–original draft and writing–review and editing. IR: writing–original draft and writing–review and editing. TB: writing–original draft and writing–review and editing.

Funding

The author(s) declare that financial support was received for the research, authorship, and/or publication of this article. DF and JY were supported through research funding from the Austrian Science Fund (FWF): I 5902-B. This research was funded in whole or in part by the Austrian Science Fund (FWF) [10.55776/I5902]. SG is supported by a joint research agreement between Siemens Healthineers and the Medical University Vienna. The funder Siemens Healthineers was not involved in the study design, analysis, interpretation of data, the writing of this article or the decision to submit it for publication. For open-access purposes, the authors have applied a CC BY public copyright license to any author-accepted manuscript version arising from this submission.

Acknowledgments

The authors thank Harald Ibeschitz, Ingrid Leitinger, and Rainer Bartosch for their contributions to this project. In addition to acquiring the PET/CT images of the participants, they provided valuable input and assistance in the development of this study.

Conflict of interest

The authors declare that the research was conducted in the absence of any commercial or financial relationships that could be construed as a potential conflict of interest.

The author(s) declared that they were an editorial board member of Frontiers, at the time of submission. This had no impact on the peer review process and the final decision.

Publisher's note

All claims expressed in this article are solely those of the authors and do not necessarily represent those of their affiliated organizations, or those of the publisher, the editors, and the reviewers. Any product that may be evaluated in this article, or claim that may be made by its manufacturer, is not guaranteed or endorsed by the publisher.

Supplementary material

The Supplementary Material for this article can be found online at: https://www.frontiersin.org/articles/10.3389/fphy.2024.1378521/full#supplementary-material

References

1. Beyer T, Townsend DW, Brun T, Kinahan PE, Charron M, Roddy R, et al. A combined PET/CT scanner for clinical oncology. *J Nucl Med* (2000) 41:1369–79.

2. Bastiaannet E, Groen H, Jager PL, Cobben DCP, van der Graaf WTA, Vaalburg W, et al. The value of FDG-PET in the detection, grading and response to therapy of soft tissue and bone sarcomas; a systematic review and meta-analysis. *Cancer Treat Rev* (2004) 30:83–101. doi:10.1016/j.ctrv.2003.07.004

3. Townsend DW. Dual-modality imaging: combining anatomy and function. *J Nucl Med* (2008) 49:938–55. doi:10.2967/jnumed.108.051276

4. Wechalekar K, Sharma B, Cook G. PET/CT in oncology—a major advance. *Clin Radiol* (2005) 60:1143–55. doi:10.1016/j.crad.2005.05.018

5. Spencer BA, Berg E, Schmall JP, Omidvari N, Leung EK, Abdelhafez YG, et al. Performance evaluation of the uEXPLORER total-body PET/CT scanner based on NEMA NU 2-2018 with additional tests to characterize PET scanners with a long axial field of view. *J Nucl Med* (2021) 62:861–70. doi:10.2967/jnumed.120.250597

6. Nadig V, Herrmann K, Mottaghy FM, Schulz V. Hybrid total-body pet scanners—current status and future perspectives. *Eur J Nucl Med Mol Imaging* (2022) 49:445–59. doi:10.1007/s00259-021-05536-4

7. van Sluis J, van Snick JH, Brouwers AH, Noordzij W, Dierckx RAJO, Borra RJH, et al. EARL compliance and imaging optimisation on the Biograph Vision Quadra PET/CT using phantom and clinical data. *Eur J Nucl Med Mol Imaging* (2022) 49:4652–60. doi:10.1007/s00259-022-05919-1

8. Sundar LKS, Hacker M, Beyer T. Whole-body PET imaging: a catalyst for whole-person research? *J Nucl Med* (2022) 64:197–9. doi:10.2967/jnumed.122.264555

9. Gutschmayer S, Muzik O, Hacker M, Ferrara D, Zuehlsdorff S, Newiger H, et al. Towards holistic assessment of human physiology: fully-automated construction of tracer independent total-body PET/CT normative database using diffeomorphisms [abstract]. In: Annual Congress of the European Association of Nuclear Medicine; October 15-19; Barcelona, Spain. Springer Science and Business Media LLC (2022). 225–6.

10. Tan H, Cai D, Sui X, Qi C, Mao W, Zhang Y, et al. Investigating ultra-low-dose total-body [18F]-FDG PET/CT in colorectal cancer: initial experience. *Eur J Nucl Med Mol Imaging* (2022) 49:1002–11. doi:10.1007/s00259-021-05537-3

11. Calderón E, Schmidt FP, Lan W, Castaneda-Vega S, Brendlin AS, Trautwein NF, et al. Image quality and quantitative PET parameters of low-dose [18F]FDG PET in a long axial field-of-view PET/CT scanner. *Diagnostics (Basel)* (2023) 13:3240. doi:10.3390/diagnostics13203240

12. Kertész H, Beyer T, London K, Saleh H, Chung D, Rausch I, et al. Reducing radiation exposure to paediatric patients undergoing [18F]FDG-PET/CT imaging. *Mol Imaging Biol* (2021) 23:775–86. doi:10.1007/s11307-021-01601-4

13. Prieto E, García-Velloso MJ, Rodríguez-Fraile M, Morán V, García-García B, Guillén F, et al. Significant dose reduction is feasible in FDG PET/CT protocols without compromising diagnostic quality. *Phys Med* (2018) 46:134–9. doi:10.1016/j.ejmp.2018.01.021

14. Tan H, Qi C, Cao Y, Cai D, Mao W, Yu H, et al. Ultralow-dose [18F]FDG PET/CT imaging: demonstration of feasibility in dynamic and static images. *Eur Radiol* (2023) 33:5017–27. doi:10.1007/s00330-023-09389-3

15. Kinahan PE, Fletcher JW. Positron emission tomography-computed tomography standardized uptake values in clinical practice and assessing response to therapy. *Semin Ultrasound CT MR* (2010) 31:496–505. doi:10.1053/j.sult.2010.10.001

16. van Sluis J, de Jong J, Schaar J, Noordzij W, van Snick P, Dierckx R, et al. Performance characteristics of the digital Biograph vision PET/CT system. *J Nucl Med* (2019) 60:1031–6. doi:10.2967/jnumed.118.215418

17. Wachabauer D, Beyer T, Ditto M, Gallowitsch H-J, Hinterreiter M, Ibi B, et al. Diagnostic Reference Levels for nuclear medicine imaging in Austria: a nationwide survey of used dose levels for adult patients. *Z Med Phys* (2022) 32:283–95. doi:10.1016/j.zemedi.2021.11.007

18. Sundar LKS, Yu J, Muzik O, Kulterer OC, Fueger B, Kifjak D, et al. Fully automated, semantic segmentation of whole-body 18F-FDG PET/CT images based on data-centric artificial intelligence. *J Nucl Med* (2022) 63:1941–8. doi:10.2967/jnumed.122.264063

19. Boellaard R, O'Doherty MJ, Weber WA, Mottaghy FM, Lonsdale MN, Stroobants SG, et al. FDG PET and PET/CT: EANM procedure guidelines for tumour PET imaging: version 1.0. *Eur J Nucl Med Mol Imaging* (2010) 37:181–200. doi:10.1007/s00259-009-1297-4

20. Fedorov A, Beichel R, Kalpathy-Cramer J, Finet J, Fillion-Robin J-C, Pujol S, et al. 3D slicer as an image computing platform for the quantitative imaging network. *Magn Reson Imaging* (2012) 30:1323–41. doi:10.1016/j.mri.2012.05.001

21. Otsu N. A threshold selection method from gray-level histograms. *IEEE Trans Syst Man Cybern* (1979) 9:62–6. doi:10.1109/tsmc.1979.4310076

22. Zincirkeser S, Sahin E, Halac M, Sager S. Standardized uptake values of normal organs on 18F-fluorodeoxyglucose positron emission tomography and computed tomography imaging. *J Int Med Res* (2007) 35:231–6. doi:10.1177/147323000703500207

23. Dias AH, Hansen AK, Munk OL, Gormsen LC. Normal values for 18F-FDG uptake in organs and tissues measured by dynamic whole body multiparametric FDG PET in 126 patients. *EJNMMI Res* (2022) 12:15. doi:10.1186/s13550-022-00884-0

24. Oliveira AL, Azevedo DC, Bredella MA, Stanley TL, Torriani M. Visceral and subcutaneous adipose tissue FDG uptake by PET/CT in metabolically healthy obese subjects. *Obesity (Silver Spring)* (2015) 23:286–9. doi:10.1002/oby.20957

25. Martí-Climent JM, Prieto E, Morán V, Sancho L, Rodríguez-Fraile M, Arbizu J, et al. Effective dose estimation for oncological and neurological PET/CT procedures. *EJNMMI Res* (2017) 7:37. doi:10.1186/s13550-017-0272-5

26. Huda W, Magill D, He W. CT effective dose per dose length product using ICRP 103 weighting factors. *Med Phys* (2011) 38:1261–5. doi:10.1118/1.3544350

27. Mattsson S, Johansson L, Leide Svegborn S, Liniecki J, Noßke D, Stabin M, et al. Radiation dose to patients from radiopharmaceuticals (2024). Available at: https://www.icrp.org/docs/Radiation%20Dose%20to%20Patients%20from%20Radiopharmaceuticals%20-%20A%20fourth%20addendum%20to%20ICRP%20Publication%2053.pdf (Accessed March 25, 2024).

28. Brix G, Lechel U, Glatting G, Ziegler SI, Münzing W, Müller SP, et al. Radiation exposure of patients undergoing whole-body dual-modality 18F-FDG PET/CT examinations. *J Nucl Med* (2005) 46:608–13.

29. Avramova-Cholakova S, Ivanova S, Petrova E, Garcheva M, Vassileva J. Patient doses from PET-CT procedures. *Radiat Prot Dosimetry* (2015) 165:430–3. doi:10.1093/rpd/ncv128

30. Sabri ASA, Wong JHD. Estimation of effective dose for whole body 18F-FDG PET/CT examination. *J Phys Conf Ser* (2019) 1248:012006. doi:10.1088/1742-6596/1248/1/012006

31. Mostafapour S, Greuter M, van Snick JH, Brouwers AH, Dierckx RAJO, van Sluis J, et al. Ultra-low dose CT scanning for PET/CT. *Med Phys* (2024) 51:139–55. doi:10.1002/mp.16862

32. Camargo EE, Szabo Z, Links JM, Sostre S, Dannals RF, Wagner HN, Jr. The influence of biological and technical factors on the variability of global and regional brain metabolism of 2-[18F]fluoro-2-deoxy-D-glucose. *J Cereb Blood Flow Metab* (1992) 12:281–90. doi:10.1038/jcbfm.1992.38

33. Minamimoto R. Series of myocardial FDG uptake requiring considerations of myocardial abnormalities in FDG-PET/CT. *Jpn J Radiol* (2021) 39:540–57. doi:10.1007/s11604-021-01097-6

34. Schaefer SM, Abercrombie HC, Lindgren KA, Larson CL, Ward RT, Oakes TR, et al. Six-month test-retest reliability of MRI-defined PET measures of regional cerebral glucose metabolic rate in selected subcortical structures. *Hum Brain Mapp* (2000) 10:1–9. doi:10.1002/(sici)1097-0193(200005)10:1<1::aid-hbm10>3.0.co;2-o

35. Shiyam SLK, Muzik O, Rischka L, Hahn A, Lanzenberger R, Hienert M, et al. Promise of fully integrated PET/MRI: noninvasive clinical quantification of cerebral glucose metabolism. *J Nucl Med* (2020) 61:276–84. doi:10.2967/jnumed.119.229567

36. Thut DP, Ahmed R, Kane M, Djekidel M. Variability in myocardial metabolism on serial tumor (18)F-FDG PET/CT scans. *Am J Nucl Med Mol Imaging* (2014) 4:346–53.

37. Karunanithi S, Soundararajan R, Sharma P, Naswa N, Bal C, Kumar R. Spectrum of physiologic and pathologic skeletal muscle 18F-FDG uptake on PET/CT. *Am J Roentgenology* (2015) 205:W141–9. doi:10.2214/ajr.14.13457

38. Weyts K, Lasnon C, Ciappuccini R, Lequesne J, Corroyer-Dulmont A, Quak E, et al. Artificial intelligence-based PET denoising could allow a two-fold reduction in [18F]FDG PET acquisition time in digital PET/CT. *Eur J Nucl Med Mol Imaging* (2022) 49:3750–60. doi:10.1007/s00259-022-05800-1

39. Boudjelal A, Elmoataz A, Attallah B, Messali Z. A novel iterative MLEM image reconstruction algorithm based on beltrami filter: application to ECT images. *Tomography* (2021) 7:286–300. doi:10.3390/tomography7030026

40. Kertész H, Traub-Weidinger T, Cal-Gonzalez J, Rausch I, Muzik O, Shyiam Sundar LK, et al. Feasibility of dose reduction for [18F]FDG-PET/MR imaging of patients with non-lesional epilepsy. *Nuklearmedizin* (2023) 62:200–13. doi:10.1055/a-2015-7785

41. Wangerin KA, Muzi M, Peterson LM, Linden HM, Novakova A, O'Sullivan F, et al. Effect of 18F-FDG uptake time on lesion detectability in PET imaging of early stage breast cancer. *Tomography* (2015) 1:53–60. doi:10.18383/j.tom.2015.00151

42. Chin BB, Green ED, Turkington TG, Hawk TC, Coleman RE. Increasing uptake time in FDG-PET: standardized uptake values in normal tissues at 1 versus 3 h. *Mol Imaging Biol* (2009) 11:118–22. doi:10.1007/s11307-008-0177-9

43. Laffon E, Adhoute X, de Clermont H, Marthan R. Is liver SUV stable over time in 18F-FDG PET imaging? *J Nucl Med Technol* (2011) 39:258–63. doi:10.2967/jnmt.111.090027

44. Liu G, Hu P, Yu H, Tan H, Zhang Y, Yin H, et al. Ultra-low-activity total-body dynamic PET imaging allows equal performance to full-activity PET imaging for investigating kinetic metrics of 18F-FDG in healthy volunteers. *Eur J Nucl Med Mol Imaging* (2021) 48:2373–83. doi:10.1007/s00259-020-05173-3

Frontiers in Physics

Investigates complex questions in physics to understand the nature of the physical world

Addresses the biggest questions in physics, from macro to micro, and from theoretical to experimental and applied physics.

Discover the latest Research Topics

See more →

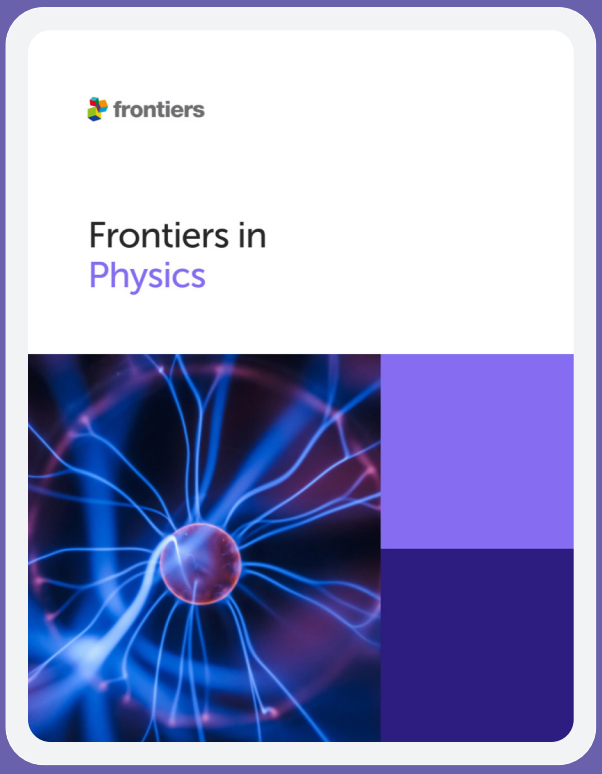

Frontiers

Avenue du Tribunal-Fédéral 34
1005 Lausanne, Switzerland
frontiersin.org

Contact us

+41 (0)21 510 17 00
frontiersin.org/about/contact